ETH
Eidgenössische Technische Hochschule Zürich
Swiss Federal Institute of Technology Zurich

DISS. ETH NO.: 26029

Effect of non-condensable gases on reflux condensation in nuclear steam generator tubes

A thesis submitted to attain the degree of
DOCTOR OF SCIENCES of ETH ZURICH
(Dr. sc. ETH Zurich)

presented by:
Filip Janasz

MSc in Mechanical Engineering, TU Lodz

Born on 11.10.1987
Citizen of Poland

Accepted at the recommendation of:

Prof. Dr. Horst-Michael Prasser
Prof. Dr. Andrey V. Mityakov
Prof. Dr. Karen Vierow Kirkland

2019

Table of Contents

Table of Contents 3
List of figures 8
List of tables 15
Nomenclature 16
Acknowledgements 18
Abstract 20
Zusammenfassung 21
Chapter 1 Introduction and motivation 22
1.1 Reflux condensation in PWR 22
1.2 Condensation in the presence of NC gases 23
1.3 Dropwise condensation - DWC 24
1.3.1 Pure vapor 24
1.3.2 Vapor with NC gases 26
1.4 Film condensation - FC 26
1.4.1 Pure vapor 26
1.4.2 Vapor with NC gases 28
1.5 Motivation summary 34
Chapter 2 Infrastructure – PRECISE facility 36
2.1 Reflux condensation modelling 36
2.2 Facility operating conditions 39
2.2.1 Overview 39
2.2.2 Counter-current flow limitation 40
2.3 Facility – technical description 41
2.3.1 Primary loop 42
2.3.2 Secondary loop 44
2.3.3 Facility location 45
2.4 Facility control and operation 47
2.4.1 Primary loop control 47
2.4.2 Secondary loop control 48

Chapter 3 Data Acquisition 50
3.1 DAS Hardware - Overview 50
3.2 Condensation tube sensor positions 51
3.3 Gradient Heat Flux Sensor 53
3.3.1 Overview 53
3.3.2 Operating principle 53
3.3.3 GHFS types 56
3.3.4 Signal acquisition 57
3.3.5 Calibration procedure 57
3.3.6 Installation in the PRECISE facility 63
3.3.7 GHFS frequency response 65
3.4 Movable conductivity and temperature probe 67
3.4.1 Overview 67
3.4.2 Probe design and installation in the PRECISE facility 68
3.4.3 Electrode array operating principles 72
3.4.4 Signal acquisition 78
3.4.5 Calibration procedure 80
3.5 Other instruments 87
3.5.1 Thermocouples 87
3.5.2 PT-100 resistive thermometers 87
3.5.3 Pressure transducers 88
3.5.4 Heating power measurement 88
3.5.5 Coolant flow 89
Chapter 4 Error propagation 90
4.1 Measurement sensors' and DAS properties 90
4.2 Measured properties errors 92
4.2.1 Temperature 92
4.2.2 Steam / water pressure 92
4.2.3 Heating voltage / current 93
4.2.4 Volumetric flow 93
4.2.5 Heat flux 93
4.2.6 Film thickness 96
4.3 Derived properties errors 99

Chapter 5 Experiments 103
5.1 General description 103
5.2 Experimental procedures 103
5.2.1 Steady state tests 103
5.2.2 Continuous injection tests 107
5.3 NC gases pre- and post-calculation 108
5.3.1 Pre-calculation procedure 108
5.3.2 Equation of state – discussion 111
5.3.3 Post-calculation procedure 112
Chapter 6 Experimental results 115
6.1 Steady state tests 115
6.1.1 Coolant velocity and wall temperature gradient 116
6.1.2 Impact of test tube pressure 122
6.1.3 Impact of NC gases – nitrogen 127
6.1.4 Impact of NC gases – helium 134
6.1.5 Impact of NC gases mixture composition 137
6.2 Continuous injection tests 141
6.2.1 Experiments summary 141
6.2.2 Mixing zone passage – calculations 141
6.2.3 Mixing zone – He and N_2 effects 145
6.3 Liquid film and thermal boundary layer 148
6.3.1 Traversing probe 148
6.3.2 Fixed array and electrical measurements 150
6.3.3 Thermal boundary layer and NC gas mixture composition 153
6.4 Heat flux measurements 154
6.4.1 Gas stratification impact 154
6.4.2 Gas mixture composition effect 156
6.4.3 Continuous injection tests 158
6.4.4 Higher frequency phenomena 160
6.4.5 GHFS derived htc and theory 163
Chapter 7 RELAP5 calculations 165
7.1 Overview 165
7.2 RELAP5 reflux condensation modelling 165

7.3 RELAP5 Variable glossary 166
7.4 PRECISE nodalization 167
7.4.1 Nodalization scheme 1 167
7.4.2 Nodalization scheme 2 169
7.4.3 Nodalization and calculation results 172
7.5 Boundary and initial conditions 175
7.6 Calculation results – reaching steady state 176
7.7 Calculation results – pure steam 179
7.7.1 Residual NC gases modelling 179
7.7.2 Gas and temperature distributions 183
7.8 Calculation results – NC gases 185
7.8.1 Nitrogen 185
7.8.2 Helium 188
7.9 RELAP5 calculations - summary 189
Chapter 8 Summary and outlook 190
8.1 Measurement technique 190
8.1.1 Movable conductivity and temperature probe 190
8.1.2 Heat flux sensor 191
8.2 Condensation experiments 192
8.2.1 Effect of test pressure, temperature and coolant water properties 192
8.2.2 Non-condensable gas plug formation 192
8.2.3 Higher frequency phenomena 193
8.3 RELAP5 simulations 193
8.4 Outlook and recommendations 194
Chapter 9 Bibliography 195
Chapter 10 Appendix 206
10.1 PRECISE facility primary loop schematic 206
10.2 PRECISE facility secondary loop schematic 207
10.3 PRECISE facility and cooling-heating loop instrumentation 208
10.4 Non-condensables estimation MATLAB function 212
10.5 PRECISE facility and instrumentation - technical drawings 217

List of figures

Figure 1-1 Reflux condensation phenomenon in a PWR steam generator ---------- 23
Figure 1-2 Comparison of simplified dropwise and film condensation processes on a vertical plate ---------- 24
Figure 1-3 Reflux condensation with NC gases - condensate and boundary layer not to scale ----- 28
Figure 1-4 Typical condensation experiment template, reproduced from Huang et al. [38] --------- 34
Figure 2-1 Reflux condensation modelling: A - PWR steam generator, B - single PWR SG U-tube, C - upward leg of a single U-tube ---------- 37
Figure 2-2 Cross-section of the test facility and an overview of the secondary coolant loop ------- 38
Figure 2-3 PRECISE facility overview, left to right: cross-section, exposed test tube, assembled facility, outer insulation ---------- 41
Figure 2-4 Primary loop - simplified schematic (parts of secondary loop greyed out) ---------- 42
Figure 2-5 Insulation between the test tube and the coolant jacket ---------- 43
Figure 2-6 Secondary loop - simplified scheme (parts of primary loop greyed out) ---------- 44
Figure 2-7 Water injection to the coolant jacket ---------- 45
Figure 2-8 PRECISE facility (without insulation) - location and mount ---------- 46
Figure 2-9 PTFE insulation between facility and fixation points ---------- 46
Figure 2-10 Primary loop control logic ---------- 47
Figure 2-11 Secondary loop coolant volumetric flow control ---------- 48
Figure 2-12 Secondary loop temperature control ---------- 49
Figure 3-1 PRECISE facility DAS and control system ---------- 51
Figure 3-2 Schematic of sensors positioning in vertical (A) and horizontal (B) direction in the test tube ---------- 52
Figure 3-3 Heat flux sensor multi-layer structure and operating principle ---------- 53
Figure 3-4 Anisotropic thermocouple in GHFS structure - $\boldsymbol{x}$, $\boldsymbol{y}$ axes parallel and perpendicular to the layers ---------- 54
Figure 3-5 Heat flux signal acquisition chain ---------- 57
Figure 3-6 GHFS sensitivity test setup ---------- 58
Figure 3-7 GHFS sensitivity dependence on heat flux at constant temperature of 20°C ---------- 59
Figure 3-8 GHFS sensitivity calibration setup ---------- 60
Figure 3-9 Double TC probe ---------- 61
Figure 3-10 Heating rod normalized temperature distribution without (A) and with (B) copper equalizer, at varying powers ---------- 61
Figure 3-11 Example of GHFS sensitivity calibration curve ---------- 62
Figure 3-12 GHFS installation on the inner surface of the test tube ---------- 63
Figure 3-13 Duralco 128 epoxy, degraded from prolonged exposure to hot steam ---------- 63
Figure 3-14 GHFS installation in the deep pocket ---------- 64
Figure 3-15 Embedded GHFS frequency response test ---------- 65
Figure 3-16 GHFS frequency response. ---------- 66
Figure 3-17 Movable conductivity and temperature probe cross-section ---------- 67
Figure 3-18 Physical realization of movable conductivity and temperature probe ---------- 68

Figure 3-19 Electrode array plug and cross-section ---------- 68
Figure 3-20 Polishing of an electrode array face, to match inner tube wall curvature ---------- 69
Figure 3-21 Traversing thermocouple/electrode cross-section, dimensions in mm ---------- 70
Figure 3-22 Actuation mechanism of the moving TC/electrode ---------- 70
Figure 3-23 MCT probe attachment to the PRECISE facility---------- 71
Figure 3-24 Photographs of the MCT probe assembly. A - guiding tube with the probe and engine, B - movable probe tip in the test tube---------- 71
Figure 3-25 Face of the electrode array (R1 - R4 - receivers, T - transmitter) ---------- 72
Figure 3-26 Transmitter electrode driving signal ---------- 72
Figure 3-27 Overview of the MTC electrode array driving circuit---------- 73
Figure 3-28 RC oscillator circuit generation analog clock signal ---------- 74
Figure 3-29 Creation of four 1 kHz time-shifted voltage pulses ---------- 75
Figure 3-30 Final step of the transmitter signal generation – Op-Amp circuit ---------- 75
Figure 3-31 Final transmitter signal creation step ---------- 76
Figure 3-32 Circuit used for sampling receiver electrodes output ---------- 76
Figure 3-33 Control signals for sample/hold units in signal receiver circuit ---------- 77
Figure 3-34 Temperature signal acquisition ---------- 78
Figure 3-35 Probe tip position signal acquisition---------- 79
Figure 3-36 Film thickness voltage signal acquisition---------- 79
Figure 3-37 Electrode array calibration stand (A) and cross-section (B)---------- 80
Figure 3-38 Electrodes designation convention (R1 - R4 - receivers, T - transmitter) ---------- 81
Figure 3-39 Electrode electrical response as a function of film thickness. A - raw signal, B - normalized signal.---------- 81
Figure 3-40 ANSYS calculation domain (A) and calculation - measurement qualitative comparison, center electrode (B)---------- 82
Figure 3-41 Fourth order polynomial fit to each electrodes' signal---------- 82
Figure 3-42 Electrode array dynamics analysis test---------- 83
Figure 3-43 Electrode array spectral analysis for liquid film oscillation frequencies from 11 to 22 Hz ---------- 84
Figure 3-44 Traversing thermocouple / electrode operation: ---------- 85
Figure 3-45 Time resolved MCT probe signal comparison. A - position, B - temperature, C – voltage full frequency range of 100kHz (red) and down sampled to 100 Hz (yellow) ---------- 86
Figure 3-46 Typical horizontal temperature distribution during condensation observed with MCT ---------- 86
Figure 3-47 Thermocouples data acquisition---------- 87
Figure 3-48 PT-100 resistive thermometers signal acquisition ---------- 88
Figure 3-49 Pressure transducer data acquisition---------- 88
Figure 3-50 Heating power data acquisition---------- 89
Figure 3-51 Coolant volumetric flow data acquisition---------- 89
Figure 4-1 Example of GHFS optical area measurement and in-software sensor edge tracking --- 94
Figure 4-2 Calculated amplifier gain error for each of four measurement channels ---------- 96
Figure 4-3 Typical observed probe position behavior at the end switch location ---------- 98
Figure 5-1 Experimental procedure, steps 1 and 2 ----------104

Figure 5-2 Experimental procedure, steps 3 and 4 ----------105
Figure 5-3 Experimental procedure, steps 5 and 6 ----------106
Figure 5-4 Experimental procedure, steps 7 through 9----------106
Figure 5-5 Continuous injections tests - NC gas injection and gas plug growth----------108
Figure 5-6 Algorithm of NC gas species partial pressures pre-calculation----------110
Figure 5-7 Typical pressure and temperature behavior during the filling of the NC gas tank the transfer of the gas into the experiment volumes----------112
Figure 5-8 Algorithm of the average gas mixture molar composition post-calculation----------114
Figure 6-1 Steady-state identification algorithm in action, applied to pressure A) and temperature B). On the second plot, the permissible band is marked with dashed black lines.----------115
Figure 6-2 Range of Reynolds and Prandtl numbers for varying coolant mass flow ----------118
Figure 6-3 Coolant side heat transfer coefficient relation to coolant mass flow----------118
Figure 6-4 Coolant side heat transfer coefficient impact on steam condensation----------119
Figure 6-5 Coolant $\boldsymbol{htc}$ impact on steam condensation flux with and without NC gases ----------119
Figure 6-6 Typical temperature distributions for A) pure steam and B) NC gases recordings -----120
Figure 6-7 Effective steady state pressure as a function of the wall temperature gradient----------120
Figure 6-8 A) PRECISE power change with increasing wall temperature gradient. B) Steam flow properties with increasing wall temperature gradient ----------121
Figure 6-9 A) Condensation mass flow response to increasing wall temperature gradient. B) Accompanying effect on coolant side heat transfer coefficient, through decreasing water temperature -121
Figure 6-10 A) Evaporation power as a function of pressure. B) Decreasing wall temperature gradient, counteracting effects of increased pressure ----------123
Figure 6-11 Normalized condensate flow as a function of pressure----------123
Figure 6-12 Steam partial pressure (A) and average N2 mole fraction (B) with increasing absolute pressure----------124
Figure 6-13 A) Vertical center temperature profiles with increasing pressure B) condensation length with increasing pressure ----------124
Figure 6-14 Calculated mass flux the with increasing absolute pressure----------125
Figure 6-15 Vertical steam mole fraction along test tube centerline with three distinct regions (A, B & C)----------125
Figure 6-16 Condensation absolute (A) and normalized (B) $\boldsymbol{m}$ with increasing pressure at three N_2 average mole fractions ----------126
Figure 6-17 Normalized temperature profiles (A) and standard deviations (B) at three pressures for 0.005 N_2 average molar fraction----------127
Figure 6-18 Test tube condensation $\boldsymbol{m}$ with an increasing content of N_2----------129
Figure 6-19 Vertical temperature profile with three characteristic parameters----------129
Figure 6-20 A - Test tube condensation length and B - N_2 gas plug size with increasing N_2 gas content ----------130
Figure 6-21 Mixing zone size without (A) and with (B) linear temperature interpolation----------130
Figure 6-22 Local heat flux as a function of steam mole fraction----------131
Figure 6-23 Heat flux (HF) (A) and wall temperature gradient (B) in normalized vertical coordinates. For data below -1, sensor is in condensation zone, -1 to 1 in the mixing zone and above in the NC gas plug ----------132

Figure 6-24 Condensation length at varying N2 mole fraction at different test runs (A) and heat flux recorded at 660 mm for the same test runs (B) ----------132
Figure 6-25 Measured (A) and normalized (B) vertical temperature distributions at various pressures ----------133
Figure 6-26 Condensation mass flow with increasing average NC mole fraction ----------135
Figure 6-27 Condensation length (A) and mixing zone length (B) for different NC gases ---------135
Figure 6-28 Temperature (A) and standard deviation (B) comparison between N2 and He tests at very close average mole fractions (0.068 for He and 0.073 for N_2) at 4 bar----------136
Figure 6-29 Wall temperature gradient (A) and heat flux (B) at the 660 mm elevation in normalized coordinates with N_2 and He ----------136
Figure 6-30 Average total mole fraction of non-condensables in the test tube at an increasing N_2 fraction in the N_2 / He mixture ----------137
Figure 6-31 NC mixture composition impact on condensation mass flow (A) and temperature distribution in the tube (B) ----------138
Figure 6-32 NC mixture composition impact on mixing zone length (A) and condensation length (B) ----------138
Figure 6-33 Temperature (A) and temperature standard deviation (B) distribution in the mixing zone at various gas fractions----------139
Figure 6-34 Temperature drop in the mixing zone in normalized coordinates ----------139
Figure 6-35 Horizontal temperature distribution in the test tube below the mixing region --------140
Figure 6-36 Mixing region as resolved by a single thermocouple ----------142
Figure 6-37 Mixing layer front vertical position in time (experiment CIN-He-4_2) ----------143
Figure 6-38 Mixing zone in time and recalculated length coordinates (experiment CIN-N2-4_2) 144
Figure 6-39 Mixing zone length for every thermocouple - CIN-HE-4_5 ----------145
Figure 6-40 Mixing zone length for every thermocouple - CIN-MIX-4_5----------145
Figure 6-41 Mixing zone length for every thermocouple - CIN-N2-4_5----------145
Figure 6-42 Mixing zone velocity, residence time and length for different NC gases (A); pressure drop in NC tank and recalculated NC gases feed rate (B). Experiments CINT-He-4_5, CINT-MIX-4_5, CINT-N2-4_5. ----------146
Figure 6-43 Mixing zone length (A) and temperature oscillations (B) with increasing steam velocity. Experiments CINT-He-4_5, CINT-MIX-4_5, CINT-N2-4_5. Linear trendlines added to support interpretation. ----------146
Figure 6-44 Mixing zone passage observed in temperature and heat flux signals and the recalculated length (A) and oscillations of temperature measurement over 0.1 Hz (B). Experiments CINT-He-4_5, CINT-MIX-4_5, CINT-N2-4_5.----------147
Figure 6-45 Mixing region arrival and departure observed with film probe in time domain (A) and frequency domain (B), experiment CINT-N2-4_2----------148
Figure 6-46 Horizontal temperature distributions at various NC gas concentrations. Filled regions represent standard deviation range of the signal. Temperature of the NC plug was offset with +13°C for readability. Experiments NC-MFR-ABS-N2-6-2, -2_5 and -4.----------149
Figure 6-47 Local temperature oscillations expressed with standard deviation at various NC gas concentrations----------149

Figure 6-48 Thermal boundary layer observed with temperature (A) and voltage (B) measurements ----------150
Figure 6-49 Voltage measured with traversing (A) and fixed (B) electrode. Median filter of the order 10000 was applied to both signals, which were recorded at 1kHz. Experiment NC-MFR-ABS-1_4_LF.151
Figure 6-50 Discrete Fourier transform spectrum of voltage signal registered with traversing and fixed electrodes. The peak frequency corresponding to tube traversing period is clearly recognizable. --151
Figure 6-51 Film probe voltage (A) and recalculated film thickness (B), experiments NC-MFR-ABS-4-X and NC-MFR-HE-X----------152
Figure 6-52 Thermal boundary layer identified with the traversing electrode, exp. NC-MFR-ABS-4-X and NC-MFR-HE-X ----------152
Figure 6-53 Horizontal temperature profiles with varying NC gas mixture compositions in (A) condensation zone, (B) mixing zone and (C) NC gas plug. Filled region represent temperature signal standard deviation calculated at each horizontal position. ----------153
Figure 6-54 Heat flux signa measured in the condensation zone (A), mixing zone (B) and NC gas plug (C) with two measurement methods. Moving average filter with span of 100 was applied for clarity of viewing and plotted in bold. Experiments NC-CMP-5, NC-MFR-ABS-2_5_4 and NC-MFR-ABS-He-4_4. ----------155
Figure 6-55 Heat flux signal recorded in each of three regions with heat flux sensors (A) and dual thermocouples (B) in frequency domain. Experiments NC-CMP-5, NC-MFR-ABS-2_5_4 and NC-MFR-ABS-He-4_4. ----------156
Figure 6-56 Heat flux signal measured in the condensation zone (A), mixing region (B) and gas plug (C) for experiments with N2 and He. Experiments NC-MFR-ABS-4_1 & NC-MFR-ABS-He-4_0, NC-MFR-ABS-4_2 & NC-MFR-ABS-He-4_1 and NC-MFR-ABS-4_6 & NC-MFR-ABS-He-4_5. ----------157
Figure 6-57 Heat flux observed in normalized coordinates, with respect to the position of the sensor (620 mm) and the mixing zone center. Experiments NC-MFR-ABS-4-X, NC-MFR-ABS-He-X and NC-CMP-X. ----------158
Figure 6-58 Mixing region passage observed with heat flux sensor and thermocouple located at 720 mm----------159
Figure 6-59 Power spectra of the heat flux signal acquired with various NC gases, computed with 0.1 Hz frequency resolution. Experiments CINT-He-4_5, CINT-MIX-4_5, CINT-N2-4_5. ----------159
Figure 6-60 Spectrograms of mixing region for He (A), mixture (B) and N2 (C) gases injection. The arrival of the mixing zone is at 2.5 min.----------159
Figure 6-61 Power spectra comparison of the measured heat flux signal recorded with two sensors and various experiments. Primary graphs on the left depict to whole available spectrum, computed with 10Hz frequency resolution. Secondary graphs on the right side depict lower end of the frequency spectrum, computed at 1Hz frequency resolution. Experiments, in order: NC-MFR-ABS-1 (A), NC-MFR-ABS-2 (B), NC-MFR-ABS-4 (C).----------160
Figure 6-62 Power spectra comparison of the measured heat flux signal recorded with two sensors in various stratification regions, computed with 0.05 Hz frequency resolution. In order: (A) - both sensors in condensation zone, (B) – GHFS1 in condensation, GHFS2 in mixing region, (C) both in gas plug.--161
Figure 6-63 Power spectra comparison of the measured heat flux signal recorded with sensor 1 (A) and 2 (B), various experiments. For clarity of viewing, second and third spectrum offset by -15dB and -30dB. Experiments NC-MFR-ABS-1, NC-MFR-ABS-2, NC-MFR-ABS-4. ----------161

Figure 6-64 Low frequency end of power spectra registered with GHFS1 and GHFS2 at three experiments, NC-MFR-ABS-1, NC-MFR-ABS-2, NC-MFR-ABS-4, computed with 0.05 Hz frequency resolution ----------162
Figure 6-65 Cross power spectral density for GHFS1 (A) and GHFS2 (B), calculated for pair of experiments 1&2, 1&3 and 2&3, in order listed in Figure 6-64. Legend lists the zones in which the sensor was immersed during the test. ----------162
Figure 6-66 Mixing zone passage impact on various local parameters at 660 mm elevation, experiment CIN-He-4_2----------164
Figure 6-67 Calculated heat transfer coefficients using three empirical correlations and GHFS data, experiment CIN-He-4_2 ----------164
Figure 7-1 PRECISE facility nodalization type 1. Mass exchange marked with yellow arrows; heat exchange marked with red / blue arrows. ----------167
Figure 7-2 PRECISE facility nodalization type 2. Mass exchange marked with yellow arrows; heat exchange marked with red / blue arrows. ----------170
Figure 7-3 Element height impact on steady state pressure----------172
Figure 7-4 Dependence of RELAP5 estimate of mass error in all volumes on element height----172
Figure 7-5 Steady state pressure calculated with different condensing annulus thicknesses for pure steam and NC gases cases----------173
Figure 7-6 Steady-state pressure calculated with RELAP5 with various nodalization schemes and experimental boundary condition values, pure steam----------174
Figure 7-7 RELAP5 steady-state pressure and experimental values – NC-MFR-ABS-6----------174
Figure 7-8 Void fraction in the test tube during calculation ----------176
Figure 7-9 Change of evaporation / condensation mass flows in various volumes. Experiment P-ABS-PURE-1, nodalization scheme 2. ----------177
Figure 7-10 Average pressure in the primary side of the simulation over time ----------177
Figure 7-11 Heat balance of RELAP5 simulation. Initial negative value of removed heat is due to warmer coolant water entering the domain that the initial condition temperature. ----------178
Figure 7-12 Comparison of two nodalization types and performance of RELAP5 NC modelling, experiments VEL-CLNT-PURE----------179
Figure 7-13 Condensation mass flow with varying coolant temperature ----------180
Figure 7-14 Reached steady-state pressure with increasing condensation flow----------180
Figure 7-15 Inventory evolution during calculation for nodalization 1 (A, B) and 2 (C, D) with NC model disabled (A, C) and enabled (B, D) ----------181
Figure 7-16 Distribution of NC gases in the tube over time - calculation based on PABS-PURE-4 experiment----------182
Figure 7-17 Mass error with NC modelling disabled (left) and enabled (right) ----------182
Figure 7-18 NC mass distribution reversal between inner the column and the condensation annulus around t=1000 s ----------183
Figure 7-19 Temperature in the condensation tube center (exp. PABS-PURE-5) ----------184
Figure 7-20 NC gas fraction along the condensation tube (exp. PABS-PURE-5)----------184
Figure 7-21 Change in the coolant water temperature along the coolant channel (exp. PABS-PURE-5) ----------184
Figure 7-22 RELAP5 steady-state pressure and experimental values – NC-MFR-ABS-4 ----------185

Figure 7-23 Increasing mass of added N_2 gas impact on condensation flow – NC-MFR-ABS-4 -185
Figure 7-24 Heat balance for simulation of experiment NC-ABS-4_2, nodalization 2----------186
Figure 7-25 NC mass distribution reversal between inner the column and the condensation annulus, exp. NC-ABS-4_2, nodalization 2----------186
Figure 7-26 Gas and liquid velocities distribution in the tube center and annulus, based on exp. NC-ABS-4_2----------187
Figure 7-27 NC gas quality (mass fraction) in the tube center an annulus, based on exp. NC-ABS-4_2 ----------187
Figure 7-28 Liquid phase (left) and gaseous phase (right) velocities, nodalization 1, based on exp. NC-ABS-4_2 ----------188
Figure 7-29 Integral heat balance (left) and mass accumulation (right) for calculations with helium, based on exp. HE-ABS-2_2----------188
Figure 7-30 Relationship between condensation mass flow and helium gas molar content, based on exp. HE-ABS-2_2 ----------189

List of tables

Table 1-1 Summary of experimental work investigating steam condensation with NC gases 30
Table 2-1 Operating conditions summary (water properties calculated based on IAPWS-IF97 [194]) 39
Table 2-2 CCFL onset velocity comparison 40
Table 2-3 Primary loop components overview 43
Table 3-1 Overview of thermoelectric anisotropy of various materials 56
Table 3-2 Summary of dynamic analysis of the electrode array signal 84
Table 4-1 Summary of sensors installed in PRECISE facility 91
Table 4-2 Properties of data acquisition equipment 91
Table 4-3 Calibration curve error summary for the fixed electrode array 97
Table 4-4 Overall measurement error of the fixed electrode array 97
Table 4-5 Summary of errors associated with properties derived from the PRECISE facility experimental data 100
Table 6-1 Initial conditions for the experimental series 116
Table 6-2 Summary of pressure experiments 122
Table 6-3 Summary of N_2 experiments 127
Table 6-4 Helium experiments summary 134
Table 6-5 Varying NC mixture composition experiments summary 137
Table 6-6 Overview of continuous injection experiments 141
7-1 RELAP5 variable names summary 166
Table 7-2 Summary of volumes for nodalization scheme 1 168
Table 7-3 Summary of heat structure for nodalization scheme 1 168
Table 7-4 Summary of junction for nodalization scheme 1 168
Table 7-5 Summary of volumes for nodalization scheme 2 171
Table 7-6 Summary of heat structures for nodalization scheme 2 171
Table 7-7 Summary of junctions for nodalization scheme 2 171
Table 7-8 Boundary and initial conditions used in RELAP5 modelling 175

Nomenclature

Greek letters

α	Angle
λ	Thermal conductivity
μ	Kinematic viscosity
ν	Dynamic viscosity
ρ	Density
σ	Surface tension
σ_{el}	Electrical conductivity
Φ	Heat flux

Symbols

A	Area
C	Capacitance
C_{em}	empirical parameter in Wallis-type CCFL correlation
Cp	Specific heat capacity
D	Diameter
δ_{film}	Condensate film thickness
E	Thermoelectric response of GHFS
Err	Error
f	Frequency
g	Gravitational acceleration
$h/w/l$	Height/width/length
H_{end}	Mixing region end elevation
H_{sens}	Sensor elevation
H_{st}	Mixing region start elevation
h_{tc}	Heat transfer coefficient
H_{vap}	Enthalpy of vaporization
I	Current
J^*	Dimensionless superficial velocities
L	Length
L_{char}	Characteristic length
L_{cond}	Condensation zone length
L_{mix}	Mixing zone length
L_{plug}	NC gas plug length
M	empirical parameter in Wallis-type CCFL correlation
$\dot{m}$	Mass flow
n	Number of moles
Nu	Nusselt number
P	Pressure

P_{el}	Electrical power
Pr	Prandtl number
$\dot{Q}$	Heat flow
R	Resistance
$\bar{R}$	Gas constant
Re	Reynolds number
S	Seebeck coefficient
s_0	GHFS sensitivity
T	Temperature
t	Time
U	Voltage
v	Velocity
V	Volume
$\dot{V}$	Volumetric flow
X	Mole fraction
x, y, z	Axes

Abbreviations

A/D	Analog-to-digital
CKT	Classical kinetic theory
CFD	Computational fluid dynamics
C-IN	Continuous injection
CH	Cooling-heating
CCFL	Counter-current flow limitation
DAS	Data acquisition system
DC	Direct current
DWC	Drop-wise condensation
FFT	Fast Fourier transform
FPGA	field-programmable gate array
FC	Film condensation
GHFS	Gradient heat flux sensor
LOCA	Loss of coolant accident
MCT	Movable conductivity and temperature probe
cRIO	National Instruments CompactRIO
NC	Non-condensable
NPP	Nuclear power plant
1D	One-dimensional
PTFE	Polytetrafluoroethylene
PRECISE	Precise reflux condensation investigation setup
PWR	Pressurized water reactor
RPM	Rotations per minute
S/H	Sample/hold
STD	Standard deviation
S-ST	Steady-state
SG	Steam generator

Acknowledgements

As no man is an island then no dissertation could be produced in isolation. The presented work is no different and during its course it was aided by the influence of many, without whom its successful completion would not have been possible.

Firstly, I would like to express my sincere gratitude to my thesis supervisor, Prof. Horst-Michel Prasser, for continuous support of my Ph.D. study and giving me the opportunity to conduct research in his laboratory. His guidance allowed me to navigate the topic of reflux condensation and insightful comments shaped the work in its entirety. I could not imagine this endeavor coming to fruition without his mentoring.

My sincere thanks also go to all the members of the Severe Accident Research group at Paul Scherrer Insitut, where I remained for most of my Ph.D. study. I would like to recognize the contribution of Dr. Detlef Suckow, whose technical expertise, unparalleled organizational skills and universal support allowed to design, commission and conduct experiments in the PRECISE facility. Furthermore, I would like to thank Dr. Abdelouahab Dehbi for his input on the theoretical part of the work, especially the design of the experiments and computational analysis. Moreover, I thank Dr. Tertaliisa Lind for overseeing the project from the perspective of a group leader, keeping close eye on the progress and asking the hard questions when necessary. Dr. Lind provided invaluable advice that helped to steer this project safely to port.

I offer my gratitude to Prof. Andrey Mityakov, for his expertise about and the supply of the novel heat flux sensors. His contribution allowed to investigate reflux condensation from a new perspective and extended the possibilities of heat flux measurements in the PRECISE facility.

These acknowledgements would not be complete if I did not thank the nuclear system codes team within SACRE group, Drs. Jonathan Birchley, Leticia Fernandedz Moguel, Adolf Rydl and Berndt Jaeckel. Their expertise was invaluable for navigating the world of RELAP5 and nuclear safety calculations. I truly hope that my countless questions did not disturb their own work too much.

Moreover, I would like to express my gratitude to my office mates, Dr. Thorsten Betschart and Dr. Vladimir Brankov as well as Dr. Jarmo Kalilainen and Petros Papadopoulos from across the corridor. Without them our floor of the OHSA building would not have been as lively and as entertaining as it was. Their useful comments and help on various topics not only established the atmosphere of friendly comradery but often allowed to gain new perspective on the challenge at hand.

Presented dissertation was aided greatly by the labor of year-long "summer interns" – Mateusz Żłobiński and Marton Szogradi, whom I had the pleasure to supervise and work with. Without their assistance, the body of experimental data would not be so complete and without their attitude the long hours in the lab would not have been so enjoyable.

Special thanks should go to Michel Furrer for his work on electronic components and assistance with PRECISE facility assembly as well as Hauke Schütt for help in creating the data acquisition system and his LabVIEW programming skills. In the spirit of practical applications, I would like to show my appreciation to the staff of PSI workshop, without whom the facility construction could not have been completed. In particular to Hueseyin Mutlukal and Francesco Pumilia whose invaluable skills in turning ideas into working devices, constructive design feedback, great attitude and free German lessons defined the laboratory experience for me.

I would also like to wholeheartedly thank Dr. Martin Ritterath who kept providing encouragement in the last stage of thesis writing. The discussions about my Ph.D. helped me to view this work from a new

perspective. In a similar manner, I would like to acknowledge my friend, Dr. Stanisław Gałęski, the source of unending discussions and useful advice in the field of physics. Together with his partner Katarzyna Karcz they managed to form an effective thesis-support group.

I express gratitude to my family, who equipped me well for the tough life of a doctoral student and remained optimistic about my graduation throughout the whole time. They inspired me to do my best through the continued interested in my progress.

Finally, and not least but closest to my heart, I want to thank my girlfriend Agata Kaźmierczak for unceasing support throughout the long years and making my life happy in general. I could not have done this without you.

Abstract

Of all the nuclear reactors in operation today, light water reactors and pressurized water reactors in particular remain one of the most common designs. With 298 functioning units as of 2019, this type accounts for over 66% of all operating reactors [1]. The presented work attempts to expand the understanding of a pressurized water reactor (PWR) steam generator (SG) in a particular mode of operation, referred to as reflux condensation. The scenario in which SG tubes operate in a reflux condenser mode remains relevant to PWR mid-loop operation as well as a possible loss-of-coolant (LOCA) accident. In these modes, steam condensation in SG tubes provides a very efficient path for heat removal from the primary circuit of the nuclear reactor. This phenomenon is capable of removing residual decay heat from the reactor coolant system, which suppresses/delays the disastrous core uncovery. At the same time, presence of non-condensable gas species, namely hydrogen and nitrogen, is very likely. NC gases in mixture with steam has been previously shown to severely reduce the efficiency of the water condensation process.

To study the interaction of steam and non-condensable gases in the geometry of PWR SG tubes, an experimental facility is designed and constructed. The Precise Reflux Condensation Investigation Setup (PRECISE) developed and located in Paul Scherrer Institut is a concentric tube condenser, in which a working-volume, vertical test tube is surrounded with a cooling water jacket. Accurate control over the volume gas inventory and operating conditions such as pressure, temperature and coolant water properties allows to study reflux condensation in detail at different concentrations of NC gases. Nitrogen and helium (in place of flammable hydrogen) are used, as well as mixtures of the two at different ratios. Besides traditional measurement methods, PRECISE facility is equipped with two novel sensor types – heat flux sensors and a movable temperature/conductivity probe. The development of these two devices allowed to observe reflux condensation with previously unavailable spatial and temporal precision.

The first part of the presented thesis provides a detailed overview of the PRECISE facility and the used measurement methods as well as explains the employed data acquisition and processing techniques. The second part discusses results from the conducted experiments and provides insight in the observe impact of the thermodynamic operating conditions on the condensation and interaction of steam and NC gases. Measurements reveal that the non-condensable gas type plays a crucial role in the plug formation. Light gas (He) forms sharp and narrow interface and limits condensation efficiently while heavy gas (N_2) develops wide, diffuse interface with gradual temperature drop.

The third part presents the effort to analyze the performance one of the most popular 1D safety codes RELAP5/MOD3.4 when applied to the geometry and operating conditions of the PRECISE facility. The calculation setup and modelling are presented along with the obtained results, which are validated against the previously acquired experimental values.

Zusammenfassung

Bei den heute in Betrieb stehenden Kernreaktoren handelt es sich mehrheitlich um Leichtwasserreaktoren, insbesondere Druckwasserreaktoren (DWR). Mit 298 Einheiten im Jahre 2019 machen diese 66% aller in Betrieb stehenden Reaktoren aus [1]. Die hier vorgestellte Arbeit verfolgt das Ziel, das Verständnis der Dampferzeuger (DE) in Druckwasserreaktoren in einem bestimmten Betriebszustand, der sogenannten Reflux Kondensation, zu erweitern. Szenarien, bei denen das Phänomen der Reflux Kondensation vorkommt, sind in DWR sowohl bei mid-loop Betrieb als auch bei potentiellen Kühlmittelverluststörfällen (LOCA) relevant. In diesem Modus ist die Dampfkondensation in den DE-Heizrohren für die Wärmeabfuhr aus dem Primärkreis sehr effizient. Die aus der Reflux Kondensation stammende Wärmeabfuhr genügt zur Nachwärmeabfuhr aus dem Reaktorkühlsystem, was zur Verhinderung / Verzögerung der Kernabdeckung beiträgt. In solchen Zuständen ist auch die Präsenz von nicht-kondensierbaren Gasen wahrscheinlich. Bisherige Untersuchungen haben ergeben, dass eine Mischung aus Nicht-kondensierbaren Gasen und Dampf zu einer erheblichen Reduktion der Effizienz des Kondensationsprozesses führen.

Der Precise Reflux Condensation Investigation Setup (PRECISE), eine am PSI entwickelte und verwirklichte Teststrecke, ist ein konzentrischer Rohrkondensator, in welchem ein vertikales Versuchsrohr von einem wassergekühlten Kühlmantel umschlossen ist. Durch eine genaue Regelung des Gasvolumens und der Betriebsbedingungen wie Druck, Temperatur und Wassereigenschaften wird eine detaillierte Untersuchung der Reflux Kondensation bei verschiedenen Konzentrationen nicht kondensierbarer Gase ermöglicht. Stickstoff und Helium (anstelle von leicht entzündlichem Wasserstoff) sowie eine Mischung aus diesen beiden Gasen bei zwei verschiedenen Konzentrationen werden für die Untersuchungen verwendet. Nebst traditioneller Messmethoden wurde die PRECISE Teststrecke mit zwei neu entwickelten Sensortypen ausgestattet. Dabei handelt es sich um Wärmestromsensoren und bewegliche Temperatur- / Leitfähigkeitssonden. Die Entwicklung dieser Messeinrichtungen erlaubt eine Beobachtung der Reflux Kondensation mit einer vorab nicht möglichen zeitlichen und räumlichen Auflösung.

Der erste Teil der hier vorgestellten Arbeit besteht aus einer detaillierten Beschreibung der PRECISE Teststrecke und der verwendeten Messeinrichtungen sowie der verwendeten Datenerfassung- und Verarbeitungsmethoden. Der zweite Teil erörtert die aus den Experimenten stammenden Ergebnisse und diskutiert die Erkenntnisse aus dem beobachteten Einfluss der thermodynamischen Betriebsbedingungen auf die Kondensation sowie die Interaktion zwischen Dampf und den nicht kondensierbaren Gasen. Die Messungen haben ergeben, dass die Zusammensetzung der nicht kondensierbaren Gase immer eine entscheidende Rolle bei der Pfropfenbildung spielt. Leichte Gase (He) führen immer zur Bildung einer spitzen und engen Grenzfläche und begrenzen die Kondensation. Schwere Gase (N_2) führen zur Bildung von weiten und ausgebreiteten Grenzflächen mit einem graduellen Temperaturabfall.

Im dritten Teil der Arbeit wird die Modellierung der PRECISE Teststrecke unter Berücksichtigung der geometrischen Verhältnisse sowie der Betriebsbedingungen im bekannten thermohydraulischen 1D Code RELAP5/MOD3.4 beschrieben. Die Modellierung und die verwendete Recheneinrichtung werden zusammen mit den Rechenergebnissen vorgestellt, die durch zuvor gemachte experimentelle Untersuchungen validiert wurden.

Chapter 1 Introduction and motivation

1.1 Reflux condensation in PWR

Sustainable and safe energy generation to cover the ever-expanding human civilization needs remains perhaps one of the most vital challenges of XXI century. In terms of energy density per unit mass of fuel, nuclear fission remains the most efficient mean to the end. While its counterpart, nuclear fusion remains a hope for the future, multiple fission reactors have been providing gigawatts of power reliably since late 1950's to this day.

The design and operation of a nuclear power plant (NPP) remains a strictly regulated field, ensuring the highest possible levels of safety to the public. In terms of deaths per TWh [2] or even accident fatalities [3], nuclear fission is safer than even the most benign-seeming renewables like wind and solar. This was only possible due thorough research and development in the field of safety. Understanding the behavior of currently operating reactors under any conditions, no matter how improbable, was the topic of interest to industry, academic community and regulatory bodies alike.

Reflux condensation phenomenon occurs inside steam generator (SG) tubes of a pressurized water reactor (PWR) during a severe accident or shutdown conditions. In the assumed scenario, water in SG tubes is drained and they are filled with steam or steam / gas mixture. With this reduced inventory water continues to boil in the reactor core and the hot vapor is carried upwards to the SG tube bundle. At least part of the steam condenses and flows back to the reactor core, which results in a counter-current flow of liquid and gas in the reactor's hot leg and SG, Figure 1-1. This is a passive phenomenon, creating a pathway for residual decay heat to be removed from the reactor's primary coolant system. Depending on the specifics of the situation, reflux condensation can become a major heat removal path, [4]–[6].

If the steam flow from the core high enough, the condensate ceases to drain and starts to accumulate above the two-phase condensation region. This is known as a flooding limit and it can occur either in the SG tubes or in the hot leg, [7]. If the steam flow increases even further, then the liquid begins to flow concurrently with the gas and is carried over to the downward leg of SG tubes, [5]. The present work describes the scenarios at which gas flows is below the flooding limit and focuses on counter-current flow patterns only.

Two major scenario classes during which reflux condensation is likely to occur can be identified, based on the primary loop pressure. First, the high pressure class is characterized by 4 – 10 MPa ([8]–[12]) and involves a loss of coolant accident (LOCA) during normal plant operation. The other class, low pressure, is characterized by close to containment pressures [13]–[15] and could occur due to loss of residual heat removal (RHR) system during a mid-loop inventory operation.

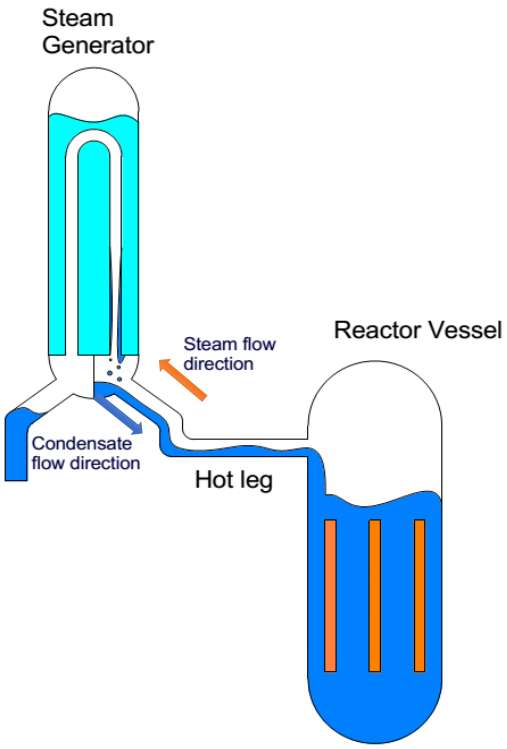

Figure 1-1 Reflux condensation phenomenon in a PWR steam generator

In either case, presence of non-condensable (NC) gases is very likely. Possible sources during high pressure scenarios include emergency core cooling system (N_2), gases normally dissolved in liquid water ([16]) and, if the incident progresses towards the severe accident conditions, oxidizing fuel rods zirconia cladding (H_2). Alternatively, in case of low-pressure scenarios, the coolant is partially drained on purpose with air occupying upper volumes of the primary system. An example being the case of reactor refueling, when the reactor pressure vessel (RPV) head is removed.

The effectiveness of reflux condensation is greatly impacted by the presence of NC gases. Evidence up to date clearly shows that they hinder the steam condensation very effectively ([17]–[23]), even at low concentrations. Hence, understanding the specifics of steam – NC gases interaction during reflux condensation regime becomes an important topic of interest to safety of PWRs.

1.2 Condensation in the presence of NC gases

The impact of non-condensable gases has been studied extensively up to date. The earliest discovery can be attributed to D. Othmer [24] who in 1929 revealed the effect of NC gases on condensation over horizontal copper tube, placed in a small volume. He observed that if the concentration of air in the gas mixture increased from 0 to 0.5%, the calculated heat transfer coefficient decreased by almost 50%. His work was quickly confirmed by other researchers. In 1930's, Meisenburg et al. [25] studied effects of small NC gas concentrations on the condensation on the outside of vertical tubes in a forced convection regime. Uchida et al. [26] and Ai-Diwany et al. [27] described condensation on vertical walls. Henderson and Marchello [28] studied horizontal pipes. Detlev et al. [29] investigated condensation of potassium vapor in the presence of argon and helium on horizontal plates. For the varying types of condensing surfaces and gases mixture, the research proved that the presence of NC gases greatly reduces condensation heat transfer.

Further studies revealed that the effect can be lessened with application of electric fields [30], mist formation [31], or increasing condensate waviness [32]–[35]. The increase of the liquid film Reynolds number also was found to enhance the heat transfer coefficient on the vapor-side for numerous gases, including air, nitrogen, argon or neon, [36]. Surface tension of the liquid was identified by Rose [37] as a crucial parameter impacting vapor-liquid mass exchange.

Overall, the established consensus in the scientific community is that even small amounts of NC gases can very effectively inhibit the condensation process. Since this is very common in heat transfer applications, such as pipe heat exchangers, nuclear industry, refrigeration, air conditioning and recently electronics, extensive effort was extended to quantify the observed effect. The wealth of collected experimental data was used to create models attempting to provide a relevant insight for industrial and scientific applications. However, the developed techniques are highly dependent on the vapor condensation mechanism. Specifically, the steam condensation can be divided in two main subtypes – film condensation (FC) and dropwise condensation (DWC), Figure 1-2.

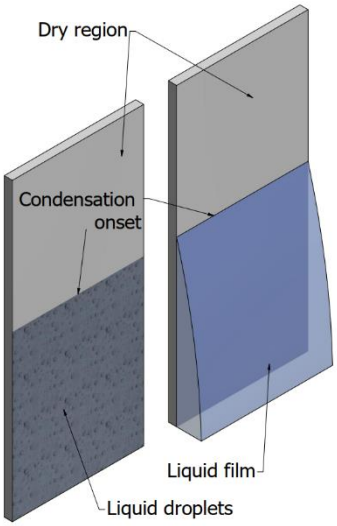

Figure 1-2 Comparison of simplified dropwise and film condensation processes on a vertical plate

In the early 30's of the last century, the qualitative distinction between the two processes was identified by Schmidt [38], who observed that the heat transfer coefficient for the DWC can be 5 to 7 times higher than corresponding values during FC process. Therefore, the research work can be effectively split in separate groups for each of the two condensation process types, described in the following chapters.

1.3 Dropwise condensation - DWC

1.3.1 Pure vapor

During dropwise condensation, the condensate vapor collects on the surface into droplets that do not coalesce and form a uniform film. Depending on the geometry, the droplets can move under gravity after growing to a certain size, exposing the solid surface to the vapor. Specifically in case of vertical surfaces the drops near to the top of the area fall very quickly after reaching critical size at which gravity overcomes the surface tension forces [39]. By sweeping the surface downstream they collect drops forming in their path, even before those can reach the critical size. Observed heat transfer coefficients were reported to be 5 to 10 times greater than during film condensation, [38]–[41].

Unfortunately, there is no well-established theory on the mechanism of the dropwise condensation. Two main hypotheses have been put forward with regard to how the drops are initially formed. First, formulated by Jakob [42] in 1936, is the liquid membrane rupture hypothesis. It states that the condensate layer forms as a film first, which breaks up into separate droplets after reaching a certain thickness due to instabilities. The mechanism is driven by tension forces [43]–[45]. Majumdar and Mezic [46] studied hydrophilic surfaces with an atomic force microscope and observed a liquid film only a few nanometers thick. They identified the critical value to be 3 nm, with films thicker than this being subject to instabilities caused by competition between strain energy, van der Waals and hydration and surface tension forces. Post film-break up, the condensation continues in discrete nucleation sites.

The second hypothesis of the mechanism of dropwise condensation is the surface nucleation. Pioneering studies conducted by Westwater et al. [44], [47], [48] studies the origins of the "primary" drops. These were found to appear on exposed condensation surface at nucleation sites. The observed primary drops were about three orders of magnitude smaller than corresponding bubbles created at nucleation sites during boiling. Their growth was fueled by condensation on their surface as well as intense coalescence with neighbors. Umur and Griffith [49] studies concluded that the most likely sites for nucleation are flaws of the condensing surface, such as pits and grooves. Using optical methods, they also were not able to observe a liquid film of a thickness greater than monolayer in between the growing drops. Further work in favor of the surface nucleation theory was conducted by Liu and Mu [50], [51] who studies condensing surface oxygen content prior and post condensation. They concluded that the initial condensate indeed forms at nucleation sites and not as a thin film.

Even though the conclusive evidence for surface nucleation or liquid membrane breakup hypothesis was not yet demonstrated, supporters of both recognized the condensing surface properties as crucial to droplet formation and impacting the droplet breakaway size. Surfaces coated with hydrophobic impurities were found to promote DWC, [52]. Methods such as plasma-ion implantation [53], [54], dynamic mixing magnetron sputtering [55] or promoting nanostructure self-assembly [56] were successfully employed to modify condensing surface properties and enhance DWC process.

The necessity of the specialized methods to promote DWC under industrial conditions limited the interest of development in this direction until 1990's, [39], [41]. This also suggests that in case of reflux condensation, where the condensing surface is the untreated inner area of SG tubes, the likelihood of observing this regime over FC is greater. Nevertheless, several experimental studies have been made to investigate the possible transition between DWC and FC regimes. Overall, the cooling intensity was found to play a crucial role - after reaching a critical value, the change from DWC to FC would occur, [55], [57]–[59]. The ratio of the condensing surface thermal conductivity and the condensation heat transfer coefficient was suggested to govern the transition characteristics, [58], [60].

The appearance of the transition regime for steam condensation was reported by Takeyama et al. [57] and Tanasawa et al. [61]. They observed the shape of large drops becoming more irregular and ultimately turning into patches of film, without a preferred location. Similar behavior was observed by Stylianou and Rose [59] for condensation of ethylene glycol. Other researchers observed streaks formed by falling drops to coalesce together and form a liquid film downstream, [58]. Overall, a few theories were formed to explain the transition mechanism. First, proposed by Rose and Wilmhurst [55] states that at high condensation rates promoted by high surface sub-cooling, the growth rate of drops overcame rate of drops coalescence. This in turn limits the rate of the drop break-away and clearing of the surface. The second mechanism suggested that increasing temperature difference between condensation surface and the vapor might increase the

number of nucleation sites, [39]. As this effect progresses, some sites would be so close to its neighbors, that wetted patches would form. Recent work widened the discussion to include the effect of surface wettability on the transition regime. Numerical simulations conducted by Li et al. [62] confirmed that larger wall sub-cooling results in a larger droplet break-away diameter and longer growth and departure cycle time. However, they both increase with the increasing wettability of the condensing surface. This finding was further confirmed with molecular simulations performed by Sheng et al. [63], who additionally argue that the mechanism of transition between FC and DWC essentially depends on the lowering of the condensation surface free energy. This effect of wettability was observed in other numerical ([64], [65]) and experimental studies ([56], [66], [67]).

1.3.2 Vapor with NC gases

Due to limited practical applicability of DWC mechanism in industry, little amount of research was conducted to study the effect of NC gases. Tanner et al. [68], [69] studied condensation on vertical wall at low vapor pressures (2800 to 10159 Pa). He observed significant reduction in measured heat transfer coefficient values, proportional to increasing concentration of NC gas. Later work confirmed this finding ([70], [71]). Bum-Jin [72] compared the condensation retardation effect of NC gases for DWC and FC regimes, and concluded that with NC gases present, observed heat transfer rates were similar in both. Hence, DWC can be well approximated with models developed for FC.

1.4 Film condensation - FC

1.4.1 Pure vapor

Film condensation is most common in industrial applications. After the temperature of a surface is below the vapor saturation temperature and in the contact with vapor, the condensate forms and wets the surface. Depending on the surface geometry, this liquid film can then flow due to gravity and / or flow shear. As more vapor condenses, the film thickness increases in the flow direction. The mass and heat exchange then occurs between condensate and vapor, with the film forming additional resistance to heat transfer, compared to exposed solid surface, [40]. Even though the two phases can seem to be in equilibrium, at or in the vicinity of the gas-liquid interface a temperature drop must occur during condensation. As discussed by Niknejad and Rose [73] this discontinuity is confined to a region in the gas phase with a thickness of a few mean free paths lengths. It has been observed that although the condensate layer itself adds resistance to heat transfer, the vapor – liquid interface in case of pure vapor poses very permeable to both heat and mass. As suggested further by Miller et al. [74], it's thickness can be as little as 1-2 molecular diameter, resulting in an effective jump in density and temperature gradients up to 108 K/m.

The classical approach to modelling involved creating correlations for the film condensation heat transfer. It was first formulated by Nusselt in 1916 [75]. He expressed condensation heat transfer coefficient analytically as a ratio of thermal conductivity and liquid film thickness. Nusselt analysis is limited however to a laminar film condensation, with other simplifying assumptions including the constant temperatures of both vapor and condensing surface, absence of convection currents in the condensate film, no drag force exerted on the condensate by the gas flow and negligible acceleration of the condensate. A modified correlation was later proposed by Rosenhow [76] and Bromley [77], to account for the condensate sub-cooling and non-linear temperature gradient in the liquid. The analysis was expanded further by Kapitsa [78] and McAdams [79] to account for condensate film waves, appearing at the interface even at lower Re number values of about 30. They recommended including a multiplicative factor of 1.2 to account for the discrepancy between experiments and classic Nusselt theory. The wave effect was studied by numerous

following work [80]–[83]. For even higher Re, up to 1800, Kutateladze [84] proposed an alternative expression. The theory was also modified to include the effect of interfacial shear stress by Sparrow [85].

An alternative approach to modelling focused on creating a semi-empirical model for the net mass flux between the liquid and gas phases. Often employed basis is the kinetic theory, [86]–[89]. The basic assumption is that two mass fluxes can be defined to exist simultaneously – from vapor to liquid $\dot{m}_-$ and in the opposite direction $\dot{m}_+$. The resulting net mass flux is then $\dot{m} = \dot{m}_+ + \dot{m}_-$. Following Knacke [90], this net flux j can be defined as:

$$j = \sqrt{\frac{M}{2\pi\bar{R}}}\left(\frac{p_g}{\sqrt{T_g}} - \frac{p_l}{\sqrt{T_l}}\right) \tag{1}$$

Where p, T are pressure and temperature (subscript g refers to gas and l to liquid properties), M is the molecular mass and $\bar{R}$ the gas constant. The first term in the brackets describes gas condensation while the second liquid evaporation, which are both assumed to depend on gas and liquid temperatures and pressure respectively. This theoretical approach was defined to hold under a set of idealized assumptions, referred to as classical kinetic theory (CKT) and summarized by Cammenga [91] and Persad et al. [92]:

1. Molecular collision rate at the gas/liquid interface satisfied Maxwell-Boltzmann velocity distribution under equilibrium.
2. Vapor can be approximated as an ideal gas in equilibrium with the liquid phase.
3. Vapor molecules are not reflected at the interface and every collision results in either evaporation or condensation.
4. The fluxes in opposite directions are independent of each other.

However, the Maxwell-Boltznmann distribution is only correct under equilibrium condition, when the net mass flux is 0. Therefore, problems where evaporation and condensation exist can only apply it if departure from equilibrium is very small [89], [93]–[95]. This simple model was further expanded by introduction of a multiplicative correction factor σ in the form of $\frac{2\sigma}{2-\sigma}$ by [96], or by introduction of separate evaporation and condensation coefficients σ_e, σ_c as formulated by Knudsen [97], resulting in a well-known Hertz-Knudsen formula, also recognized as Hertz-Knudsen-Langmuir equation:

$$j = \sqrt{\frac{M}{2\pi\bar{R}}}\left(\sigma_c\frac{p_g}{\sqrt{T_g}} - \sigma_e\frac{p_l}{\sqrt{T_l}}\right) \tag{2}$$

The condensation coefficients are also referred to literature as mass accommodation coefficients, [98]–[100]. Their physical meaning can be interpreted as what fraction of molecules colliding with the gas/liquid interphase actually transfers to the other phase. Under idealized assumptions described earlier, both coefficients can be set to unity and eq. (2) becomes eq. (1). Otherwise, a method is required to obtain the values of σ_e and σ_c. Unfortunately, numerous undertaken efforts resulted in inconsistent values being proposed for the coefficients. Some researchers assumed $\sigma_e = \sigma_c$ and $T_g = T_l$, for simplicity of application, [98], [101]–[104], but this approach results in disagreement with experiments, as noted by Persad et al. [92]. For the liquid most relevant to this work – water – the reported values of the coefficients ranged from 10^{-3} to 1, [102], [103], [105]. Hence, the applicability of derived coefficients was limited to only relevant

geometries and conditions, resulting in various classes of applications. To address the limitations of eq. (2) further modifications and more sophisticated approaches were introduced, presented in the work of Schrage [106], Barret and Clement [94], Tsuruta [107] or Bond and Struchtrup [87]. Alternate approaches to kinetic theory were developed, including quantum-mechanics based statistical rate theory ([108], [109]), successfully applied to studies of water [109]–[111].

1.4.2 Vapor with NC gases

Even though an accurate calculation of condensation heat transfer for pure vapor poses a significant challenge, the situation takes a very different turn with addition of NC gases. The starting for most of the modelling endeavors is the 1916 pioneering work of Nusselt [75], which described laminar FW condensation on a flat vertical wall. Ever since, it has been theorized that near to the condensate film surface a concertation gradient in the water vapor / NC gas mixture exists ([112]–[117]), Figure 1-3.

This layer is thought to forms due to asymmetry of gas/liquid interface's permeability to different gas species. Vapor molecules can efficiently pass the boundary while NC gases can only do so at a very limited rate, by becoming dissolved in the liquid layer. As a result, a boundary layer with increased NC species concentration and, correspondingly, decreased vapor pressure is formed at the condensate surface. This creates a barrier which must be passed by vapor through diffusion and convection during the condensation process, resulting in heat and mass transfer degradation. Additionally, due to accumulation of NC gases, the temperature at the gas/liquid interface is lowered, as it corresponds to the partial pressure of vapor.

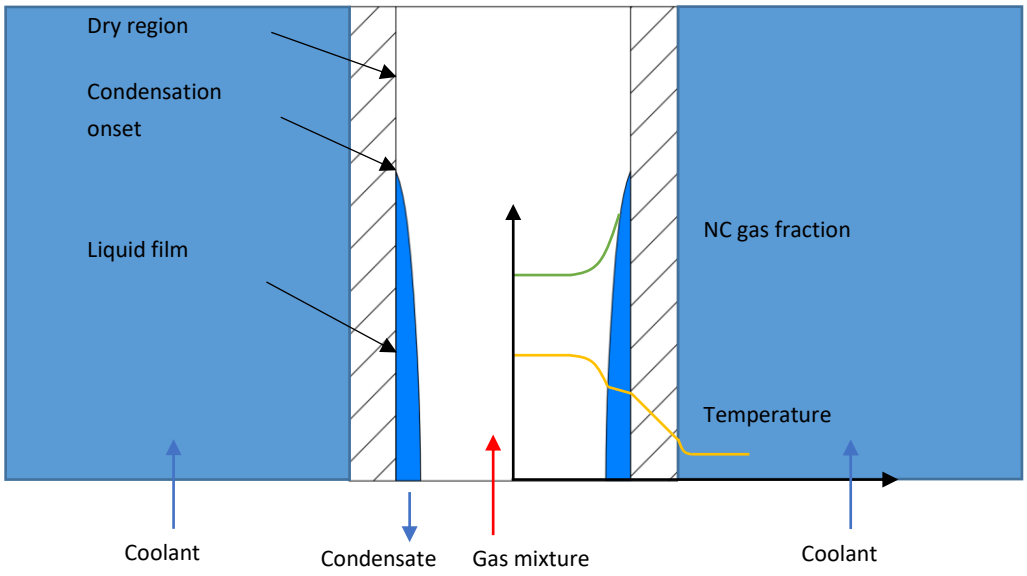

Figure 1-3 Reflux condensation with NC gases - condensate and boundary layer not to scale

Over the years various attempts to create an accurate model of the phenomenon were created. Due to limitations of the available experimental techniques, early research focused on simply correlating the concentration of non-condensable gases with the observed heat transfer coefficient. Later, the discussion was expanded to create more sophisticated semi-theoretical and theoretical models. The impact of condensing surface geometry and orientation was studies (e.g. [33], [34], [118], [119]). The effect of waves was also investigated with conclusion that condensate surface oscillations reduce enhance the condensation with NC gases (e.g. [34], [81], [83], [120]). The condensation retardation effect was compared between

different gas species (e.g. [27], [121]–[124]). Free ([31], [125]) and forced convection ([126]–[128]) flow regimes were analyzed.

Sophisticated correlations for varying scenarios were continually developed over the years. This approach can be found in the work of Uchida [26], Othmer [24], Al-Diwany [27] and Rose [127]. Other examples should include the work of Meisenburg et al. [25] (forced convection steam flow condensing on the outside of a vertical tube, Henderson and Marchello [28] (film condensation of vapors on the outside of horizontal pipes) and Borishanskiy et al. [129]–[131] (steam-nitrogen mixtures condensing downward in a vertical tube). Dehbi [132] investigated condensation on the outside of a vertical cylinder placed in a larger vessel.

Among the various correlations, the degradation factor method became very prominent. The first was proposed by Vierow [133] and is based on comparing the theoretical heat transfer coefficient obtained with Nusselt analysis to measured experimental values. Factors such as NC mass fraction and Reynolds number were incorporated, and a degradation factor relation established. Ogg [134] developed such a correlation for forced convection flow regime in tubes with large diameter. Similarly, Kuhn et al. [124] also included the liquid film thickness into the factor derivation and measured the heat transfer coefficients for pure steam condensation. Additionally, he compared the impact of NC gas species, using air and helium. More recently, Lee and Kim [135] conducted work in a U-tube geometry and included the impact of condensate flow rates and NC gas fraction on the heat transfer coefficient. They studied the effect of shear force and concluded that positive relationship exists between higher shear and heat transfer.

Another popular approach to modelling is the heat and mass transfer analogy. It is based on the parallels that can be drawn between mass and heat transfer and uses well established tools for the latter to describe the former. It was first proposed by Colburn and Hougen [115] in 1934 and introduced a heat transfer coefficient composed of a sum of coefficients of sensible heat and latent heat. The first was proposed to be transferred to the condensate by conduction, with the second is due to the condensation process. They used the relation developed by Chilton and Colburn [136] to calculate the mass transfer coefficient. This approach was later expanded by Akers [137] et al. to the natural convection regime.

Heat and mass transfer analogy was widely accepted by the research community. Votta and Walker [138] developed a method that defined the total heat flux as a product of a total heat transfer coefficient and difference of equivalent temperature gradient from the bulk to the interface. Corradini et al. [139], [140] used the difference between saturation temperatures at bulk at interface to define the total heat transfer coefficient. Peterson et al. [116] derived the heat transfer coefficient using fundamental thermodynamic relationships.

Numerous computational models were created based on the mass and heat transfer analogy. In 2002 No and Park [141] developed a model for condensation with NC gases in vertical tube. They assumed that both gas and liquid were in saturated state and that the radiation heat transfer can be safely omitted. In 2004 Maheshwari [142] et al. presented a similar model but with the vapor mixture flowing downwards. The model included the impact of tube roughness, suction effect and interfacial shear stress, which all impact the condensation as previously mentioned. Oh and Revankar [143] created a model for NC gas condensation in vertical tubes and compared their results against obtained experimental data and found them to be in acceptable agreement. Their model indicated that NC gas concentration increases along the condensation length, as the steam is continuously removed from the gas phase, which impact the performance of long condensers. Recently, Chantana and Kumar [144] used the equation by Oh and Revankar [143] and proposed an iterative model for condensation on the outside of vertical tubes. Compared against their

experimental data, the model has shown good agreement and confirmed the effect of film waviness and importance of the suction effect.

Notable experimental work

Up to date there were numerous attempts to quantify the condensation-retardation effect of NC gases. Table 1-1 attempts to provide an extensive summary of previously mentioned references and expand by other relevant work. The listing includes distinguishing characteristics for each of the presented experiments.

Table 1-1 Summary of experimental work investigating steam condensation with NC gases

Authors	Year	Geometry	Dimensions	NC gas	Mass fraction range	Flows	Pressure	Comment
Henderson [28]	1969	Vertical tube	D:L = 29:1220	Air	0.1-0.83	-	-	-
Slegers [145]	1970	Vertical plate	127x50.8	Air	0-0.01	~0	0.004-0.03 MPa	Low Re values to avoid condensate ripple formation
Al-Diwany and Rose [27]	1973	Vertical plate	97*97*12.5	Air, Ar Ne, H_2	0.02-32	-	0.04-1.24	Natural convection FC
Lee and Rose [127]	1984	Horizontal tube	7.5:109.5	Air	0.02-32	0.3-26 m/s	0.04-1.24	Created the accurate measurement
Legay [146]	1985	Vertical plate	800 x 200	Air	0.42-0.55	4-5.3 m/s	0.1 MPa	Removed condensate film to maintain laminar flow
Galamba, Dhir and Taghavi [147]	1986	Vertical plate	-	Air	0.12-0.59	0.02 kg/s	1 atm	Melting plate of naphthalene or Wood's metal
Barry [148]	1987	Horizontal tube	D:L = 10:610	Air	0.47-0.92	2.1-6.9	1 atm	Direct-contact condensation on sub-cooled liquid
Kutsuna [149]	1987	Vertical plate	500x100	Air	0-0.15	2-6 m/s	-	-
Stein, Cho and Lambert [150]	1988	Horizontal disk	D=137 mm	Air/He	0-0.1.4e-5	~0	0.31-1.24	Plate facing down with stagnant conditions
Robinson [151]	1988	Vertical disk	D = 46 mm	Air	0.16-0.87	~0	0.27-6.2 MPa	-
Bannwart [152]	1990	Horizontal tube	D:L=20:4000	Air	0.02-0.3	5-50 m/s	0.1-0.15 MPa	Saturated steam-air mixture
Dehbi [132]	1991	Vertical tube	D:L = 38:3500	Air	0.28-0.90	Pool boiling with 36 kW heater	1.5-4.5 bar	Free convection on the outside of a tube
Vierow and Schrock [153]	1991	Vertical tube	D:L = 22:2100	Air	0-14	5.9-24.95 kg/h	0.03-0.45	Loop heat pipe

Huhtiniemi and Corradini [123]	1993	Plate	60x102, inclined between 0° and 72°	Air	0.24-0.87	1-3 m/s	1 - 1.64 bar	Co-current mixture and condensate flow
Murase, Kataoka and Fujii [154]	1993	Vertical plate	500x4200	Air	0.4-0.95	30 kg/h	0.5 MPa	Steam supplied through a suppression pool
Siddique et al. [155]	1993	Vertical tube	D:L = 46:2540	Air/He	10-35	7.9-31.9 kg/h	0.1-0.5	Local h_{tc} for forced-convection condensation and compare Air/ He
Kang and Kim [33]	1994	Horizontal plate	100*150*1520	Air	0-0.78	1-7 m/s	1	Wavy water film
Akaki et al. [118]	1995	Vertical tube	D:L = 49.5:2000	Air	0-24	9.0-58.0 kg/h	0.15-0.25	Inside vertical tube; Re < 2300
Karapantsios and Karabelas [32]	1995	Vertical tube	D:L = 50:2660	Air	0.15-0.75	26-416 g/s	1 atm	Stagnant gas mixture
Kuhn [156]	1995	Vertical tube	D:L = 47.5:2400	Air/He	0-4	-	0.1-0.5	Turbulent films at high Reynolds numbers
Oh, Yoon, Kwon, Chen and Tien [157]	1995	Vertical tube	D:L = 14.2:1030	Air	0.7-0.98	100-500 kg/m2s	1.02 bar	Forced convection
Hasanein, Kazimi and Golay [126]	1996	Vertical tube	D:L = 46:2540	Air/He	0.022-0.2	25 kg/h	1.14-6.03 bar	Forced convection
Park and Kim [34]	1996	Vertical plate	24*150*1510	Air	0.1-0.7	3,5,7 m/s	0.19-0.49	Wavy water film
Lee, Liu, Way, and Hsia [158]	1996	U-tubes	D:L = 15.4:4080	Air	Varying during the exp.	Varying during the experiment	0-2.1 MPa	IIST facility; loss of RHR during mid-loop operation scenario
Kuhn, Schrock and Peterson [124]	1997	Vertical tube	D:L = 50:3370	Air/He	0.01-0.4	30-60 kg/h	100-500 kPa	Concurrent mixture and condensate flow
Noel and Dumont [159]	1997	Vertical U-tubes	D:L = 19.68 : 19450	He	0-2.18 kg He	-	0.2-0.8 MPa	Bethsy 10.2
Anderson, Herranz and Corradini [160]	1998	Simulated containment wall	-	Air/He	0.47-0.88	0-0.027 kg/s	1-3 bar	Simulated AP600 reactor containment
Moon, No, and Bang [161]	1999	Vertical tube	D:L = 16.56:2400	Air	0.118-0.55	1.348-3.282 kg/h	1,1.5,2.5 bar	Countercurrent gas and condensate flow
Park and No [120]	1999	Vertical tube	D:L = 47.5:2400	Air	10-70	7.6-40.0 kg/h	0.17-0.5 MPa	Inside vertical tube
Chataing [122]	1999	Single vertical tube; 3-tube bundle	D:L = 20:4000	N_2/He	0-1	0-4 g/s per tube	2-70 bar	COTURNE test facility

Kim and No [162]	2000	Vertical tube	D:L = 46.2:1800	Air	0-30	-	0.35 – 7.2 MPa	Height pressure inside vertical tube
Liu, Todreas and Driscoll [163]	2000	Vertical tube	D:L = 40:2000	Air/He	0.3-0.65	27 kW heater	2.5-4.6 bar	Condensation on the tube's outside
Moon, Park and Bang [164]	2000	Vertical tube	D:L = 19.05:2400	Air	0.118-0.55	1.875-4.443	1, 1.5, 2 bar	Reflux condensation regime
Liu [165]	2001	U tube	D:L = 15.4:2000	Air	0-5	-	0.1-0.5 MPa	NC accumulation in U tube
Sarrette [166]	2003	Horizontal tube	D:L = 16:2819	Air	varying in the facility	0.08 kg/s	0-0.75 MPa	Simulated LOCA in SG tubes in PACTEL test facility
Vierow, Nagae, Wu [167]	2003	PWR SG tubes	D:L = 19.3:1780	Air	0.022-0.069	0.44-2.2 g/s	0.1-0.45 MPa	Reflux condensation regime simulating NPR mid-loop operation regime
Al-Shammari, Webb, and Heggs [168]	2004	Vertical tube	D:L = 28.25:3000	Air	47-97	5.24-11.3 kg/h	0.19-0.33 MPa	Steam or steam-NC enter from the bottom of tube
Murase, Tagae, Minami [169]	2005	Vertical tube	D:L = 19.3:1780	Air	P_{steam} / P_{air} = 0.0054:120	0.49-1.9 g/s	0.1, 0.2, 0.4 MPa	The same facility as in Vierow 2003
Oh and Revankar [170]	2005	Vertical tube	D:L = 26.60:984	Air	0-0.1	2.5-5.5 g/s	0.1-0.4 MPa	Inside vertical tube
Wu, Vierow [171]	2005	Horizontal tube	31.75x2.1	Air	0-15	6.0-11.5	0.1,0.2,0.4 MPa	Double pipe, countercurrent flow, concentric-tube heat exchanger
Lee et al. [135]	2006	U tube	D:L = 16.2:2800	Air	0.12-0.96	1.08-3.59 kg/h	0.1 MPa	U tube heat transfer
Oh and Revankar [143]	2006	Vertical tube	D:L = 26.60:2400	Air	0-10	2.5-5.5 g/s	0.12-0.4 MPa	Inside vertical tube
Wu and Vierow [172]	2006	Horizontal tube	D:L = 27.5:3000	Air	0-20	8.2-38.0 m/s	0.1,0.2,0.4 MPa	Inside horizontal tube
Park et al. [173]	2007	Vertical tube	D:L = 10.9:1000	Air	0-0.22 kg/s	-	40, 70, 100 bar	High pressure
Zhu et al. [174]	2007	Vertical tube	D:L = 10:(1000-2500)	Air	34-81	1.08-10.8 m/s	0.1 MPa	High mass fraction NC in steam; annulus around a vertical tube
Nagae, Murase, Chikusa and Vierow [175]	2007	Vertical tube	D:L = 19.3:1780	Air	P_{steam} / P_{air} = 0.0039:22	0.48-1.9 g/s	0.2, 0.4 MPa	The same facility as in Vierow 2003
Lee and Kim [176]	2008	Vertical tube	D:L = 13:2800	Air	0-40	6.5-28.2 kg/h	0.1-0.13 MPa	Local heat transfer in vertical tube

Li, Wang and Yu [177]	2008	Vertical u-tubes	D:L = 12:1000	Air	A lot	4.5-6.55 kg/h	0.12 MPa	Inclined U tube
Kim, Lee, Ahn and Park [178]	2009	Vertical tube	D:L = 40:650	N_2	0.06-0.72	20 kW heater	4-20 bar	Condensation on the tube's outside
Umminger et al. [179]	2011	Vertical u-tubes	Prototypical SG tubes	N_2	varying in the facility	35 kg/s	0-45 bar	PKL - III test facility
Caruso, Maio and Naviglio [119]	2013	Three different finned copper tubes	Inclination 7°,12°,30° and 45°	Air	0.05-0.4	Re from 7500 - 12000	1 atm	Condensation on the tube's outside
Chantana and Kumar [144]	2013	Vertical tube	D:L = 26.7:2000	Air	0.88-0.97	1.8-5.5 m/s	0.1 MPa	Wet air condensation
Czubinski, Mantelli and Passos [180]	2013	Vertical and downward inclined tube	116.2x100, 142.8x100, 200x100	Air	0-0.5	2.4 g/s	1 atm	Raising streams of a vapor-air mixture over grooved surfaces
Su, Sun, Fan and Ding [181]	2014	Vertical tube	D:L = 38:2000	Air/He	0.07-0.52 air and 0.08-0.4 He	240 kW heater	0.2-0.6 MPa	Outside vertical tube
Caruso and Vitale [182]	2014	Horizontal and inclined tube	D:L = 22:1587	Air	0-26	0.828-8.28 kg/h	0.1 MPa	Inclined tube
Ren, Zhang, Cao, Xu and Tao [183]	2015	Horizontal tube	D:L = 16:1750	Air	0-40	24.8-165.8 kg/m2s	0.1-0.4 MPa	Double pipe, countercurrent flow heat exchanger
Jang et al. [184]	2015	Vertical tube	D:L = 40:1000	Air	0.1-0.8	120 kW heater	2, 3, 4 bar	Condensation on the tube's outside
Hu, Tang and Niu [185]	2016	45 horizontal smooth and finned tube bundles	D:L = 14.1:251	Air	0-0.75	0-1000 m3/h	0.1-0.7 MPa	Condensation on the tube's outside
Yi et al. [186]	2016	Vertical plate	100x50	Air	0.05-0.5	0-1 m/s	0.1 MPa	High-speed camera investigation
Wen, Cheng, Zeng and Wang [187]	2016	Horizontal tube and multi-head spiral channel	D:L = 50:1000 (tube) / D:L 48.5:1000 (MHSC)	Air	0-0.1	28-65 kg/h	0.3-0.7 MPa	Countercurrent flow gas and cooling water
Xu, Sun, Gu and Li [128]	2016	Horizontal tube	D:L = 25:1500	Air	0.05-0.32	17.27-33.65 m/s	0.15-0.4 MPa	Forced convection
Xu, Gu and Sun [121]	2017	Horizontal tube	D:L = 25:1500	Air/He	0-0.9	8-34 m/s	0.13-0.2 MPa	Multiple flow regimes of liquid film
Fan, Tong, Sun and Chen [188]	2018	Vertical smooth & corrugated tube	D:L = 30:2000	Air	0.1-0.95	-	0.2-0.5 MPa	Natural convection regime

1.5 Motivation summary

As presented in the previous chapter, a very exhaustive effort was committed to study the condensation processes with and without NC gases. Nevertheless, the complicated nature, multiphase and geometry dependent nature of the process prevents the researchers from presenting a comprehensive model and theory fitting all the possible use cases.

This limitation has a strong impact on the field of nuclear energy safety, which employs elaborate models and calculation tools incorporating those models to predict the possible dangers and accident scenario developments. Therefore, as a protective measure most of the modern tools employ conservative approaches, often underestimating the heat removal potential of the condensation process ([164], [189], [190]). Various studies have attempted to deal with this issue up to date. Most of the test facilities consist of a flow-through condenser ([161], [167]–[169], [191]) in which a mixture of steam and NC gas is injected in the condensation tube. Additionally, a few large scale facilities were constructed, to study loss of residual heat during mid-loop operation ([14], [158], [179], [192], [193]).

Nevertheless, almost all previous experimental studies employed only thermocouples, pressure transducers and flow meters as a main source of data to provide descriptive information about the condensation process. A very descriptive template of condensation experiments was presented by Huang et al. [41], Figure 1-4.

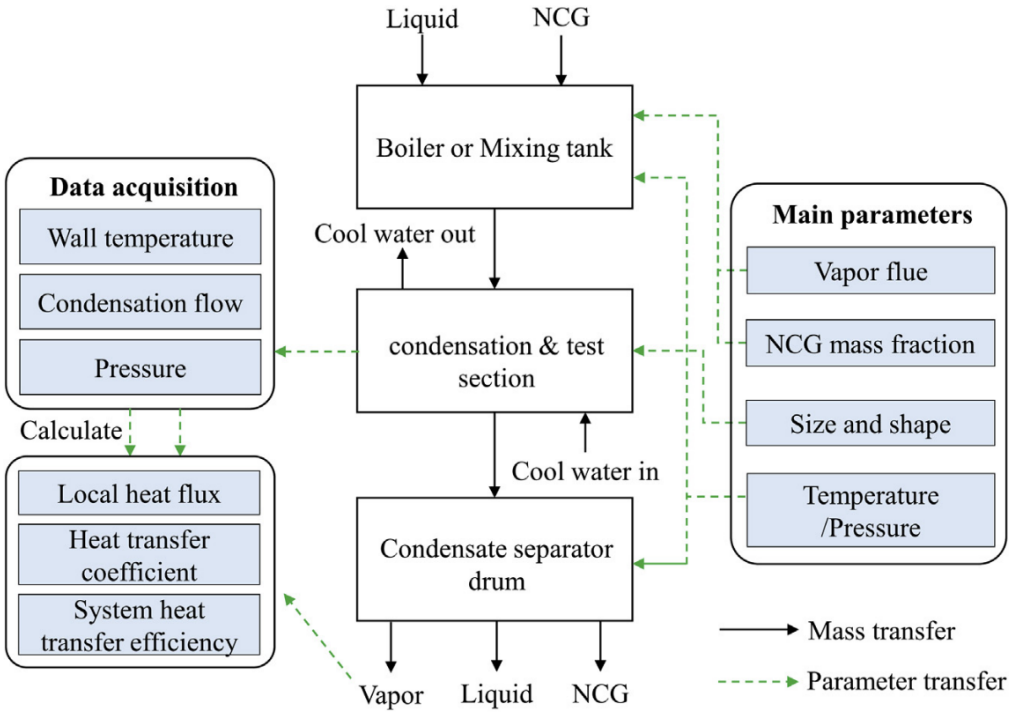

Figure 1-4 Typical condensation experiment template, reproduced from Huang et al. [38]

This works expands the extensive body of research by incorporating direct heat flux measurements and characterization of cross-sectional temperature profiles in the condensing volume. Moreover, the higher frequency domain of condensation processes is explored, thanks to the developments of the measurement technique, with hopes of uncover the higher-order effects of condensate film behavior and NC gas – vapor mixing – a topic completely untouched up to date. With the promise of more accurate understanding of the steam condensation in the vertical tube obtained experimentally in the course of this work comes the hope

of improving the accuracy of the currently employed models used nuclear codes. Therefore, the gathered experimental results are compared to the calculations conducted with the current stable release of the Reactor Excursion and Leak Analysis Program (RELAP5/MOD3.4).

Chapter 2 Infrastructure – PRECISE facility

The PRECISE facility acronym stands for Precise Reflux Investigation Setup. This name was chosen to underscore the novel measurement methods and high temporal resolution of the collected data. This chapter explains the way of experimental modeling of the reflux condensation phenomenon and the design of test facility. It provides a detailed technical description of the used components and their role in the experiments. For selected components, technical drawings are provided in the appendix section 10.5.

2.1 Reflux condensation modelling

To investigate reflux condensation, an experimental facility was designed and constructed. The design principles focused on simplifying the PWR steam generator assembly while at the same time keeping the crucial elements that ensure gathered data remained relevant. Since primary interest of this project was to investigate the impact of non-condensable gases, the phenomena relating the interaction of different individual tubes in the steam generator bundle were not investigated. Thus, the bundle assembly was reduced to just a single tube. To simplify the design further, just the upward leg of the whole U-tube was chosen as a proper model as only this part experiences counter-current flow of gas and condensate. The problem simplification steps are shown in Figure 2-1.

The facility was then designed to model the single vertical tube. It can be subdivided into two main subsystems – primary loop, with steam generation and condensation tube and secondary loop which supplies and maintains steady coolant water flow on the secondary side, as shown in Figure 2-2. The upward leg of the PWR SG tube is modeled by the condensation tube (marked in yellow) with the upper end sealed. This simplification, by design, ensures the inherent consistency in the supplied heat and the thermal energy removed by through condensation. This simplifies the instrumentation and reduces uncertainties.

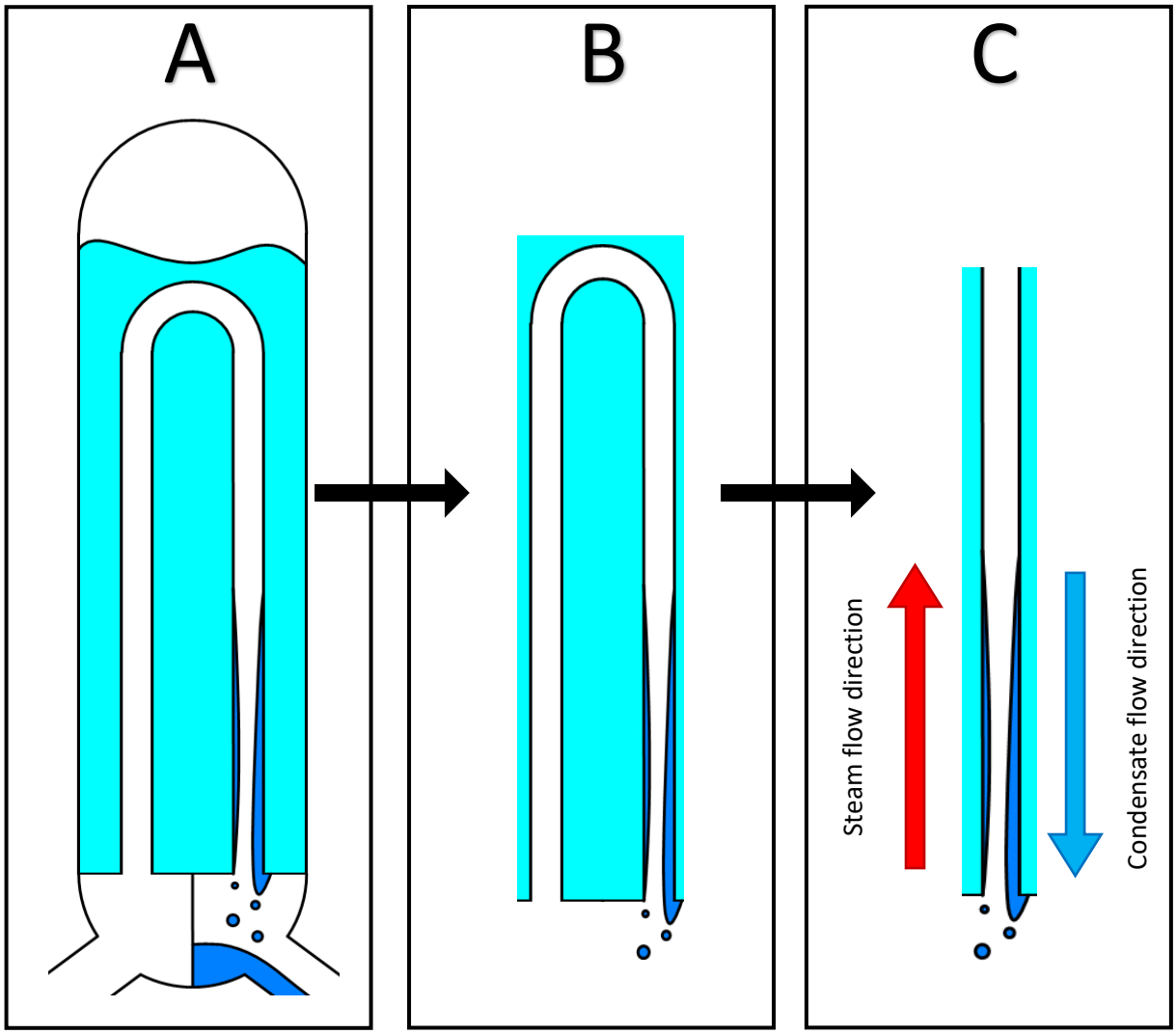

Figure 2-1 Reflux condensation modelling: A - PWR steam generator, B - single PWR SG U-tube, C - upward leg of a single U-tube

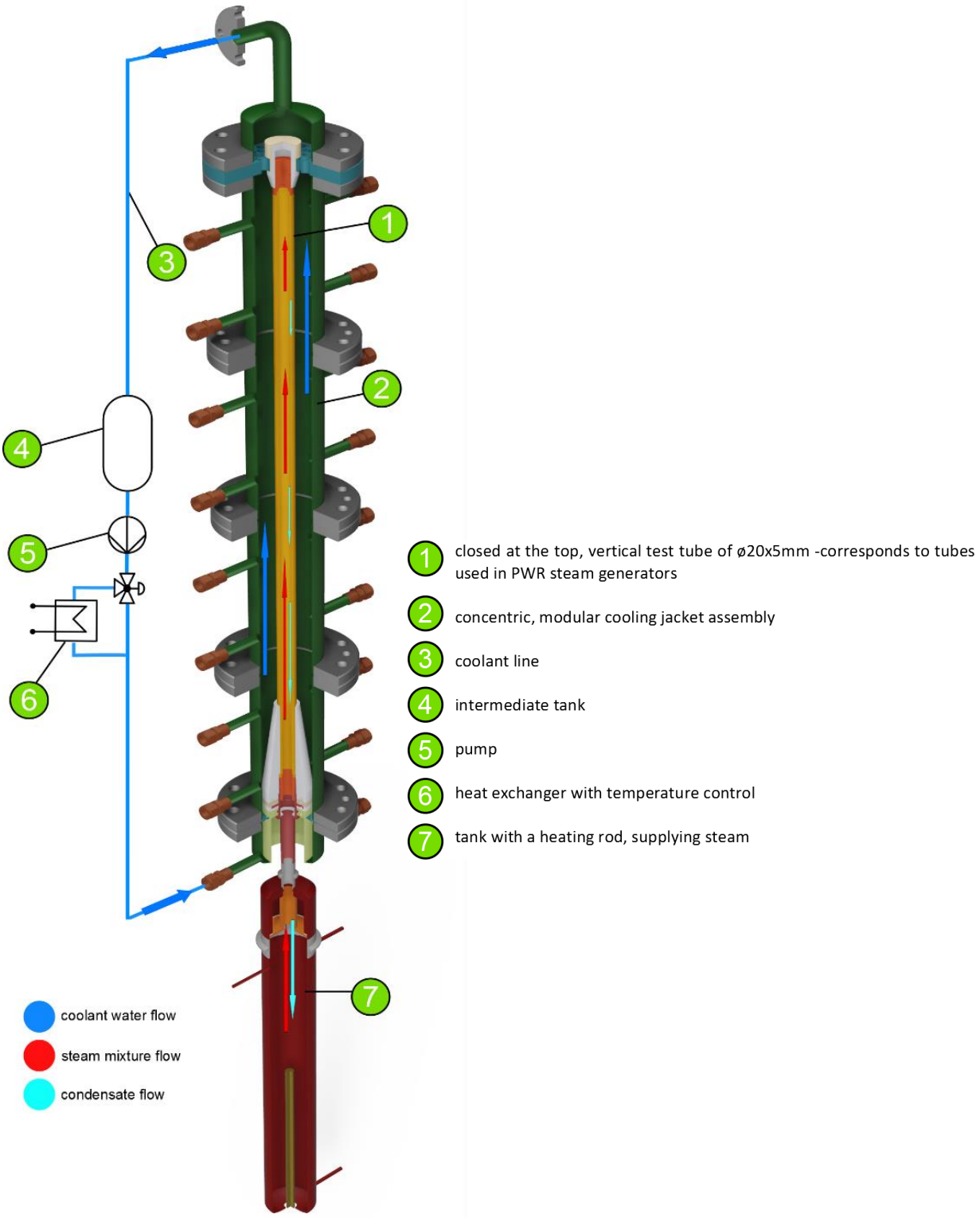

Figure 2-2 Cross-section of the test facility and an overview of the secondary coolant loop

2.2 Facility operating conditions

2.2.1 Overview

The PRECISE facility can be operated safely with absolute primary and secondary side pressure reaching 10 bar. Installed passive safety valves are set to open at 12 bar to release overpressure. The corresponding temperature range is from 20 °C to 180°C. The average molar fraction of non-condensables can be set to any value between 0 and 1 average mole fraction. Non-condensable gases used in the PRECISE facility are helium (as a safe hydrogen substitute), nitrogen and a mixture of both, with varied volume fraction ratios.

With the installed 2 kW heater, a maximum steam production in between 0.88 to 1 g/s can be reached at 1 and 10 bar of pressure respectively. Setting the maximum test pressure to 10 bar was a compromise between ensuring flexible test conditions and reducing test section design difficulties combined with possibility to employ novel sensors such as the movable conductivity and temperature probe. The summary of the operating conditions is given in the Table 2-1.

Table 2-1 Operating conditions summary (water properties calculated based on IAPWS-IF97* [194]*)

Parameter	**Value range**	**Unit**
PRIMARY LOOP		
Electrical heating power	0 – 2	kW
Pressure	1 – 10	bar
Temperature	20 – 180	°C
Steam vapor density	0.59 – 5.147	kg/m^3
Steam mass flow	0 – 1	g/s
Steam velocity	0 – 5	m/s
Steam Reynolds number[1]	0 – 25000	-
Condensate mass flow	0 – 1	g/s
NC gas mole fraction	0 – 1	-
NC gas species	N_2 & He	-
NC gas – N_2 to He ratio	0 – 1	-
Safety pressure release	12	bar
SECONDARY LOOP		
Liquid	Demin. water	-
Pressure	1 – 10	bar
Temperature	20 – 180	°C
Water mass flow rate	0 – 5000	kg/h
Water velocity	0 – 0.175	m/s
Water Reynolds number[2]	0 – 70000	-
Safety valve release pressure	12	bar
ENVIRONMENT		
Lab temperature	15-25	°C

[1] Re number calculated using the test tube diameter

[2] Re number calculated using the coolant jacket hydraulic diameter (for an annulus: $D_{out} - D_{in}$)

2.2.2 Counter-current flow limitation

The phenomenon of counter-current flow limitation (CCFL) is not a subject of investigation of this work. Hence, measures were taken to verify that at higher steam velocities in the test tube a condensate flow reversal and a flooding of the test tube would not occur. Various empirical correlations were used to calculate the limiting velocity. The correlations of Issa [7], and Jeong, [5], [195] are Wallis-type correlations [196], following the general form of eq. (3):

$$m(J_L^*)^{1/2} + (J_G^*)^{1/2} = C_{em} \qquad (3)$$

Where J_L^* and J_G^* are dimensionless superficial velocities of the liquid and the gas phases, defined by eq. (4), which represents Froud number extended by a density ratio:

$$J_i^* = J_i \left(\frac{\rho_i}{gD(\rho_L - \rho_g)} \right)^{1/2} \qquad (4)$$

The two empirical parameters, m and C_{em} must be determined experimentally, as they are dependent on the geometry of the flow duct. Jeong shows that values of 0.85 and 1 respectively show good agreement with data gathered during reflux condensation in steam generator tubes. On the other hand, Issa suggests using values of 0.32 and 0.48 for tubes with length to diameter ratio over 40 and if superficial liquid velocity is below 0.3.

Another well-established empirical correlation is the Kutateladze correlation [197]. It is similar to the previous two, but it lacks parameter m and defines superficial velocities using surface tension σ instead of tube diameter D and sets parameter C_{em} to $\sqrt{3.2}$, according to eq. (5).

$$J_i^* = J_i \left(\frac{\rho_i}{g\sigma(\rho_L - \rho_g)} \right)^{1/2} \qquad (5)$$

where the denominator is the Laplace constant $[g\sigma(\rho_L - \rho_g)]^{1/2}$ [198]. The diameter D of the tube is replaced by capillary length scale as a characteristic dimension [199]. This is suitable for tubes with sufficiently large diameters so that the curvature effect is overcome by the surface tension impact. Value of 50 mm was suggested as a transition size, over which the Kutateladze correlation improves prediction accuracy over Wallis-type ones [200]. Therefore, for the discussed problem, the Kutateladze correlation may strongly overestimate the flooding onset velocity.

For the full range of experimental conditions, Table 2-2 summarizes the actual steam velocity (assuming the highest achievable steam mass flow, generated at 2 kW delivered electrical power) and limiting velocities according to the three correlations.

Table 2-2 CCFL onset velocity comparison

Press. [bar]	Sat. Temp [K]	Actual velocity [m/s]	Issa [m/s]	Jeong [m/s]	Kutateladze [m/s]
1	373.76	4.79	3.99	9.64	13.64
3	407.68	1.79	2.33	5.24	7.24
5	425.99	1.13	1.80	3.91	5.32
8	444.56	0.75	1.42	2.96	3.96
10	454.04	0.62	1.27	2.58	3.42

As predicted, the Kutateladze correlation produces the highest values, which can be safely diagnosed as overprediction. For a most conservative comparison, the Issa correlation can be therefore used. At the lowest test pressure, it suggests that a flooding limit might be reached, however one must account for ±20% accuracy listed by authors. Nevertheless, for high power – low pressure experiments, special care was taken, to monitor if the flooding onset was reached. Ultimately, none of the gathered data suggested CCFL conditions were met during the experiments. During the steady state, no sudden changes in pressure were observed. Similarly, temperature in the center did not exhibit the oscillations ([164], fig. 2.8) in the regions with largest steam velocity where flooding could be possible.

2.3 Facility – technical description

The PRECISE facility can be subdivided into two main subsystems – the primary and the secondary loops. The primary loop comprises of the steam generation tank and the condensation tube, while the secondary loop includes a cooling jacket and the accompanying equipment which supplies and maintains steady coolant water flow. The cross-sectional overview of the facility and its physical implementation are shown in Figure 2-3. The test rig is additionally equipped with water and NC gases feeding tanks, which allow for a precise control of the gas inventory in the test tube.

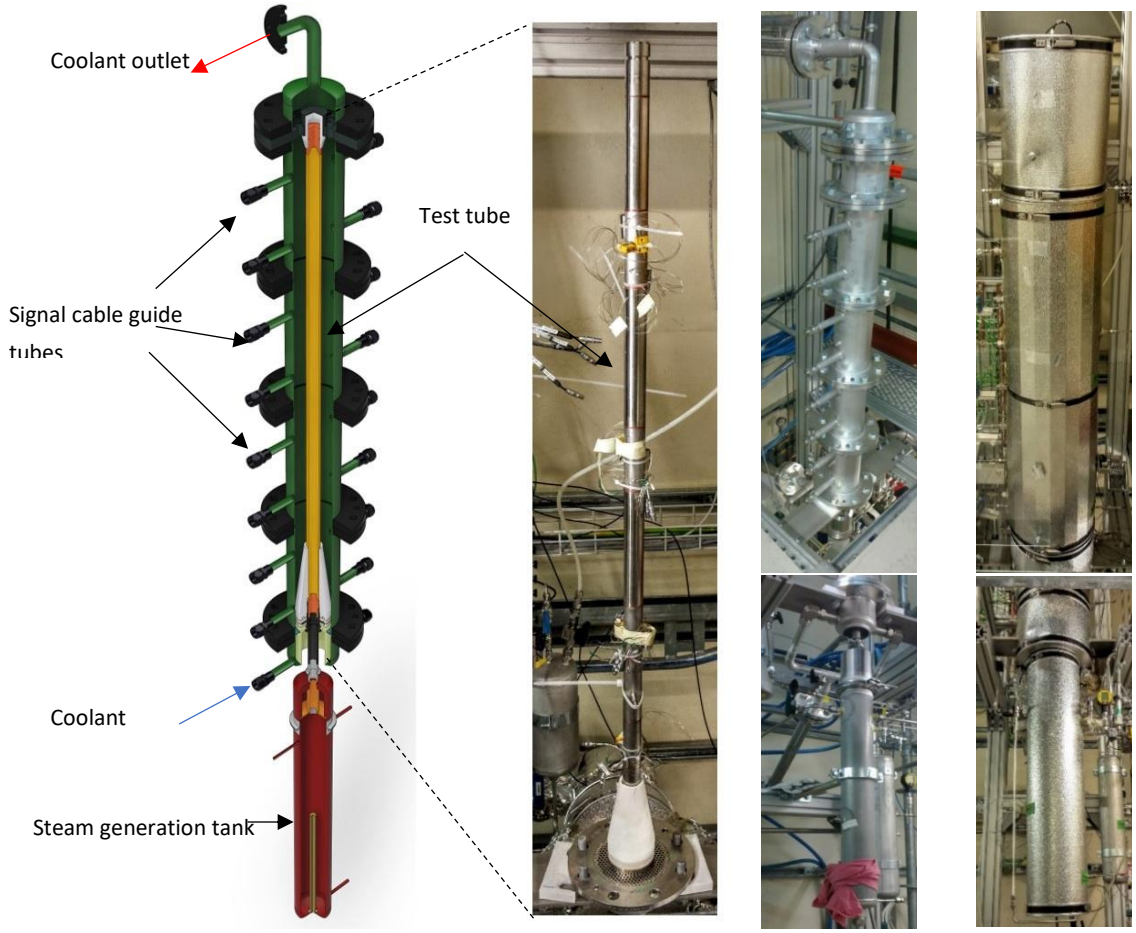

Figure 2-3 PRECISE facility overview, left to right: cross-section, exposed test tube, assembled facility, outer insulation

For detailed technical drawings of the PRECISE facility components please refer to the appendix section 10.5.

2.3.1 Primary loop

A simplified schematic of the primary loop is presented in Figure 2-4 (a fully detailed schematic can be found in the appendix section 10.1).

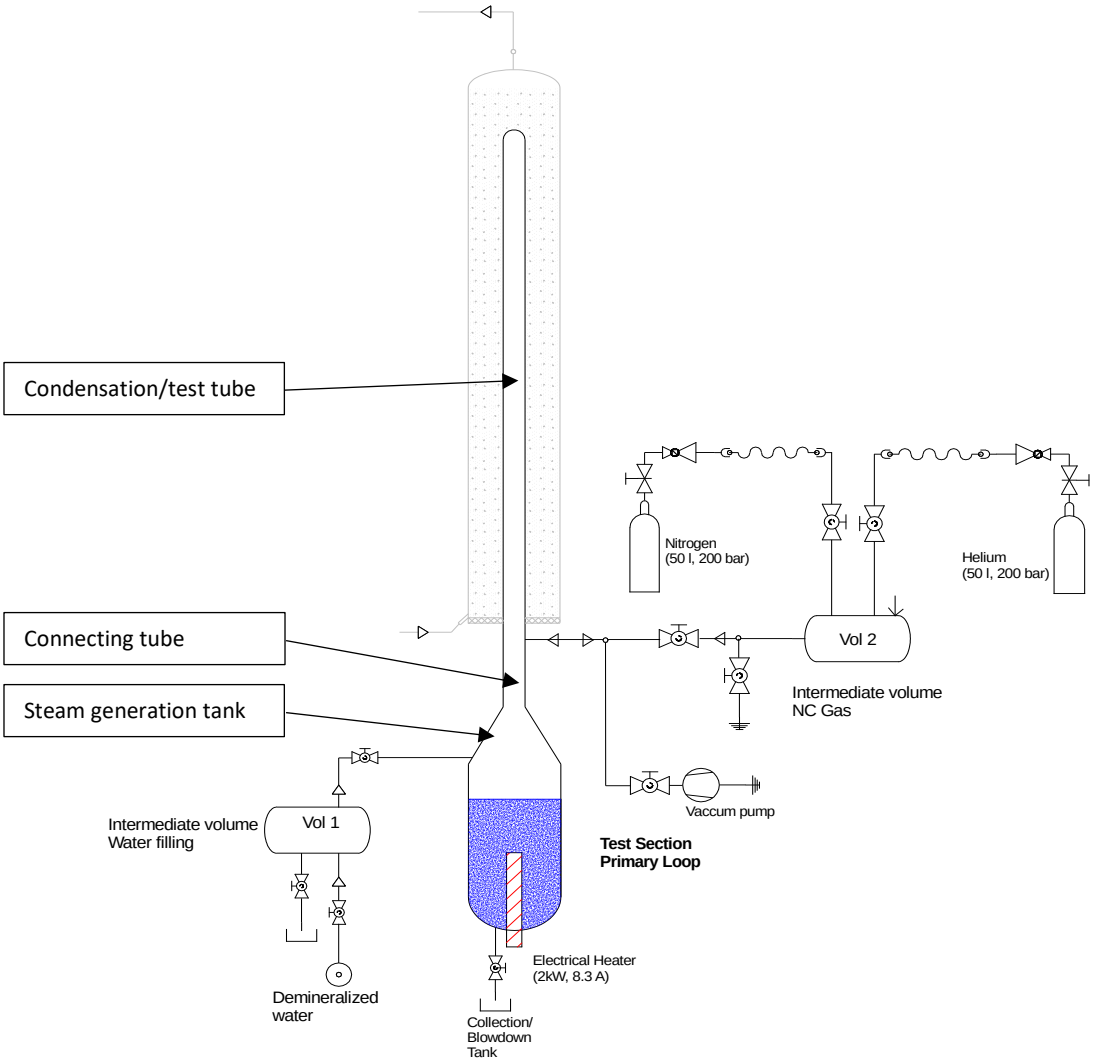

Figure 2-4 Primary loop - simplified schematic (parts of secondary loop greyed out)

The primary loop can further be divided in two main parts: the test volume and the accompanying equipment. The test volume is comprised of a vertical condensing tube, a connecting tube and a steam generator tank (listed in frames in Figure 2-4). The tubes are located above the tank and connected to it, forming a single volume in which the experiments take place. To ensure a maximum control over primary loop inventory, the accompanying equipment includes two intermediate tanks used for filling demineralized water and NC gases that are separated from the rest of the loop with shut-off valves for the duration of the tests. A short summary of the main dimensions and materials of the main components is presented in Table 2-3. The operation of the loop is explained in the chapter 2.4.1.

Table 2-3 Primary loop components overview

Component	Height [m]	Inner diameter [m]	Volume [m³]	Material
Test tube	1.3	0.02	0.000377	1.4404 (ASTM 316/ 316L) steel
Connecting tube	0.4	0.02	0.000126	1.4404 (ASTM 316/ 316L) steel
Steam generation tank	0.64	0.0837	0.0035	1.4404 (ASTM 316/ 316L) steel
NC filling tank (Vol 2)	0.5	0.1091	0.005	1.4404 (ASTM 316/ 316L) steel
Water filling tank (Vol 1)	0.23	0.1091	0.0025	1.4404 (ASTM 316/ 316L) steel

Furthermore, the following accompanying equipment was installed:

- Electrical heater rod (2kW), located in the steam generation tank and used to produce steam
- Vacuum pump, for the preconditioning of the facility
- NC gas supply pressurized bottles (He and N_2), connected to the NC gas tank, for the preconditioning of the facility
- Tubing connecting intermediate volumes and steam generation tank
- Shut-off and needle valves, controlling the flow of gases and water during preconditioning

All the parts were chosen to withstand temperatures up to 200°C – the range planned for the experiments. The prevailing materials included stainless steel (tubing and valves), PTFE (seals and fittings) and Viton (O-rings). All heated parts exposed to the environment are thermally insulated with mineral wool insulation.

The test tube is not permanently attached to the remainder of the facility. Instead, a bayonet mount with two sealing O-rings is used to position and keep it in place. The test tube is inserted from the top and rotated to lock in place and the top of the tube is fixed with a flange – this allows for a tube exchange. Additionally, to limit the heat transfer between test tube and cooling jacket at contact points, PTFE heat resistors (minimum thickness of 5 mm) were introduced in all relevant areas (Figure 2-5).

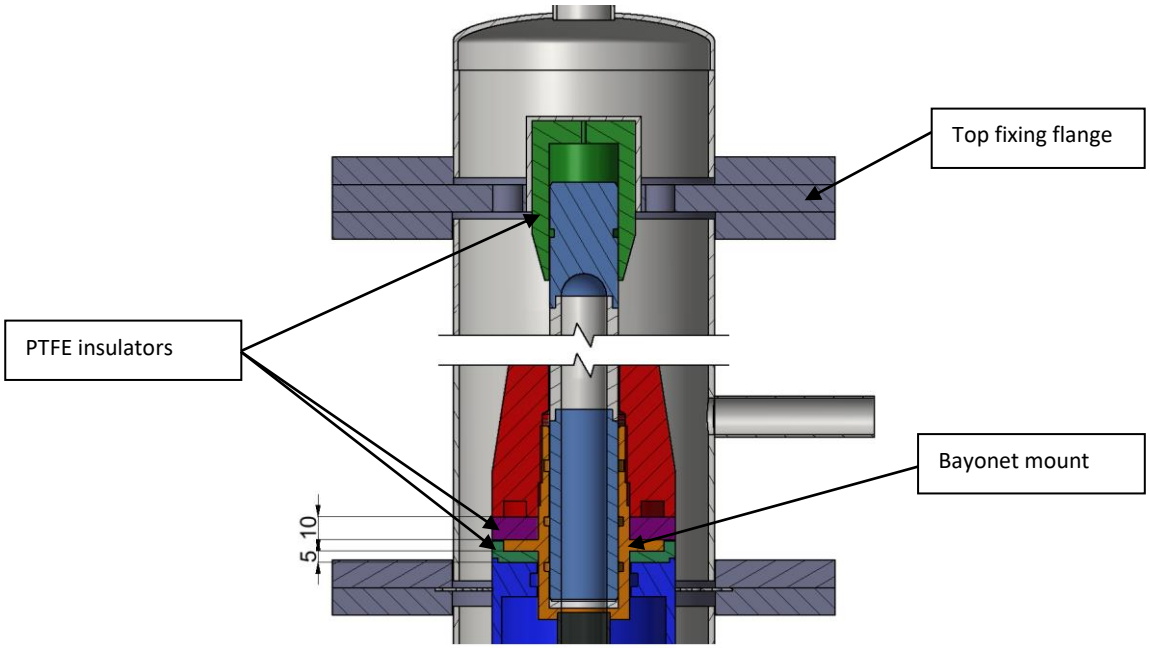

Figure 2-5 Insulation between the test tube and the coolant jacket

2.3.2 Secondary loop

A simplified scheme of the secondary loop is presented in Figure 2-6 (for fully detailed scheme, please refer to the appendix sections 10.1 and 10.2).

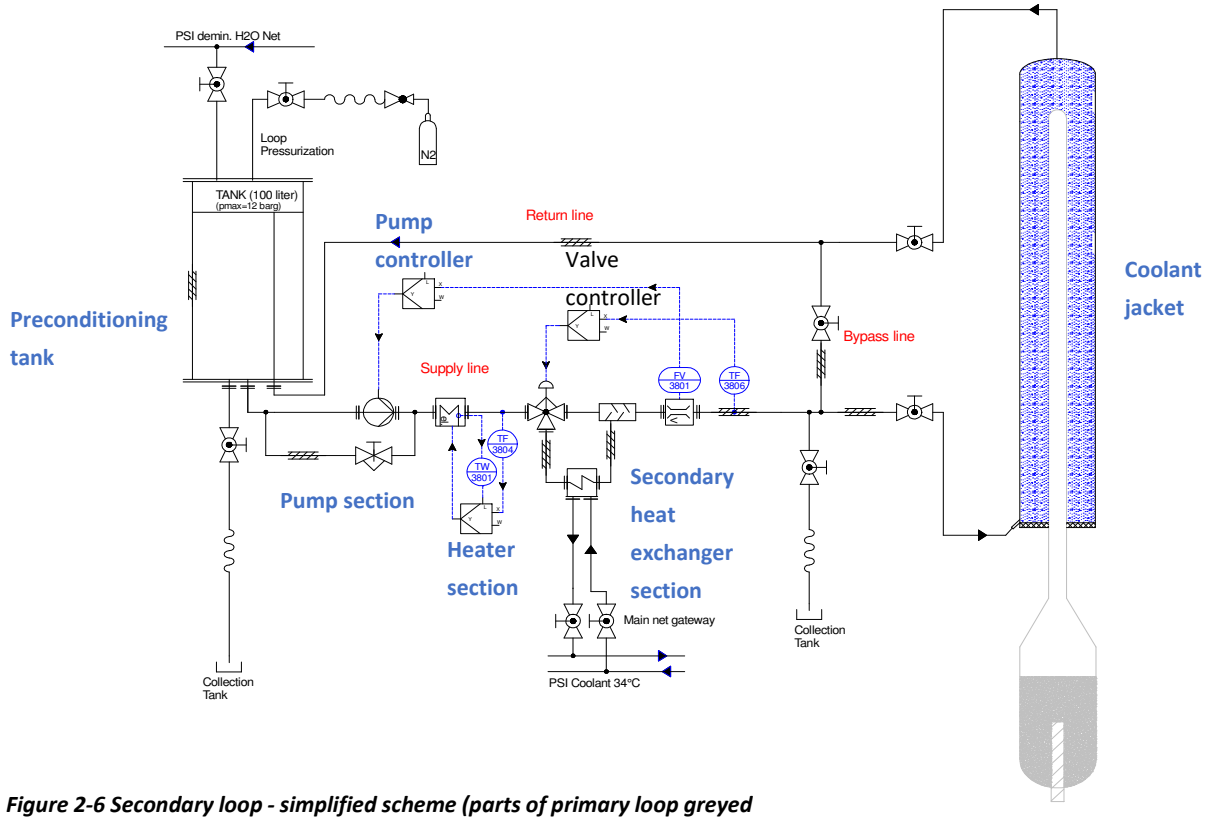

Figure 2-6 Secondary loop - simplified scheme (parts of primary loop greyed

To remove the condensation heat, the test tube is surrounded with coolant water, flowing through a concentric cooling jacket. The water is supplied from a preconditioning tank (100 l). The system is equipped with a rotary pump (Grundfos CRN5-4 A-FGJ-G-E-HQQE) which can supply a steady flow up to 5.8 m^3/h, high enough to ensure turbulent flow and limit the effect of water heat-up along the test tube wall. The coolant water heat-up was limited to 1K, measured precisely with PT100 resistance thermometer elements installed at the inlet and outlet of the coolant jacket. The temperature of the coolant water can be exactly set, thanks to the installed electrical heater and tertiary heat exchanger, connected to an institute-wide cooling water network with a constant temperature of 30°C. The pressure can be adjusted injection of N_2 gas in the preconditioning tank. Additionally, the coolant jacket can be separated from the rest of the loop, and through the bypass line, the loop can be operated independently to condition the water. The operation of the loop is explained in detail in the chapter 2.4.2.

A few steps were taken to limit the entrance effects on the coolant water flow into the cooling jacket, Figure 2-7. First, the water is injected into the jacket from two opposite sides, to equalize the flow distribution. Second, a perforated plate was placed just after the inlet plenum, at the inlet to the jacket. Finally, a PTFE cone with the height of 150 mm was installed in the bottom part of the channel, which created a gradual transition of the diameter of the duct. The total height between water injection point and direct contact with the condensation tube is 256 mm.

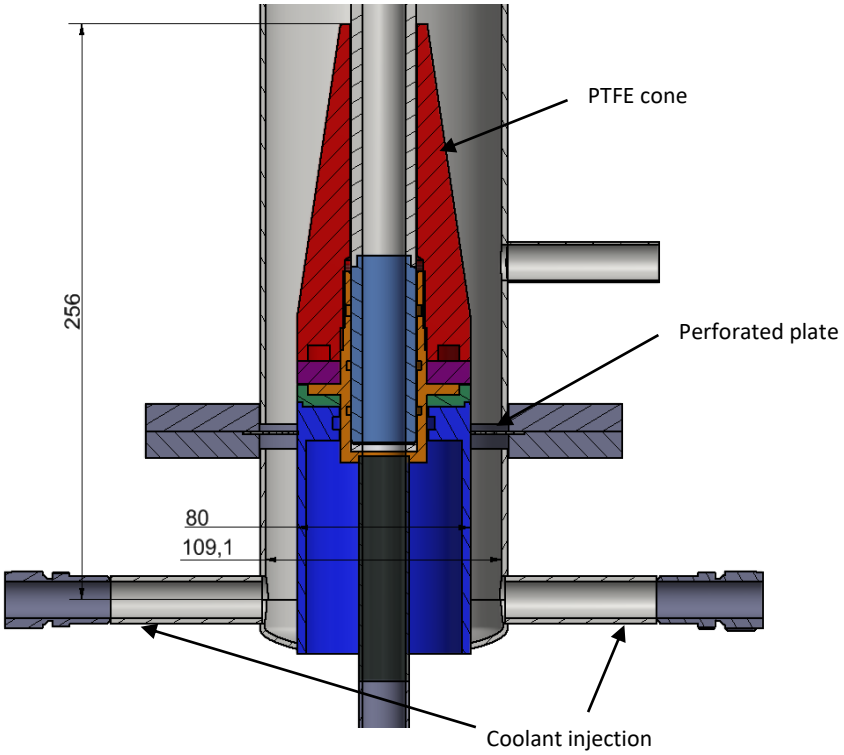

Figure 2-7 Water injection to the coolant jacket

2.3.3 Facility location

The PRECISE facility is located in an underground cavity, the bottom of which lies approximately 8 m under the ground level (Figure 2-8). The cavity provided space and convenient temperature conditions throughout the year, ranging from 15 to 25˚C on average.

The facility had to be mechanically fixed to the support structure made of aluminum – profiles (Bosch manufactured). To minimize heat losses through the connections, PTFE insulation layers were introduced in all relevant locations (Figure 2-9).

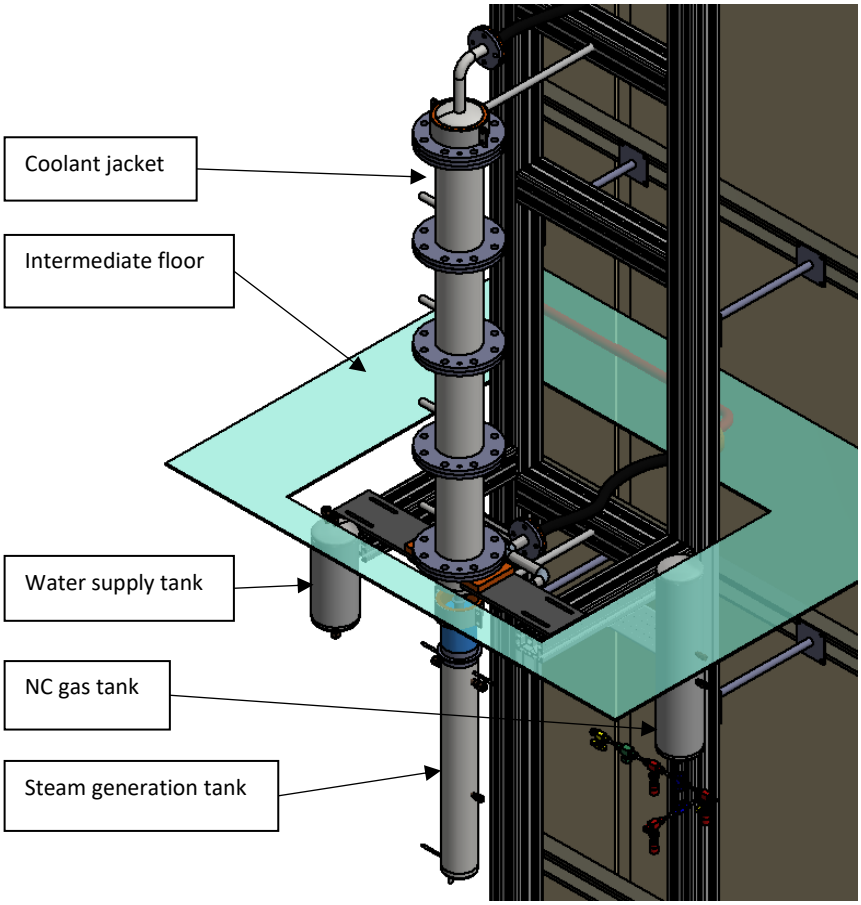

Figure 2-8 PRECISE facility (without insulation) - location and mount

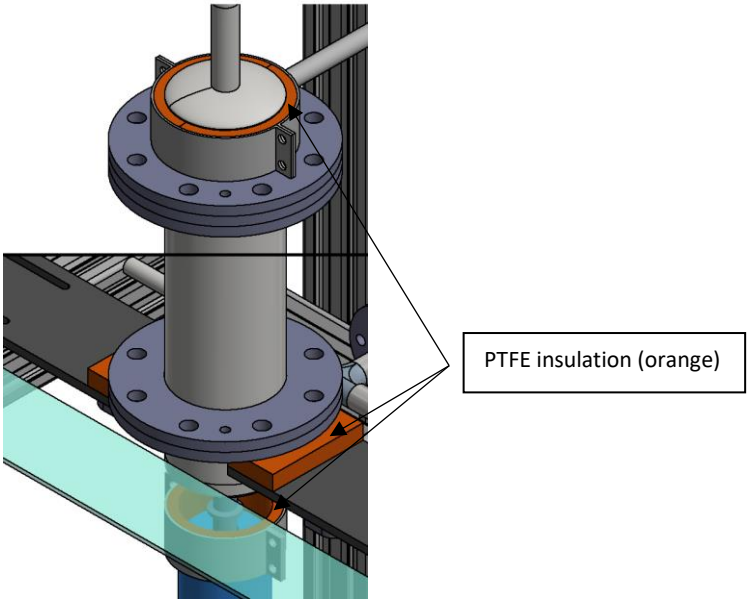

Figure 2-9 PTFE insulation between facility and fixation points

2.4 Facility control and operation

There are two main control circuits in the PRECISE facility. The first one is used to set and maintain the desired pressure in the primary loop and the second one to control the temperature and the flow rate of the cooling water. The following sections provide a detailed description for each one.

2.4.1 Primary loop control

The pressure of the primary loop is controlled by the amount of power supplied through the electrical heating rod. The heater boils water and generates enough steam to reach the set point pressure. Afterwards, the heating power is adjusted to compensate for the heat removed by steam condensation on the test tube walls and the accompanying heat losses, so that pressure remains constant at that defined level. An overview of the controller logic is given in Figure 2-10.

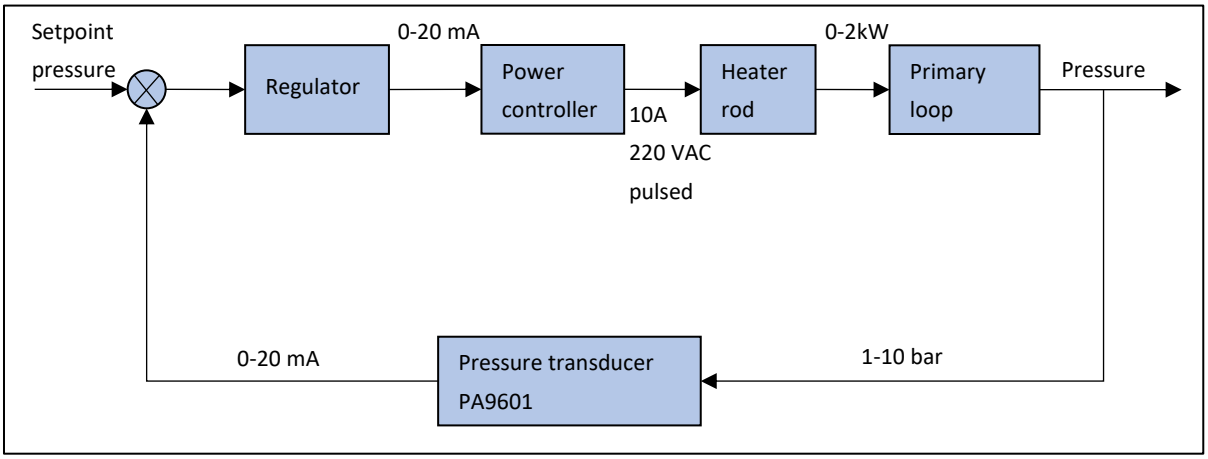

Figure 2-10 Primary loop control logic

This control loop includes two safety measures, to prevent facility over pressurization and heating rod damage. An electronically controlled valve will open if the gauge pressure exceeds 12 bar and release steam to the safety tank equipped with a condensation pool. Should this valve fail to open, as mentioned in the previous chapter, a passive spring-loaded safety valve will open at 12 barg instead. Additionally, surface temperature of the heating rod is monitored, and the control system will cut power if the value exceeds 300˚C.

At this quasi steady-state condition measurements are taken. The delivered electrical power is closely monitored through the operating controller and used to recalculate the stem mass flow. When the pressure inside the test tube remains constant, the total amount of generated team is condensed along the tube wall. From this follows the equality of vapor production $\dot{m}_{ev}$ and condensation $\dot{m}_{cond}$ which can be expressed as:

$$\dot{m}_{cond} = \dot{m}_{ev} \tag{6}$$

Equation (6) can be further expressed in terms of evaporation heat:

$$\dot{m}_{cond} = \dot{Q}_{ev} * \frac{1}{H_{vap}(T)} \tag{7}$$

where $H_{vap}(T)$ is the enthalpy of vaporization, temperature dependent. Since the Joule heating process through the electrical rod heater has a coefficient of performance of unity, the evaporation heat can

be calculated from the recorded electrical power. After subtracting heat losses of the facility, the final expression for the steam condensate mass flow takes the following form:

$$\dot{m}_{cond} = (P_{el} - \dot{Q_{loss}}) * \frac{1}{H_{vap}(T)} \qquad (8)$$

2.4.2 Secondary loop control

Two parameters are directly controlled in the coolant loop – the water volumetric flow rate and its temperature. The first of the two is simply done by pump control based on the readings of a volumetric flow meter. This system worked well, but due to the pump properties, it had trouble to achieve good consistency in case of low volumetric flow rates when they were required. Therefore, there's a manual by-pass line, that can be adjusted with a valve, thus allowing a part of the flow to recirculate, allowing the pump to operate at higher flow rate. The control logic schematic is presented in Figure 2-11.

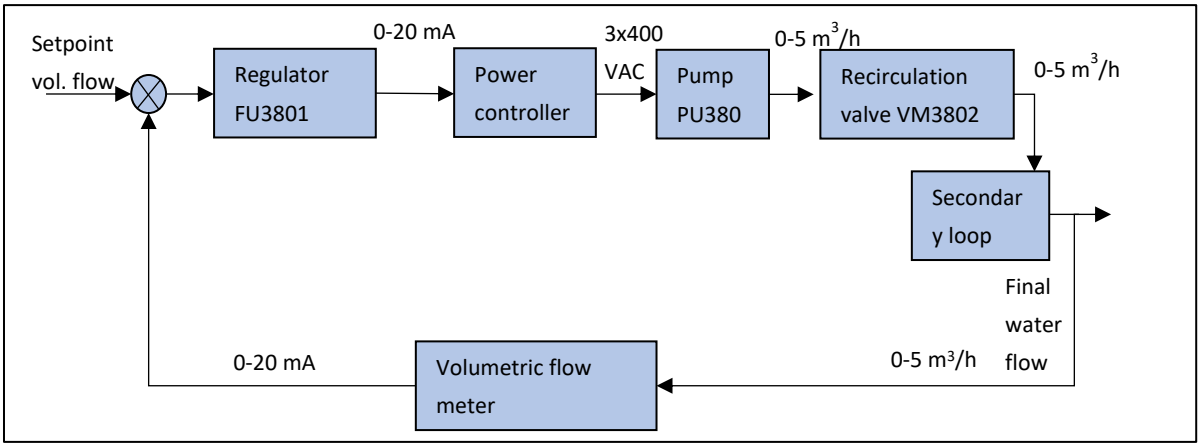

Figure 2-11 Secondary loop coolant volumetric flow control

The implemented temperature control of the coolant water works in two steps. First the water from the storage tank is pre-heated with an electrical heater. The heater is monitored for safety purposes and in case temperature increases over 200°C the system shuts down automatically.

Afterwards, the coolant flows through a three-way valve, which directs a part of it straight to the cooling jacket, while another part is circulated through an additional heat exchanger, for cooling. The two streams are then mixed together, and the resulting final temperature is verified and used to control the opening of the three-way valve. This allows for an efficient fine-tuning of the temperature and increases the stability of the whole system. The logic is presented in Figure 2-12.

The pressure of the secondary loop is monitored and in case of overpressure, spring-loaded safety valve will open at 12 barg. It is important to mention, that the user must monitor the coolant loop pressure and adjust it, so that the water temperature remains below the boiling point, in particular during experiments with a coolant temperature above 100°C. This is achieved through a pressurization of the loop with N_2 gas in the intermediate water storage tank. To lower the pressure, gas can be manually released from the tank.

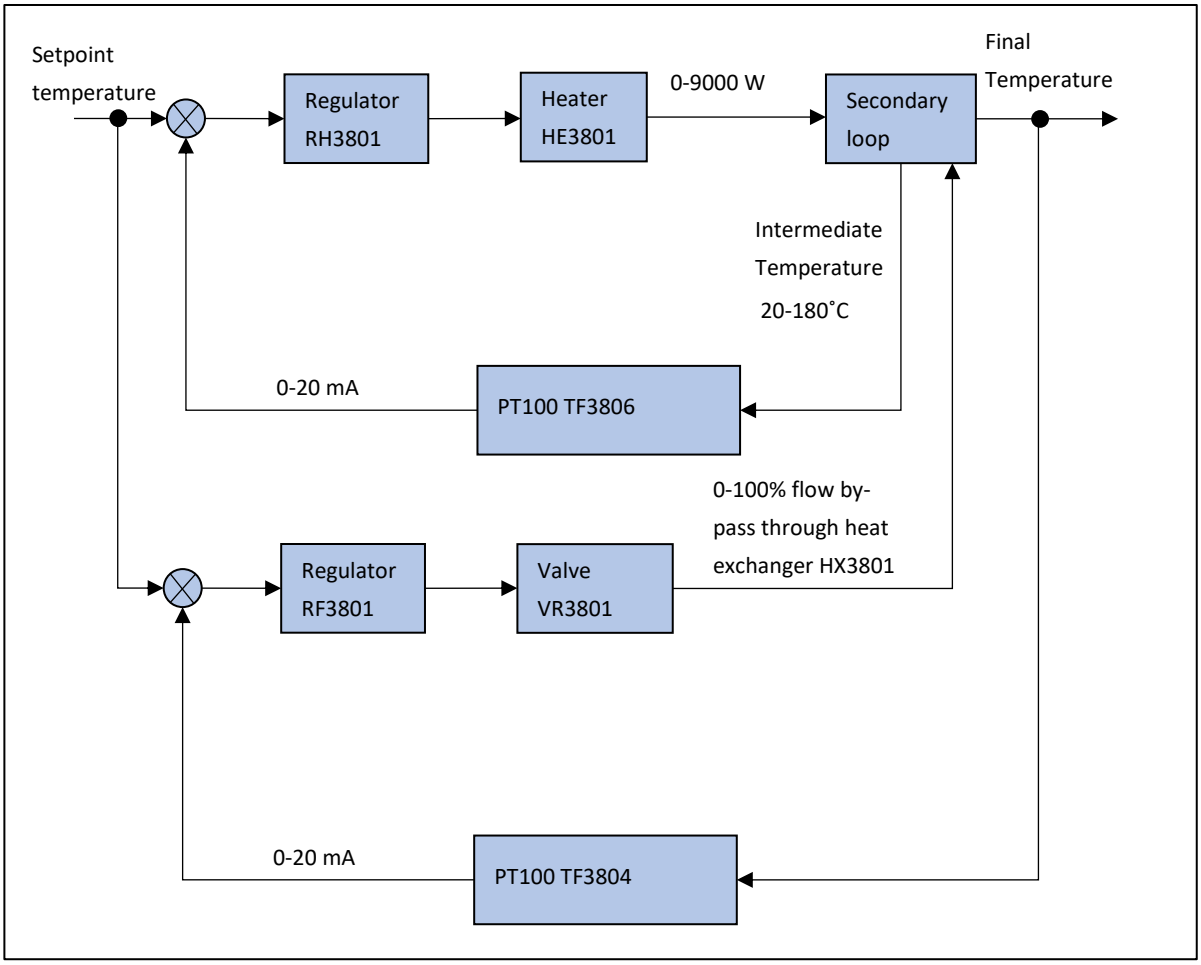

Figure 2-12 Secondary loop temperature control

Chapter 3 Data Acquisition

In the PRECISE facility various instruments are used to measure the thermohydraulic parameters of interest. In general, hardware from National Instruments is mostly used for data acquisition. On the software side, LabVIEW programming language was used to create data logging client as well as general control graphical user interface for the facility. This chapter describes in detail the data acquisition chain as well as various sensor types and their application in the PRECISE facility.

3.1 DAS Hardware - Overview

The PRECISE facility, including the primary side as well as the coolant loop and accompanying intermediate volumes has over 100 independent data channels. National Instruments CompactRIO (cRIO) platform was chosen to handle the data gathering and control purposes. This is a real-time embedded controller, with a x86 processor and a field-programmable gate array (FPGA). Each controller is accompanied with an adjustable frame that can be populated with various I/O modules, which provide direct connection to sensors and controlled devices.

With cRIO functionality in mind, data channels were bundled into groups depending on their purpose (data acquisition / system control) signal type (analog voltage / current / digital) and desired acquisition speed (low speed 1-10 Hz / high speed up to 100 kHz). Then, for each group an appropriate module was identified and installed into the frame. As a final result, two cRIO frames handle almost all data acquisition in the PRECISE facility. The only other equipment included is a 4-Channel resistive thermometer measuring module[3] that handles measurements of PT100 elements. All three components communicate with a lab PC through a local Ethernet connection. The logical structure of the data acquisition system (DAS) is shown in Figure 3-1. Full list of all the sensor included in the facility is provided in the appendix section 0.

[3] Omega PT104A

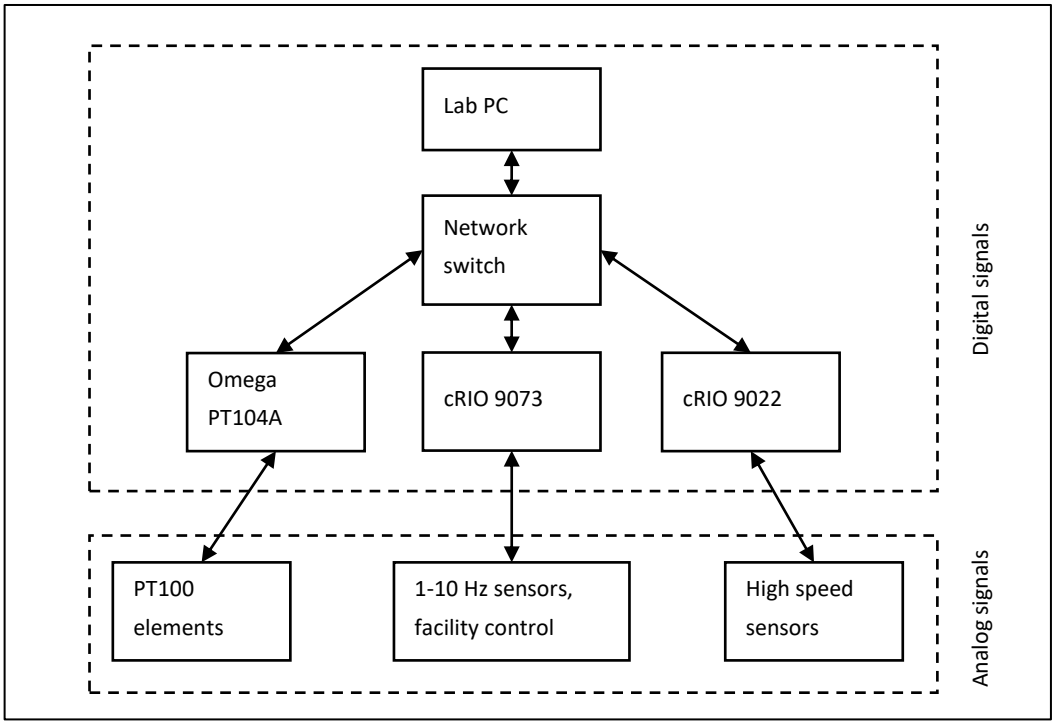

Figure 3-1 PRECISE facility DAS and control system

3.2 Condensation tube sensor positions

The condensation test tube is equipped with 20 K-type thermocouples (⌀0.5mm), 12 of which are located along the centerline (positioning explained in Figure 3-2A). The vertical temperature profiles measured in the tube provided the basis for assessment of the behavior and location of NC gas plug. Moreover, four thermocouples are mounted inside the tube wall close to the inner surface (T_{in}) and additional four are mounted inside the tube wall, close to the outer surface (T_{out}), positions marked A to D. In the same four positions, four gradient heat flux sensors were embedded in the wall, behind a 0.5 mm layer of steel. As can be seen in Figure 3-2B, the distance between T_{in} and T_{out} for every vertical position was fixed to 3.5 mm, to ensure that appearing temperature gradient would be high enough for low-z measurements. Finally, movable conductivity and temperature probe (MCT) was placed at the elevation of 371 mm, measured from the tube entrance.

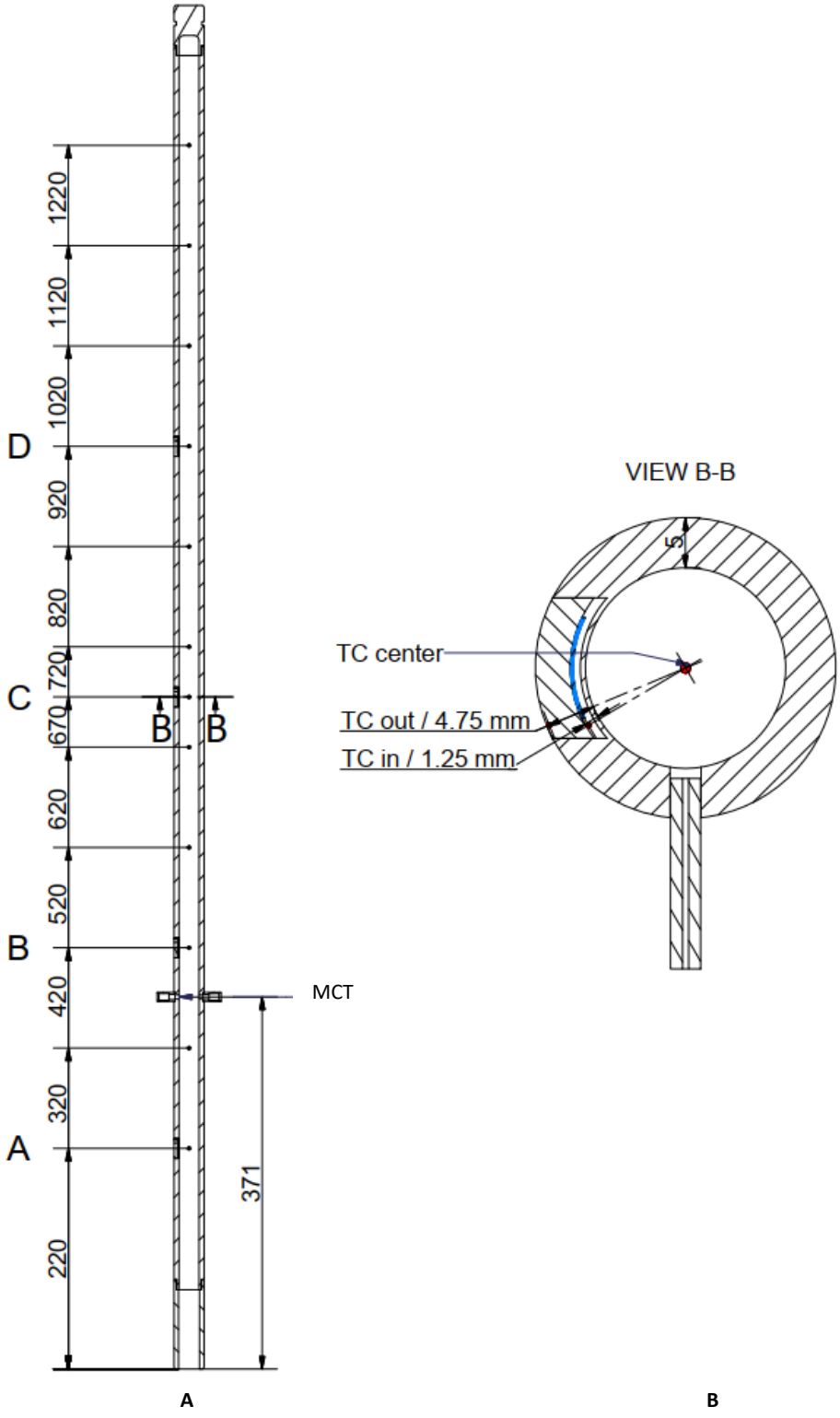

Figure 3-2 Schematic of sensors positioning in vertical (A) and horizontal (B) direction in the test tube

3.3 Gradient Heat Flux Sensor

3.3.1 Overview

The gradient heat flux sensor was developed by Mityakov et al. ([201], [202]), and its use in the PRECISE facility was accomplished in collaboration with Prof. A. Mityakov from Saint-Petersburg State Polytechnic University and Lappeenranta University of Technology. The gradient heat flux sensors (GHFS) used in the PRECISE facility is made of sintered, alternating layers of stainless-steel and nickel foils of 0.1 mm thickness. Its properties can be summarized as follows:

- Working temperature up to 1300 K
- Sensitivity 0.4 mV/W
- Response time estimated in the range of 10^{-9} s
- 0.2 - 0.3 mm thickness
- 95-100 mm^2 area

Due to its small thickness and thermal properties similar to those of the surrounding material in which the sensors are mounted (stainless steel tube), the GHFS introduced minimal disturbance to the measured system. Their fast response time permitted signal sampling rates up to 100 kHz, which allowed to use super-sampling techniques to filter the noise caused by low signal amplitude. Ultimately four sensors were mounted in the test tube, distributed along its height, to observe steam condensation and heat transfers at varying NC gases fraction during each experiment.

3.3.2 Operating principle

The sensors used in the PRECISE facility are made of an artificially constructed material which structure exhibits anisotropic electrical and thermal properties. The artificial anisotropy is achieved by alternate-layering a pair of materials with different Seebeck coefficients. The layers are bonded and cut at a certain angle. The result is a tilted multi-layered structure. Heat flux applied perpendicular to the sensor leads to appearance of proportional transverse thermoelectric voltages, parallel to the surface. This effect is called transverse Seebeck effect. Transverse voltages appear only in the direction along which the layering and thermal anisotropy are present, Figure 3-3.

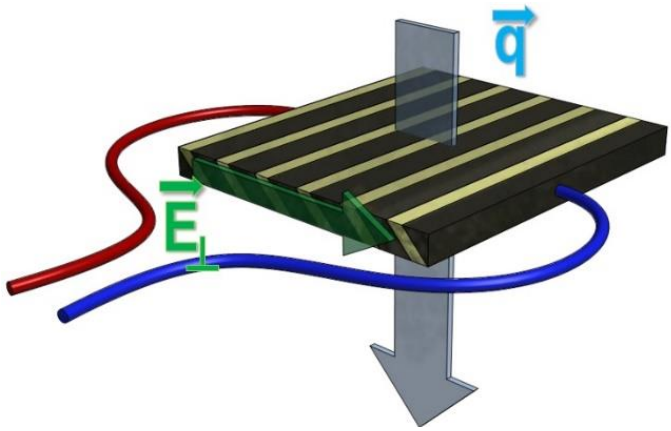

Figure 3-3 Heat flux sensor multi-layer structure and operating principle

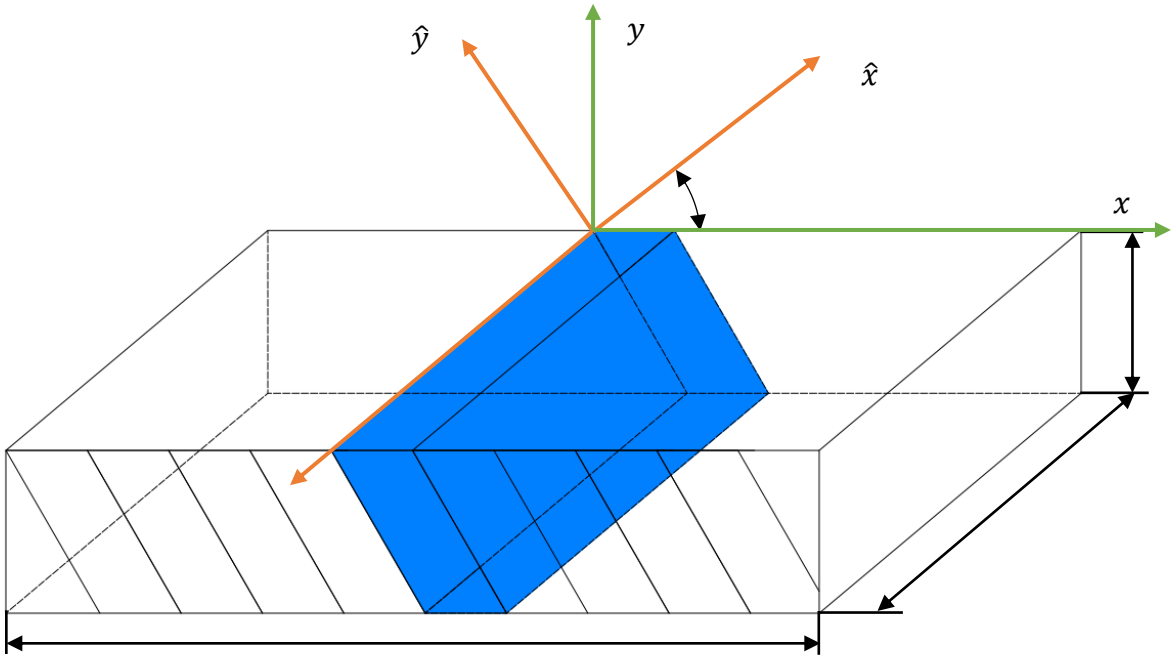

Figure 3-4 Anisotropic thermocouple in GHFS structure - $\hat{x}$, $\hat{y}$ axes parallel and perpendicular to the layers x, y, z – laboratory coordinate system; l, w, t – length, width and thickness of the sensor

The overall thermoelectric response E of an anisotropic element as given is described by eq. (9):

$$\hat{E} = \hat{S}\,\nabla T \tag{9}$$

where ∇T is the temperature gradient and $\hat{S}$ is the Seebeck coefficients tensor. Since the artificial anisotropy is only introduced in one plane of the sensor (Figure 3-4), the problem can be reduced to two dimensions by ignoring Z axis. The reduced tensor in crystallographic axes $\hat{x}$ and $\hat{y}$ is given by eq. (10):

$$\hat{S} = \begin{pmatrix} S_{\hat{x}\hat{x}} & 0 \\ 0 & S_{\hat{y}\hat{y}} \end{pmatrix} \tag{10}$$

Similar expressions can be derived for thermal λ conductivity. All of these can be expressed in previously defined laboratory axes x and y (Figure 3-4), using the rotation angle α, describing the layer tilt:

$$\hat{S} = \begin{pmatrix} S_{\hat{x}\hat{x}}\cos^2\alpha + S_{\hat{y}\hat{y}}\sin^2\alpha & (S_{\hat{x}\hat{x}} - S_{\hat{y}\hat{y}})\sin\alpha\cos\alpha \\ (S_{\hat{x}\hat{x}} - S_{\hat{y}\hat{y}})\sin\alpha\cos\alpha & S_{\hat{x}\hat{x}}\sin^2\alpha + S_{\hat{y}\hat{y}}\cos^2\alpha \end{pmatrix} \tag{11}$$

Similarly, for thermal conductivity tensor, eq. (12):

$$\hat{\lambda} = \begin{pmatrix} \lambda_{\hat{x}\hat{x}}\cos^2\alpha + \lambda_{\hat{y}\hat{y}}\sin^2\alpha & (\lambda_{\hat{x}\hat{x}} - \lambda_{\hat{y}\hat{y}})\sin\alpha\cos\alpha \\ (\lambda_{\hat{x}\hat{x}} - \lambda_{\hat{y}\hat{y}})\sin\alpha\cos\alpha & \lambda_{\hat{x}\hat{x}}\sin^2\alpha + \lambda_{\hat{y}\hat{y}}\cos^2\alpha \end{pmatrix} \tag{12}$$

As one can see, adjustments to the angle α have huge implications to the anisotropic properties of the structure, and significantly affect the produced thermoelectric power in response to an applied heat flux ([202]–[204]). Therefore, a relation between GHFS sensitivity and the layer tilt angle α is crucial to define. The term s_0 describing GHFS sensitivity [V/W] can be introduced following eq. (13):

$$s_0 = \frac{e_x}{\Phi_\perp A} \tag{13}$$

where e_x is the produced thermopower along x direction, A is the sensor area and $\Phi_\perp$ is the heat flux applied at the sensor surface, coinciding with y axis. It can be expressed by Fourier's law for a steady-state regime through a plate:

$$\Phi_\perp = -\lambda_{yy}\frac{\Delta T_{yy}}{h} \tag{14}$$

where λ_{yy} is the thermal conductivity tensor component and ΔT_{yy} is temperature difference along y direction and h is the sensor thickness. The only relation left to be defined is the thermopower of an anisotropic element in terms of temperature gradient and material properties:

$$e_x = S_{xy}\frac{\partial \mathrm{T}}{\partial \mathrm{y}}l \tag{15}$$

which, due to one-dimensionality of the applied temperature gradient can be simplified to:

$$e_x = S_{xy}\frac{\Delta T_{yy}}{h}l \tag{16}$$

Combining eq. (16) with eq. (14) yields:

$$e_x = -S_{xy}\frac{\Phi_\perp}{\lambda_{yy}}l \tag{17}$$

Remembering that sensor area is described as $A = w \times l$, the equation (13) takes the form:

$$s_0 = \frac{e_x}{\Phi_\perp A} = \frac{S_{xy}}{\lambda_{yy} l} \tag{18}$$

Substituting the previously derived expressions for Seebeck coefficient and thermal conductivity in terms of laboratory axes, the final expression for GHFS sensitivity is:

$$s_0 = \frac{1}{l}\frac{(S_{\hat{x}\hat{x}} - S_{\hat{y}\hat{y}})\sin\alpha\cos\alpha}{\lambda_{\hat{x}\hat{x}}\sin^2\alpha + \lambda_{\hat{y}\hat{y}}\cos^2\alpha} \tag{19}$$

Following [202], the derived function extremum, with respect to the layer tilt angle α_{max} is:

$$\alpha_{max} = \pm\tan^{-1}\sqrt{\frac{\lambda_{\hat{x}\hat{x}}}{\lambda_{\hat{y}\hat{y}}}} \tag{20}$$

which depends in turn on thermal conductivity coefficients of the resulting anisotropic material. The said properties are dependent on the constituent layered materials. The thermo-electric properties of constituent materials define the Seebeck coefficients $S_{\hat{x}\hat{x}}$ and $S_{\hat{y}\hat{y}}$, as well as the respective electrical and thermal conductivities ($\sigma_{el\hat{x}\hat{x}}$, $\sigma_{el\hat{y}\hat{y}}$, $\lambda_{\hat{x}\hat{x}}$, $\lambda_{\hat{y}\hat{y}}$). Kirchhoff's rules ([203], [205]) can be used to find expressions for Seebeck and thermal conductivities, which take the form described in eq. (21) - (24), where subscripts refer to corresponding layering materials and d is the thickness ratio between layers.

$$S_{\hat{x}\hat{x}} = \frac{S_1\sigma_{el1} + dS_2\sigma_{el2}}{\sigma_{el1} + d\sigma_{el2}} \quad (21)$$

$$S_{\hat{y}\hat{y}} = \frac{S_1\lambda_2 + dS_2\lambda_1}{\mathrm{d}\lambda_1 + \lambda_2} \quad (22)$$

$$\lambda_{\hat{x}\hat{x}} = \frac{\lambda_1 + d\lambda_2}{1 + d} \quad (23)$$

$$\lambda_{\hat{y}\hat{y}} = \frac{\lambda_1\lambda_2(1 + d)}{\mathrm{d}\lambda_1 + \lambda_2} \quad (24)$$

Substituting these into eq. (19) and eq. (20), final expressions for GHFS sensitivity and optimal angle based on constituent layer materials are:

$$\mathrm{s}_0 = \frac{1}{l}\frac{\left(\frac{S_1\sigma_{el1} + dS_2\sigma_{el2}}{\sigma_{el1} + d\sigma_{el2}} - \frac{S_1\lambda_2 + dS_2\lambda_1}{\mathrm{d}\lambda_1 + \lambda_2}\right)\sin\alpha\cos\alpha}{\frac{\lambda_1 + d\lambda_2}{1 + d}\sin^2\alpha + \frac{\lambda_1\lambda_2(1 + d)}{\mathrm{d}\lambda_1 + \lambda_2}\cos^2\alpha} \quad (25)$$

$$\alpha_{max} = \pm\tan^{-1}\sqrt{\frac{\frac{\lambda_1 + d\lambda_2}{1 + d}}{\frac{\lambda_1\lambda_2(1 + d)}{\mathrm{d}\lambda_1 + \lambda_2}}} \quad (26)$$

3.3.3 GHFS types

Up to date, many varying material pairs, as well as naturally occurring anisotropic crystals, were successfully used in creating heat flux sensing elements. The choice of a certain pair for producing a sensor is a compromise between desired robustness, foreseen operating conditions and maximizing the signal amplitude. Naturally, choosing materials with largest anisotropy $\Delta S = S_{\hat{x}\hat{x}} - S_{\hat{y}\hat{y}}$ would result in highest measurable output. Table 3-1 shows resulting values in some previously tested materials.

Table 3-1 Overview of thermoelectric anisotropy of various materials

GHFS material	ΔS [μV/K], 300K	
Bismuth	50	([206])
Copper – constantan	35	([207])
Constantan – chromel	5	([206])
Aluminum - silicon	1500	([203])
Stainless steel – nickel	40	([208])
Brass - steel	12	([209])

In this work, stainless steel (18% Cr, 9% Ni, 2% Mn, 0.8% Ti) and nickel GHFS were used, as their material composition closely resembles properties of the surrounding tube material, minimizing the disturbance introduced in the system. Moreover, their resistance to corrosion and high allowable operating temperatures are appropriate, considering the anticipated exposure to high-temperature steam and water. Lastly, sensor made of metal was easy to shape and bend, to match the curvature of the tube wall.

3.3.4 Signal acquisition

The major shortcoming of the stainless steel / nickel GHFS is a relatively low signal amplitude. The order of magnitude of heat flux present during experiments in the PRECISE facility is estimated at a maximum of 10000 W/m². Considering the volt/watt sensitivity of around 0.4 mV/W and small sensor area of 100 mm² the expected maximum signal amplitude is in the range of up 0-400 μV. Therefore, a signal amplification was included in the signal acquisition chain, Figure 3-5.

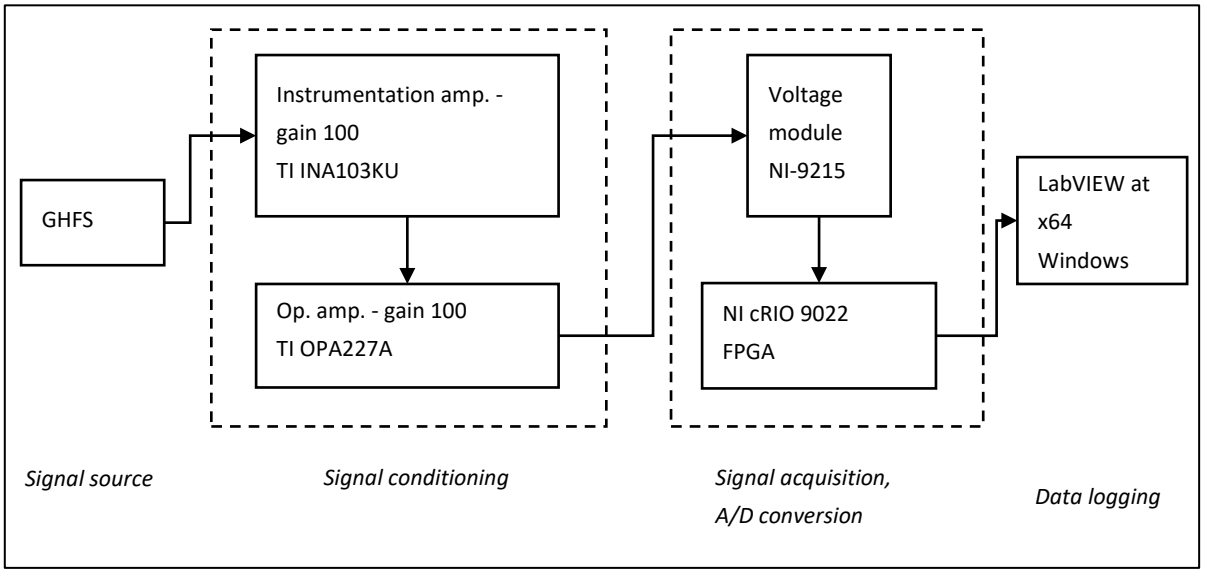

Figure 3-5 Heat flux signal acquisition chain

Two amplifiers are used – first, a high precision, low noise instrumentation amplifier, suitable for processing a floating voltage signal and powered by batteries, to minimize the noise. It is followed by an operational amplifier. After the first stage, the signal is referenced to the common ground, to reduce the noise levels. Afterwards, signal is acquired using National Instrument voltage input module NI-9215. This module is a four-channel device with a A/D converter, capable of simultaneous and continuous 100 kHz signal sampling with 16-bit accuracy of each channel. The signal is then filtered using a FPGA available in a cRIO-9022 embedded real-time controller frame, in which the NI-9215 module is installed. Four low-pass filters were programmed – one for each channel – with an adjustable cut-off frequency. Lastly, data is buffered in the cRIO-9022 controller and send over the network to a laboratory PC computer running a LabVIEW program acting as a data logger.

NI-9215 module input range is from -10V to +10V. Considering the 16-bit accuracy, this means a resolution of about 300 μV. Therefore, to effectively utilize the available range, the total amplification of 10000 was included in the chain, each amplifier providing a 100 gain. As a result, the maximum expected signal is increased to about 4V.

3.3.5 Calibration procedure

To properly interpret the measured GHFS voltages, a calibration procedure had to be devised to obtain precise values of a sensitivity S_0 for each installed sensor. Moreover, since sensitivity of GHFS depends on its constituent material properties it is thus dependent on the sensor's temperature. Such relation was observed in previous works ([202], [203], [209]–[213]). To address this issue, the calibration procedure

must control two parameters independently – sensor temperature and delivered heat flux. Ultimately, for each sensor, a sensitivity parameter function $S_0(T_{GHFS})$ had to be found.

3.3.5.1 Sensitivity stability at constant temperature

First, a verification test was made, to ensure GHFS sensitivity stability at a given temperature but with varying heat flux values. A simple experimental setup, shown in Figure 3-6, that allowed precise control of the delivered heat flux and sensor temperature was constructed.

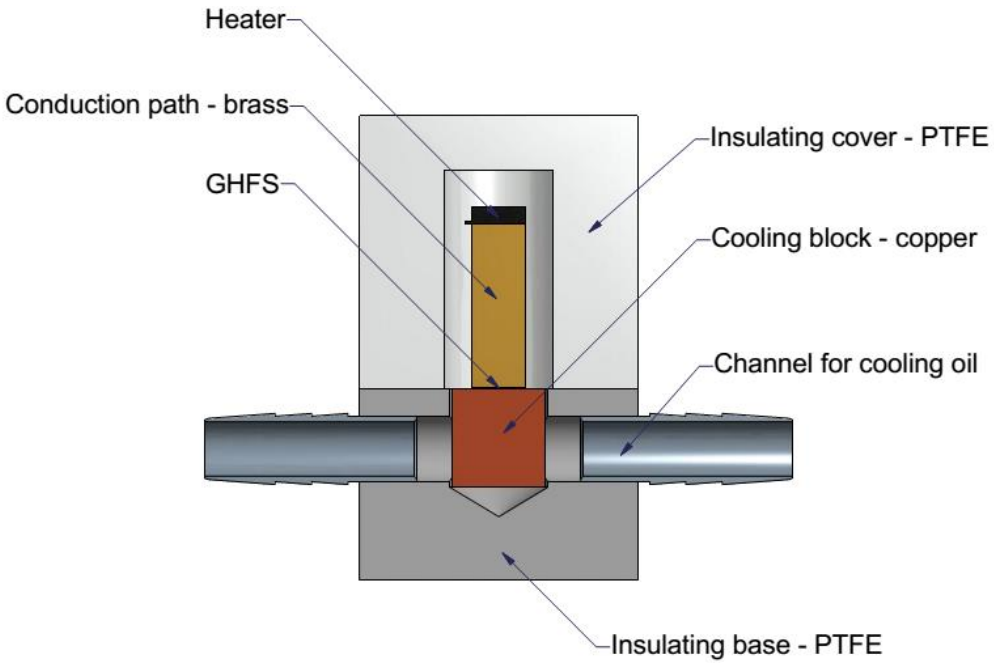

Figure 3-6 GHFS sensitivity test setup

The setup consists of an electrical heater (100 Ω resistor, 20W rated) accompanied by a ⌀0.5 mm K-type thermocouple, both sitting on top of a brass block, underneath which GHFS is placed. Under the sensor, a copper block with cooling fins is installed. Cooling oil is circulated through the copper block to remove the heat. Oil temperature is maintained with a recirculation bath with a programmable controller[4]. Temperature of the sensor is monitored with another ⌀0.5 mm K-type thermocouple and delivered power source is controlled with a laboratory DC power supply[5]. The delivered electrical power P is converted to heat flux by resistive heating of the installed heater / resistor, following the standard equation:

$$P = UI \qquad (27)$$

where U is the voltage drop across the resistive element and I is the current. The whole setup is embedded in a block of PTFE, to minimize the heat losses to the environment.

The 30 mm long brass column provides a path for heat conduction from the electrical heater, through the GHFS to the cooling block. The dimensions of the block cross-section are 10x10 mm matching the area of the sensor. The 30 mm length of brass allowed for temperature gradient to develop and allowed ΔT

[4] Haake DC5, temperature range -50 to 200°C, temperature accuracy +/- 0.01 K acc. to DIN 58966

[5] Thurlby Thandar Instruments EL302T

measurement with two included thermocouples. Additionally, GHFS is electrically insulated from the metal blocks with sheets of mica mineral, cut to size and with >0.05 mm thickness. All the elements are bonded with an epoxy[6] possessing high thermal conductivity and working temperature. This ensures adequate and stable thermal contacts between all the parts.

At the start of the experiment the heater is turned on, followed by 5-10 minutes of wait time, allowing the temperature to stabilize. Then, the temperature of the coolant oil is adjusted so that the temperature of GHFS would remain constant at varying heat flux levels. GHFS response is recorded without amplification with a Keithley multimeter[7]. Afterwards, GHFS sensitivity is calculated from the recordings, following the eq. (13). Obtained results verify that indeed, sensor sensitivity does not vary with changing heat flux, provided that the sensor temperature remains constant, Figure 3-7.

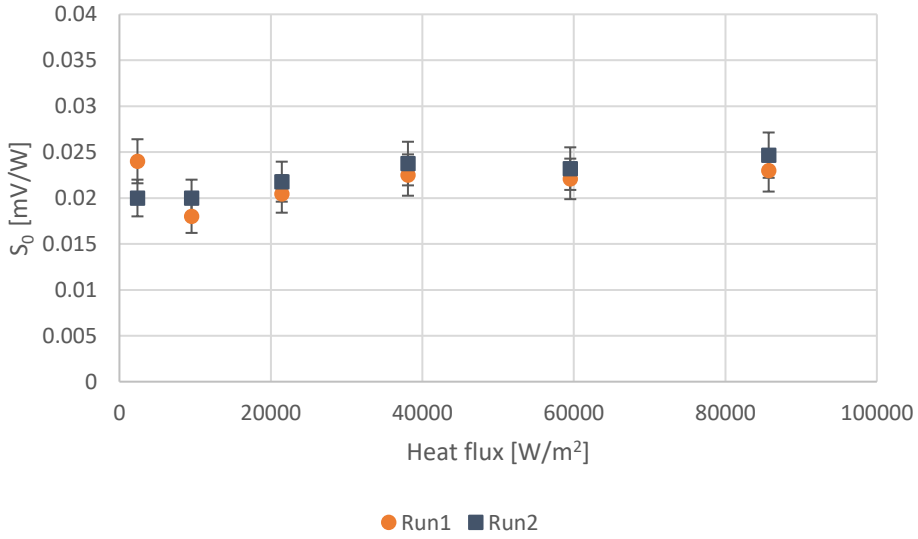

Figure 3-7 GHFS sensitivity dependence on heat flux at constant temperature of 20˚C

[6] Cotronics Duralco™ 128

[7] Keithley Model 2001 7½-Digit Multimeter, resolution down to 0.1μV

3.3.5.2 GHFS sensitivity – temperature relation

To determine the sensitivity functions, each GHFS is placed in a tube section, embedded in its wall, Figure 3-8. Top and bottom of the tube are sealed. Through the bottom connector, a rod heater is inserted, extending the whole height of the tube section. Air is removed from the assembly with a vacuum pump.

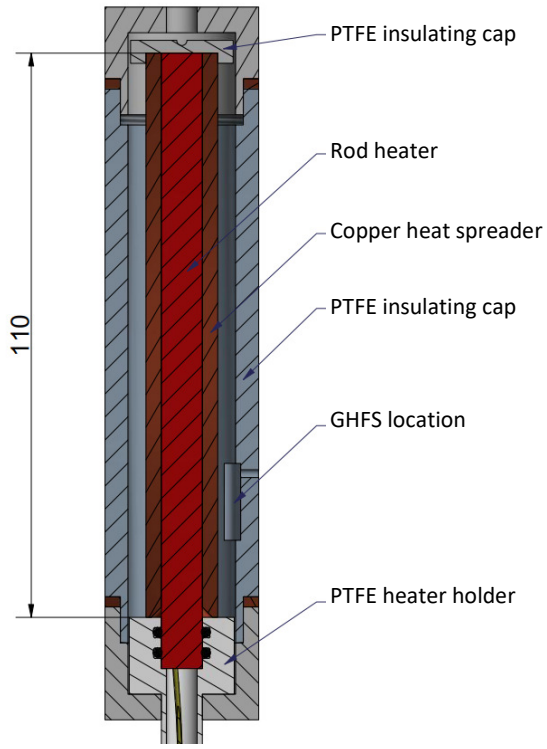

Figure 3-8 GHFS sensitivity calibration setup

The whole device is then placed inside an oil bath, equipped with temperature control[8]. Electrical cartridge heater[9] is powered with a lab power supply[10]. For every GHFS, calibration is run at eleven temperature levels. For each measurement an average heat flux is recalculated based on the wall ΔT, measured with calibrated K-type thermocouples, eq.(28):

$$\dot{Q} = \lambda \nabla T \tag{28}$$

where λ is the thermal conductivity of the wall material and ∇T is the temperature gradient, which can be defined here as:

$$\nabla T = \frac{\Delta T}{\Delta x} \tag{29}$$

where Δx is the distance between the temperature measurement points. Parameter λ is material and temperature dependent, and for the calculation, data for 316L stainless steel is used [214]. To ensure precise

[8] Haake DC5, temperature range -50 to 200°C, accuracy +/- 0.01 K acc. to DIN 58966

[9] Ø 8.0mm, length 130mm (unheated approx. 18mm), 230V, 800W, T/C type K, Backer ELC AG

[10] Thurlby Thandar Instruments TTi EL302T

information about the distance between thermocouples, a special double-thermocouple probe was assembled, where two 0.1 mm thermocouples are placed inside a ceramic cylinder, Figure 3-9. Distance between measurement points, as well as between the front point and the probe face was then evaluated under a microscope. Thermocouples are embededd in heat conductive epoxy (Duralco 128) and covered with a thin stainless-steel tube. Afterwards, the probe is calibrated to the precision of 0.1°C. The unit is inserted in the wall, next to the heat flux sensor, into a hole that was manufactured using electrical discharge machining, achieving precise depth of 4.5 mm.

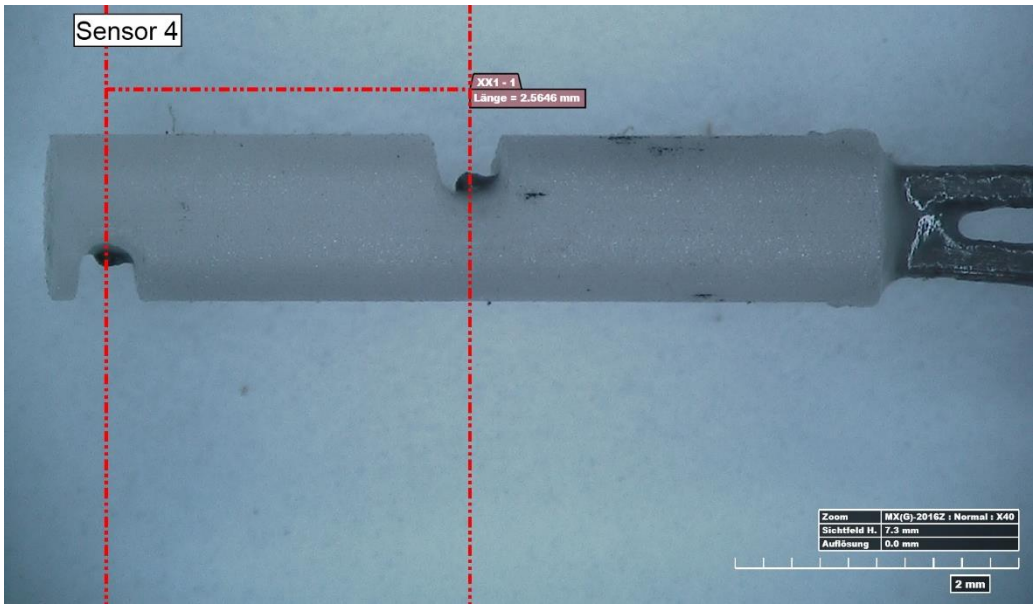

Figure 3-9 Double TC probe

Additionally, temperature distribution along the heating rod was measured at different operating powers, to verify equal heat delivery. Unfortunately, nonhomogeneous distribution was observed, Figure 3-10A. To fix this problem, a copper heat spreader (shown in Figure 3-8), possessing high thermal conductivity, was placed over the heater, with high-performance thermal paste in-between. Updated measurement verified homogenous temperature distribution with this upgrade in place, Figure 3-10B.

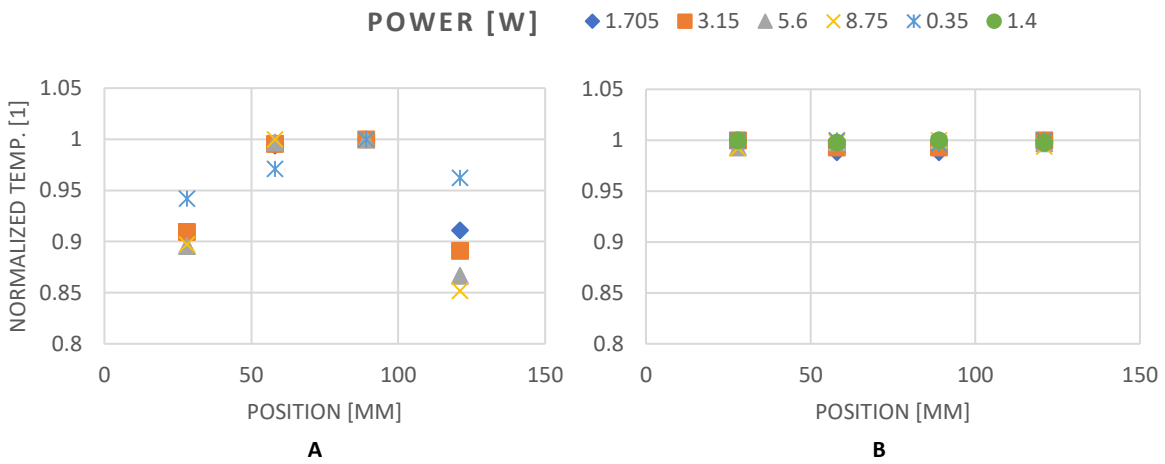

Figure 3-10 Heating rod normalized temperature distribution without (A) and with (B) copper equalizer, at varying powers

After recording the data, sensor sensitivity is calculated using previously established formula (eq. (13)) for every temperature. Then, a second order polynomial is fitted to the data, and this establishes the sensitivity – temperature dependance for every GHFS, further used in calculations, Figure 3-11. Second order polymial was chosen, as this type of sensitivity dependence was observed in the previous works [201], [209], [213].

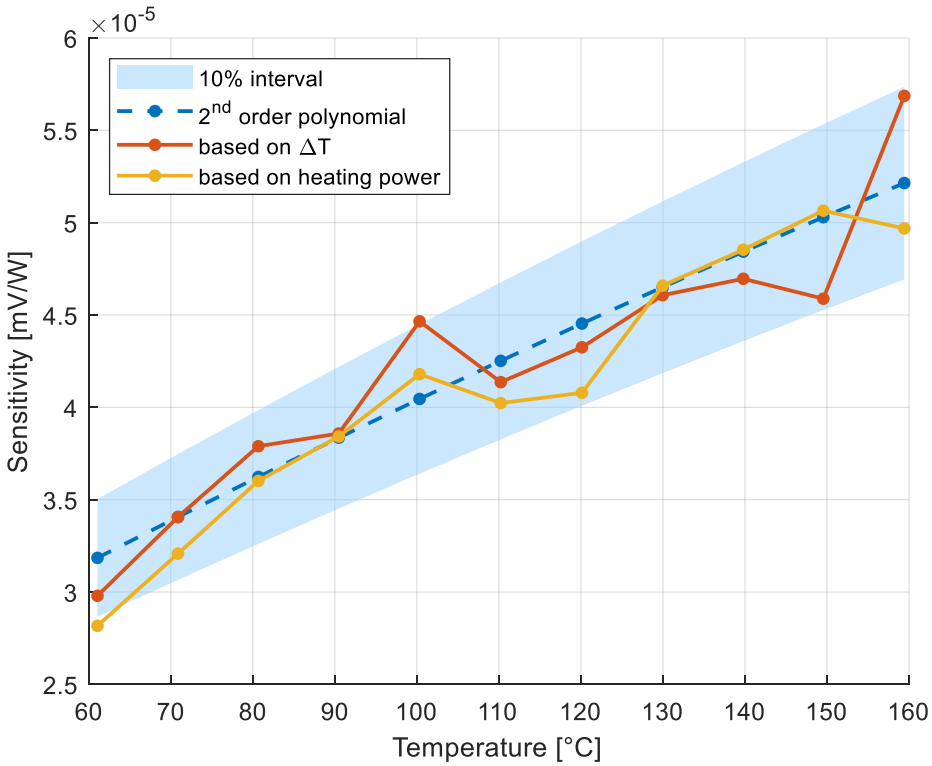

Figure 3-11 Example of GHFS sensitivity calibration curve

3.3.6 Installation in the PRECISE facility

GHFS's were mounted in the PRECISE facility in two distinct ways. At first, a groove of 1 mm thickness was cut in the inner wall of a test tube section (108 mm long), in which sensor was placed and embedded in an epoxy layer. GHFS was bent to match the inner curvature of the tube and the excess epoxy was polished, so that the resulting surface would sit flush with the tube wall, Figure 3-12. Signal cables were laser-welded to GHFS and insulated with PTFE. They were placed slightly underneath the sensor, also embedded in the epoxy. They were removed to the outside through a penetrating hole. The whole assembly formed a pressure seal as well electrically insulated the sensor from the tube wall.

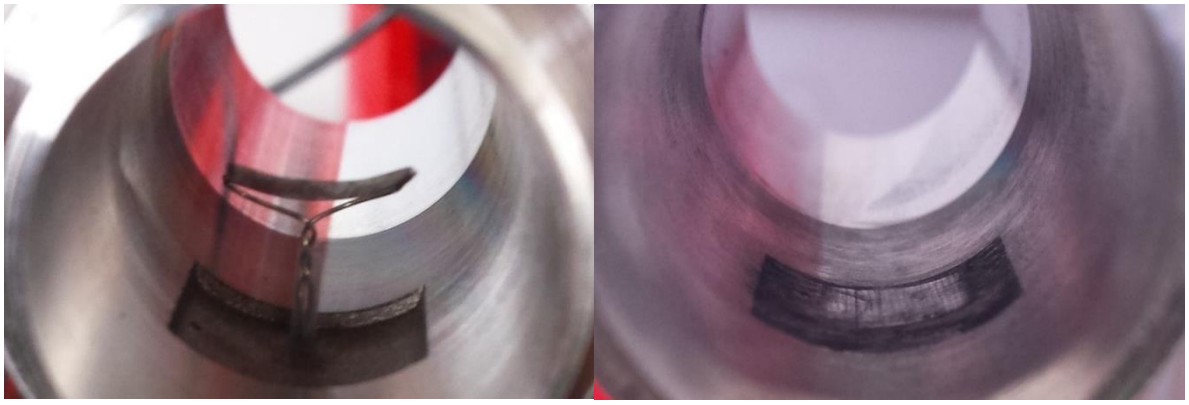

Figure 3-12 GHFS installation on the inner surface of the test tube

Tube sections where then screwed together forming a test tube of 1360 total length, using thread-locking compound (Loctite 272) and copper O-rings to ensure pressure seal. The initial results with this technique were very promising. Unfortunately, after prolonged exposure (over 2 months, 30 experiment runs) to hot steam at elevated pressures, the epoxy degraded, and sensors detached from the machined grooves, Figure 3-13.

Figure 3-13 Duralco 128 epoxy, degraded from prolonged exposure to hot steam

Hence, a secondary approach was developed. Instead of leaving the sensors exposed to the hot steam, a groove is machined in the tube wall from the outside, using electric-discharge die-sinking. The residual layer of steel, protecting GHFS from the steam is set to 0.5 mm, to limit the heat flux signal delay at the sensor location. The GHFS, along with a 0.5 mm K-type thermocouple is placed in the machined pocket. Empty space is filled with the epoxy and a thick cover s placed on top. Epoxy provides electrical insulation

as well as fills any voids in the pocket and, therefore, reduces the local heat flux disturbance. The cover is then laser-welded, to provide a pressure-tight seal, Figure 3-14.

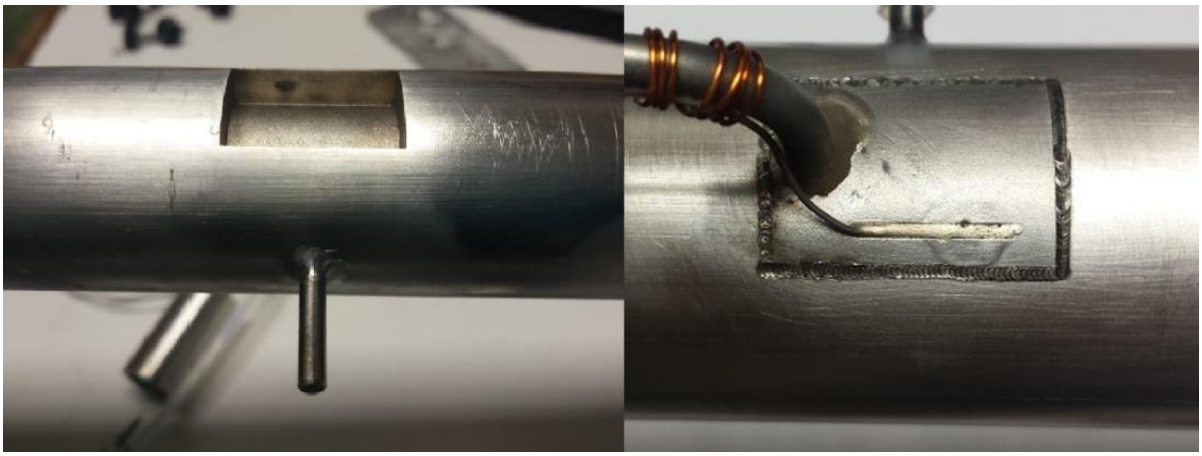

Figure 3-14 GHFS installation in the deep pocket

As with the previous approach, GHFS is bent to match the curvature of the eroded pocket. Signal cables were passed to outside through a pressure-sealed tubing. The sensor is accompanied by two thermocouples – one located right next it in the machined pocket and the second hard-soldered to the cover's outer surface. This technique proved robust and allowed to complete all the planned experiments with no equipment failure.

The only drawback of the second technique is that protecting GHFS with a 0.5 mm layer of steel desensitizes the sensor to a potential high-frequency variation in heat flux, due to the thermal inertia of the additional material. Since GHFS response time is in the range of 10^{-9} s, high sampling rates of the signal were expected to potentially uncover higher frequency phenomena in heat flux, possibly due to condensate film waviness. Therefore, a small test was designed to investigate how large was the impact of the 0.5 mm layer of steel.

3.3.7 GHFS frequency response

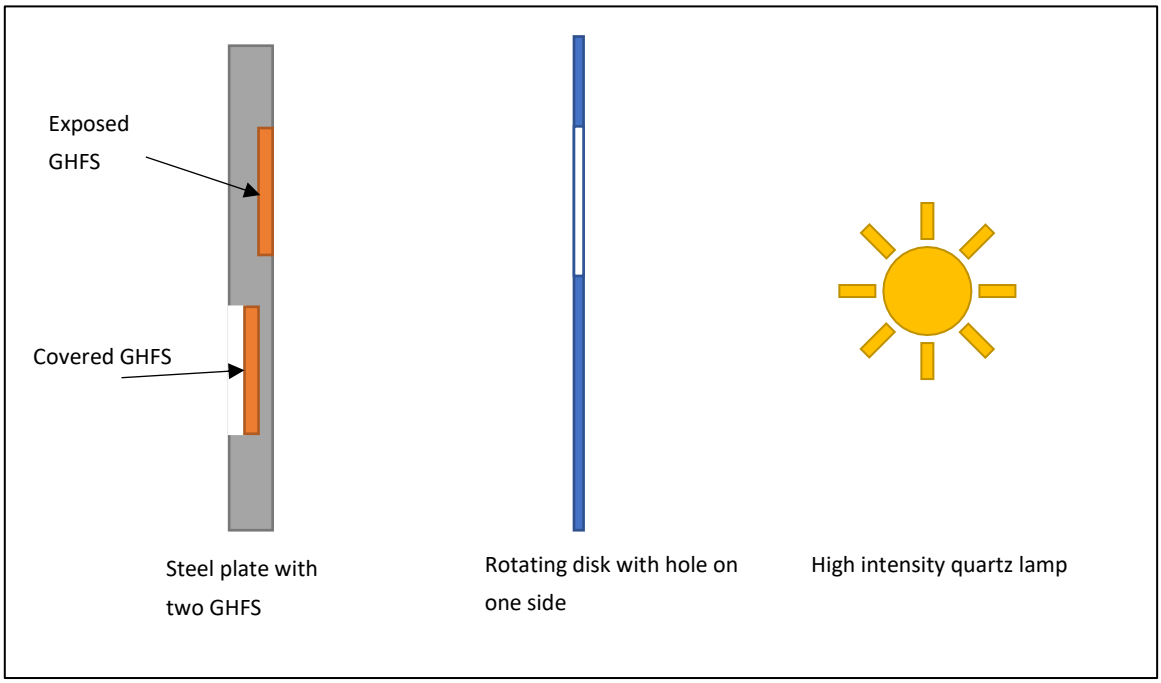

Figure 3-15 Embedded GHFS frequency response test

A small setup with two GHFS was created. Both sensors are embedded in a stainless-steel plate using the same epoxy as in the previous steps. One is left exposed and the other is put behind a 0.5 mm layer of steel, exactly as during the second installation technique. In front of the plate, a disk with a hole on one side is placed, attached to an electrical motor. The disk is rotated, and the rotation frequency is user adjustable. Behind the disk, a high intensity halogen lamp is placed. Heat produced by the lamp is easily detectable with both GHFS. Additionally, a light sensor[11] is added, to verify the plate's exposure frequency. The experiment was conducted during which a disk would be rotated at a low frequency at first, increased in steps, followed by waiting periods for data acquisition after each change. Experiment would continue until no signal was detectable in the covered GHFS anymore.

Gathered data reveals that frequencies of heat flux variation are still observable with the GHFS up to 10 Hz. Above this value, the signal is indiscernible anymore, Figure 3-16. At higher frequencies, one starts to notice a growing oscillation at twice the frequency of the heat exposure.

[11] TSL 252R - Light-to-voltage sensor

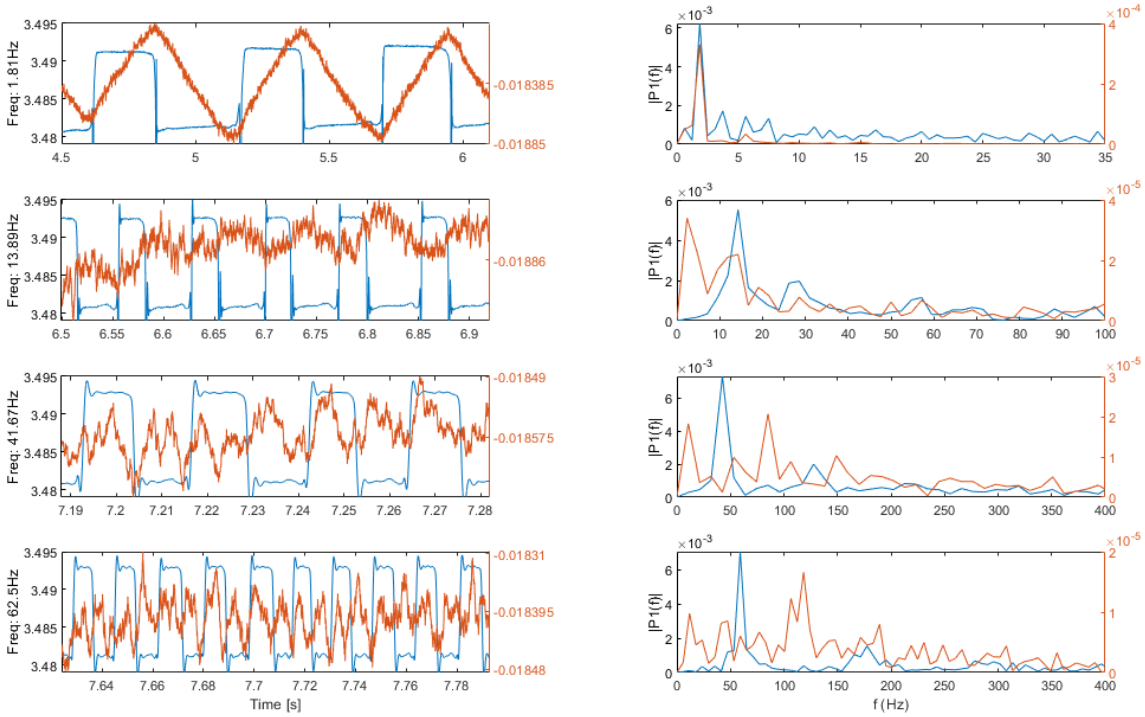

Figure 3-16 GHFS frequency response.
A - varying GHFS voltage signal (red) due exposure to heat/light (blue) measured with a light sensing diode, at varied exposure frequencies
B – Signals in frequency domain (GHFS – red, light sensing diode – blue)

3.4 Movable conductivity and temperature probe

3.4.1 Overview

The combined movable conductivity and temperature probe (MCT) provides information about the condensate film thickness, oscillations and the temperature profile across the test tube. The basic concept is a combination of traversing conductance probe ([215]–[218]) and stationary electrode array probe ([219]).

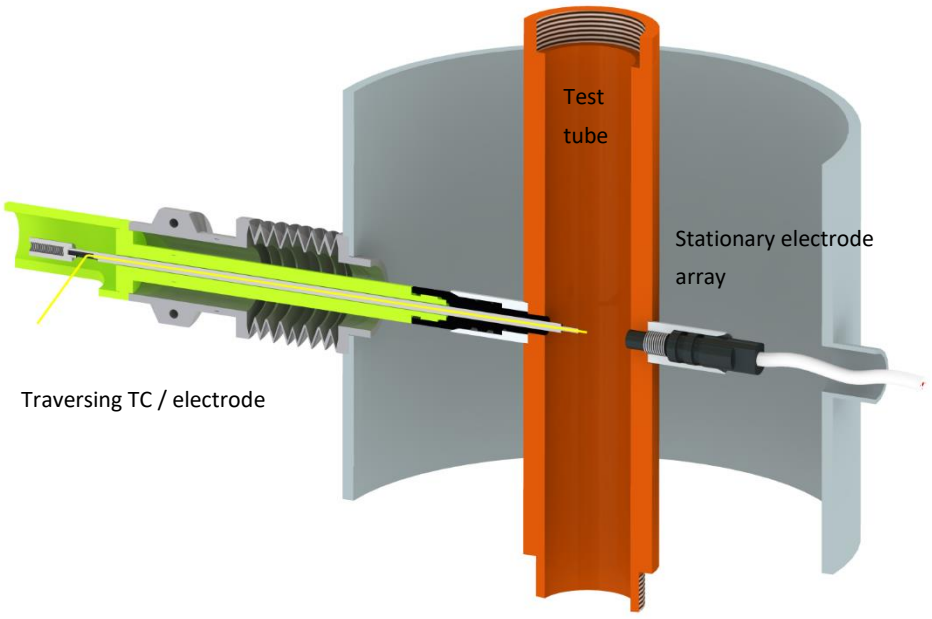

Figure 3-17 Movable conductivity and temperature probe cross-section

The probe is comprised of two main components, attached to the condensation test tube, (Figure 3-17, Figure 3-18). First part is a stationary, flush mounted to the wall, embedded transmitter and receiver electrodes, performing high frequency measurements of the conductance of the condensate film flowing on top of the probe. The function of this part of the probe is to provide information on the condensate film thickness and waviness.

The second part of the probe consist of a receiving electrode combined with a thermocouple, which continuously traverses across the test tube, recording temperature distribution along its path. Additionally, when the electrode encounters the condensate film surface on top of the electrode array, it detects a voltage delivered by the transmitter electrode. Thus, identification of the interface between gas and liquid phases in the test tube is alternatively achieved. This interface detection is able to measure thicker water films at which the electrode array could already be saturated. However, the interface location is sampled at a low frequency, depending on the traversing speed of the electrode. The amplitude of movement is 20 mm, which is the diameter of the test tube. The probe is actuated with a precise traversing system, equipped with motor drives and trigger switches, for exact position measurement. The information about the probe position in the instant of contact with condensate film is used to validate the signal from the continuously measuring electrode array, allowing for cross-checking the signals.

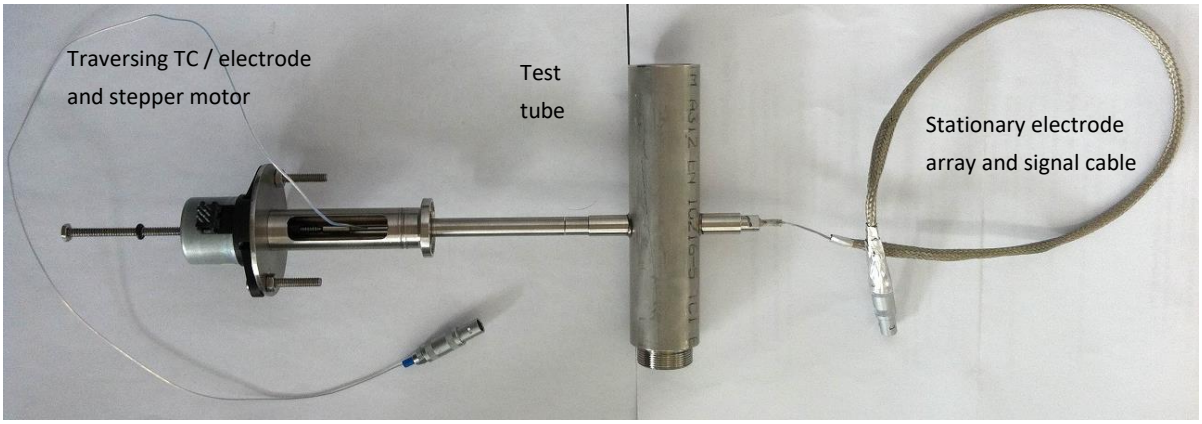

Figure 3-18 Physical realization of movable conductivity and temperature probe

3.4.2 Probe design and installation in the PRECISE facility

This chapter summarizes the design and technical aspects of combined conductivity and temperature probe. Mounting in the PRECISE facility is also discussed. Technical drawings of the probe components are shown in the appendix section 10.5.

3.4.2.1 Electrode array

The electrode array consists of stainless-steel wires embedded in a ceramic guiding tube. The ceramic tube is then inserted and bonded to a steel plug, Figure 3-19. Ceramic material chosen is Alsint or 99.7% sintered alumina[12] and steel is 316L stainless steel. These materials are chosen due to their resistance to corrosion in the environment of the PRECISE facility. Additionally, ceramic material electrically insulates the electrodes.

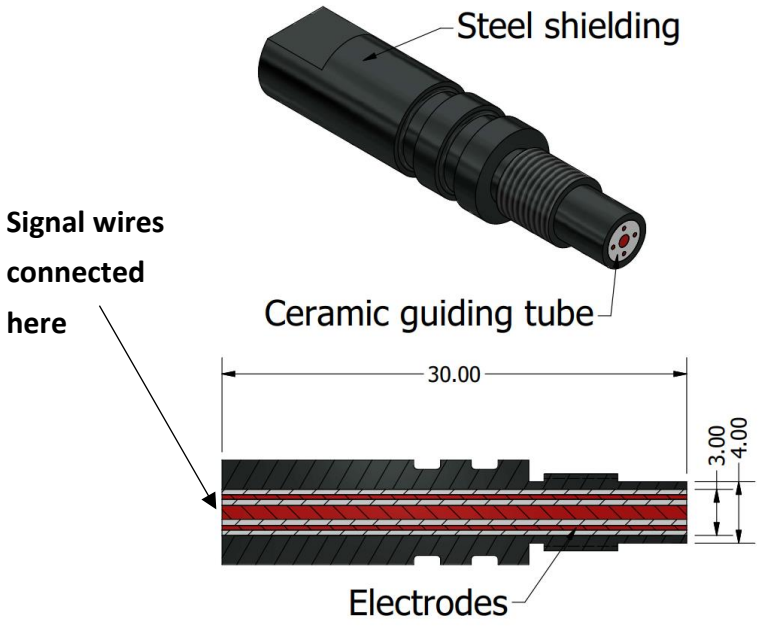

Figure 3-19 Electrode array plug and cross-section

[12] W. Haldenwanger Tech. Keramik 50AL7, Alsint 99,7 5-LOCHROHRE 1 hole 0,9mm, 4 holes 0,3mm

The plug is screwed into a corresponding port, welded to the test tube wall. This type of connection ensures reliable sealing, thanks to two included high-temperature Viton O-rings, as well as replaceability of the probe. The components are bonded using temperature resistant epoxy[13] that fills all the gaps between electrodes, ceramic tubing and steel shroud, forming a single part. PTFE-coated signal cables are then laser-welded to the backside of each electrode wire. The whole bunch of five is inserted in a PTFE tubing and evacuated through the coolant jacket.

The probe face is set to sit flush with the surrounding test tube wall, hence the wall curvature must be reproduced. In this way, the sensor impact on the condensate film flow is minimized. This is achieved by precision milling with a diamond polishing disk operated by a 3-axis milling machine, Figure 3-20.

Figure 3-20 Polishing of an electrode array face, to match inner tube wall curvature

[13] Cotronics Duralco 128

3.4.2.2 Traversing TC/electrode

The moving part of the probe is a 0.5 mm K type thermocouple (insulated junction) inserted in a ceramic guiding tube and a stainless-steel shroud, Figure 3-21. The same materials (99.7 Alsint, 316L steel, Duralco 128 epoxy) are used as with the electrode array. The assembly traverses the horizontal cross-section of the tube, recording the temperature distribution. It is located opposite to the fixed electrode array, thus when a liquid film is encountered, the thermocouple shroud conducts the transmitter signal to the connected electronic receiver.

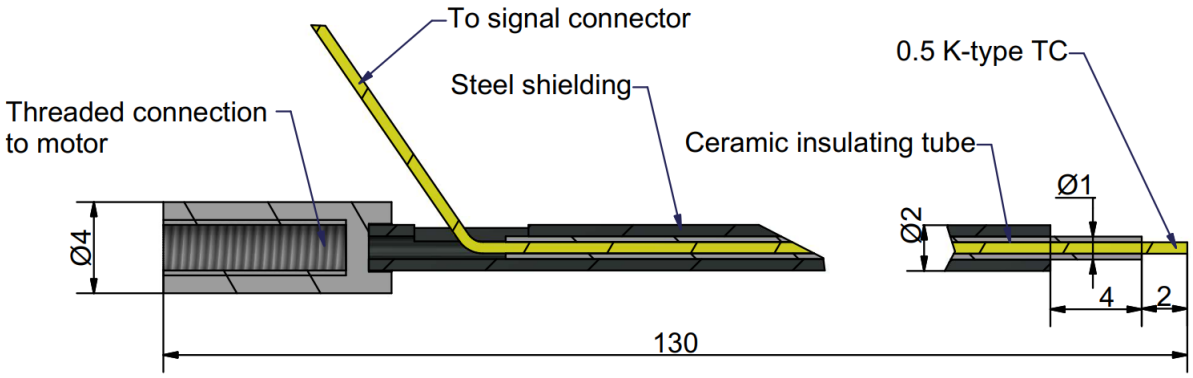

Figure 3-21 Traversing thermocouple/electrode cross-section, dimensions in mm

The probe is actuated with a linear stepper motor[14] possessing a minimum of 41 μm/step travel and up to 8.33 m/s speed. Movement of the probe takes place in a guiding tube, attached to the test tube via a plug connector, similar to the electrode array. The guiding tube has a built-in high-temperature Viton O-ring that creates a pressure boundary around the moving probe. The tube extends to the outside, ending with a mounting plate which aligns the probe and the engine. It also provides support for the end switches, and thus all the parts form a single rigid structure, Figure 3-22 & Figure 3-24A.

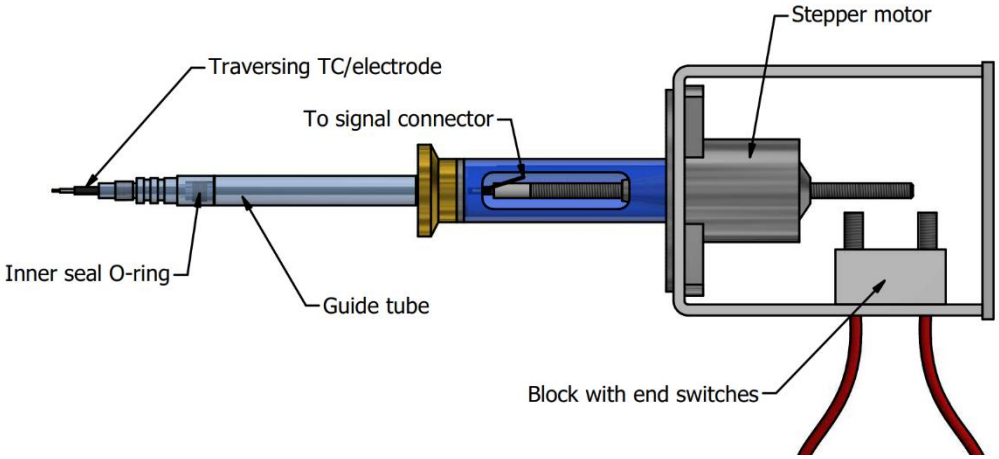

Figure 3-22 Actuation mechanism of the moving TC/electrode

The whole assembly is attached from the outside to the coolant jacket and the guiding tube penetrates through the flow of the coolant water. Since the coolant can be pressurized there is a need for another leak-tight pressure boundary. The probe assembly is fixed to the test tube and due to the manufacturing tolerances, the screw terminal and the penetration in the cooling jacket can have vertical misalignment of up to 1 mm, there is a need for a flexible, compensating component. Therefore, a custom made, flexible

[14] Johnson Electric UCL53 Linear Stepper Motor

bellow with a clamp flange[15] is welded to the coolant jacket. Corresponding clamp is welded to the probe assembly and the two come together, providing a leak-proof barrier with position compensation, Figure 3-23 & Figure 3-24B.

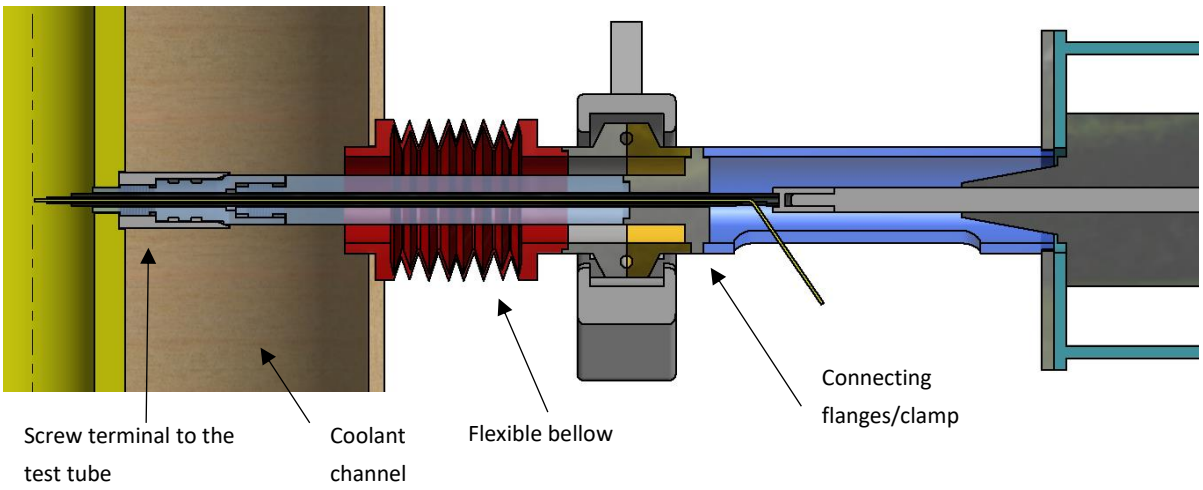

Figure 3-23 MCT probe attachment to the PRECISE facility

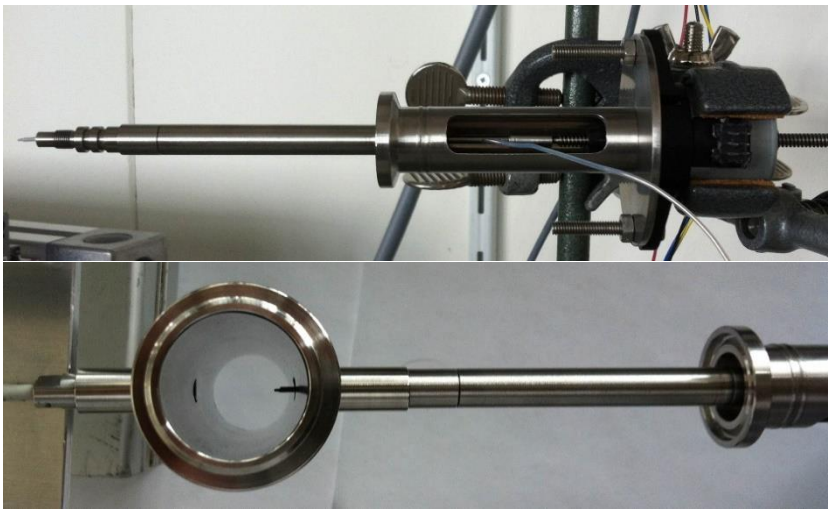

Figure 3-24 Photographs of the MCT probe assembly. A - guiding tube with the probe and engine, B - movable probe tip in the test tube

[15] Tri-clamp DN10 ferrule 210.017.014d

3.4.3 Electrode array operating principles

The first part of the probe is a five-electrode array, mounted flush at the condensing tube wall. A voltage pulse is supplied to the transmitting electrode T and a signal is registered at each of the receiving electrodes R1 to R4, which are put to zero potential, Figure 3-25. The measured response magnitude is proportional to the thickness of the conducting liquid layer covering the array.

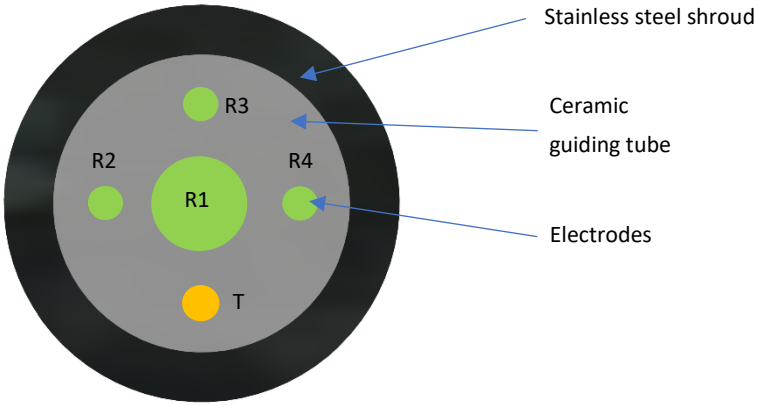

Figure 3-25 Face of the electrode array (R1 - R4 - receivers, T - transmitter)

Probes of these type were used previously, mostly as electrode pairs ([220], [221]), parallel wires ([222]–[224]) or extensive electrode arrays ([219], [225]). In the case of the PRECISE facility, narrow space and harsh conditions limited the possibility of using a large electrode array and the desire to limit condensate flow disturbance pointed to the flush electrodes as the best solution. The probe electrodes are made of wires of two various thicknesses and placed at three distinct distances from the transmitter. Hence, each electrode measured response to voltage pulse is unique, which made them sensitive to a variation of film thicknesses.

The electronic unit driving the transmitter electrode generates two subsequent voltage pulses with 1 kHz frequency and 0.25 ms duration, Figure 3-26. The pulses have an amplitude of +5V followed by a -5V. Oscillating signal with varying sign is used rather than constant supplied voltage to avoid water electrolysis on the electrodes, which would produce additional ions, distort the measurement and cause corrosion.

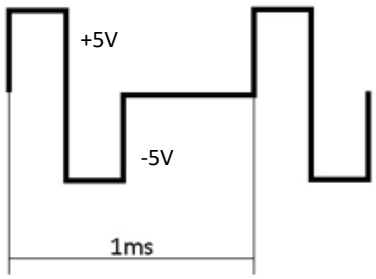

Figure 3-26 Transmitter electrode driving signal

Each voltage pulse packet is sampled at the high and low values, and an electronic circuit calculates the difference, effectively doubling the signal amplitude.

3.4.3.1 *Electrode array – circuit overview*

The scheme of the signal generation / acquisition circuit is shown in Figure 3-27. The basic design of operation logic was devised by prof. H-M Prasser and implemented by Mr. Michael Furrer. Parts of the circuit are discussed in detail in the separate, following sections.

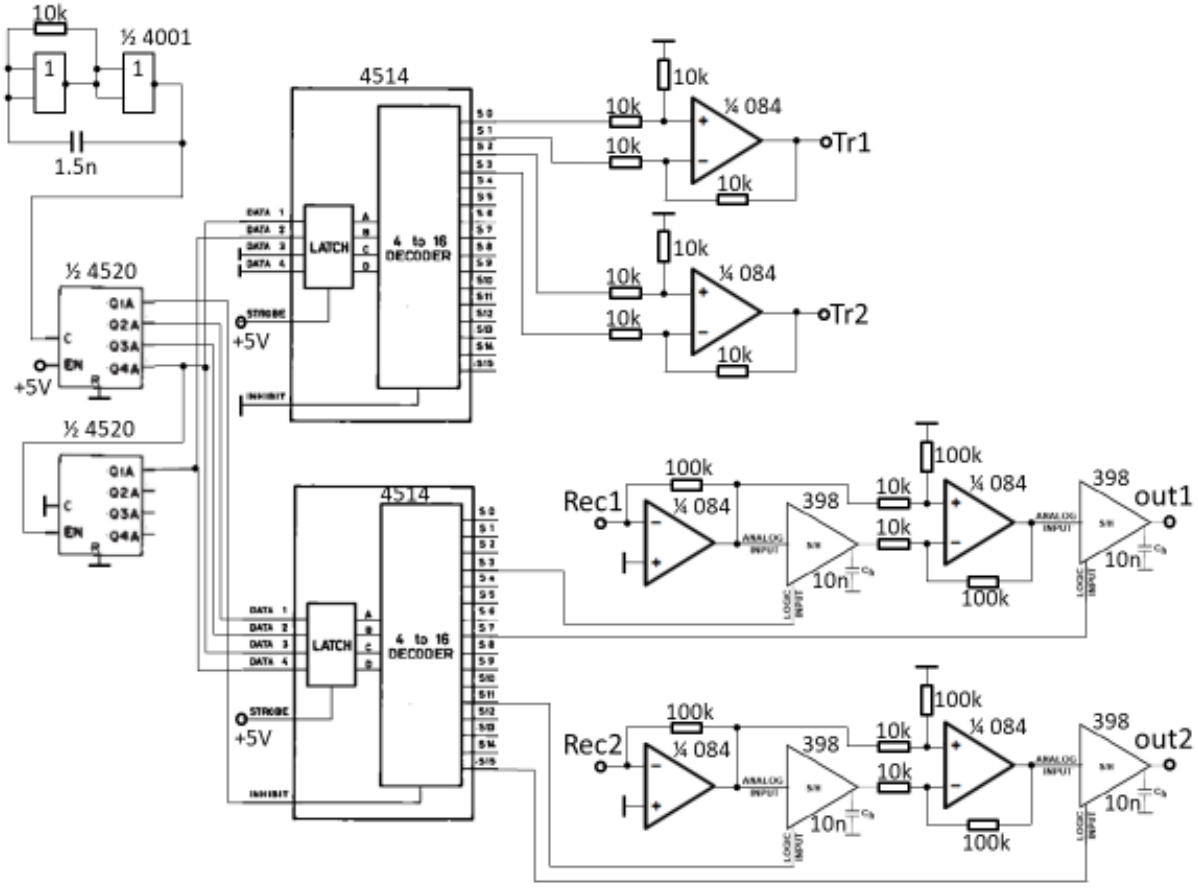

Figure 3-27 Overview of the MTC electrode array driving circuit

3.4.3.2 Electrode array – transmitter signal

At the heart of the signal generation lies the astable circuit with a RC oscillator, Figure 3-28. This clock signal is also used to synchronize the data acquisition circuit.

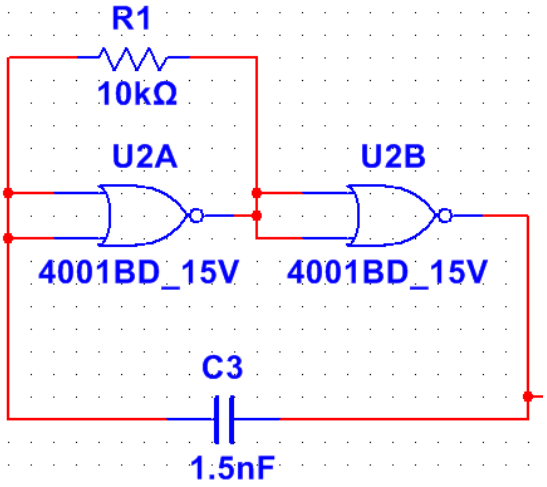

Figure 3-28 RC oscillator circuit generation analog clock signal

Capacitor C3 is charged and discharged via resistor R1 and the two included NOR Gates[16] are used to trigger the signal. As a result, this circuit generates a rectangular signal out of the sinusoidal voltage. Since the NOR gates runtime specifications are in the range of nanoseconds, the frequency f of the circuit can be defined as purely dependent on the RC components:

$$f = \frac{1}{2RC} \qquad (30)$$

The components used define 33.(3) kHz frequency, or a pulse with about 0.3 ms period. This oscillating signal is then fed to a 4bit counter[17]. It is counting rising edges of the square wave and, at 4bit, it is able to reach 16 before restarting. Four output pins provide respective binary values for each of the four bits. This results in dividing the original signal frequency by 2, 4, 8 and 16, while still maintaining the square wave as an output at the respective output pins. The slowest signal obtained in this way has the frequency of about 2kHz (exactly 33.(3) / 16 = 2.08(3)), and it is passed to a second four-bit counter, of which only the first output pin is used, providing frequency of about 1kHz.

The two last frequencies are further passed to a decoder unit[18]. Its role is to translate those two signals to four time-shifted 1 kHz voltage pulses, each available at a separate output pin, Figure 3-29. The high-voltage pulse at each of these pins lasts only a quarter, or 0.25 ms of every full period.

[16] Texas Instruments SN7401N

[17] Texas Instruments CD4520B

[18] ST Microelectronics HCC 4514B 4-bit Latch/4-to-16 Line Decoder

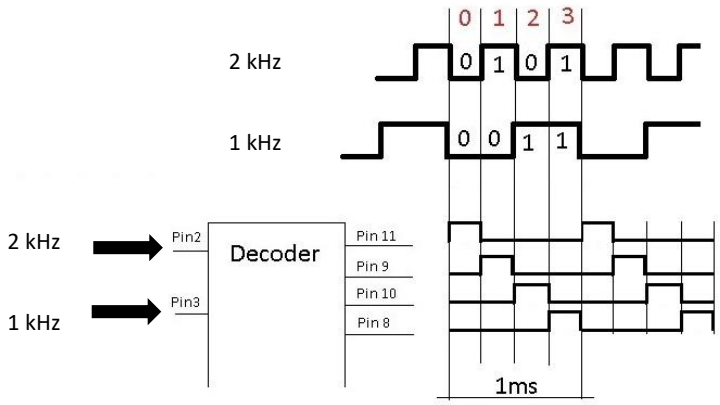

Figure 3-29 Creation of four 1 kHz time-shifted voltage pulses

Finally, the two first output pins from the decoder are connected to positive and negative inputs of an operational amplifier circuit, Figure 3-30. The Op-Amp[19] is implemented to operate in a differential amplifier mode. During every given cycle, high voltage pulse is delivered first to the positive input, followed by a high voltage at negative one, for a quarter-period of 0.25 ms each.

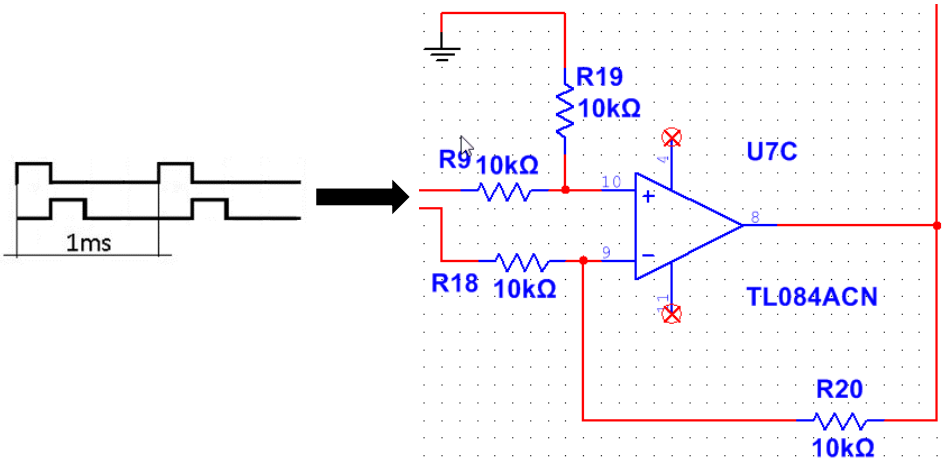

Figure 3-30 Final step of the transmitter signal generation – Op-Amp circuit

Depending on whether positive or negative input is set to high, following formulas apply:

$$U_{out+} = \frac{R_{19} + R_{20}}{R_{18}} * \frac{R_{19}}{R_{19} + R_9} * U_{in+} \qquad (31)$$

$$U_{out-} = -\frac{R_{20}}{R_{18}} * U_{in-} \qquad (32)$$

Since all the resistors in the circuit are the same, the overall gain is set to unity in both cases. The result is flipping the signal at the output to -5V when the high voltage is applied to a negative input. The

[19] Texas Instruments TL084ACN

total output signal consists of a logic high of +5V, followed by -5V and a period of zero potential for the remaining half of the cycle, Figure 3-31.

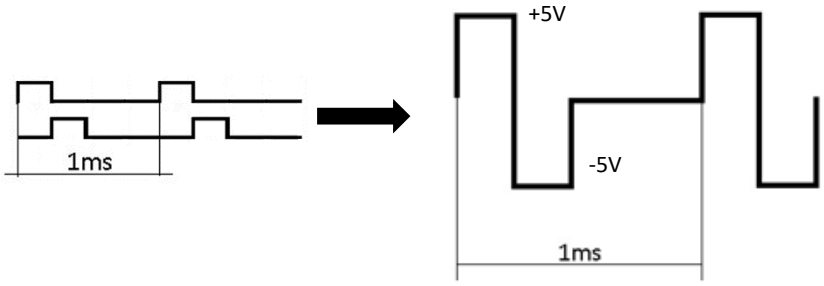

Figure 3-31 Final transmitter signal creation step

3.4.3.3 Electrode array – receiver electrodes

Each of the receiving electrodes is connected to a separate receiving circuit. It is built in such a way, to make use of the whole +/-5V range of the transmitter signal. Since high and low voltage pulses are supplied consecutively some form of memory is required. Therefore, a sample/hold component is used to retain the signal information collected during high state, which is later subtracted from signal during the low voltage pulse. Complete circuit used for sampling a single receiving electrode output is shown in Figure 3-32.

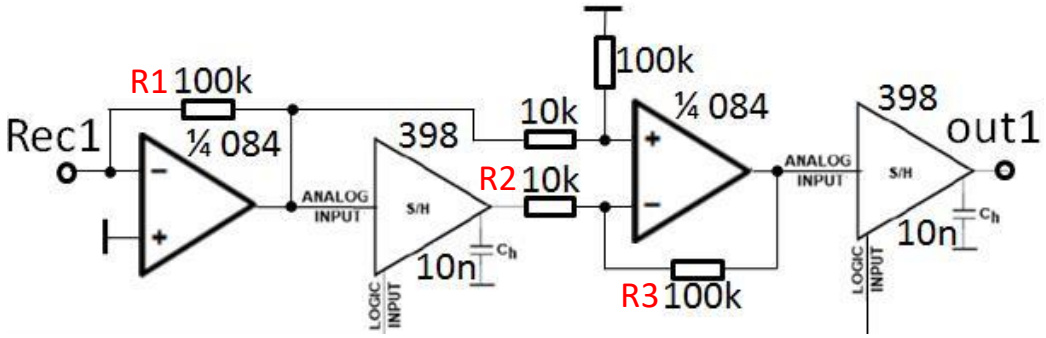

Figure 3-32 Circuit used for sampling receiver electrodes output

The first operational amplifier[20] is set to operate as an inverting amplifier, and thus the gain is defined as:

$$a_1 = \frac{R_1}{R_{MCT}} \qquad (33)$$

where R_{MCT} is the resistance of the probe, which value is dominated by the resistance of the condensate film layer covering the electrodes. The recorded signal is thus a multiplication of the variable gain and voltage incoming from the receiver electrode. This value is then stored in the first sample/hold gate. A crucial issue here is to make sure that S/H gate samples the incoming signal at the right time.

To achieve this, the S/H module is controlled by a clock signal that varies its behavior between sample mode at logic high and hold mode, at logic low. This clock signal is generated from the signal that controls the transmitting circuit, which ensures proper synchronization between transmitting and receiving

[20] Texas Instruments TL084ACN

tasks. Here however, after passing a 4bit counter, a second decoder[21] is used, Figure 3-33. Instead of supplying it with only two slowest outputs of the counter, all four inputs pins are utilized.

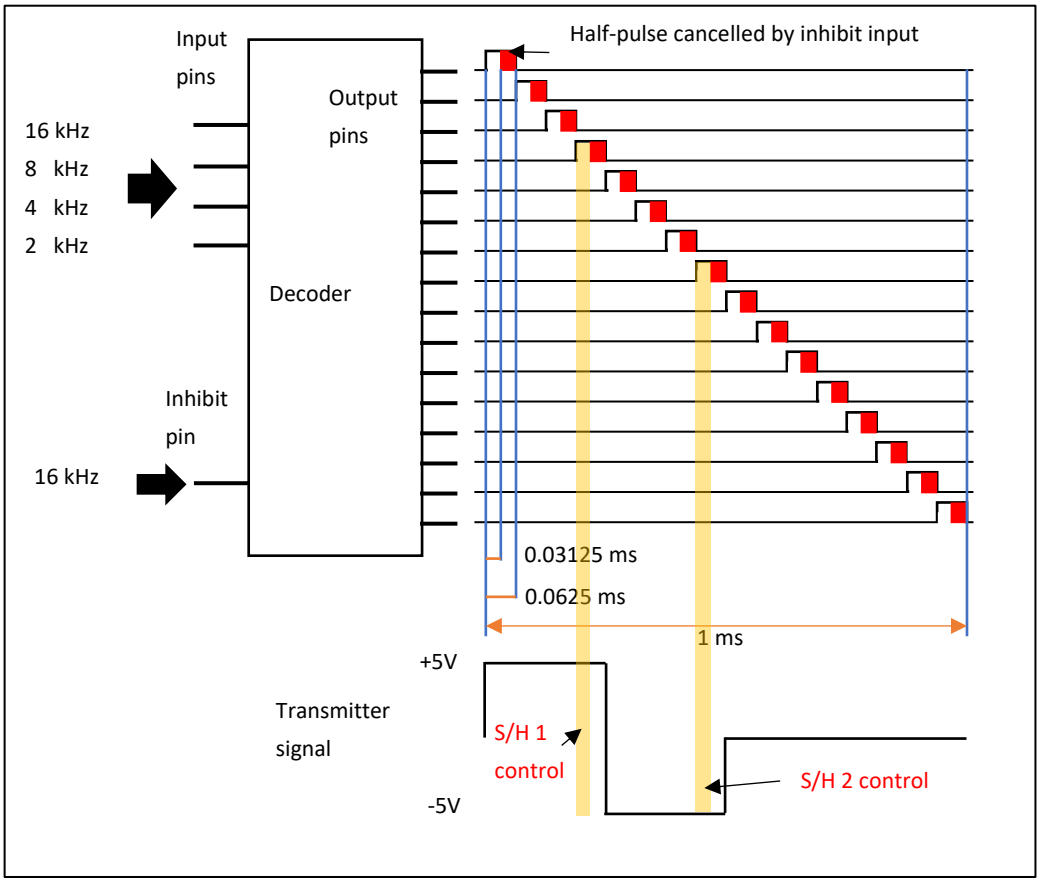

Figure 3-33 Control signals for sample/hold units in signal receiver circuit

As a result, each of the sixteen output pins is active for a 1/16 of a full 1 ms period, supplying time-shifted logic high voltage pulses. Moreover, an inhibit pin of the decoder is connected to a 16kHz signal, coming from the 4bit clock. When the inhibit is set to high, it sets all the output lines to the ground potential, which effectively cuts the duration of each output voltage high signal in half. Overall, each output line would have been active for a 1/16 ms, but coupled with the inhibit signal, the result is a 1/32 or 0.03125 ms pulse duration.

Out of the sixteen output signals, two are used to control the S/H units. First occurs during the 7/8th of the voltage high transmitter pulse and controls behavior of the first S/H gate. Therefore, the first S/H samples only the voltage high pulse and stores this value for the remainder of the cycle. Only 1/8th of the whole pulse duration, and towards the end, is chosen to allow some time for the system to settle and limit the impact of the system response on the measurement.

[21] ST Microelectronics HCC 4514B 4-bit Latch/4-to-16 Line Decoder

The second amplifier is working as a differential amplifier, set to subtract the response of the receiving electrode and the output of the first S/H unit. The output is defined as:

$$U_{2out} = \frac{R_3}{R_2} * (U_+ - U_-) \qquad (34)$$

U_+ and U_- stand for voltages at positive and negative inputs of the amplifier. It is followed by a second S/H unit, which only samples, during the last 7/8th of the negative transmitter pulse. As a result, the output of the circuit is a difference between probe's response at transmitter high and low signal pulses, adjusted every 1 ms cycle.

3.4.4 Signal acquisition

Three types of distinct signals are acquired with the MCT probe – temperature, position and the electrical response of the electrodes. For each signal type, a separate signal acquisition path is created. Temperature signal is acquired in the same way as for the remaining thermocouples in the PRECISE facility, Figure 3-34.

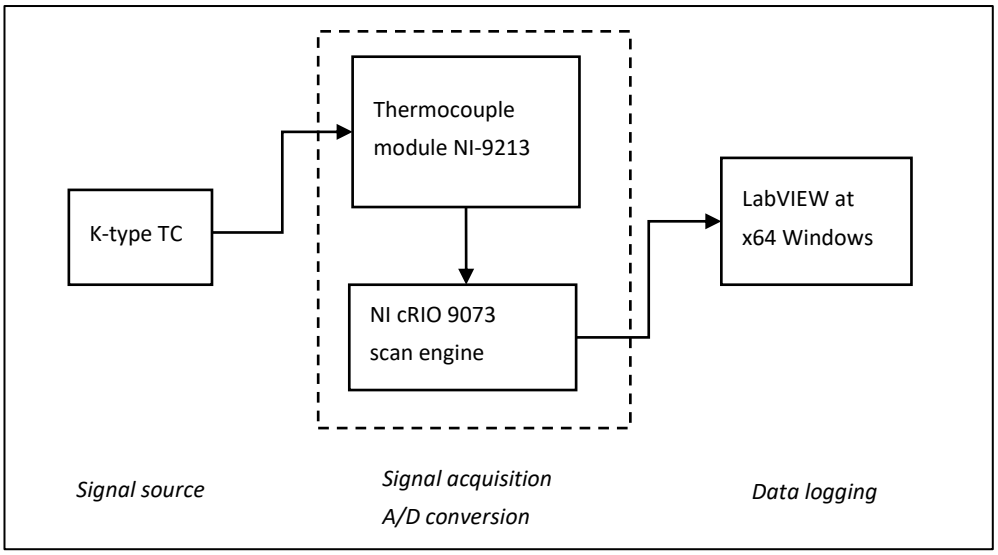

Figure 3-34 Temperature signal acquisition

The position signal acquisition system also acts as the movement controller of the probe. The engine is operated via National Instruments NI SMD-7610 stepper drive control and NI-9512 Stepper Drive Interface Module with a LabView program, Figure 3-35. The move request is initiated by the lab PC and transferred to the stepper drive control, which directly supplies power to the motor. This unit also sends feedback to the program, verifying the move command execution and updating the probe's tip position. Furthermore, two end switches are triggered every time the probe arrives at its movement boundary. Thus, every time a switch is tripped, SMD-7610's position reading is verified in the software and the position error is reset. This prevents the error accumulation over the course of continuous traversing of the probe. Trigger of an end switch also prompts the software to reverse the engine direction, according to user programming.

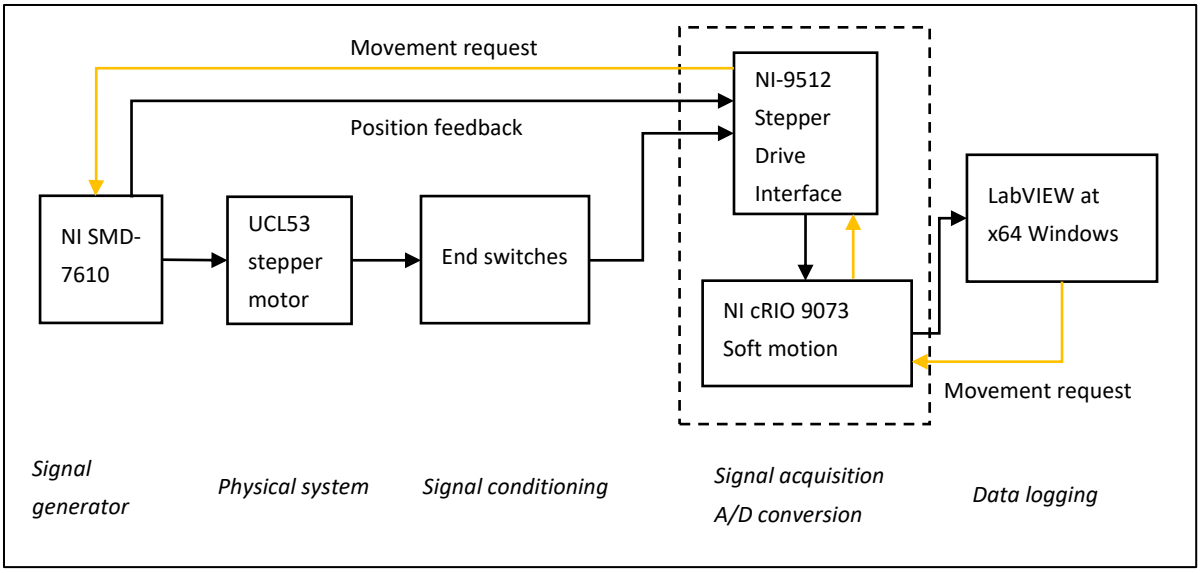

Figure 3-35 Probe tip position signal acquisition

Finally, the film thickness signal is generated and processed with the MP electronics unit, described in detail in the section 3.4.3. The produced output signal is then sampled with a NI-9215 voltage acquisition card and forwarded to the lab PC, Figure 3-36. The sampling frequency is set to 10 kHz – an order of magnitude faster than the MP receiver electronics is updating its output. In this way multiple samples are recorded for a single film thickness measurement, allowing for effective noise filtering.

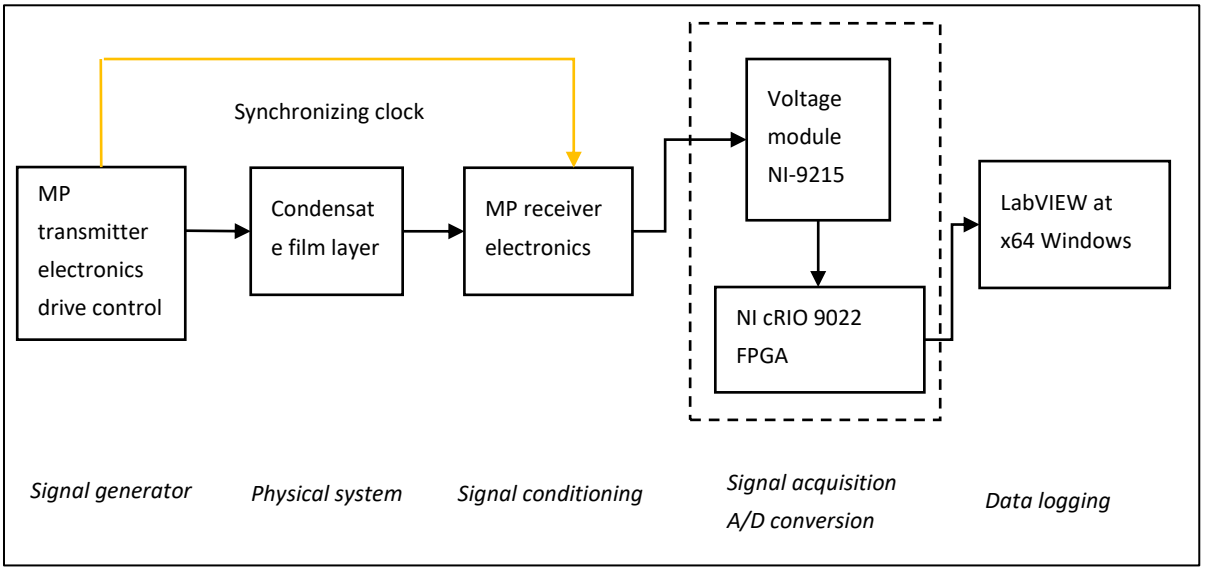

Figure 3-36 Film thickness voltage signal acquisition

3.4.5 Calibration procedure

3.4.5.1 Electrode array – static calibration

The calibration setup for the electrode array consist of a vertical piece of tube 120 mm long with the same diameter (⌀20) as the PRECISE facility test tube, Figure 3-37. The array plug is screwed in a terminal welded on the side wall. From the bottom of the tube, another plug is placed, that limits the possible water flow to the volume directly in front of the electrodes. An adjustable piston controlled manually with a micrometer screw is used to adjust the simulated film thickness. The piston face has a curvature matching the curvature of the test tube inner wall.

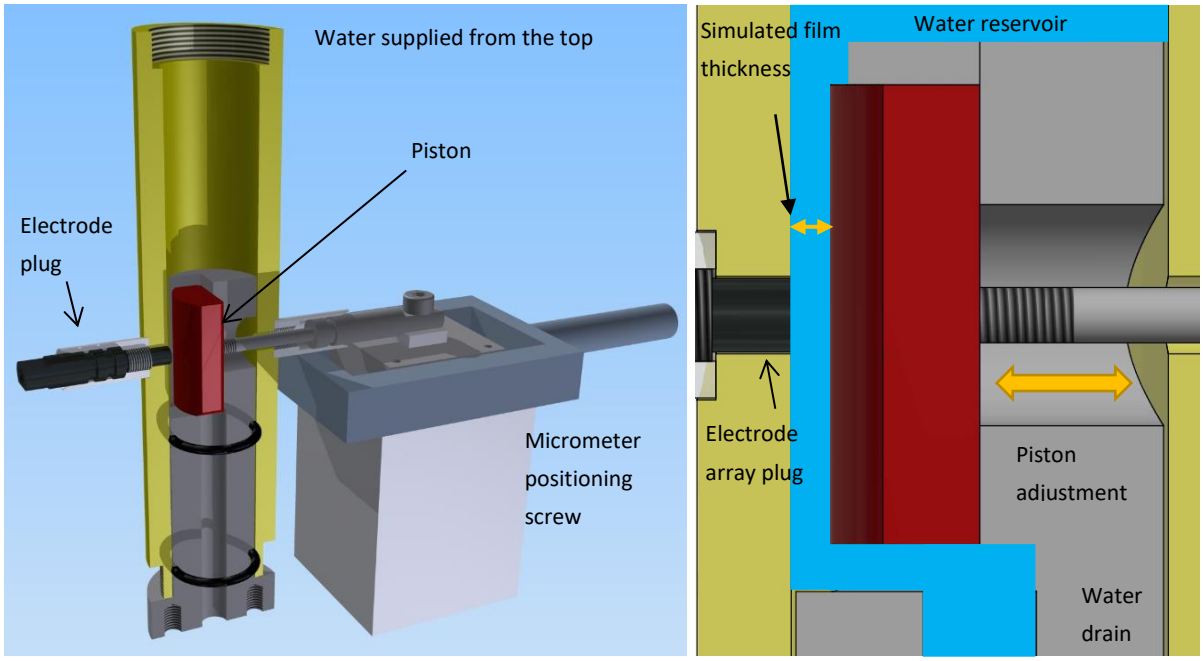

Figure 3-37 Electrode array calibration stand (A) and cross-section (B)

During the calibration procedure water is supplied from the top and flows through the piston-controlled gap and out of the rig through the bottom. The water is recirculated back to the top with a use of a small pump. Flowing water rather than stagnant is used as it better reflects the possible characteristics of the flowing condensate liquid film (i.e. minimizes ion concentration around the electrodes). The water is fed through a reservoir, ensuring a constant and uniform flow. Produced water layer has a homogeneous thickness over an area much larger (>300%) than the probe face. The water reservoir formed over the piston plug ensures continuous flow with no air bubbles ingress.

Data is recorded using the acquisition system described in the section 3.4.4. Signal acquisition rate is set to 100 kHz, with a possibility to engage a FPGA-programmed low-pass filter with a cut-off frequency of 100 Hz, to limit the noise. Lowering the recording frequency below 100 Hz is not affecting the measurement results in this case, since the thickness of the simulated film remains constant.

During the calibration procedure the piston starts at the zero position, pressed into the wall around the electrode array. Then it would be retracted with 100 μm steps until 2 mm film thickness was achieved. Films over 2 mm were not predicted to be present in the PRECISE facility, hence the limiting value. At each position of the piston, data was recorded for around 30 seconds.

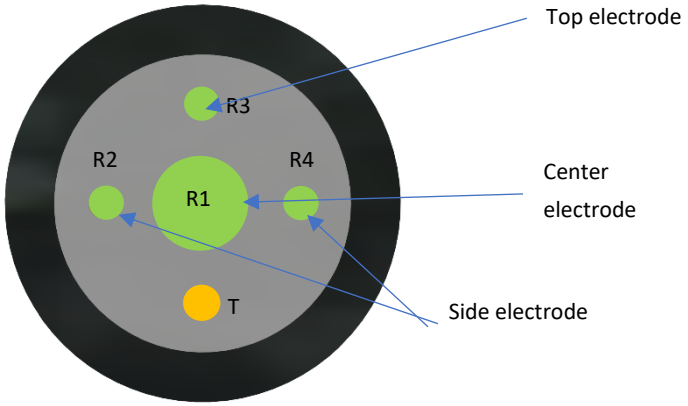

Figure 3-38 Electrodes designation convention (R1 - R4 - receivers, T - transmitter)

Since the receiving electrodes vary in size (Figure 3-38) and distance from the transmitting electrode, their response is expected to be different. This was exactly observed, with electrodes being the largest (center electrode) providing the highest signal amplitude, followed by the small electrode close to the transmitter (side) and at the last, the small electrode furthest away, Figure 3-39A. When the response curves are normalized (against maximum values, to the range 0-1), it is clear, that the general behavior of the signal is the same among all the electrodes, just the amplitude varies (Figure 3-39B).

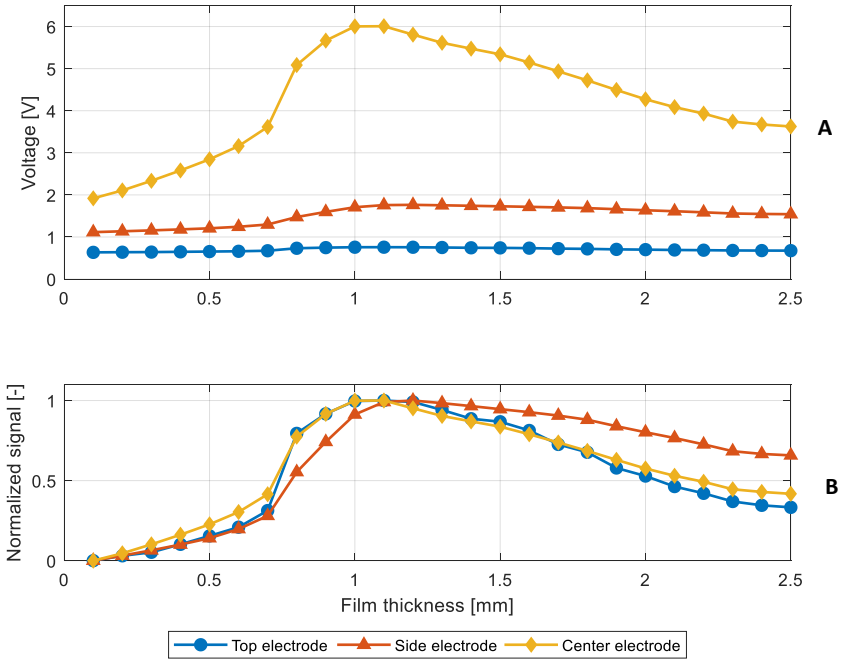

Figure 3-39 Electrode electrical response as a function of film thickness. A - raw signal, B - normalized signal.

One interesting feature of the observed behavior is the existence of the maximum signal value at around 1 mm of liquid film thickness, after which the amplitude gradually drops off. This phenomenon can be explained due to an increasing amount of signal escaping to the surrounding tube steel wall, which acts as a large grounding electrode. A finite element method (FEM) simulation using ANSYS 15.1 Electrical package was setup to verify this assumption. The calculation domain included a section of the tube wall with an embedded electrode array as well as a liquid layer, Figure 3-40A. The curvature of the actual device was

kept in the simulation. The liquid layer's thickness was varied from 0 to 2 mm and for each thickness a current density was calculated and used as a parameter to compare against the values observed during calibration.

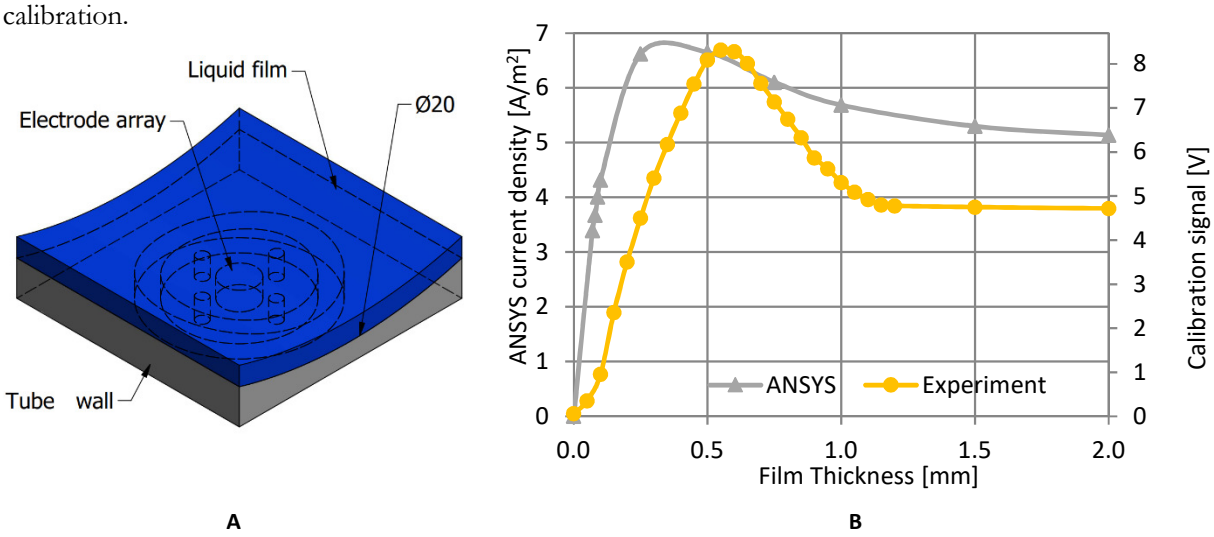

Figure 3-40 ANSYS calculation domain (A) and calculation - measurement qualitative comparison, center electrode (B)

The results show that the calculation predicts the gradual signal amplitude decrease after reaching a maximum for a certain film thickness as well. The exact shape of the curve was not perfectly reproduced, but the general behavior pattern was observed. Therefore, the usefulness of the electrode array remains up to the 1 mm film thickness, as observed during the calibration procedure. The moving electrode which accompanies the array can verify if for a given experiment condensate film thickness remains within this range. For every electrode, a fourth order polynomial fit of the gathered data up to 1 mm provides a good calibration function, Figure 3-41.

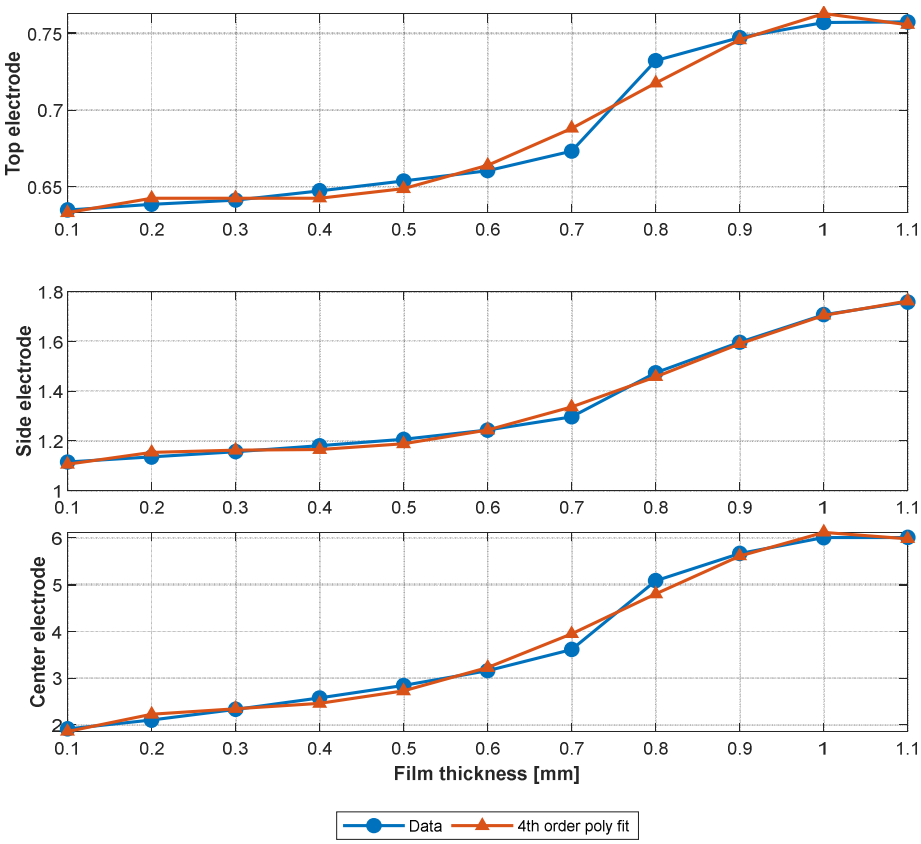

Figure 3-41 Fourth order polynomial fit to each electrodes' signal

3.4.5.2 *Electrode array – film dynamics*

Besides the static response of the electrode array, it is important to understand the time-resolved behavior of the measured signal. This information is useful in interpreting the liquid film dynamics, i.e. waviness. Wavy linear film has a bigger effective interfacial area, which tends to enhance the heat transfer rates ([170], [226], [227]). Assessing the electrode array ability to observe this parameter is thus of importance.

The setup consists of the same test tube section with screwed-in electrode array plug, but with all the other equipment removed. The tube was tilted at about 60° angle, to ensure supplied water would flow on top of the array. Water was supplied from the top with a peristaltic pump[22] with a variable flow rate of 1.7 – 5400 ml/min and maximum rotation of 220 RPM. This model is a triplex pump, possessing three rollers that in turn compress an elastic hose. Due to these compressions, during a single rotation of a pump there are 3 major flow pulses delivered – one for each roller. These are accompanied by three minor pulses, occurring due to intake and exhaust timing mismatch of the pump – in the middle of the main pulse, next roller starts a new compression.

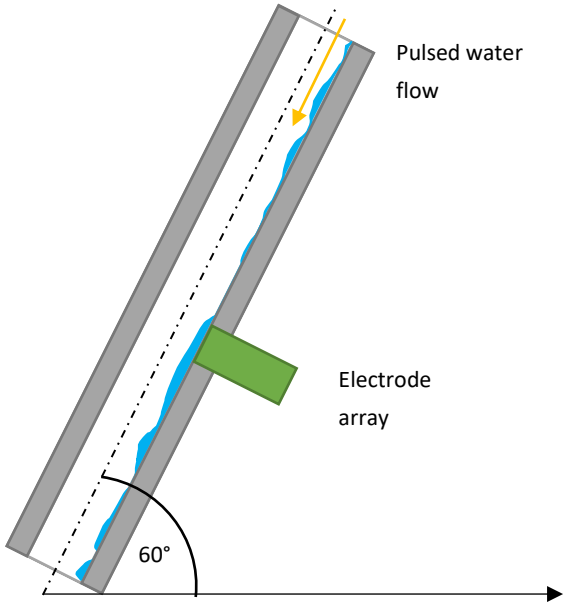

Figure 3-42 Electrode array dynamics analysis test

The speed of the pump is user adjustable, therefore knowing the rotations per minute, one can easily estimate the produced film oscillations frequency:

$$f_{film} = 6 * \frac{Pump_{RPM}}{60} \ [Hz] \qquad (35)$$

Spectral analysis using fast Fourier transform of the signal measured with the central electrode in the electrode array is compared against the theoretical film oscillation frequency calculated based on the pump settings. Tested frequency range spanned from 11 to about 22Hz, the latter being the highest value achievable with the used equipment. Figure 3-43 shows the observed FFT peaks overlaid with the values calculated from the pump setup.

[22] Ismatec™ ECOS 380 Pump

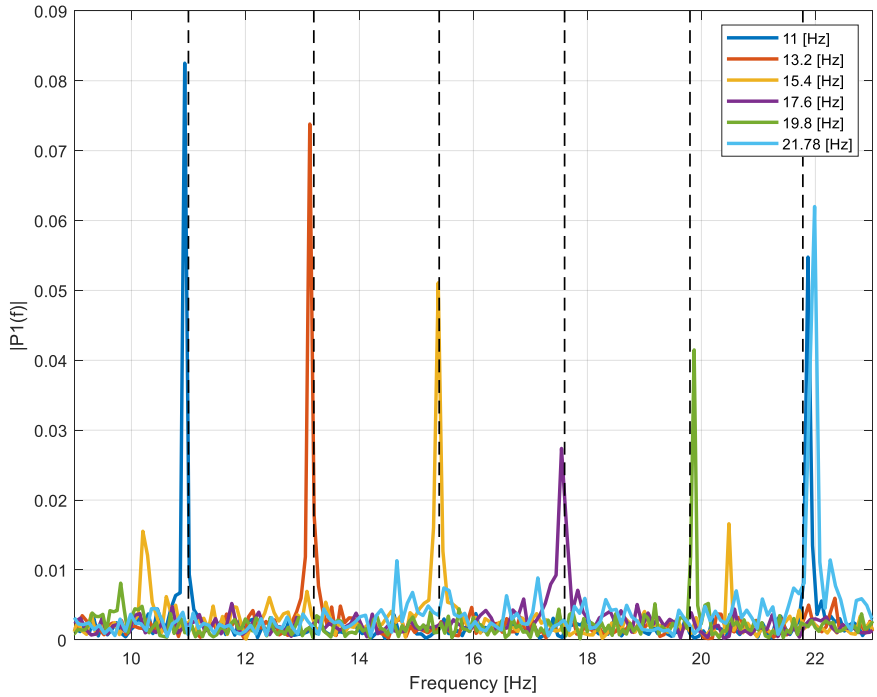

Figure 3-43 Electrode array spectral analysis for liquid film oscillation frequencies from 11 to 22 Hz

For every measured frequency, a comparison was made between the two. The discrepancy for every measured case remains below 1%, verifying that the electrode array is accurately measuring the liquid film dynamics, Table 3-2. Should regular waves appear during experiments in the PRECISE facility, it should be possible to observe them.

Table 3-2 Summary of dynamic analysis of the electrode array signal

Electrode Array FFT [Hz]	Pump Freq [Hz]	Error [%]
10.94	11	-0.55%
12.09	12.1	-0.08%
13.13	13.2	-0.53%
14.25	14.3	-0.35%
15.38	15.4	-0.13%
16.47	16.5	-0.18%
17.55	17.6	-0.28%
18.81	18.7	0.58%
19.87	19.8	0.35%
21.11	20.9	0.99%
21.99	21.78	0.95%

3.4.5.3 Traversing TC/electrode

The MCT probe provides three types of signals – position of the probe tip, voltage on the probe shroud and temperature. Starting with the last, the thermocouple was calibrated in a thermocouple oil calibrator, to the precision of 0.1°C. The voltage measurement was done by the electrode array electronics, described in the section 3.4.3. Here, the actual value of the observed signal was not of importance – the signal detection was though enough to determine electrical contact. This information, cross-referenced with the position measure of the probe gave an indication that a liquid film interface was encountered, Figure 3-45. Which brings the third signal, the position measure into the picture. As described in the section 3.4.4, the position of the probe was supplied by the stepper motor drive by confirming execution of each desired move command issued by the governing program. At the start and end of the probe movement interval, an appropriate end switch would trigger, verifying the stepper motor drive information and thus the probe position measure was continuously calibrated during operation, elimination position error accumulation.

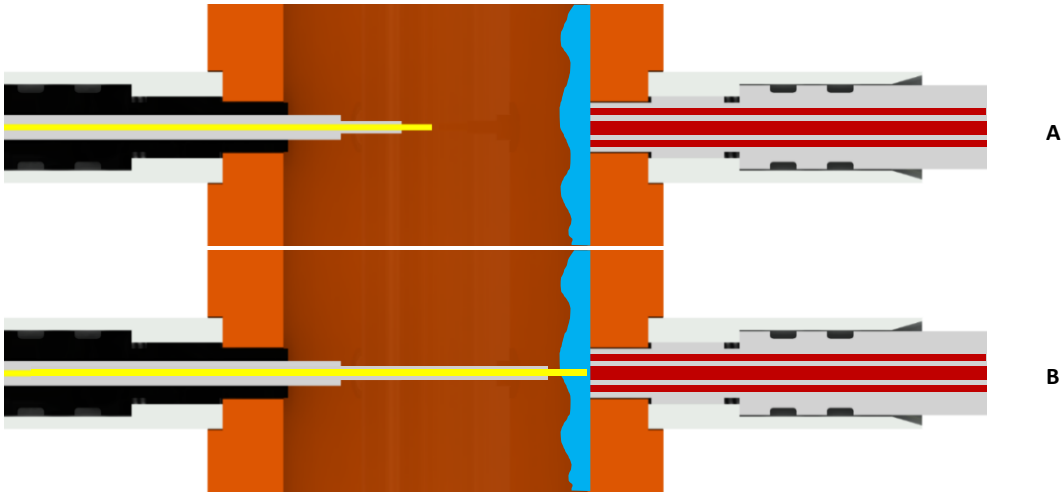

Figure 3-44 Traversing thermocouple / electrode operation:
A - tube middle position: high temperature, no voltage signal
B - end position: lower temperature, electrical signal detected

The typical three-signal, time resolved behavior is shown in Figure 3-45. One can notice in the position reading (Figure 3-45A) that the speed of the probe was varied along its path. 2.5 mm from the wall surface the probe slowed down, to collect data at an increased number of positions, which resulted in an increased spatial resolution in the region of interest. When the tube wall is approached, a pronounced temperature drop is observed (Figure 3-45B), accompanied by a gradual increase of the potential measured on the probe shroud (Figure 3-45C). After cross-referencing position measurement at temperature reading and voltage readings, the data can be displayed in modified coordinates, using position as the x-axis. Here, for each recorded position, temperature and voltage data would be binned and processed, resulting in time-averaged values, Figure 3-46.

Temperature drop is clearly visible in the recorded data. At the same time, to extract a useful voltage signal, significant filtering / signal processing was required. One must be thus very careful when drawing strong conclusions based on the observed electrical signal.

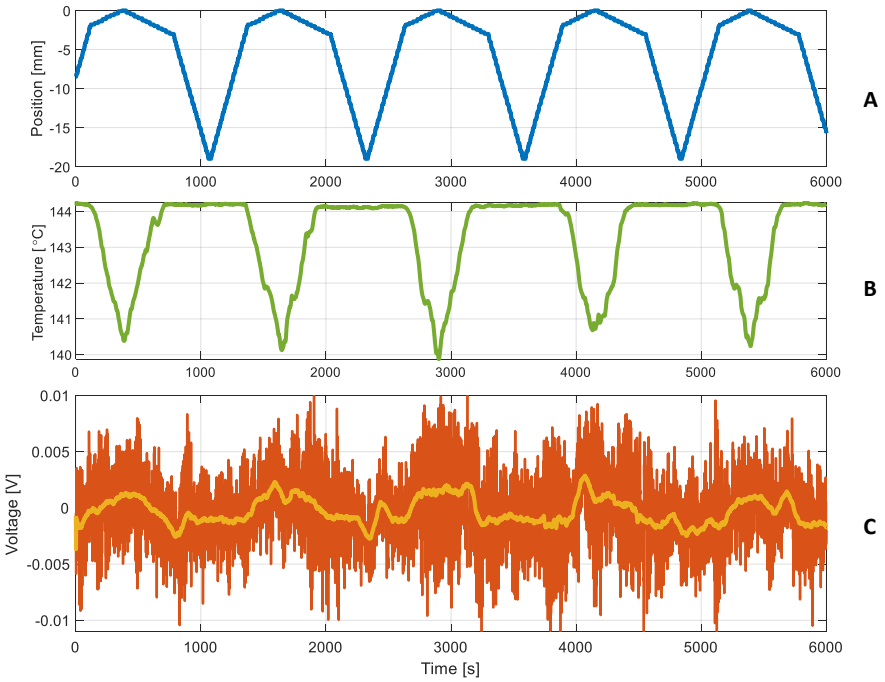

Figure 3-45 Time resolved MCT probe signal comparison. A - position, B - temperature, C – voltage full frequency range of 100kHz (red) and down sampled to 100 Hz (yellow)

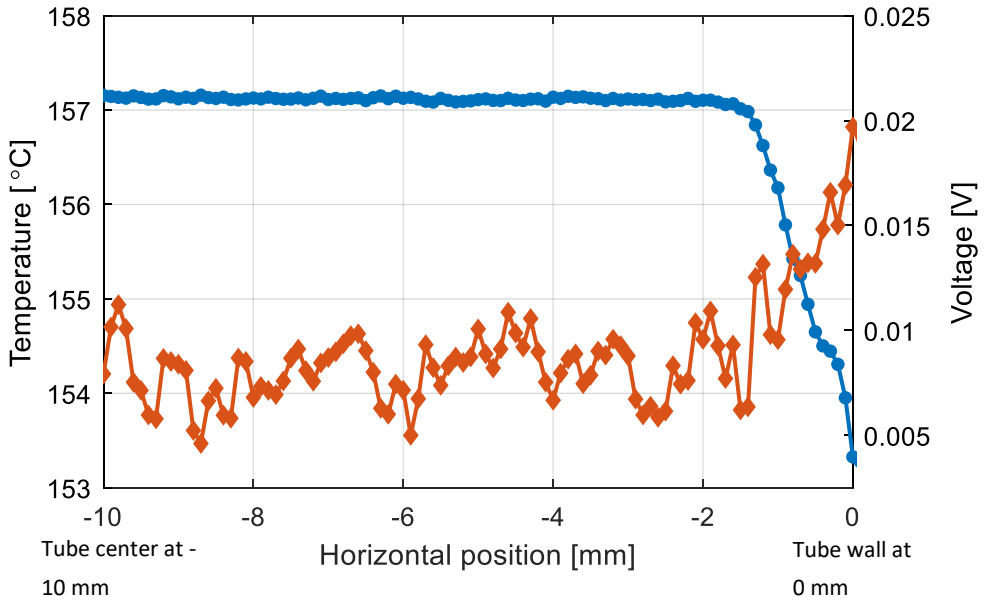

Figure 3-46 Typical horizontal temperature distribution during condensation observed with MCT

3.5 Other instruments

This chapter summarizes remaining instruments used for data acquisition in the PRECISE facility. Detailed discussion on the sensors accuracy and error propagation is given in Chapter 4 .

3.5.1 Thermocouples

In the PRECISE facility K-type alumel/chromel thermocouples (insulated junctions) are used for general temperature measurement. Their signal is acquired with three NI-9213 high-density, 16-channel, 75 S/s Aggregate, ±78 mV thermocouple input modules, Figure 3-47.

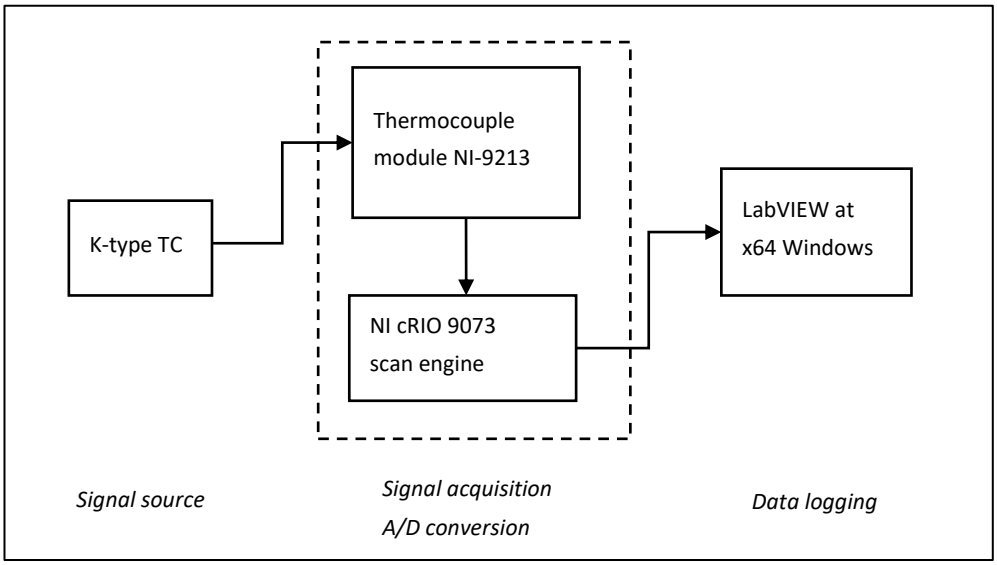

Figure 3-47 Thermocouples data acquisition

In the PRECISE facility thermocouples are installed to measure vertical temperature gradients in the test tube center, test tube wall, coolant water channel as well as outer wall of the coolant jacket. Additionally, a few thermocouples are located in the heater tank, directly underneath the test tube and on its surface. The thermocouples mounted on the outside walls of the facility were used for heat-losses estimation.

Each thermocouple mounted in the PRECISE facility was calibrated prior to installation. Correction based on the recorded calibration parameters is included in the data processing software. Thermocouple signal in the PRECISE facility was sampled at 10 Hz (thermocouples in the test tube center) and 1 Hz (remaining ones).

3.5.2 PT-100 resistive thermometers

In total, four PT-100 resistive thermometers[23] are installed in the PRECISE facility. They are placed in the locations where highest precision of the temperature measurement is necessary. This include the inlet and outlet of the coolant water channel, the heater tank and the NC gases intermediate tank. Their signals were acquired with a PT-104A, a 4 channel, high accuracy (0.01°C) and resolution (0.001°C) module, Figure 3-48. PT-100 thermometer signal is sampled at 1 Hz frequency.

[23] PICO SE012, temperature range: -50 to +250°C, accuracy: ±0,03K at 0°C, Ø4 x 150 mm

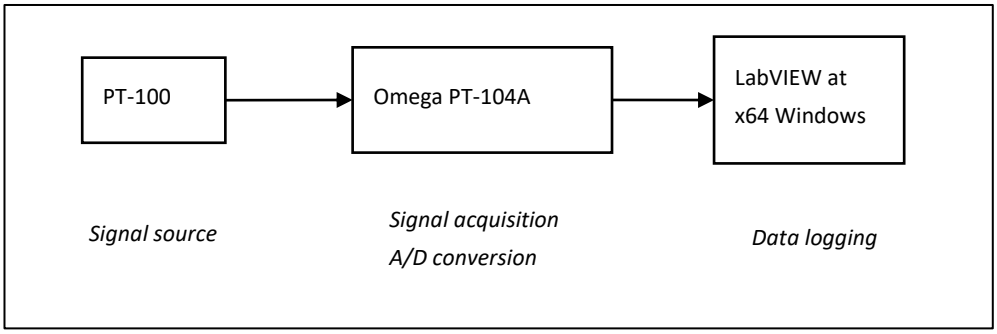

Figure 3-48 PT-100 resistive thermometers signal acquisition

3.5.3 Pressure transducers

Three pressure measurements are of interest in the PRECISE facility:

a) Experimental volume pressure
b) Coolant loop pressure
c) NC gases intermediate tank pressure

The a) and b) are relevant during the steady-state properties calculation while a) and c) used for the evaluation of the pre-filled NC gases mixture. The signal of the piezoresistive pressure transducers[24] is directly acquired with a NI-9208 current module, as their output signal is the 10 bar range translated into 4-20 mA. Pressure signals are sampled with 1Hz frequency.

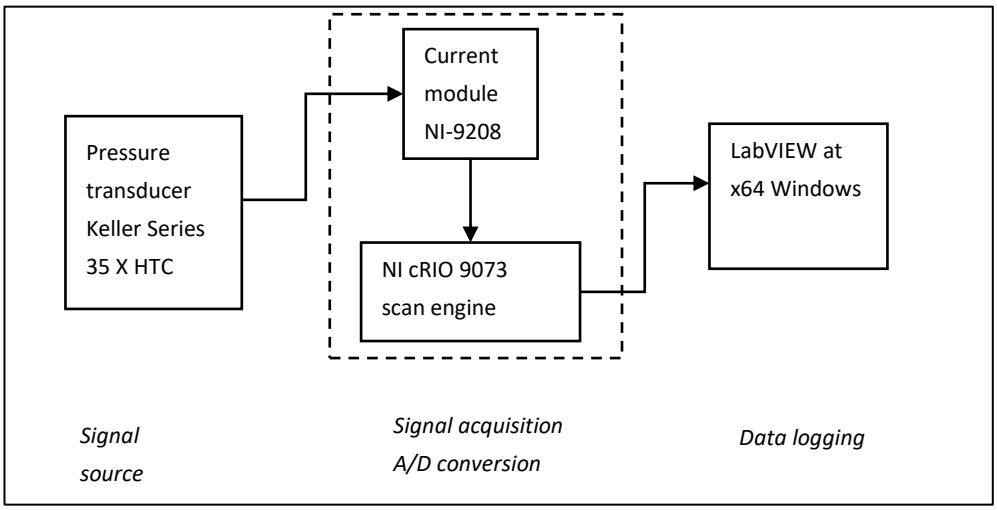

Figure 3-49 Pressure transducer data acquisition

3.5.4 Heating power measurement

The essential parameter measured in the PRECISE facility is the power delivered to the heating rod located in the water heater tank, located underneath the test tube. This power can be used directly to estimate the steam mass flow during steady-state conditions of the experiment.

[24] Keller Series 35 X HTC

The heating rod is powered with 230 VAC, passed through a thyristor-based control unit. The power controller[25] adjusts the delivered power based on the pressure reading in the experimental volumes. The heater is controlled in burst-firing mode, i.e. in a period of time, only some amount of sine wave is switched on. By adjusting the time on vs time off ratio, the thyristor-based unit manipulates amount of delivered power. Delivered current is sampled with current transducer, converting it to 4-20 mA range and then acquired with NI-9208 current module.

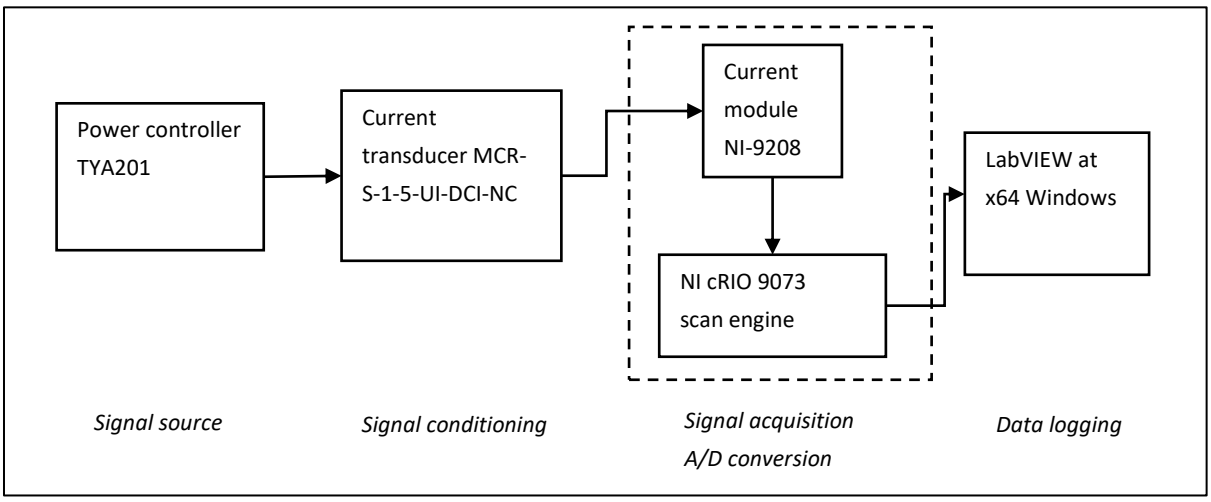

Figure 3-50 Heating power data acquisition

3.5.5 Coolant flow

Flow of the coolant water is measured with a vortex flow meter[26]. Acquired value is used both in data processing as well as during the experiment for coolant pump control. Therefore, signal is first converted to the 4-20 mA range and then duplicated, for logging and control respectively. Flow data is sampled at 1 Hz frequency.

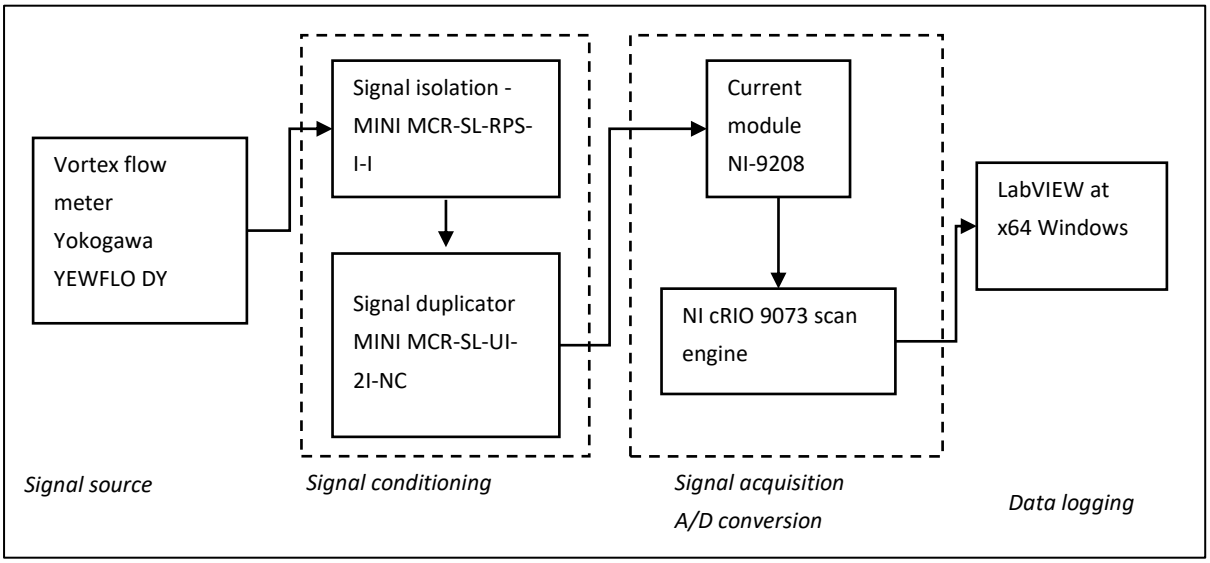

Figure 3-51 Coolant volumetric flow data acquisition

[25] JUMO TYA 201 - Single-Phase Thyristor Power Controller

[26] Yokogawa YEWFLO DY

Chapter 4 Error propagation

Every physical measurement is inherently burdened with accompanying errors. Quantification of these errors is therefore crucial for the proper analysis of gathered data. This chapter presents a short overview and analysis of equipment accuracy and discussion on error propagation.

In PRECISE facility DAS design and construction, as well as the choice of sensors, considerable efforts were devoted to minimizing the corruption of recorded data through excessive noise. However, for two experimental type of devices – heat flux sensors and film thickness probe – many characteristics were unknown prior to the calibration and usage in the facility. This chapter presents best efforts to estimate correct accuracy of these new devices.

Finally, based on the measured parameters, many properties of gas/liquid system were calculated, basing on well-established formulas, or engineering resources (e.g. IAPWS-97 steam tables). Error propagation through these calculation procedures is also discussed and presented.

4.1 Measurement sensors' and DAS properties

Six basic parameters were measured in the PRECISE facility:

- Temperature T
- Pressure P
- Heating voltage / current U_{evap}, I_{evap}
- Coolant volumetric flow $\dot{V}_{cl}$
- Heat flux $\dot{Q}$
- Liquid film thickness δ_{film}

Every other property presented in the results section is derived from above parameters. Clear understanding of the accuracy of each of these measurements is crucial for the proper error assessment downstream. Table 4-1 provides a short summary of employed equipment and its characteristics. Extensive description of data acquisition chain for each sensor is provided in the chapter 0.

Table 4-1 Summary of sensors installed in PRECISE facility

Sensor Type	Type	Model / brand	Range	Output	Base accuracy	Resolution	Drift	Connected to
Thermocouple	Type K	N/A	10-200°C	0.798 - 8.138 mV	1.5 K	0.0025 K[27]	N/A	NI9213
Resistive thermometer	PT100	SE012, PT100 Probe for PT-104	10-200°C	100-175 Ω	0.03 K	N/A	N/A	Omega PT-104A
Pressure Transmitter	Piezoresistive	Keller Series 35 X HTC	0-15 bar	24 VDC, 4-20 mA	0.5 %	0.002 %[28]	0.2 %[28]	NI9208
Volumetric flow meter	Vortex meter	Yokogawa YEWFLO	0-5 m^3/h	4-20 mA	0.75 %	N/A	N/A	NI9208
Heat flux senor	experimental	Andrey Mityakov	0-200kW/m^2	±100 µV	N/A	N/A	N/A	amplifier circuit and NI9215
Film thickness probe	experimental	author	0-1 mm	0-10 V	N/A	N/A	N/A	custom electronic circuit and NI9215

Each sensor was connected to an appropriate data acquisition unit, where its signal was then measured and converted into digital domain. The two experimental types of sensors used custom produced signal-forming electronic components: two step amplification in case of heat flux sensors and emitter/receiver unit for film thickness probe, as described in sections 3.3.4 and 3.4.4. Table 4-2 provides summary of the acquisition devices used for sampling and converting analogue to digital signal.

Table 4-2 Properties of data acquisition equipment

Type	Name	Manufacturer	Accuracy reading	Gain error	Offset error	Resolution	Resolution A/D	Gain drift	Offset drift
TC module	NI 9213	National Instruments	>1 K	±0.03%	4 µV	0.02 [K]	24 bit	N/A	N/A
PT100 module	PT-104A	Omega	0.01 K	N/A	N/A	0.001 [K]	24 bit	3 ppm/K	N/A
Current module	NI 9208	National Instruments	N/A	±0.76%	0.04[29] / 8.8 µA	50 nArms	24 bit	20 ppm/K	62 nA/K
Voltage module	NI 9215	National Instruments	N/A	±0.02%	0.014%[29] / 1.456 mV	0.153 mV	16 bit	10 ppm/K	60 µV/K

[27] http://www.picotech.com/applications/thermocouple.html

[28] Of full scale

[29] Of input range

4.2 Measured properties errors

In this section estimation of measurement errors for each of the six measured properties is discussed. Errors attributed to sensors and DAS units are taken from the Table 4-1 and Table 4-2 respectively.

4.2.1 Temperature

Temperature measurements in PRECISE facility were accomplished with type K thermocouples and PT100 elements. The latter were used in several critical locations – inlet and outlet of the coolant channel, the steam generator tank and the NC preconditioning volume. Especially the coolant inlet and outlet temperature reading precision was crucial to estimate the coolant temperature pickup along the condensing tube. Since this value was estimated to fall in the range of 0.5 to 2K, reading errors caused by type K thermocouples were deemed too high to provide meaningful results. For the PT100 elements, both for the probe and for the DAS unit, the values of absolute errors were available. Hence the calculated measurement error is:

$$T_{PT100\_err} = \sqrt{0.03^2 + 0.01^2} = \pm 0.0316\ K \qquad (36)$$

For the used thermocouples, the uncertainty that can be ascribed to the sensor itself and the DAS unit was quite high by comparison. To address this issue, calibration procedures were established for each of the used devices. For every thermocouple, its response was measured against a well-established reference, provided by the specialized calibration device[30]. Offset from the reference was recorded at 6 discrete temperatures of – 50°C, 75°C, 85°C, 120°C, 150°C and 180°C – which covered the full measurement range. All the offset values were then stored in a table, accessible for data processing code written in Matlab as a reference. During data processing, the offset values were linearly extrapolated from the available reference data and added to the measured values to increase accuracy. Therefore, the overall error of the thermocouple temperature reading can be understood as an error of the reference calibration device (+0.11°C[30]) and the national instruments acquisition module accuracy (>1K, according to the device data sheet) as follows:

$$T_{T\_K\_err} = \sqrt{0.11^2 + 1^2} = \pm 1.006\ K \qquad (37)$$

4.2.2 Steam / water pressure

As with the temperature measurement, pressure measurement errors appear due to the used sensor and the data acquisition device. First, for the DAS unit, the absolute error can be estimated according to the formula:

$$\begin{aligned} P_{DAS\_err} &= P \times Err_{gain} + Err_{offset} \\ &= 0.0076 \times P + 0.0004 \times 15\ [bar] \end{aligned} \qquad (38)$$

Secondly, taking the listed accuracy of the pressure transmitter:

$$P_{sens\_err} = P \times Err_{accuracy} = 0.005 \times P \qquad (39)$$

The cumulative error is then:

[30] Ametek ATC650B

$$P_{err} = \sqrt{{P_{DAS\_err}}^2 + {P_{sens\_err}}^2} \quad (40)$$

For the range of values measured in the PRECISE facility, the pressure error varies linearly from 0.0145 at 1 bar to 0.096 at 10 bars.

4.2.3 Heating voltage / current

Power delivered to the PRECISE facility was set through JUMO TYA 201 power controller. According to the manufacturer's data sheet, the error for the setpoint current and voltage are both 1%. Therefore, the overall delivered electrical power error is:

$$Pow_{err} = \sqrt{{U_{evap\_err}}^2 + {I\_evap\_err}^2} = \sqrt{1\%^2 + 1\%^2} = 1.41\% \quad (41)$$

4.2.4 Volumetric flow

Volumetric flow data was acquired using the same current module NI9208 as pressure, hence:

$$\begin{aligned} \dot{V}_{cl\_DAS\_err} &= \dot{V}_{cl} \times Err_{gain} + Err_{offset} \\ &= 0.0076 \times \dot{V}_{cl} + 0.0004\ [m^3/h] \end{aligned} \quad (42)$$

Secondly, taking the listed accuracy of the Yokogawa YEWFLOW unit:

$$\dot{V}_{cl\_sens\_err} = \dot{V}_{cl} \times Err_{accuracy} = \dot{V}_{cl} \times 0.0075 \quad (43)$$

The cumulative absolute error is then:

$$\dot{V}_{cl\_err} = \sqrt{{\dot{V}_{cl\_DAS\_err}}^2 + {\dot{V}_{cl\_sens\_err}}^2} \quad (44)$$

For the range of values measured in the PRECISE facility, the coolant volumetric flow error varies linearly from 0.0155 at 1 m^3/h to 0.0578 at 5 m^3/h.

4.2.5 Heat flux

Heat flux sensors installed in the PRECISE facility are, as described in the chapter 3.3, a novel and experimental device produced by prof. Andrey Mityakov in small quantities. Therefore, each batch of sensors can exhibit considerable variation in final performance and thus no established data sheet for the sensors exists. Taking this into account, in this work the sensors are treated as voltage sources which must be calibrated to properly correlate the measured output to the heat flux values, as described in the section 3.3.2. Heat flux is then calculated using the formula:

$$\dot{Q} = \frac{E}{A \times s_0} \quad (45)$$

where E is the measured output of the sensor, A is the sensor area and Q is the heat flux passing through the sensor. From the eq. (45), to quantify the resulting heat flux measurement error three main factors must be considered:

1. The accuracy of each sensor's sensitivity factor obtained through the calibration procedure
2. Estimation of each sensor's area
3. Measurement error of DAS

To begin with estimating the first source of error, each heat flux sensor sensitivity is calculated according to the rearranged eq. (45):

$$s_0 = \frac{E}{A \times \dot{Q}} \tag{46}$$

Each of these quantities contributes to the overall error, and since the equation contains only multiplication and division operations, the overall sensitivity error can be calculated as follows:

$$s_{0\_err} = \sqrt{{E_{err}}^2 + {A_{err}}^2 + {\dot{Q}_{err}}^2} \tag{47}$$

The sensor measured output error can be defined as the accuracy of the Keithley mustimeter[31] used to record the signal. According to the manufacturer's data sheet, it can be assumed as better than 0.1 % for signals below 1 Hz. In these measurements the DC component of the signal was investigated, thus E_{err_rel}=0.1% was assumed as the worst-case value.

The sensor area was calculated based on photographs taken with Leica DFC320 digital camera attached to the Leica MZ16 stereomicroscope. The resolution / pixel size of pictures taken was about 9 μm. The calculation of the area was done in the dedicated MZ16 software and was based on tracing the edge of the sensor photographed on a wider background and integrating the number of pixels, Figure 4-1.

Figure 4-1 Example of GHFS optical area measurement and in-software sensor edge tracking

[31] Keithley Model 2001 7½-Digit Multimeter, resolution down to 0.1μV

The source of error when counting pixels belonging to the photographed sensors outlines can be traced to the recognized boundary. For the sensor shown in Figure 4-1 the estimated boundary length was 38.4318 mm, thus it was composed of approximately 4269 individual pixels. The total area of boundary pixels is 0.3458 mm² versus the estimated sensor area of 81.6386 mm², or about 0.42%. Since there was some variation of this value for each of the sensors measured, the value of 0.45% was defined as a good enough but slightly overestimated area measurement error.

Finally, the error of the heat flux value can be derived from the accuracy of used heat delivery system, as described in the chapter 4.2.3. The delivered amount of heat was set with a JUMO TYA 201 power controller. According to the manufacturer's data sheet, the error for the setpoint current and voltage are both 1%. The delivered heat was converted to heat-flux basing on the calculated inner area of the calibration tube (see Figure 3-8). The error associated with this area can be attributed to the manufacturing tolerances, defined as 0.1 mm for diameter and length, resulting in 0.51% of the total value. Resulting total area of over which the delivered heat was distributed can be then defined as:

$$\dot{Q}_{err} = \sqrt{1\%^2 + 1\%^2 + 0.51\%^2} = 1.5\% \qquad (48)$$

Finally, the sensitivity error is:

$$s_{0\_err} = \sqrt{0.1\%^2 + 0.45\%^2 + 1.5\%^2} \approx 1.57\% \qquad (49)$$

Recorded sensitivity values vary as a function of sensor's temperature (Figure 3-11). Therefore, measurement of the HFS temperature is another source of heat flux estimation error. Each GHFS is accompanied by a calibrated thermocouple, which measurement error is defined by the eq. (37). Thus, for each sensor a second order polynomial defining $s_0(T)$ is calculated, (Figure 3-11). Checking the sensitivity of this polynomial to inaccurate temperature measurement of 1.006 K, yields additional sensitivity error of up to 0.7%. Incorporating this value in the overall expression yields:

$$s_0(T)_{err} = \sqrt{1.57\%^2 + 0.7\%^2} \approx 1.72\% \qquad (50)$$

The second main source of error of the heat flux measurement comes due to the measurement of HFS signal in the facility. Each of the four channels of NI-9215 DAS is accompanied by custom, two-stage amplifier designed to provide 10000 gain. Performance of each amplifier was assessed to verify whether a nominal gain value was achieved for each channel. For this purpose, high accuracy Keithley multimeter[32] was used to measure the output of every amplifier. DC signal of known amplitude was provided via a signal generator with claimed resolution of 0.001 mV. As a reference, the non-amplified signal was also measured. Obtained values were then used to calculate gain error, Figure 4-2.

[32] Keithley Model 2001 7½-Digit Multimeter, resolution down to 0.1μV

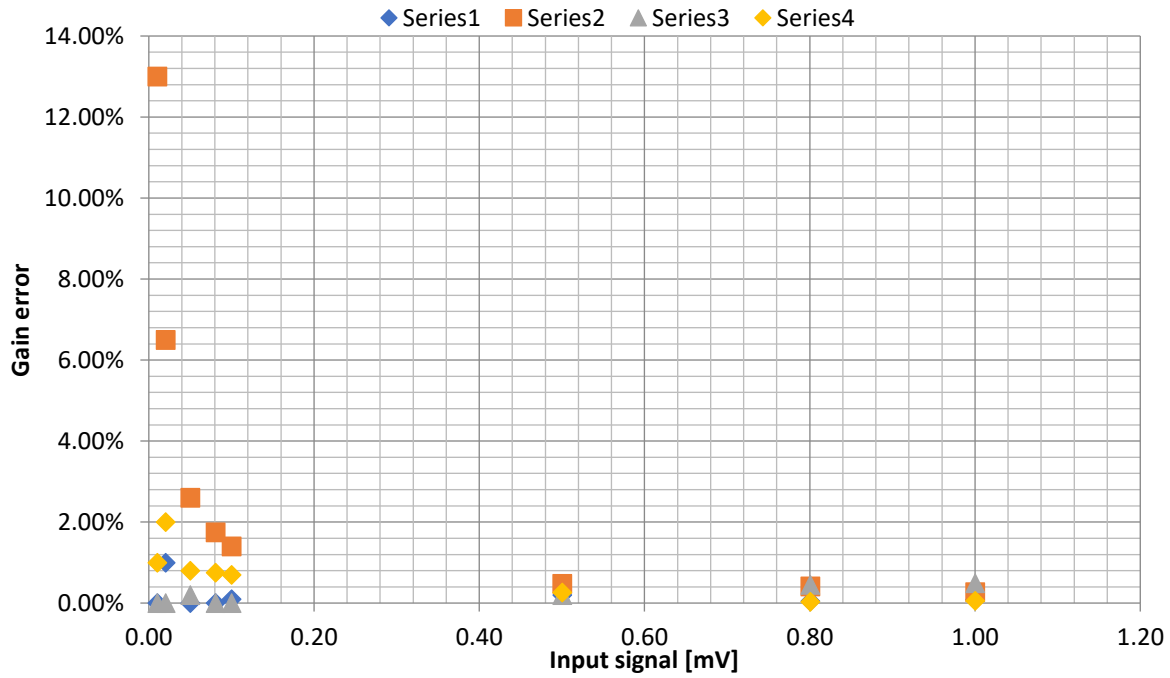

Figure 4-2 Calculated amplifier gain error for each of four measurement channels

For very low signals <20μV one of the amplifiers exhibited quite large errors up to 13%. Every other amplifier gain was within +/- 2% of the nominal value. Such very low signals were not expected during steam condensation, and as such, the gain error value of 2% was considered an accurate estimate. Including the error coming from the NI-9215, it can be estimated according to the formula:

$$E_{DAS\_err} = E \times Err_{gain} + Err_{offset} = 0.0002 \times E + 0.001456\ [V] \quad (51)$$

For the range of voltages measured in the PRECISE facility, 100% of cases fall below 1% error due to NI-9215 card accuracy. Therefore, overall DAS and amplification error can be summarized as:

$$E_{DAS\_total\_err} = \sqrt{2\%^2 + 1\%^2} \approx 2.24\% \quad (52)$$

With the last error source, all parameters can be considered together. Since eq. (45) consists of only division/multiplication operations, heat flux error can be calculated according to the following formula:

$$\dot{Q}_{err} = \sqrt{{s_{0\_err}}^2 + {A_{err}}^2 + {E_{DAS\_total\_err}}^2} = \sqrt{1.72\%^2 + 0.45\%^2 + 2.24\%^2} \approx 2.86\% \quad (53)$$

4.2.6 Film thickness

4.2.6.1 Fixed electrode array

As is the case with the heat flux sensors, the film thickness probe is a new and experimental device, and as such its accuracy had to be established through the employed calibration procedure, described in

detail in the section 0. Each electrode response was measured by a NI-9215 card, but without the amplification stage employed for HFS described in the previous section. The error coming from the measurement can be estimated according to eq. (51), and for the range of voltages measurable by the electrode array (0-10V) varies from 0.001456 to 0.003456 V. Considering previously obtained calibration curves (Figure 3-41), in the region with highest slope - the worst case - voltage measurement error translates to +/-0.082 mm for the central electrode, +/-0.017 mm for side electrode and +/- 0.929 mm for top-most electrode.

Additionally, during the calibration procedure, the reference thickness of the liquid film was controlled with a piston attached to a manual micro-meter screw. The "zero" position of the piston was established by contact with the inner tube's wall. As such, the accuracy of the reference film was very easily controllable with resolution equal to that of the used screw, thus 0.05 mm.

Overall, the error of the calibration procedure can be summarized as:

$$\delta_{film\_calib\_err} = \sqrt{{\delta_{film\_DAS\_err}}^2 + {\delta_{film\_screw\_err}}^2} \tag{54}$$

For each electrode the resulting calibration curve errors are presented in the Table 4-3.

Table 4-3 Calibration curve error summary for the fixed electrode array

Electrode	Calibration curve error:
Center	0.096 mm
Side	0.053 mm
Top	0.931 mm

Due to the very low signal obtained with the top electrode, the value of error was extremely significant. Results presented in the following chapters were composed without relying on this electrode.

Incorporating the measurement error of NI-9215 card acquired during the experiments together with the calibration curve error, the overall error can be expressed as:

$$\delta_{film\_err} = \sqrt{{\delta_{film\_calib\_err}}^2 + {\delta_{film\_DAS\_err}}^2} \tag{55}$$

Table 4-4 Overall measurement error of the fixed electrode array

Electrode	Film thickness error
Center	0.126 mm
Side	0.055 mm
Top	1.315 mm

Overall, calculated uncertainties for the electrode array make it clear that only the side and center electrodes can provide useful signals. In terms of the expected thicknesses of the condensate film, which can range anywhere from close to zero up to 1 / 1.5 mm, it is clear that, especially for thinner films, the measurement error can easily match the signal values. Thus, any data acquired with the electrode array has to be treated with caution, due to possible poor signal-to-noise ratio.

4.2.6.2 Traversing thermocouple

A secondary measure of film thickness is derived from the voltage signal measured on the shielding of the traversing thermocouple. As soon as electrical connection is made between the thermocouple and water on top of the electrode array, a response should be observable in the reading. The thermocouple is actuated with a stepper motor[33] controlled via NI SMD-7610 stepper drive control and NI-9512 Stepper Drive Interface Module. According to the data sheet, the spatial resolution of the stepper motor is 0.041 mm/step travel. Along the traversing length of 20 mm with a step size of 0.1 mm, in the worst case, this error could accumulate up to 8.2 mm. However, end switches provide means to eliminate the extended error accumulation over multiple cycles. Moreover, such extensive error accumulation, that would present itself as a steep jump in position reading as soon as an end-switch would activate, was never observed in the collected data, Figure 4-3 .

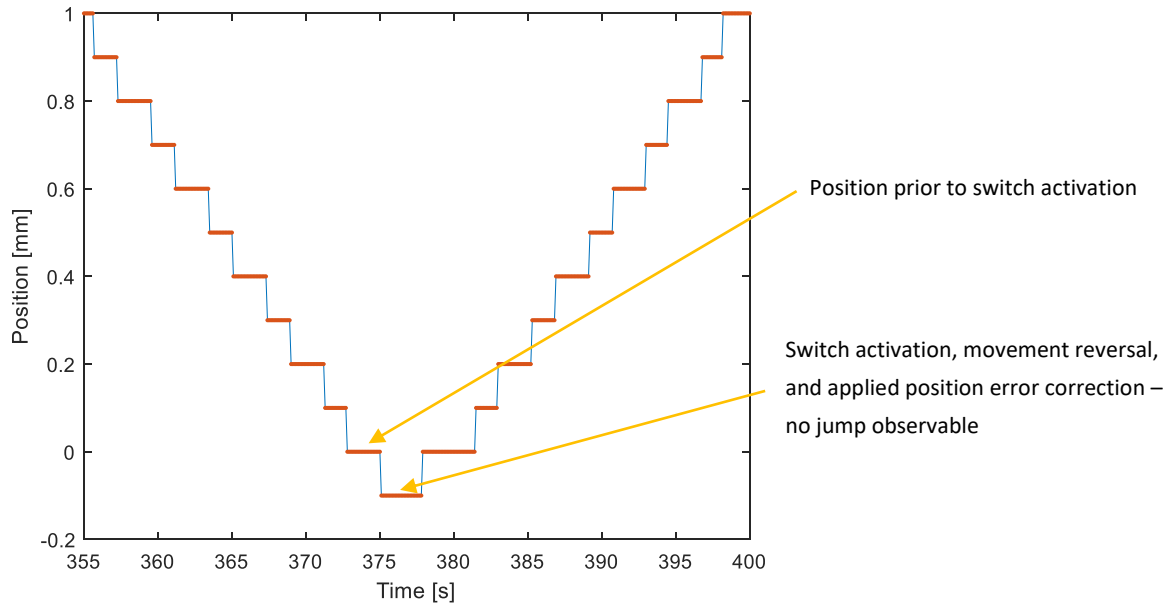

Figure 4-3 Typical observed probe position behavior at the end switch location

Theoretical spatial resolution of the traversing thermocouple can thus be quantified as 0.041 mm step size of the stepper motor. However, during the operation, huge quantities of electrical noise were recorded, and only with extensive filtering any meaningful signal could be restored (chapter 3.4.5.1). Moreover, the observed voltage signal did not present the expected step response at liquid film contact, but rather a gradual increase. This effect could be to some extend explained by capacitive coupling between the thermocouple shielding and the liquid film. Similar behavior was observed in temperature data, with gradual decrease in recorded values starting at approximately 2 mm away from the wall down to a minimum at the wall contact. The decrease can be attributed partially to the thermal boundary layer developed on top of the liquid film and partially to the lower temperature of the film itself. Thus, detection of the film interface and its distinction from the thermal boundary layer using either voltage or temperature signal was not possible.

[33] Johnson Electric UCL53 Linear Stepper Motor

4.3 Derived properties errors

Every other property presented in this work is derived from the abovementioned six basic measurements. Some of these properties (e.g. ΔT, coolant velocity) could have been easily and directly calculated and thus error propagation for these is straightforward. Assuming Y is the derived property from parameters a, b, c, …, z, if the formula is a combination of sum or differences following the template formula:

$$\delta Y = \sqrt{\delta a^2 + \delta b^2 + \delta c^2 + \cdots + \delta z^2} \tag{56}$$

Where δY is the derived property Y absolute error and $\delta a, \delta b, \ldots, \delta z$ are the constituent parameters individual absolute error contributions. Alternatively, if the calculation involved only multiplication / division:

$$\frac{\delta Y}{Y} = \sqrt{\frac{\delta a^2}{a} + \frac{\delta b^2}{b} + \frac{\delta c^2}{c} + \cdots + \frac{\delta z^2}{z}} \tag{57}$$

Where each $\frac{\delta x^2}{x}$ term can be understood as a relative or fractional error (expressible in percentages). If constant C were involved in the derivation, the error propagated simply as:

$$\delta Y = C \times \delta a \tag{58}$$

In more complex situations, the derived property Y can be viewed as a general function F of possible multiple observables a, b, c, … i.e. F(a, b, c, …). In those cases, the error was obtained by calculating partial derivatives with respect to each of them and the following addition:

$$\delta Y = \sqrt{\left(\frac{\partial F}{\partial a} \times \partial a\right)^2 + \left(\frac{\partial F}{\partial b} \times \partial b\right)^2 + \left(\frac{\partial F}{\partial c} \times \partial c\right)^2 + \cdots} \tag{59}$$

This was the case when derived properties required the use of steam-water tables (e.g. water density, steam heat capacity). For highest possible accuracy, relations established by The International Association for the Properties of Water and Steam (IAPWS) latest recommended formulation (2008 Revised IAPWS-IF97) were used. Since the PRECISE facility data was processed using Matlab, specific implementation written in this programming language developed by Mark Mikofski and distributed freely through MathWorks File Exchange platform[34] was used.

For some of the properties partial derivatives were readily available to calculate using the provided functions, and thus the eq. (59) was followed. For others however, the partial derivatives of IAPWS functions were not available. Likewise, for calculation of NC gas content in the PRECISE facility a complex set of iterative functions was used and direct approach to error propagation was not applicable.

[34]Downloaded from: https://uk.mathworks.com/matlabcentral/fileexchange/35710-iapws_if97-functional-form-with-no-slip?focused=3841004&tab=example (accessed 05.10.2015)

Assuming again that Y is the derived property, and requires use of operation O taking observable a as an argument:

$$\begin{aligned} Y &= O(a) \\ Y + \delta Y &= O(a + \delta a) \\ \delta Y &= O(a + \delta a) - Y \end{aligned} \tag{60}$$

where δY is the derived property error and δa is the observable's error. Taking δa as a reference change in the observable property is reasonable, as this is the actual source of uncertainty in the derived property. In case of multiple observables involved in Y derivation partial differences with respect to each of the parameters were calculated, while keeping the other constant

$$\begin{aligned} \frac{\Delta F}{\Delta a} &= \frac{O(a + \delta a, b, c, \dots) - Y}{\delta a} \\ \frac{\Delta F}{\Delta b} &= \frac{O(a, b + \delta b, c, \dots) - Y}{\delta b} \\ \frac{\Delta F}{\Delta b} &= \frac{O(a, b, c + \delta c, \dots) - Y}{\delta c} \\ &\dots \end{aligned} \tag{61}$$

Then, the overall error was calculated according to modified eq. (59):

$$\delta Y = \sqrt{\left(\frac{\Delta F}{\Delta a} \times \delta a\right)^2 + \left(\frac{\Delta F}{\Delta b} \times \delta b\right)^2 + \left(\frac{\Delta F}{\Delta c} \times \delta c\right)^2 + \cdots} \tag{62}$$

Table 4-5 presents the overview of the derived properties, including which observables / properties were used to calculate the values and which formula was followed.

Table 4-5 Summary of errors associated with properties derived from the PRECISE facility experimental data

Subject	Derived property	Symbol	Unit	Formula	Error range absolute	Error range relative
Coolant water	Temperature increase	ΔT_{cl}	$°C$	$T_{in} - T_{out}$	0.071	9.054 - 112.1%
	Density	ρ_{cl}	kg/m^3	$IAPWS(T_{cl}, P_{cl})$	0.0002 - 0.0028	0.00026 - 0.0003%
	Mass flow	$\dot{m}_{cl}$	kg/h	$\rho_{cl} \times \dot{V}_{cl}$	9.8 - 40	1.6%
	Enthalpy	H_{cl}	kJ/kg	$IAPWS(T_{cl}, P_{cl})$	0.13 - 0.14	0.024 - 0.032%'
	Specific heat capacity	C_{P_cl}	$J/kg * K$	$IAPWS(H_{cl}, P_{cl})$	4.20e-05 - 7.20e-05	1.00e-06 - 1.69e-06%
	Removed heat	P_{cl}	W	$\frac{\dot{m}_{cl}}{3600} \times C_P \times \Delta T_{cl}$	-140.6 - 277.8	6.7 - 69.3%
	Dynamic viscosity	v_{cl}	$Pa * s$	$IAPWS(T_{cl}, P_{cl})$	5.01e-08 - 9.21e-08	0.025 - 0.033%

	Kinematic viscosity	μ_{cl}	$m^2/_s$	ν_{cl}/ρ_{cl}	5.39e-11 - 9.62e-11	0.025 - 0.033%'
	Thermal conductivity	λ_{cl}	$W/_{m*K}$	$IAPWS(T_{cl}, P_{cl})$	2.72e-06 - 1.30e-05	0.0004 - 0.0019%
	Prandtl number	Pr_{cl}	$-$	$C_{P\_cl} \times \nu_{cl}/\lambda_{cl}$	0.032 - 0.070	0.96 - 1.03%
	Reynolds number	Re_{cl}	$-$	$V_{cl} \times \rho_{cl} \times D_{H_{cl}}/\nu_{cl}$	11.41 - 44.97	0.1%
	Velocity	V_{cl}	$m/_s$	$\frac{\dot{V}_{cl}}{3600}/A_{cl}$	0.011 - 0.042	1.07%
Coolant water	Heat transfer coefficient Dittus-Boelter correlation	h_{cl_DB}	$W/_{m^2*K}$	$0.023 \times Re_{cl}^{0.8} Pr_{cl}^{0.4} \times \frac{\lambda_{cl}}{D_{H_{cl}}}$	0.012 - 0.035	0.003%
	Heat transfer coefficient Gnielinski correlation	h_{cl_GN}	$W/_{m^2*K}$	$\frac{\frac{f}{8}(Re-1000)Pr}{1+12.7\left(\frac{f}{8}\right)^{0.5}\left(Pr^{\frac{2}{3}}-1\right)} \times \frac{\lambda_{cl}}{D_{H_{cl}}}$ where $f = \sqrt{(0.79 log_n(Re) - 1.64)}$ [35]	9.47 - 29.20	2.47 %
	Heat transfer coefficient laminar flow correlation	h_{cl_L}	$W/_{m^2*K}$	$7.37 * \kappa_{cl}/D_{H\_cl}$	0.0003-0.0012	0.0004 - 0.0019%
	Boiling point	T_{boil}	$°C$	$IAPWS(P)$	0.35 - 0.39	0.24 - 0.31%
	Enthalpy - gaseous phase	H_{gas}	$kJ/_{kg}$	$IAPWS(P)$	0.40 - 0.47	0.015 - 0.017%
	Enthalpy - liquid phase	H_{liq}	$kJ/_{kg}$	$IAPWS(P)$	1.51 - 1.70	0.24 - 0.32%
	Evaporation heat	ΔH_{vap}	$J/_{kg}$	$(H_{gas} - H_{liq}) * 1000$	1581 - 1745	0.073 - 0.083%
	Evaporation power	P_{evap}	W	$U_{evap} * I_{evap}$	4.67 - 25.92	1.41%
Steam	Evaporation mass flow	$\dot{m}_{evap}$	$kg/_s$	$P_{evap}/\Delta H_{vap}$	2.16e-06 - 1.23e-05	1.42%
	Density	ρ	$kg/_{m^3}$	$IAPWS(P, T)$	0.00021 - 0.00307	0.01 - 0.23%
	Evaporation volumetric flow	$\dot{V}_{evap}$	$m^3/_s$	$\dot{m}_{evap}/\rho$	9.81e-07 - 9.38e-06	1.42 - 1.44%
	Velocity	V	$m/_s$	$\dot{V}_{evap}/A$	0.0028 - 0.0270'	1.42 - 1.44%

[35] Darcy friction factor calculated with the Petukhov correlation for smooth tubes

Tube wall	Local wall ΔT	ΔT_{wall}	$°C$	$T_{wall\_in} - T_{wall\_out}$	2.001	6.78 - 12.09%
	Wall thermal conductivity	λ_{steel}	$W/_{m*K}$	$0.0117 * \frac{T_{wall_{in}} + T_{wall_{out}}}{2} + 13.7431$ [36]	0.017	0.11%
	Wall heat transfer coefficient	h_{tc_wall}	$W/_{m^2*K}$	$\frac{\lambda_{steel}}{R_{in} * \ln(\frac{R_{out}}{R_{in}})}$	0.017	0.00043 - 0.00045%
	Local wall heat flux	$\dot{Q}_{wall}$	$W/_{m^2}$	$\Delta T_{wall} * h_{tc\_wall}$	51.31 - 2066	6.78 - 12.09%

[36] 1st order polynomial fit for steel 1.4404 properties obtained from engineering source (accessed 03.03.2013): http://www.ssina.com/composition/temperature.html

Chapter 5 Experiments

This section summarizes the types of experiments conducted in the PRECISE facility. A detailed description of the experiments as well as the procedures is provided.

5.1 General description

Two types of experiments were conducted in the PRECISE facility – steady state tests (S-ST) and continuous injection tests (C-IN). In tests of the first type, a known amount of NC gas was fed to the primary circuit, the set point pressure was defined along with coolant water temperature and flow rate. The heater was started, and the facility would heat up to reach the setpoint value. After the pressure remained stable for a period of at least 30 minutes quasi-steady state was identified and data was recorded.

For this type of experiments, the following test parameters were varied:

- Test tube pressure
- Average NC gases mole fractions in the test tube (introduced during set up of a test run)
- NC gas mixture composition (pure N_2, pure He, a mixture of the two)
- Steam flow in the test tube (by means of varying coolant mass flow and temperature)
- Temperature gradient across the test tube wall (by means of coolant water mass flow and temperature)

In the second type of experiments, continuous injection tests, initially no NC gas was fed to the primary circuit and only after the steady state was reached with pure steam, a valve connecting primary circuit to NC gas tank was opened. The overpressure NC gas tank ensured that gas was fed into the test tube and the average mole fraction of steam would decrease continuously. The experiment would last until no condensation was observed in the tube anymore. The data was collected for the whole time the gas was being fed.

For this type of experiments, the following test parameters were varied:

- Test tube pressure
- NC gas mixture composition
- Pressure in the NC gas tank
- Valve opening between the NC gas tank and the test tube

5.2 Experimental procedures

The following summarizes the sequence of actions taken during each type of experiments. Each step is described in detail to explain its purpose.

5.2.1 Steady state tests

The Sequence of experimental steps:

1. Preconditioning the coolant water in the cooling / heating loop (CH loop) in bypass mode
2. Venting the facility with the use of a vacuum pump
3. Filling demineralized water into the water tank

4. Filling demineralized water from water tank into the heater tank
5. Filling a calculated amount of Helium / Nitrogen to the intermediate NC gas volume
6. Filling the NC gas mixture to the heater tank
7. Redirecting the coolant water to the coolant jacket
8. Setting the desired test pressure and starting the main heater
9. Acquiring data once the steady state was achieved

To begin with, the CH loop is set in a bypass mode to allow to run it separately from the rest of the facility (Figure 5-1, left). In this mode, the desired temperature is entered through the control panel. In case of test runs with a coolant water temperature over 100˚C, higher than atmospheric pressure is required to avoid boiling. This is accomplished by manually adding pressurized nitrogen to the water storage tank until the desired pressure is reached. After the CH loop heat-up, the pressure is verified and in case of a deviation from the desired value, nitrogen is added or released accordingly.

While the coolant water is heating up, the rest of the facility is prepared for the experiment. First, all volumes (test tube with heater tank, water tank and NC gas tank – if NC gases are used in the experiment) are emptied using a vacuum pump (Figure 5-1, right). The residual pressure is monitored by means of a pressure gauges as well as with pressure transducers connected to the data acquisition system of the test facility. After reaching satisfactory vacuum levels (less than 0.01 bar residual pressure), all valves connecting the different volumes are shut off, while relevant pressures are continuously monitored to verify that no air ingress occurs.

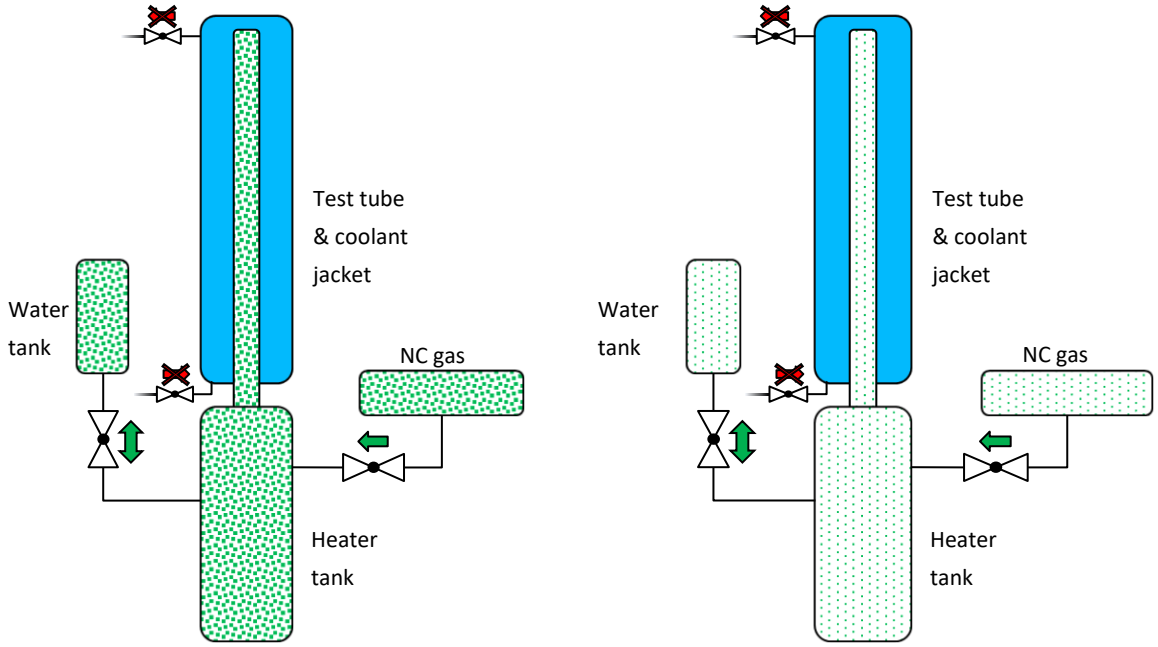

Figure 5-1 Experimental procedure, steps 1 and 2

As a next step, demineralized water is filled in the water tank, until it overflows (Figure 5-2, left). The overflow valve is connected to the highest point of the tank, which ensures that no air pockets remain in this volume. Afterwards, the valve connecting the water tank and the heater tank is opened, and water flows to the latter (Figure 5-2, right). The water level is monitored with a water level indicator in the heater tank. Once it stabilizes, it is verified that an appropriate amount was fed into the facility and the connection to the water tank is closed.

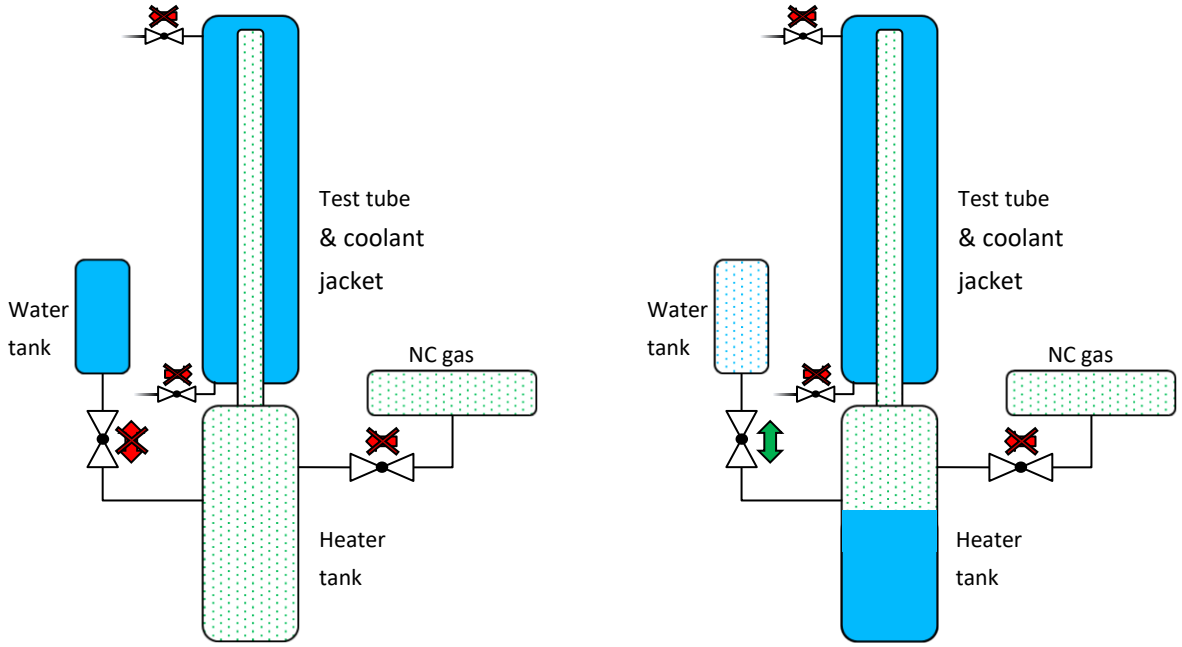

Figure 5-2 Experimental procedure, steps 3 and 4

In case the tests include NC gases, two additional steps are performed. First, the NC gases tank is filled with previously calculated amounts of N_2, He or a mixture of both (Figure 5-3, left). The amount of gas fed is monitored with pressure and temperature readings. A MATLAB script was developed that, based on the desired tests conditions, calculates the appropriate pressure levels to which NC gas tank must be filled with each gas species. After this is completed, the valve connecting NC gas tank and the heater tank is opened and some time is allowed for the pressure to stabilize (Figure 5-3, right) and then the connection is severed. The pressure and temperature readings from the NC gas tank are recorded throughout the procedure for the verification of the final amount of gas used in the experiment. It is important to mention, that since this calculation uses some idealized assumptions and depends on pressure and temperature measurements which carry an error, as well as on the manual operation of valves, the verification step was important to achieve a reliable value of actual molar composition of the gas mixture in the experiment. The details of employed script and filling procedure are explained in section 5.3.

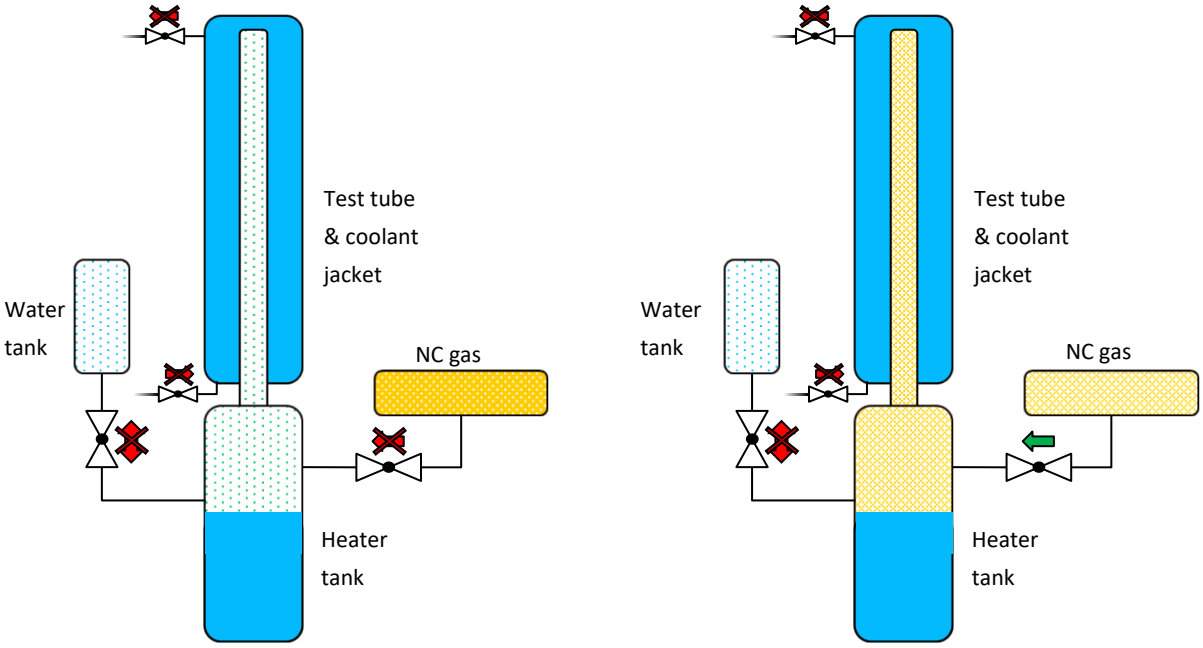

Figure 5-3 Experimental procedure, steps 5 and 6

When the cooling water has reached the desired temperature, the flow is redirected towards the cooling jacket around the test tube. The desired experiment pressure is entered in the control software and electrical heater starts. In the early phase of the experiment the coolant water, usually at a higher temperature then the ambient, helps to heat up the facility initially, reducing the start-up time. Nevertheless, 60 to 90 minutes were allowed for the facility to reach operating conditions and for all temperatures to settle. In these quasi steady-state conditions (Figure 5-4), the data acquisition was started.

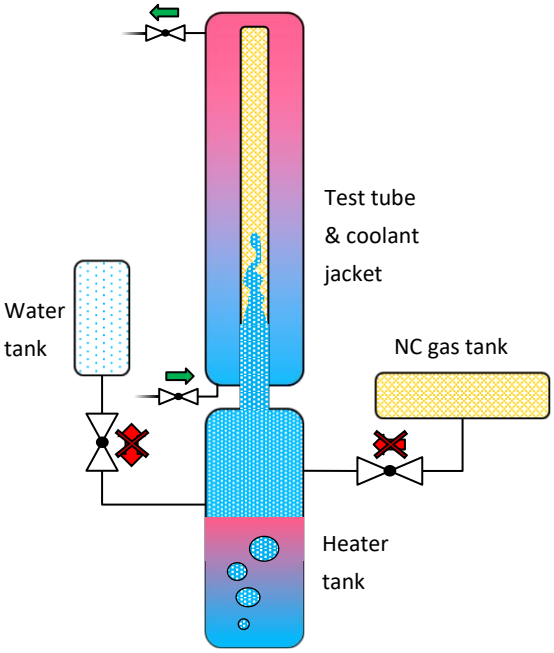

Figure 5-4 Experimental procedure, steps 7 through 9

5.2.2 Continuous injection tests

Summary of experimental steps:

1. Preconditioning the coolant water in the cooling / heating loop in bypass mode
2. Venting the appropriate volumes with the use of vacuum pump
3. Filling demineralized water to the water tank
4. Filling demineralized water from water tank to the heater tank
5. Filling NC gas tank to a pressure level 0.5 bar higher than facility operating pressure.
6. Redirecting the coolant water to the coolant jacket
7. Setting the desired test pressure and starting the main heater
8. Once steady state was reached, start the NC feeding and acquire data

When compared to the steady state tests, most of the experimental steps were also used during the continuous injection tests. The procedures start to diverge after the heater tank is filled with demineralized water. In these tests, the NC gas tank is filled with the desired gas to a pressure level slightly higher (0.5 bar) than the experiment operating pressure in the facility, instead of a previously precisely calculated value. Additionally, the NC gas is not immediately fed in the facility.

The slight difference allowed for a well-controlled and a stable continuous flow of NC gas into the facility during the test. Additionally, a low overpressure allowed to slow down the process, which then could have been precisely monitored. Finally, the overpressure as well as a one-way valve installed between the two volumes, ensured a flow of gas in only one direction – into the experimental volumes. After preparing the NC gas water is redirected towards the cooling jacket, the desired test pressure is set, and the heater is started, as with was the case with the steady state tests. When steady state conditions are reached, the data acquisition is engaged, and the valve connecting NC gas tank to the heater tank is opened. The NC gas enters the facility with a small well-reproducible flow rate and is carried with the flow of steam and accumulated at the top of the test tube, forming a plug (Figure 5-5). The plug continuously grows downwards, and the test is stopped as soon as the full volume of the test tube is filled with NC gas. This state is indicated by the observed end of the condensation process. This process usually takes between 30 to 45 minutes.

The continuous NC gas allow to observe the temperature profile at the boundary between the NC plug and the vapor-rich region with stationary sensors, as this boundary moves slowly downwards during the NC gas feeding. From a known velocity of the front and the time history of the temperature, the axial profiles of temperature, heat flux and film thickness. Moreover, under the assumption of a local thermodynamic equilibrium, the profile of the molar fraction of NC gas can be extracted from the experimental data.

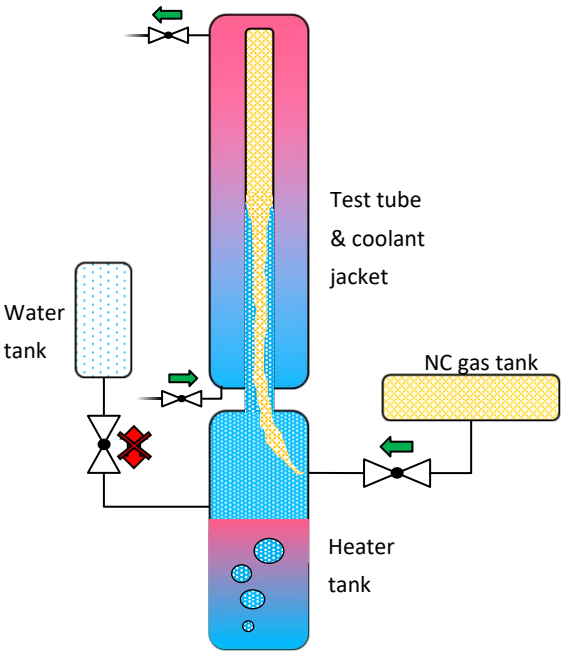

Figure 5-5 Continuous injections tests - NC gas injection and gas plug growth

5.3 NC gases pre- and post-calculation

5.3.1 Pre-calculation procedure

One of the parameters varied during steady sate experiments is the average mole fraction and species of the non-condensable gas present in the test tube. Reproducible conditions are achieved by filling the test tube with a known amount of NC gas prior to starting the experiment. After specified values are reached, observed temperature and pressure along with the a priori set amount of NC gas are sufficient to calculate the average molar fractions. Moreover, since the gas is not evenly distributed in the test tube, the recorded temperature gradients along the height of the tube allowed to identify regions in which NC gas would accumulate.

To achieve sufficient precision, NC gases were not directly fed to the test facility, but instead an intermediate volume – the NC gas tank – was used to act as a buffer, in which the gas mixture could be precisely preconditioned. All the necessary calculations are bundled together in a MATLAB script that takes the desired average mole fraction under test conditions, NC gas mixture species ratio and test pressure as an input and, as an output, produces the relevant pressure for each gas mixture subspecies to be filled in the NC gas tank.

The detailed calculation algorithm to determine the partial pressures of the NC gas species is shown in Figure 5-6. The algorithm follows, in reverse, the experimental steps 8, 6 and 5 of the steady state tests. For each step, it calculates temperature, pressure and molar composition of gas present in the experimental volumes (steps 8 and 6) and the NC gas tank (steps 6 and 5). The script starts calculating at experimental conditions input by the user and then calculates the would-be preceding conditions when the facility is fully primed, but the heating was not yet engaged, the pressure is low, and the temperature is close to ambient.

The calculation considers that when reversing back to conditions before heating, a significant portion of steam condenses. Two significant assumptions are made at this point:

a) Before heating is engaged, the interior of experimental volumes is at thermodynamic equilibrium and steam is at saturation conditions
b) Before heating is engaged, the interior of experimental volumes is at ambient temperature, the assumed temperature is 20℃
c) NC gas is not accumulating in the water during condensation

In practice, the script continually removes a portion of steam from the domain and based on a chosen equation of state (EOS), recalculates the resulting pressure, temperature and molar composition. When the resulting temperature reaches 20˚C within a +0/-0.0001 uncertainty interval, this step is finished, and the final values are stored for further computations.

As a next step, the obtained pressure is assumed to be the pressure present in the NC tank after NC gases were fed to the experimental volumes. Based on this pressure, the volume and the assumed ambient temperature of 20˚C, as well as the desired molar composition of NC gas mixture, the number of moles of every species present in the tank is calculated.

The final step is to sum the number of moles for every NC gas species present in experimental volumes and NC gas tank and calculate the partial pressure for each of them at ambient temperature. These partial pressures are taken as a guide for filling the gas tank during the facility conditioning. An assumption made here is that all NC gas present in experimental volumes comes from the NC gas tank.

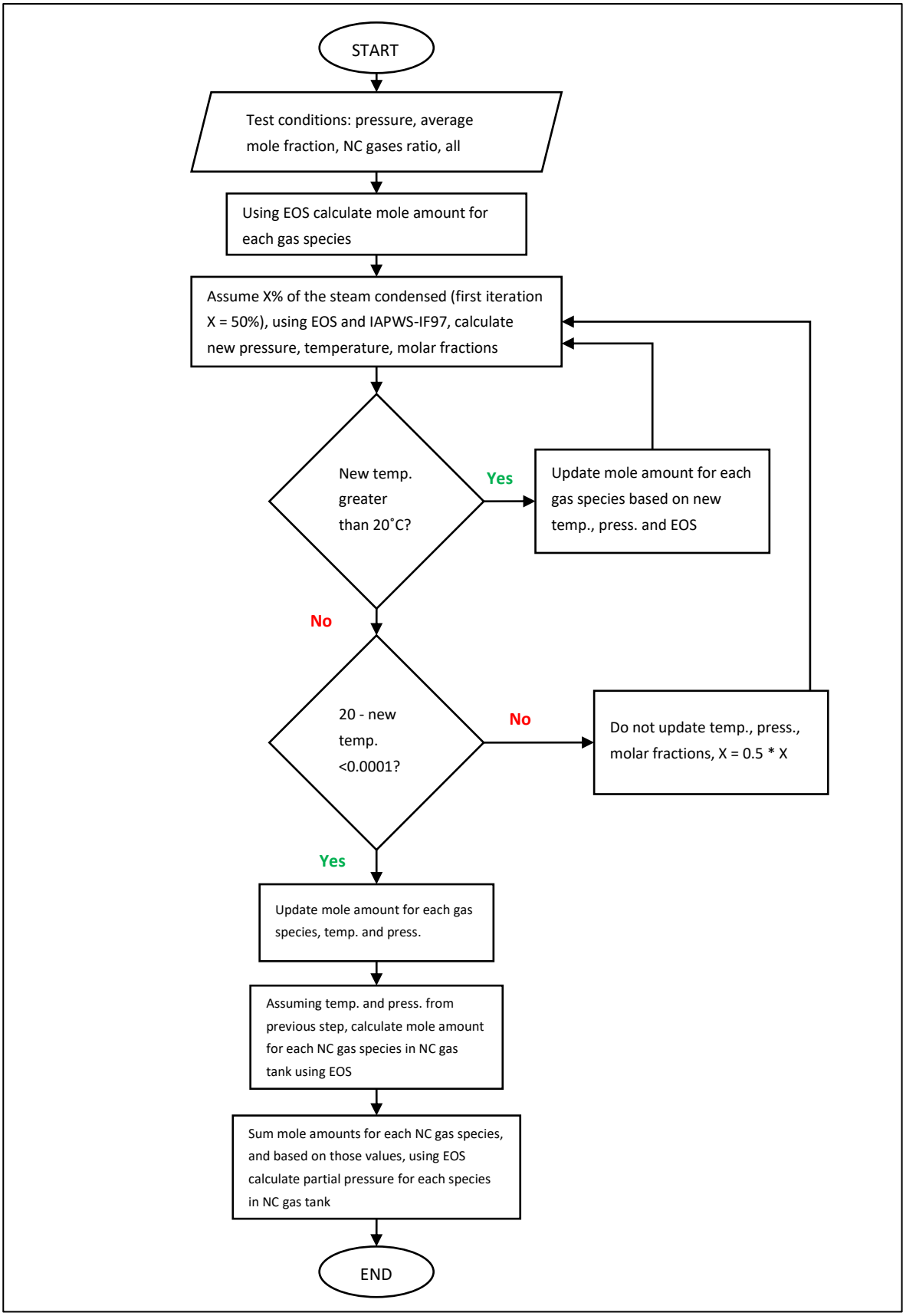

Figure 5-6 Algorithm of NC gas species partial pressures pre-calculation

5.3.2 Equation of state – discussion

As mentioned in the previous section, the script used to calculate the NC gases content relies on the usage of an equation of state for the gas mixture. Transcript of the code is in the appendix section 10.4. The script was written in such a way, that the user is able to easily substitute different equations without having to rewrite a significant portion of the code. To begin with, the ideal gas law was used, as given in (63):

$$PV = nRT \tag{63}$$

This basic equation is used to establish functions for pressure and temperature, based on remaining variables, which are then used in the code directly.

The ideal gas law was used as a first approximation. As a more accurate alternative, the Redlich-Kwong equation was tested. Especially for the vapor of water it is expected that its real gas behavior causes some uncertainties when the ideal gas equation is used. Redlich-Kwong is a two parameter, cubic equation, which was demonstrated to produce more accurate results than ideal gas low in some applications [228]. It is also sensitive to variation in composition of analyzed gas mixtures. The basic for of the equation is described in Eq. (64).

$$P = \frac{\bar{R}T}{V_m - b} - \frac{a}{\sqrt{T}V_m(V_m + b)} \tag{64}$$

where:

$$a = \frac{1}{9\left(\sqrt[3]{2} - 1\right)} \frac{\bar{R}^2 T_c^{2.5}}{P_c} \tag{65}$$

$$b = \frac{\sqrt[3]{2} - 1}{3} \frac{\bar{R}T_c}{P_c} \tag{66}$$

In Eq. (64) - (66), T_c and P_c stand for critical temperature and pressures for each gas species. Parameters a and b are dependent directly on the type of the gas. The a term represents the attractive forces between molecules and the b term represents the molecular volume. When the equation is applied to a mixture of gases, the terms a_i and b_i must be calculated for each species, and then these are used to calculate overall a and b values. In case of a, a first and a cross term is calculated for each pair of gas species present in the mixture (Eq. (67)) and then, the overall average is calculated, weighted by the species mole fractions for each pair X_i, X (Eq. (68)).

$$a_{ij} = \sqrt{a_i a_j} \tag{67}$$

$$a = \sum_i \sum_j X_i X_j a_{ij} \tag{68}$$

For the b term, an average weighted by respective mole fractions is calculated, Eq. (69).

$$b = \sum_i X_i b_i \tag{69}$$

It is important to mention here, that, due to the a and b parameters variation, the functions of pressure and temperature derived from the Redlich-Kwong equation change every time the composition of the gas mixture changes. In the presented case, when condensation was taken into account in the calculation,

the parameters a and b had to be recalculated at every step, which was considerably more computationally expensive compared to the simple ideal gas law.

Practical comparisons between the performance of both equations of state have shown an average discrepancy of less than 0.5% between the calculated values of the NC gases partial pressures. This uncertainty is reasonable, considering rather low temperatures and pressures encountered during the experiment. Ultimately, the Redlich-Kwong equation of state was used to perform conditioning calculations for the PRECISE facility.

5.3.3 Post-calculation procedure

The typical pressure and temperature behavior during steps 2,4,5 and 6 in the NC gas tank as well as in the experimental volumes (heater tank and test tube) is shown in Figure 5-7. As one can immediately note, there some discrepancies between the pre-calculated and the actual behavior.

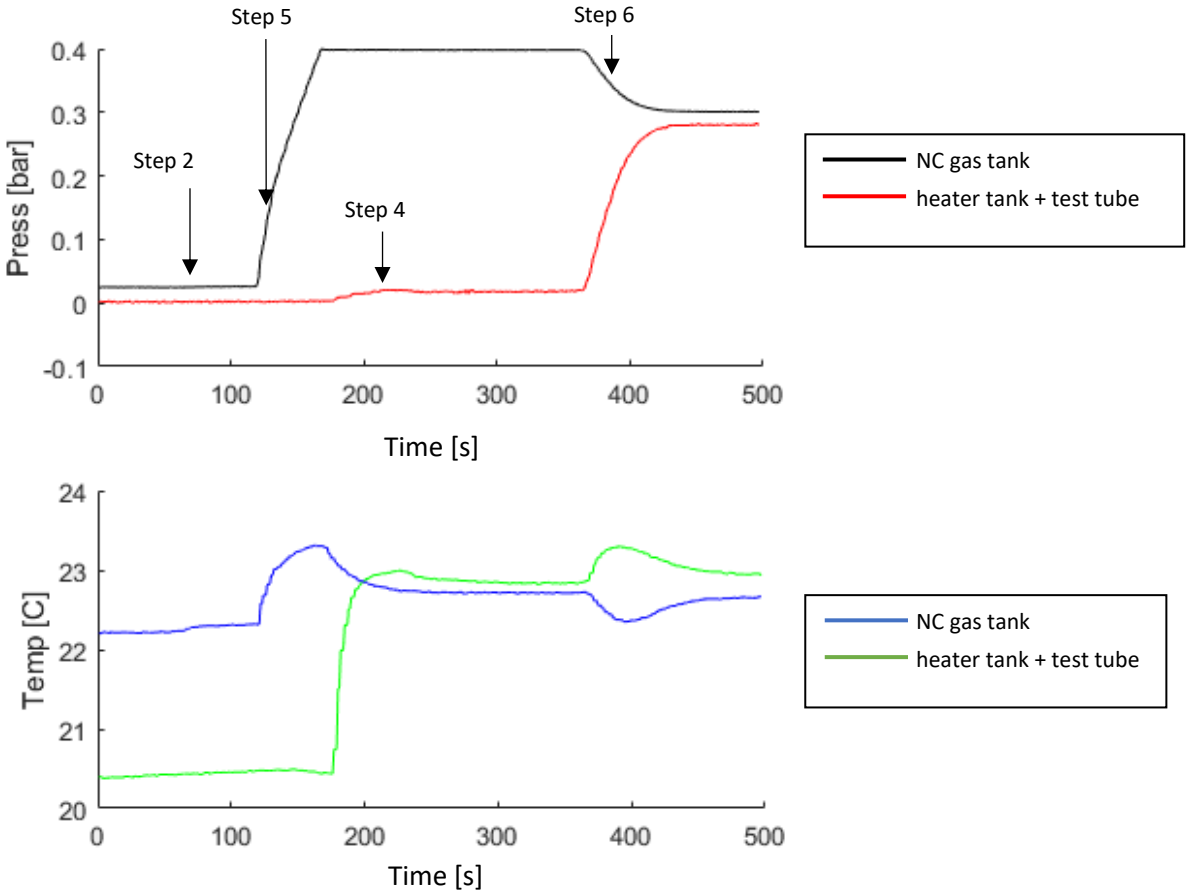

Figure 5-7 Typical pressure and temperature behavior during the filling of the NC gas tank the transfer of the gas into the experiment volumes

First, due to the presence of a spring-loaded one-way valve between NC gas tank and the experimental volumes, the pressures in these two volumes never fully equalize during step 6. The discrepancy is small, roughly 0.02 bar, but nevertheless it affects the precision of the of the initial condition's prediction. Secondly, the temperature in both volumes fluctuates during the filling procedure, and depending on the yearly season, would vary between 18˚C and 25˚C. The pre-calculation code relied on a constant ambient temperature of 20˚C and thus the accuracy of its predictions is affected. Moreover, the feeding of each NC gas species to the NC gas tank was performed manually, with the operator controlling

the flow of gases and monitoring the pressure. This technique necessarily incurred additional uncertainties in the filling procedure. Therefore, it was deemed necessary to develop a post-filling calculation script, which, based on recorded temperatures and pressures and all filling steps, would give a proper estimate of the actual amount of NC gas present in the facility during an experiment.

This script follows similar principles as the pre-calculation script, but, in contrast, performs calculations for steps 2, 4, 5, 6 and 8 in the forward order. For each step, recorded temperatures and pressures, as shown in Figure 5-7, are used to estimate the molar composition of the gas mixture.

The code starts by estimating how much, if any, residual gas remained in experimental volumes and NC gas tank after vacuuming during step 2. The estimated amount of gas, due to very small observed amounts, are treated as pure N_2 for simplicity, without introducing significant error.

As a next step, the code estimates the amount of steam created during water feeding to the experimental volumes due to a close-to-vacuum pressure level. Then, an average mole fraction during the step 4 is estimated, based on which a part of the previously observed residual moles of N_2 are removed from the experimental volumes and transferred into the water tank, as the water is replaced by gas during feeding. This further reduces the impact of the residual gas after step 2 on the overall experimental conditions.

Following, the actual amounts of each NC gas species fed to the NC gas tank during step 5 are calculated – here, the error of manual gas feeding, and variable temperature not accounted for in pre-calculation is corrected for. The step 6, during which NC gases are fed to the experimental volumes is treated in such a way that the code considers a small condensation period. The reason for this is that during this step the absolute pressure increases due to NC gas feeding and causes a small part of the steam to turn into liquid water. The code includes this in the overall calculation, however, it was observed that the actual amounts are very small and have little (<0.5%) impact on the overall final gas composition.

Lastly, the code calculates the final average molar composition of the gas mixture during experimental conditions, the step 8. While transitioning between step 6 and step 8, it is assumed that the pressure increase is due to a boil-off of water and the generation steam only. The algorithm of this calculation is shown in Figure 5-8.

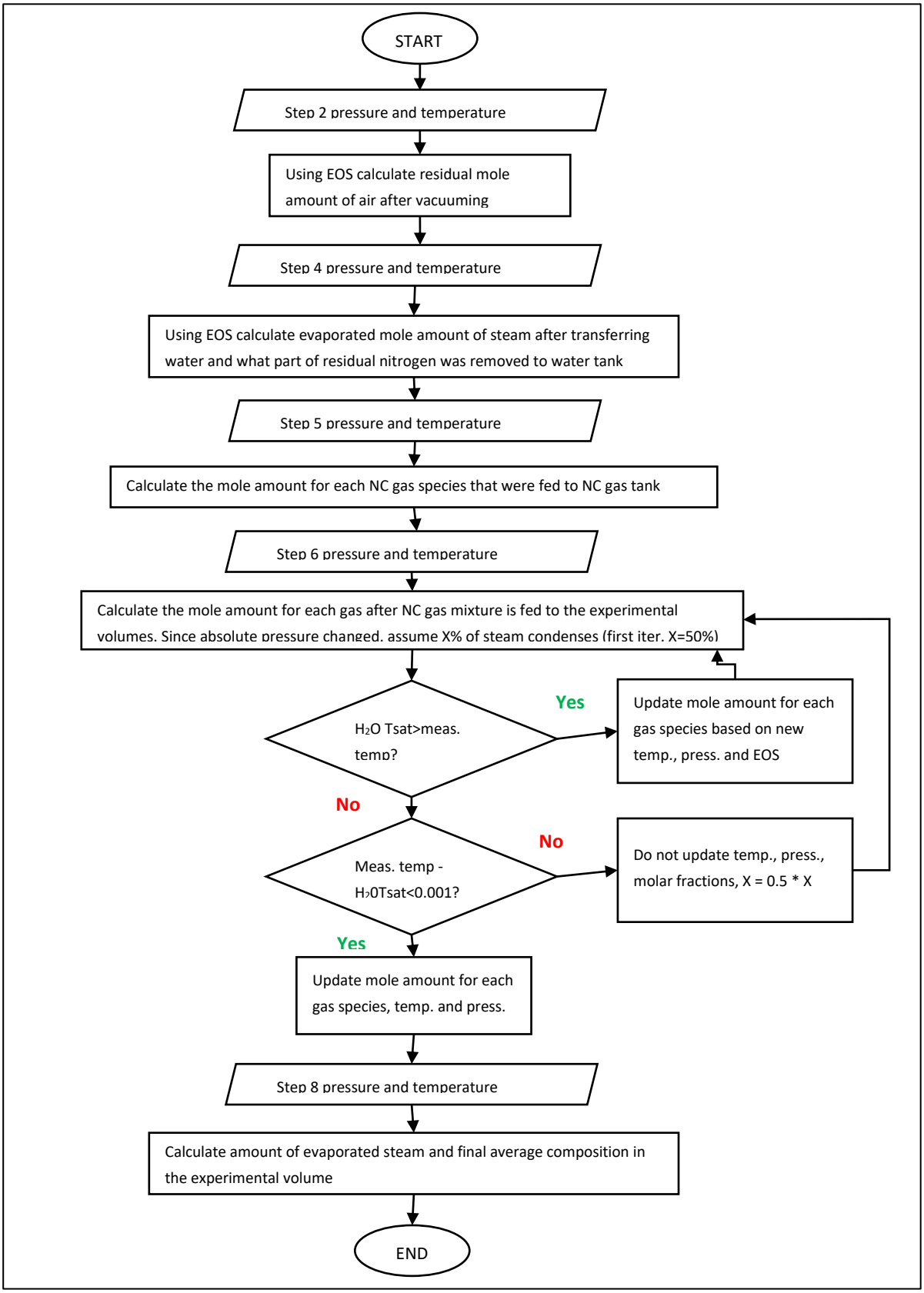

Figure 5-8 Algorithm of the average gas mixture molar composition post-calculation

Chapter 6 Experimental results

This chapter describes results of the experiments performed in the PRECISE facility. The analysis is divided into steady-state tests and continuous injections tests. For each type of the tests, investigation is subdivided by the controlled variable, including coolant velocity, wall temperature gradient, pressure and non-condensable gases content as well type. Data obtained with traversing temperature/conductivity probe and heat flux sensors are examined separately in two separate sections.

6.1 Steady state tests

As described previously in the Chapter 5 , these types of tests were performed with a well-controlled primary tube inventory and fixed control parameters for every run. Data was collected after a prolonged wait time, when the facility reached a quasi-steady-state, as indicated by stable pressure and temperature field. Since the steady-state identification during experiment was done manually, it was further verified during data processing step. For each acquired data set, the test tube pressure and steam temperature were analyzed in terms of stability. There were two parameters of concern – local oscillations and gradual mean change over a longer period, both of which were excluded from final analysis. The applied algorithm normalized the signal by dividing by the median value. In this way, the median value of the resulting data set was set to 1. Then, it located data points that lie within a prescribed band around the signal median – value that were found to work well was half of the standard deviation. Additionally, a hard limit of +/- 0.00075 around the new median was applied, in case the normalized standard deviation would have been too great in a given recording. Of all the data points located in this way, the longest continuous chain was picked for further analysis. This algorithm was applied twice to every data set, to further increase its effectiveness. The first pass (Figure 6-1 A) used test tube pressure and the second the steam temperature in the boiler, but only worked on previously identified steady-state candidate period (Figure 6-1 B). Both pressure and temperature were used, since the first tended to stabilize a bit faster than the latter, but sometimes exhibit larger oscillations during the test.

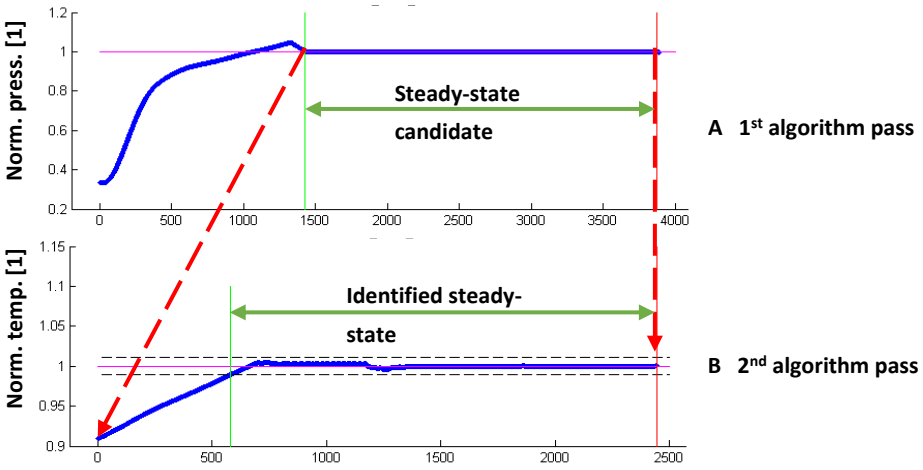

Figure 6-1 Steady-state identification algorithm in action, applied to pressure A) and temperature B). On the second plot, the permissible band is marked with dashed black lines.

6.1.1 Coolant velocity and wall temperature gradient

In this chapter the influence of coolant velocity and temperature on the condensation process is investigated. Experiments were conducted with and without addition of NC gases to the test tube. The motivation for this series of tests was to investigate how effective the increased wall temperature gradient or coolant flow can be in countering the negative impact of NC gases on condensation. A secondary goal was to find a wall temperature gradient value optimal for the PRECISE facility, so that well developed temperature and heat flux vertical profiles could be observed.

6.1.1.1 Experiments summary

In total, four different experimental runs were performed, two with and two without NC gases present. Two parameters were adjusted for every of the sets – coolant volumetric flow and coolant temperature. The former was freely adjusted, within the range of pump specification, and the latter was set relative to the test tube temperature. All the remaining parameters were unchanged between the tests. Pressure was set at 5 Bar absolute, as a middle point of the PRECISE facility capabilities. This ultimately could not be achieved for the series of tests where wall sub cooling was varied, and pure steam was used. The condensation was too efficient; it overcame the capabilities of the 2 kW heater in the steam generation tank. Hence, for these tests (VEL-DT-PURE-X), operating pressure of 3.00 bar was used instead, as this was the maximum achievable value. The overview of performed tests is shown in the Table 6-1. In case of some tests, the desired setpoint conditions were not reached – it is marked in the table as A/B, where A is the desired value and B is the achieved one.

Table 6-1 Initial conditions for the experimental series

File Name	NC gas mix mole fr.	N_2 fraction in NC gas mixture	Test press.	Test temp.	Coolant temp.	Coolant v. flow	Wall ΔT
Units	[1]	[1]	[bar]	[°C]	[°C]	[m³/h]	[°C]
Impact of coolant mass flow with NC gas							
VEL-CLNT-PURE-1	0.00	-	5.00	151.8	131.8	1.00	20.0
VEL-CLNT-PURE-2	0.00	-	5.00	151.8	131.8	2.00	20.0
VEL-CLNT-PURE-3	0.00	-	5.00	151.8	131.8	3.00	20.0
VEL-CLNT-PURE-4	0.00	-	5.00	151.8	131.8	4.00	20.0
VEL-CLNT-PURE-5	0.00	-	5.00	151.8	131.8	5.00	20.0
Impact of coolant mass flow with NC gas							
VEL-CLNT-NC-1	0.50	1.00	5.00	127.4	107.4	1.00	20.0
VEL-CLNT-NC-2	0.50	1.00	5.00	127.4	107.4	2.00	20.0
VEL-CLNT-NC-3	0.50	1.00	5.00	127.4	107.4	3.00	20.0
VEL-CLNT-NC-4	0.50	1.00	5.00	127.4	107.4	4.00	20.0
VEL-CLNT-NC-5	0.50	1.00	5.00	127.4	107.4	5.00	20.0
Impact of wall sub cooling with pure steam							
VEL-DT-PURE-1	0.00	-	3.00	134.0	129.0	2.00	5.0
VEL-DT-PURE-2	0.00	-	3.00	134.0	124.0	2.00	10.0
VEL-DT-PURE-3	0.00	-	3.00/2.69	134.0/130.0	114.0	2.00	20.0/16.0
VEL-DT-PURE-4	0.00	-	3.00/2.07	134.0/121.6	104.0	2.00	30.0/17.6
VEL-DT-PURE-5	0.00	-	3.00/1.26	134.0/106.8	84.0	2.00	50.0/22.8
VEL-DT-PURE-6	0.00	-	3.00/0.65	134.0/89.0	54.0	2.00	80.0/35.0

Impact of wall sub cooling with pure steam							
VEL-DT-NC-1	0.50	1.00	5.00	127.4	122.4	1.00	5.00
VEL-DT-NC-2	0.50	1.00	5.00	127.4	117.4	1.00	10.0
VEL-DT-NC-3	0.50	1.00	5.00	127.4	107.4	1.00	20.0
VEL-DT-NC-4	0.50	1.00	5.00	127.4	97.4	1.00	30.0
VEL-DT-NC-5	0.50	1.00	5.00	127.4	77.4	1.00	50.0
VEL-DT-NC-6	0.50	1.00	5.00	127.4	47.4	1.00	80.0

6.1.1.2 Coolant mass flow with pure steam (VEL-CLNT-PURE-X)

Coolant mass flow directly affects the turbulence characteristics of the coolant flow, changing the heat removal potential significantly. For the water flow in the cooling jacket, heat transfer coefficient can be estimated, through the Nusselt number, following eq. (70):

$$Nu = \frac{h_{tc} L_{char}}{\lambda} \tag{70}$$

where h_{tc} is the convective heat transfer coefficient, L_{char} is the characteristic length and λ is the liquid thermal conductivity. In case of PRECISE facility, since coolant flow takes place in an annulus around the test tube, the characteristic length can be defined as a hydraulic diameter D_h, equal to the difference between test tube outer diameter and cooling jacket outer diameter pipe flow ([229], pg. 520). There are several empirical correlations derived for flow in smooth, circular tubes, available to estimate the Nusselt number. With the modified hydraulic diameter, they can be successfully applied to the annular flow [229]. For a developed laminar flow, where outer wall is insulated, and inner wall is kept at constant temperature, and the ratio of inner to outer annulus diameter is close to 0.25 (0.275 in case of PRECISE), $Nu \approx 7.37$ can be used [229], [230]. For the turbulent flow either Dittus-Boelter equation (eq. (71)) or Gnieliski correlation (eq. (72)) are suitable:

$$Nu = 0.023 Re^{4/5} Pr^{0.4} \tag{71}$$

$$Nu_{Gn} = \frac{(f/8)(Re - 1000)Pr}{1 + 12.7(f/8)^{0.5}(Pr^{2/3} - 1)} \tag{72}$$

Where f is the Darcy friction factor, defined by Petukhov correlation as:

$$f = (0.79 \ln(Re) - 1.64)^{-2} \tag{73}$$

Where Re is the Reynolds number based on the coolant channel geometry and Pr is the Prandtl number. Dittus-Boelter equation is valid for ranges of $0.6 < Pr < 160$, $Re > 10000$ and $L/D > 10$. Gnielinski's correlation is valid for ranges of $0.5 < Pr < 2000$ and $2300 < Re < 5 \text{ x } 106$ [229] respectively. For the range of tested mass flows, values of Re and Pr are shown in Figure 6-2. The small variation in Prandtl number values was caused by slight coolant temperature instability at low flow values. The used control system had troubles maintaining set-point values for flows at this range. Overall, this result verifies the validity of eq. (71) and eq. (72) to estimate Nu values in these conditions.

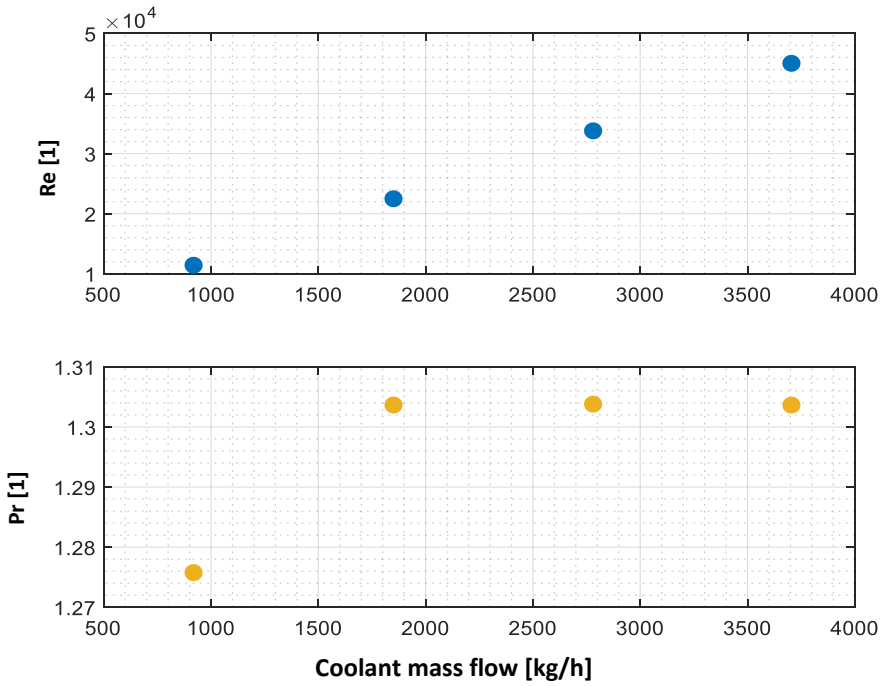

Figure 6-2 Range of Reynolds and Prandtl numbers for varying coolant mass flow

The impact on overall coolant side heat transfer coefficient of varying mass flow in the PRECISE facility is shown in Figure 6-3. Values of h_{tc} calculated with both correlations lie within 1% value of each other, hence the rest of the analysis is done basing on Gnielinski equation.

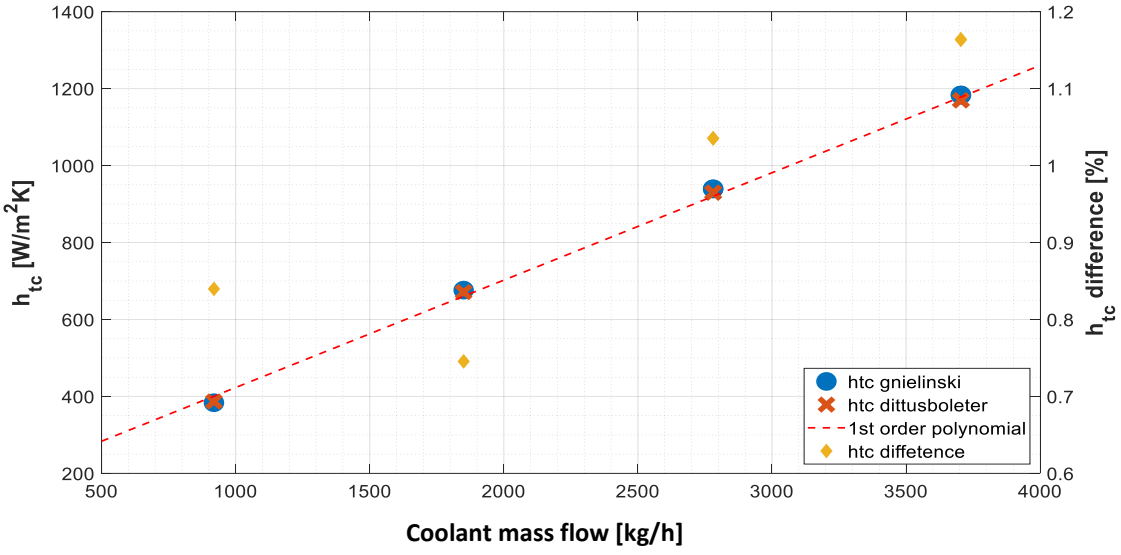

Figure 6-3 Coolant side heat transfer coefficient relation to coolant mass flow

Since pure steam condensation is a very efficient process, the heat removal in this experiment is controlled primarily through coolant side properties, as shown on the Figure 6-4. Overall, even tripling the coolant side convective h_{tc} (and almost quadrupling the actual mass flow rate) results in a modest increase in steam side condensation flux of 18.67%. It is important to mention however that for all recordings the coolant flow is turbulent ($Re > 10000$). With the used components it was not possible to decrease the flow

enough to achieve laminar flow, and presumably the observed increase in condensation flux between the two would have been significantly increased.

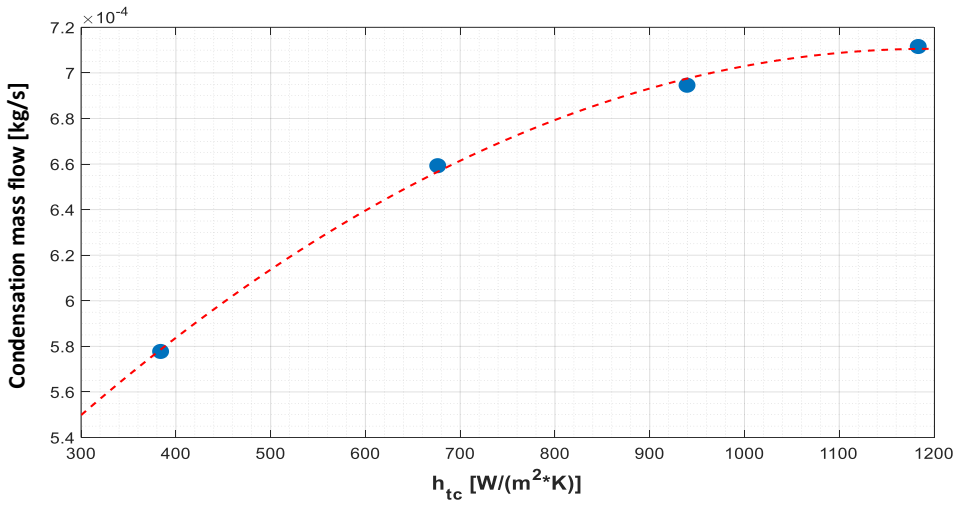

Figure 6-4 Coolant side heat transfer coefficient impact on steam condensation

6.1.1.3 Coolant mass flow with NC gases (VEL-CLNT-NC-X)

The effect of increasing coolant side heat transfer coefficient clearly has an impact on condensation process. However, when NC gases are present, the main barrier to heat transfers moves from coolant side to the primary side. This series of experiments was designed to investigate whether increased coolant flow is an effective counter-action to ingress of NC gases.

The average mole fraction in the test tube was set to ~0.2 and best effort was put forward to maintain it constant between measurements. The varied variable was the coolant water mass flow. Figure 6-5 shows comparison of condensation flux at various levels of coolant side h_{tc}. For all recordings, condensation flux never approached the values observable at pure steam experiments. Effectiveness of NC gases at plugging the condenser tube was too high to overcome with increasing coolant side flow.

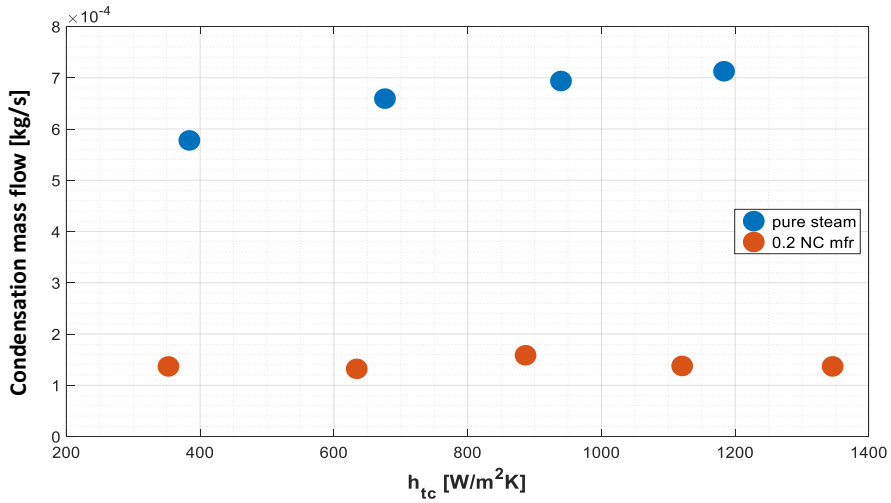

Figure 6-5 Coolant h_{tc} impact on steam condensation flux with and without NC gases

For the same value of htc, two typical temperature distributions along the tube center, tube wall (1.25 mm from the inner surface) and in the coolant are presented in Figure 6-6. It is clearly visible, that with 0.2 average mole fraction of NC gases present, no condensation takes place, no matter how much the coolant side mass flow is increased.

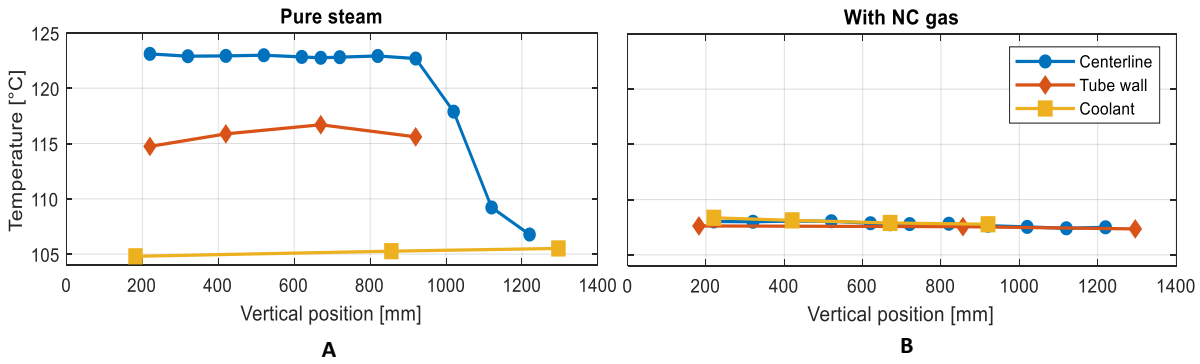

Figure 6-6 Typical temperature distributions for A) pure steam and B) NC gases recordings

6.1.1.4 Wall sub cooling with pure steam (VEL-DT-PURE-X)

In this series of tests, coolant water temperature was varied, with reference to steam boiling point temperature, calculated for the test pressure. Unfortunately, for the ΔT over 15°C, the system was not able to maintain desired setpoint pressure, and the desired steady state was never reached, as shown in Figure 6-7.

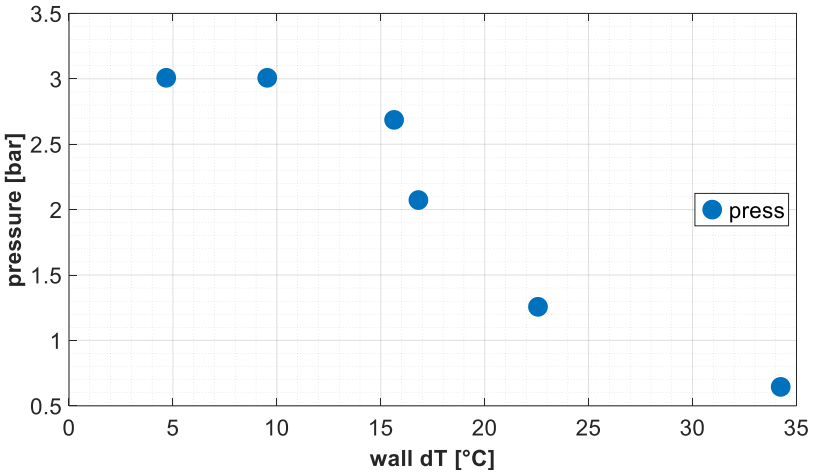

Figure 6-7 Effective steady state pressure as a function of the wall temperature gradient

At all ΔT values higher than 15°C, the heater was operating at maximum power (Figure 6-8 A), but since evaporation heat increases with decreasing temperature, the steam mass flow calculated on this basis seems to decrease. At the same time, steam density decreases, resulting in much increased volumetric flow and thus steam velocities, increasing turbulence levels and further increasing already high heat removal rates, (Figure 6-8 B).

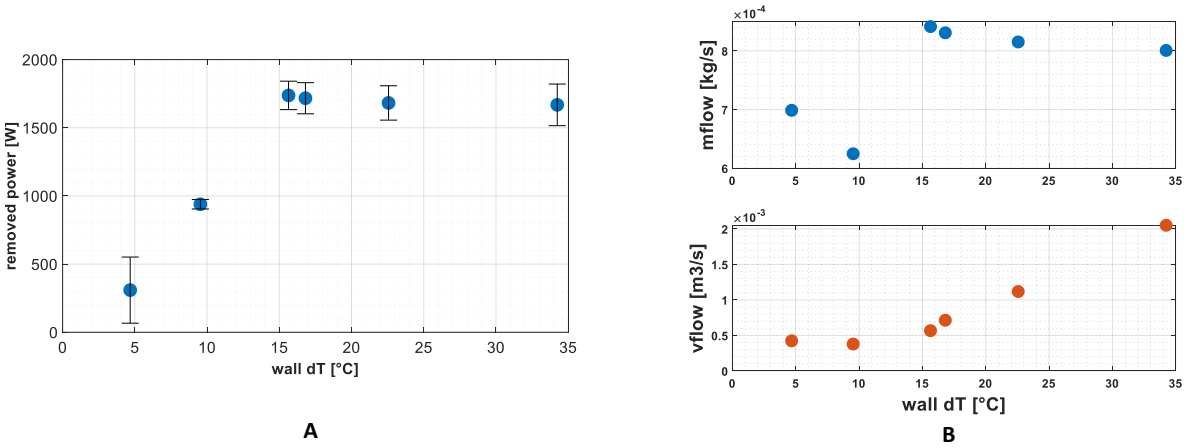

Figure 6-8 A) PRECISE power change with increasing wall temperature gradient. B) Steam flow properties with increasing wall temperature gradient

Overall, increasing the wall temperature gradient was too effective to properly investigate this effect with the heater which was installed in the PRECISE facility. This points to decreasing coolant temperature being much more a more suitable way to increase heat removal rates from condensing tubes.

6.1.1.5 Wall sub cooling with NC gases (VEL-DT-NC-X)

The same regime as in the previous series of tests was applied, but with 0.2 average mole fraction N_2 present in the test tube. Contrary to pure steam tests, higher test pressure was possible to reach and maintain throughout the whole range of previously studied wall temperature gradient values (ΔT 5-35°C). Therefore, the range was extended further, up to maximum ΔT of 100°C, and observed effect on condensation flow is approximately linear, Figure 6-9 A. One must bear in mind however, that the increasing wall temperature gradient is achieved through decreasing coolant water temperatures, which, in turn, affects its properties, overall slightly decreasing coolant side h_{tc}, Figure 6-9 B. However, clearly the heat exchange process is in this case mainly controlled through the test tube inner side properties.

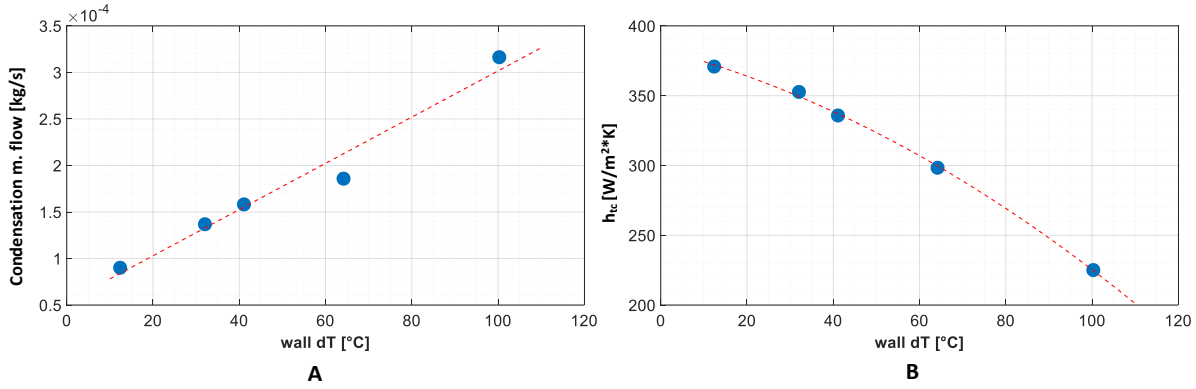

Figure 6-9 A) Condensation mass flow response to increasing wall temperature gradient. B) Accompanying effect on coolant side heat transfer coefficient, through decreasing water temperature

Of note is that even for the highest wall temperature gradient, the condensation flow values are much less (<50%) than those for even the smallest temperature gradient at pure steam tests. This once again underlines the effectiveness of NC gases at tube plugging. Overall, decreasing coolant temperature is much more efficient way of countering the effect of NC gases in condenser tubes than increasing the coolant water flow.

6.1.2 Impact of test tube pressure

This series of tests was designed to investigate the effect of pressure on condensation rates, with and without NC gases. Since pressure affects a range of thermal-hydraulic parameters, most important here being the temperature at which water will boil and condense, understanding its effects is of highest interest to the reflux condensation phenomenon.

6.1.2.1 Experiments summary

Three series of tests were conducted – first (Pabs-PURE-X) with pure steam only, to establish a baseline, and the second two with NC gases present. The two latter are distinguished by the way in which the partial pressure of steam was treated. The first of them, Pabs-PART-X, maintains the partial pressure of steam at a constant value of 2 bars. The absolute pressure increase between 2 and 10 bars is achieved with addition of N_2 only. Hence, theoretically, only the partial pressure of NC gases part of the mixture is affected.

The second scheme, marked as Pabs-MFR-X, maintains a constant average mole fraction of N_2, thus partial pressures of both mixture components are modified at the same rate. The overview of all conducted tests is presented in the Table 6-2.

Table 6-2 Summary of pressure experiments

File name	**NC gas mix mole fr.**	**N_2 fraction in NC gas mixture**	**Test press.**	**Test temp.**	**Coolant temp.**	**Coolant v. flow**	**Wall ΔT**
Units	[1]	[1]	[bar]	[°C]	[°C]	[m³/h]	[°C]
Impact of absolute pressure with pure steam							
Pabs-PURE-1	0.00	-	2.00	120.2	100.2	1.00	20.0
Pabs-PURE-2	0.00	-	4.00	143.6	123.6	1.00	20.0
Pabs-PURE-3	0.00	-	6.00/5.71	158.8/156.9	138.8	1.00	20.0/18.1
Pabs-PURE-4	0.00	-	8.00/7.46	170.4/167.6	150.4	1.00	20.0/17.2
Pabs-PURE-5	0.00	-	10.00/9.18	179.9/176.1	159.9	1.00	20.0/16.2
Impact of NC gases partial pressure							
Pabs-PART-1	0.00	-	2.00	120.2	100.2	1.00	20.0
Pabs-PART-2	0.50	1.00	4.00	120.2	100.2	1.00	20.0
Pabs-PART-3	0.67	1.00	6.00	120.2	100.2	1.00	20.0
Pabs-PART-4	0.75	1.00	8.00	120.2	100.2	1.00	20.0
Pabs-PART-5	0.80	1.00	10.00	120.2	100.2	1.00	20.0
Impact of absolute pressure with NC gases							
Pabs-MFR-1	0.50	1.00	2.00	99.6	79.6	1.00	20.0
Pabs-MFR-2	0.50	1.00	4.00	120.2	100.2	1.00	20.0
Pabs-MFR-3	0.50	1.00	6.00	133.5	113.5	1.00	20.0
Pabs-MFR-4	0.50	1.00	8.00	143.6	123.6	1.00	20.0
Pabs-MFR-5	0.50	1.00	10.00	151.8	131.8	1.00	20.0

6.1.2.2 Pabs-PURE-X

The tests done with pure steam have proven how efficient steam condensation is at heat removal. The test matrix was designed such that for every investigated pressure, a constant wall temperature gradient of 20°C was maintained. This was achievable only at lower pressures, 2 and 4 bars. For the higher values, the setpoint pressure was not reached ultimately, even though the electrical heater was operating at full power, Figure 6-10A. This, in turn, reduced the steam boiling point, and allowed the facility to reach a stable steady state at a decreased wall temperature gradient, Figure 6-10B.

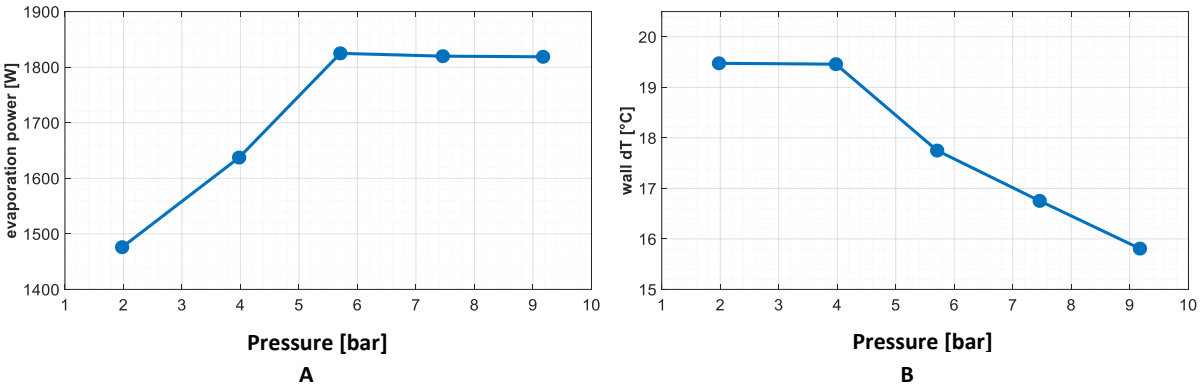

Figure 6-10 A) Evaporation power as a function of pressure. B) Decreasing wall temperature gradient, counteracting effects of increased pressure

Since, as previously identified, the condensation mass flow has a linear relationship with wall temperature gradient, and to overcome this experimental drawback, the wall temperature gradient was used as a normalizing factor. The resulting $\frac{\dot{m}}{\Delta T}$ has a good proportionality to the test pressure, as presented on the Figure 6-11.

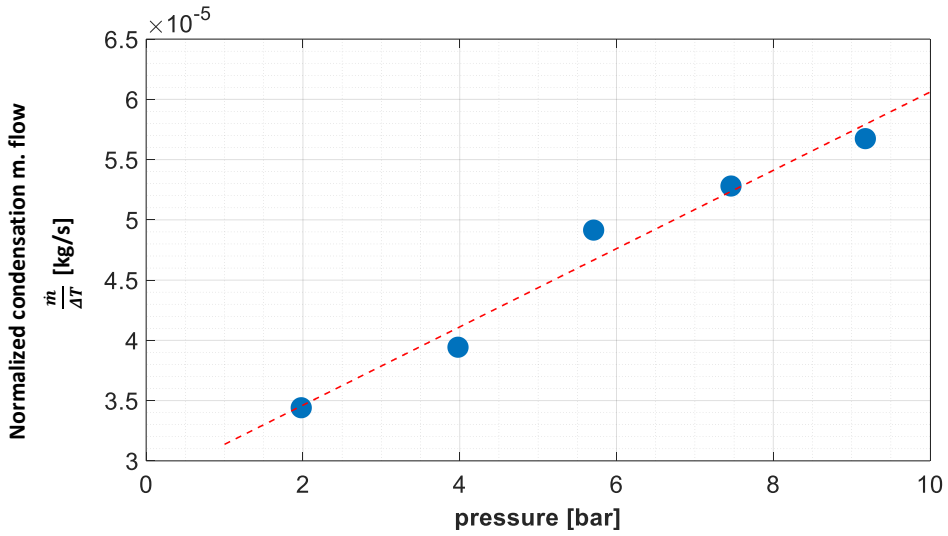

Figure 6-11 Normalized condensate flow as a function of pressure

The straightforward conclusion that can be drawn from the obtained data is the fact that increased pressure assists the process of condensation.

6.1.2.3 Pabs-PART-X

In this series of tests, the absolute pressure increase was realized with an increase of N_2 content, while partial pressure of steam remained unchanged between the tests, Figure 6-12A. As a result, the average mole fraction of nitrogen increases linearly for each increase in absolute pressure, Figure 6-12B.

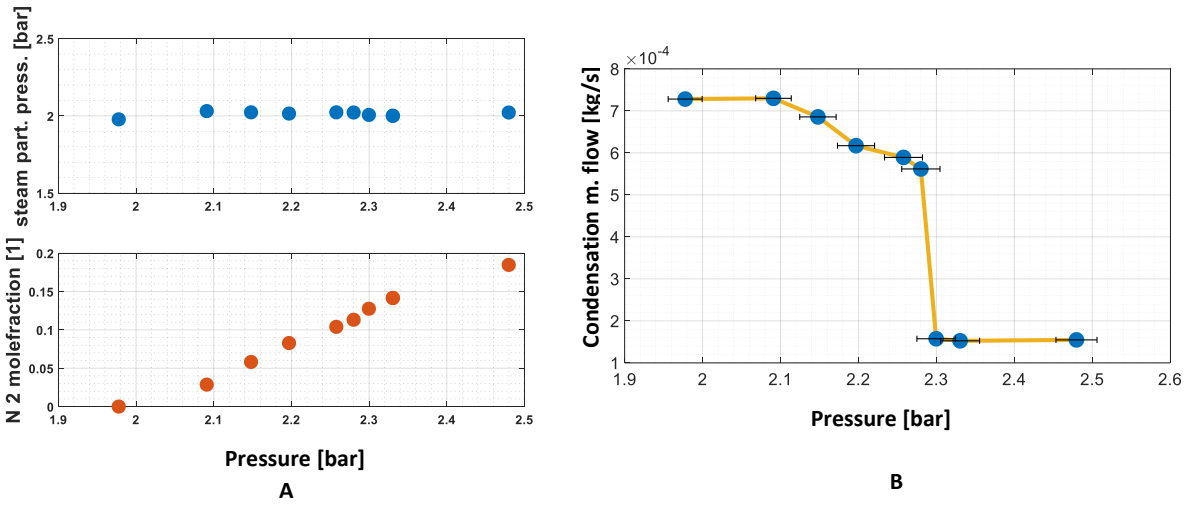

Figure 6-12 Steam partial pressure (A) and average N2 mole fraction (B) with increasing absolute

As shown in Figure 6-12, the absolute pressure range starts at 2 bars with pure stream, a reference case and goes up to 2.48 bar and 0.185 average N_2 mole fraction. The reason why it was not extended further to the full range of 10 bars, is that no condensation was observed beyond 2.28 bar pressures, Figure 6-12C. This rather sharp cutoff might seem sudden, but it can be explained through the analysis of the temperature profiles in the test tube.

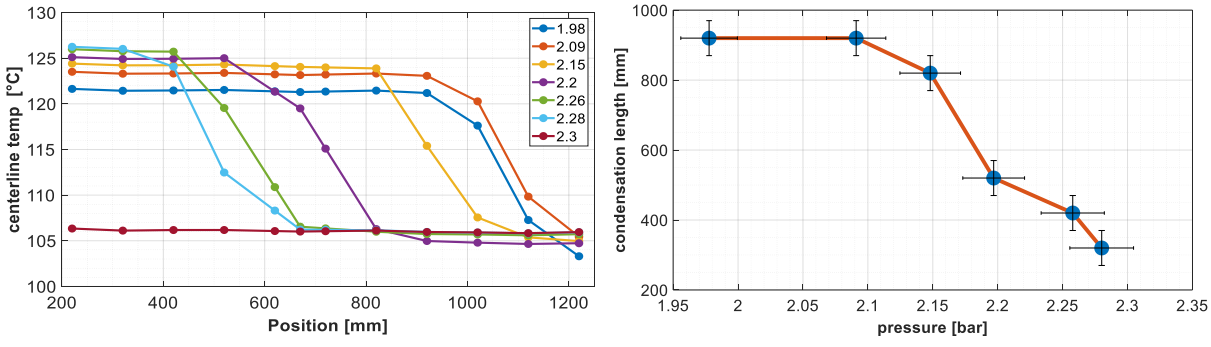

Figure 6-13 A) Vertical center temperature profiles with increasing pressure B) condensation length with increasing pressure

Even though for most of the tested pressure range the decrease in condensation mass flow is small, it is accompanied by a significant variation in temperature distribution inside the tube, Figure 6-13A. As a remark, the change in the maximum temperature in the tube corresponds to the increase in absolute pressure between the tests. The same holds for the changing minimum value, which was determined by the set coolant temperature, which, in turn, was adjusted with respect to the boiling point for each test, to maintain constant wall temperature gradient.

The condensation zone, taking up to the full height of the tube for low pressure / low N_2 content tests consistently decreases, Figure 6-13B. This points to two simultaneous phenomena taking place – gradual plugging of the test tube, and increased condensation taking place in the still available region. The

relation to the absolute pressure can be expressed in terms of condensation mass flux, calculated as condensation mass flow $\dot{m}/A$ where A is the tube area in the steam reach zone, Figure 6-14

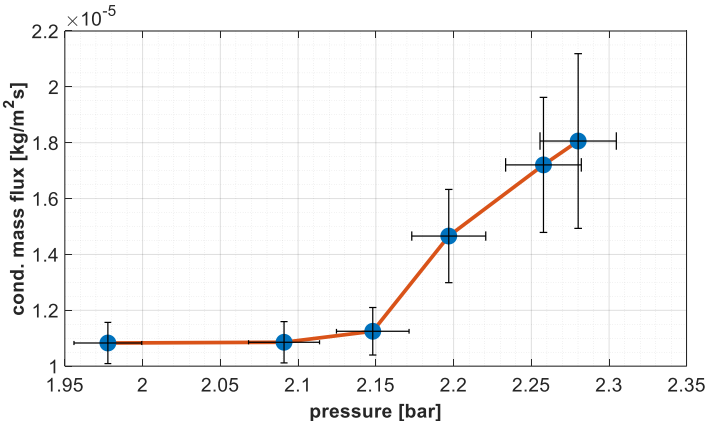

Figure 6-14 Calculated mass flux the with increasing absolute pressure

The large measurement errors of the mass flux are a result of a spatial resolution of the thermocouple array used to measure the vertical temperature distribution. The condensation area A estimation is based on this distribution, and hence inherits the uncertainty, passed further to mass flux. This result further confirms findings from experiments with pure steam, that increased pressures have a positive correlation with an increase in condensation mass flux.

However, the limitation of this study is the poor mixing between N_2 and steam. Taking measured temperature profiles as a basis and assuming that the local temperature corresponds to steam boiling point at a given mixture composition, it is possible to calculate the steam mole fraction distribution along the tube, Figure 6-15.

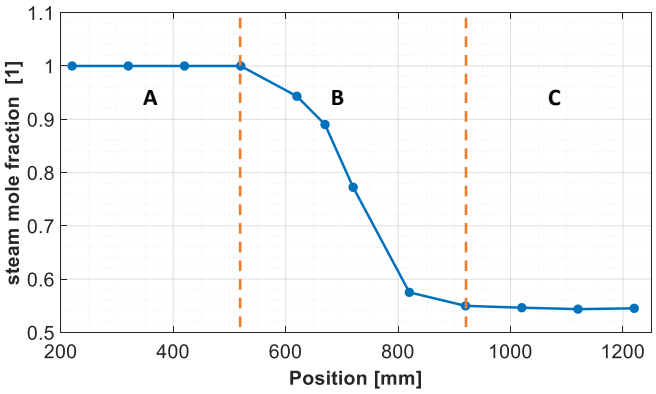

Figure 6-15 Vertical steam mole fraction along test tube centerline with three distinct regions (A, B & C)

It is clear, that some mixing between the phases occurs, but three distinct regions can be identified. Following the Figure 6-15 naming:

1. A is a steam only region extending from the test tube inlet, where most condensation occurs
2. B is the mixing zone, where both steam an NC gas reside in a varying composition as one moves up the tube and where condensation gradually subsides
3. C is a cold region, where no condensation occurs and a plug with high NC gases content is formed

In the A region, the partial pressure of steam corresponds to the absolute pressure of the system. During the experiment design, an assumption was made that the steam temperature can be estimated based on the steam partial pressure calculated from the set average molar fraction of NC gas present. However, it is clear, that a heavy stratification of gases was always happening inside the test tube. Therefore, the goal of maintaining constant steam partial pressure in this test run was not achieved and no inference can be made on how it impacts the condensation process as a function of the absolute pressure.

6.1.2.4 Pabs-MFR-X

In this series of test, the average ratio between gas mixture species was kept constant, while the absolute pressure of the system was increased. The tube wall temperature gradient was also maintained at a constant 20°C value. Correspondingly to the Pabs-PART-X series of tests, significant stratification of gas species was observed. The main challenged experienced during these tests was maintaining a constant gas species ratio between the tests. Therefore, several runs were done at different mole fractions, to investigate whether effect of pressure would persist at different conditions.

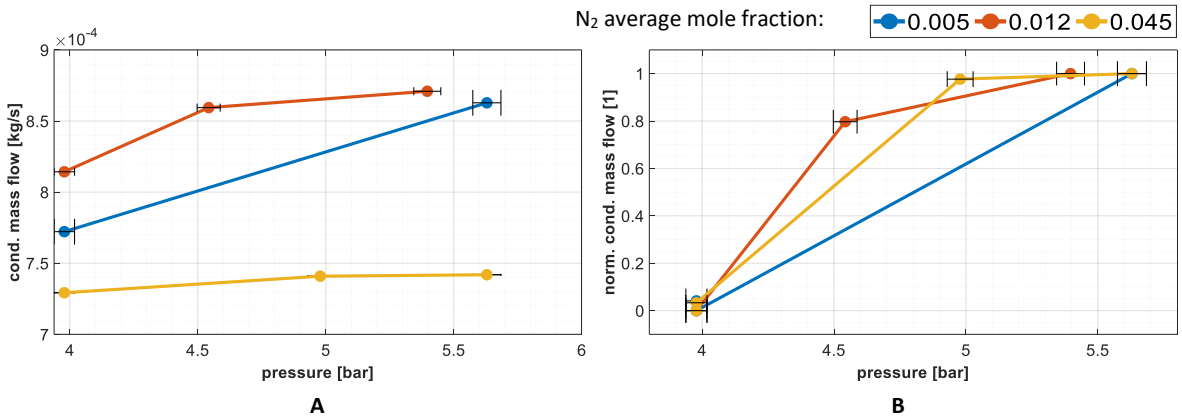

Figure 6-16 Condensation absolute (A) and normalized (B) $\dot{m}$ with increasing pressure at three N_2 average mole fractions

Figure 6-16A shows the observed slight increase in condensation mass flow at three N_2 mole fractions. Of course, increasing amount of NC gas affects to condensation, thus the relation is better observed with data normalized to the interval 0-1 (divided by maximum), Figure 6-16B. The correlation between pressure and condensation mass flow is positive for each mixture ratio.

For a given average NC mole fraction, the effect of pressure can be observed in temperature distribution profiles. Figure 6-17A shows the normalized temperature profiles (normalization is necessary for visualization, as the change in absolute pressure affects the steam boiling point). There is little variation, with a slight tendency of mixing zone to move towards the tube inlet with increasing pressure. The mixing zone region is also reflected in the dynamics of the recorded temperature data, showing increased variation. This can be visualized in terms of standard deviations, Figure 6-17B. Here, clearly the standard deviation values peak, indicating the mixing zone, moves towards the tube inlet with increased pressure. Thus, even though the condensation mass flow is increased, it takes place in a shorter length of the tube, in a similar way to what was observed in the chapter 6.1.2.3, indicating an increase in condensation effectiveness, Figure 6-16

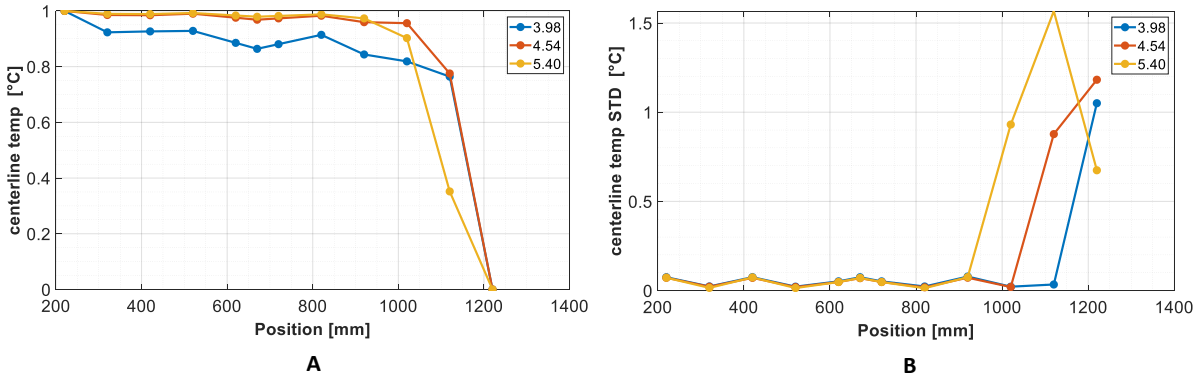

Figure 6-17 Normalized temperature profiles (A) and standard deviations (B) at three pressures for 0.005 N_2 average molar fraction

6.1.3 Impact of NC gases – nitrogen

In this series of experiments impact of increasing content of N_2 in the mixture on the steam condensation was investigated. The data was analyzed in terms of impact on amount of steam condensed and the distribution of the gases in the tube. As was the case with previously described tests a stratification was observed, and thus the two gases did not really form a uniform mixture, instead maintaining the basic three region pattern as shown in Figure 6-15. The impact of thermodynamic conditions on the distribution shape and size was investigated.

6.1.3.1 Experiments summary

The tests were performed in four test series, with series 1 to 3 performed at constant pressures, ranging from 4 to 5.6 bars and varying fraction of NC gas. In these experiments, partial pressure of steam was assumed to vary according to the used gas fractions. In contrast, in series 4 the absolute pressure of the test was not constant, but the total amount of steam of the system was not changing. The full list of tests is presented in the Table 6-3.

Table 6-3 Summary of N_2 experiments

File name	NC gas mix mole fr.	N2 fraction in NC gas mixture	Test press.	Test temp.	Coolant temp.	Coolant v. flow	Wall ΔT
Units	[1]	[1]	[bar]	[°C]	[°C]	[m3/h]	[°C]
Absolute pressure – 4 bar							
NC-MFR-ABS-4_1	0.0000	-	4.00	143.6	123.6	2	20.0
NC-MFR-ABS-4_1.5	0.0250	1.00	4.00	142.7	122.7	2	20.0
NC-MFR-ABS-4_2	0.0500	1.00	4.00	141.8	121.8	2	20.0
NC-MFR-ABS-4_2.5	0.0750	1.00	4.00	140.8	120.8	2	20.0
NC-MFR-ABS-4_3	0.1000	1.00	4.00	139.9	119.9	2	20.0
NC-MFR-ABS-4_4	0.1500	1.00	4.00	137.9	117.9	2	20.0
NC-MFR-ABS-4_6	0.2500	1.00	4.00	133.5	113.5	2	20.0
NC-MFR-ABS-4_7	0.3000	1.00	4.00	131.2	111.2	2	20.0
NC-MFR-ABS-4_8	0.4000	1.00	4.00	126.1	106.1	2	20.0
NC-MFR-ABS-4_9	0.5000	1.00	4.00	120.2	100.2	2	20.0
NC-MFR-ABS-4_10	0.6500	1.00	4.00	109.3	89.3	2	20.0

Absolute pressure – 5 bar							
NC-MFR-ABS-5_1	0.0000	-	5.00	151.8	131.8	1	20.0
NC-MFR-ABS-5_1.5	0.0500	1.00	5.00	149.9	129.9	1	20.0
NC-MFR-ABS-5_2	0.1000	1.00	5.00	147.9	127.9	1	20.0
NC-MFR-ABS-5_2.5	0.1500	1.00	5.00	145.8	125.8	1	20.0
NC-MFR-ABS-5_3	0.2000	1.00	5.00	143.6	123.6	1	20.0
NC-MFR-ABS-5_4	0.3000	1.00	5.00	138.9	118.9	1	20.0
NC-MFR-ABS-5_5	0.5000	1.00	5.00	127.4	107.4	1	20.0
NC-MFR-ABS-5_6	0.7000	1.00	5.00	111.4	91.4	1	20.0
NC-MFR-ABS-5_7	0.9000	1.00	5.00	81.3	61.3	2	20.0
Absolute pressure – 6 bar							
NC-MFR-ABS-6_0	0.0000	-	5	158.8	138.8	2	20.0
NC-MFR-ABS-6_0.5	0.0250	1.00	5.60	157.9	137.9	2	20.0
NC-MFR-ABS-6_1	0.0500	1.00	5.60	156.8	136.8	2	20.0
NC-MFR-ABS-6_1.25	0.0625	1.00	5.60	156.3	136.3	2	20.0
NC-MFR-ABS-6_1.5	0.0750	1.00	5.60	155.8	135.8	2	20.0
NC-MFR-ABS-6_2	0.1000	1.00	5.60	154.8	134.8	2	20.0
NC-MFR-ABS-6_2.25	0.1250	1.00	5.60	153.7	133.7	2	20.0
NC-MFR-ABS-6_2.5	0.1375	1.00	5.60	153.1	133.1	2	20.0
NC-MFR-ABS-6_3	0.1500	1.00	5.60	152.6	132.6	2	20.0
NC-MFR-ABS-6_4	0.1750	1.00	5.60	151.5	131.5	2	20.0
Partial pressure							
NC-MFR-PART-1.0	0.0000	0.00	2.00	120.2	100.2	1	20.0
NC-MFR-PART-1.5	0.0500	1.00	2.11	120.2	100.2	1	20.0
NC-MFR-PART-1.75	0.0750	1.00	2.16	120.2	100.2	1	20.0
NC-MFR-PART-2.0	0.1000	1.00	2.22	120.2	100.2	1	20.0
NC-MFR-PART-2.25	0.1125	1.00	2.25	120.2	100.2	1	20.0
NC-MFR-PART-2.35	0.1250	1.00	2.29	120.2	100.2	1	20.0
NC-MFR-PART-2.5	0.1500	1.00	2.35	120.2	100.2	1	20.0
NC-MFR-PART-3.0	0.2000	1.00	2.50	120.2	100.2	1	20.0
NC-MFR-PART-4.0	0.3000	1.00	2.86	120.2	100.2	1	20.0
NC-MFR-PART-5.0	0.5000	1.00	4.00	120.2	100.2	1	20.0
NC-MFR-PART-6.0	0.7000	1.00	6.67	120.2	100.2	1	20.0
NC-MFR-PART-7.0	0.8000	1.00	10.00	120.2	100.2	1	20.0

6.1.3.2 NC-MFR-ABS-X

The basic results of all the conducted tests is in good agreement with literature and indicates that increasing the amount of NC gases have a negative impact on overall condensation phenomenon, Figure 6-18A. However, this cannot be simply attributed to increasing molar fraction of N_2 in a uniform mixture. In the conducted experiments raising the amount of nitrogen resulted in strongly affecting the vertical distribution of gases.

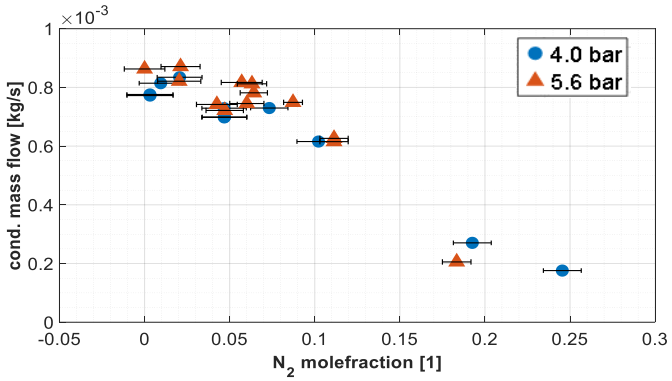

Figure 6-18 Test tube condensation $\dot{m}$ with an increasing content of N_2

To describe this phenomenon, let us recall the basic shape of vertical temperature distribution, Figure 6-19. Three distinct regions of pure steam condensation, mixing region and dead plug are visible here. These were observed in virtually all of experiments discussed in this chapter, with exception of extreme NC gas content cases. For very low NC amounts the plug was not observed, and the mixing zone remained at the top of the tube, while for very high gas content the pure steam region was missing, or plug would extend all through the tube. For every region, starting from the tube bottom, the following parameters describe their sizes: L_{cond}, L_{mix} and L_{plug}, Figure 6-19.

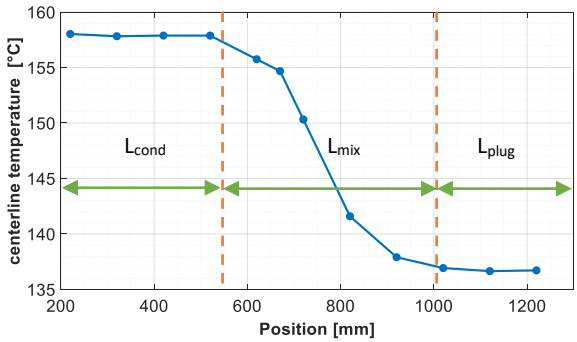

Figure 6-19 Vertical temperature profile with three characteristic parameters

The boundaries between the regions are not sharp and the distinction has to be based on some assumptions. In this case, the zone identification is done automatically during data processing step, following a simple algorithm. First, the temperature distribution is normalized to range 0-1. Then, data is divided in three ranges:

1. 0 – 0.1 – NC plug
2. 0.1 – 0.9 – mixing zone
3. 0.9 – 1 – steam reach condensation zone

Vertical position for each data point is noted and the points losing closest to cutoff values are defined as region boundaries, h_{st} and h_{end}. Due to spatial resolution of the thermocouple array along the tube centerline, accuracy of the calculated sizes is 100 mm.

Following this method allows to observe that increasing N_2 content results shortening the active condensation length L_{cond} in the test tube, Figure 6-20A. Thus, the primary mechanism of condensation retardation is through formation of a plug with high NC gas content. This region cannot be reached by fresh steam entering the test tube at the bottom and prevents effective heat removal.

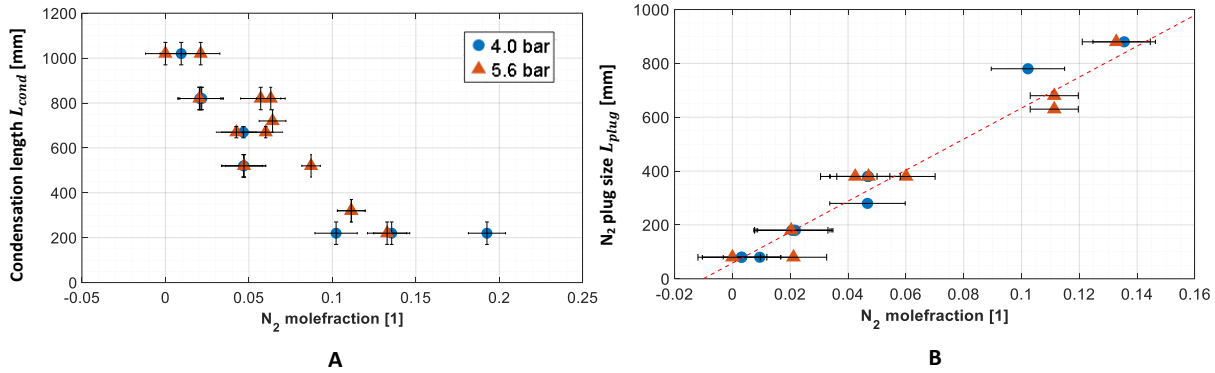

Figure 6-20 A - Test tube condensation length and B - N_2 gas plug size with increasing N_2 gas content

The size of the plug L_{plug} is proportional to the supplied amount of N_2, Figure 6-20B. Thus, the mixing region is being pushed towards the bottom of the tube. At the same time, the size of this intermediate transition region, L_{mix}, remains relatively unchanged at all gas fractions and does not scale with pressure either. However, since the thermocouple array has a 100 mm spatial resolution, the estimation of the mixing zone size inherits a large uncertainty. Furthermore, the values are strongly discretized, following the physical locations of measuring thermocouples, Figure 6-21A. To avoid this limitation, a 1D interpolation of temperature data with a vertical spacing of 10 mm was applied to the signal. The resulting estimated plug size is shown on the Figure 6-21B. On average, with this method, the spread of data was reduced from 200-400 mm to 150-300 mm range for plug size. A correlation with increasing N_2 content could not be identified.

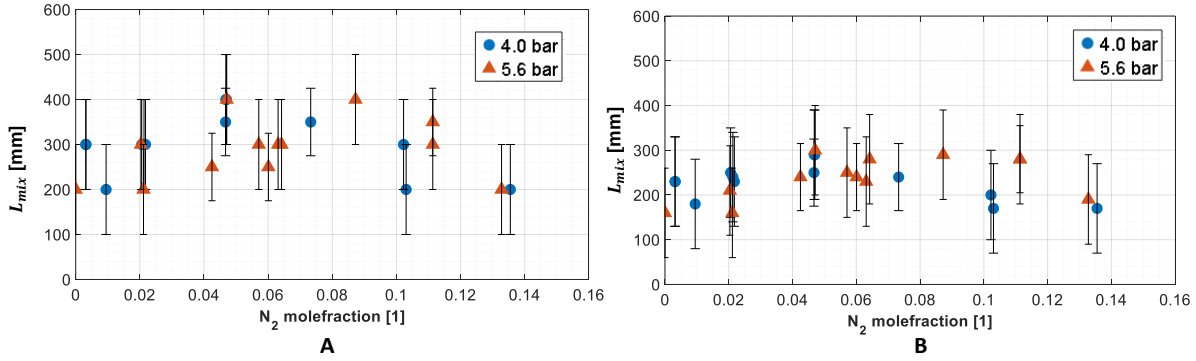

Figure 6-21 Mixing zone size without (A) and with (B) linear temperature interpolation

The pronounced stratification of gas species in the test tube and the resulting division in three distinct regions are each characterized by unique heat transfer properties. This effect is visible in local heat flux

measurement and the local wall temperature gradient. To best visualize it, for a given location, a transformed vertical coordinate system is proposed:

$$x = \frac{\left(h_{sens} - \frac{(h_{st} + h_{end})}{2}\right)}{\frac{1}{2}L_{mix}} \tag{74}$$

where h_{sens} is the elevation of an analyzed sensor, either thermocouple or GHFS. The numerator can be interpreted as the distance from the current sensor vertical position to the center of the mixing zone. Zero value of x indicates perfect overlap and negative values mean mixing zone center being at elevation higher than the sensor. The denominator provides normalization by a half of the current mixing zone size. In this way a unitary value can be interpreted as the sensor being half a mixing zone size from its center, thus at the start h_{st} (+1) or end h_{end} (-1) of the region.

Figure 6-23 presents data recorded at the elevation of 660 mm, where a heat flux sensor and a double thermocouple are embedded in the wall. Here, the difference in local heat transfer, as expressed in heat flux and the wall temperature gradient with respect to the mixing zone positioning is evident. What is additionally interesting is the fact that in both, condensation region and NC plug region, there's very little variation in said parameters. Basing on the measured temperature, the local steam mole fraction can be estimated. This allows to plot the condensation heat flux as a function of local gas mixture composition, Figure 6-22. Unfortunately, only a few data points fall between the extremes, and even though the correlation is evidently positive, little can be learned from this data set. Similar issues were present for other sensor locations. To address this issue, a different set of experiments was designed, with continuous NC gas injection, in which a good spatial resolution of the mixing zone was obtained. These results are presented further in the section 6.2.

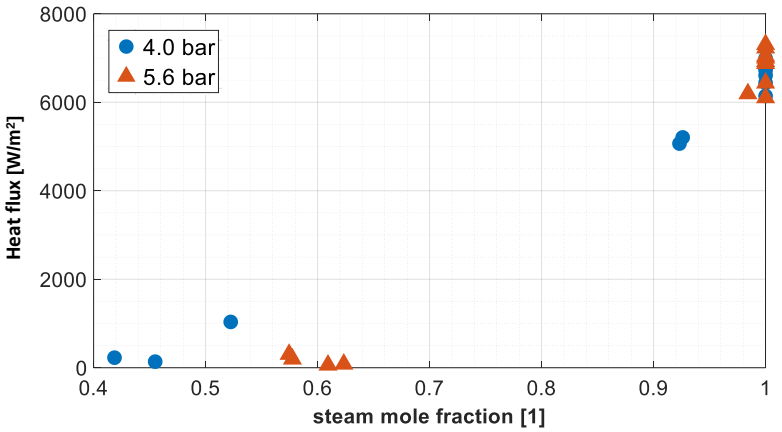

Figure 6-22 Local heat flux as a function of steam mole fraction

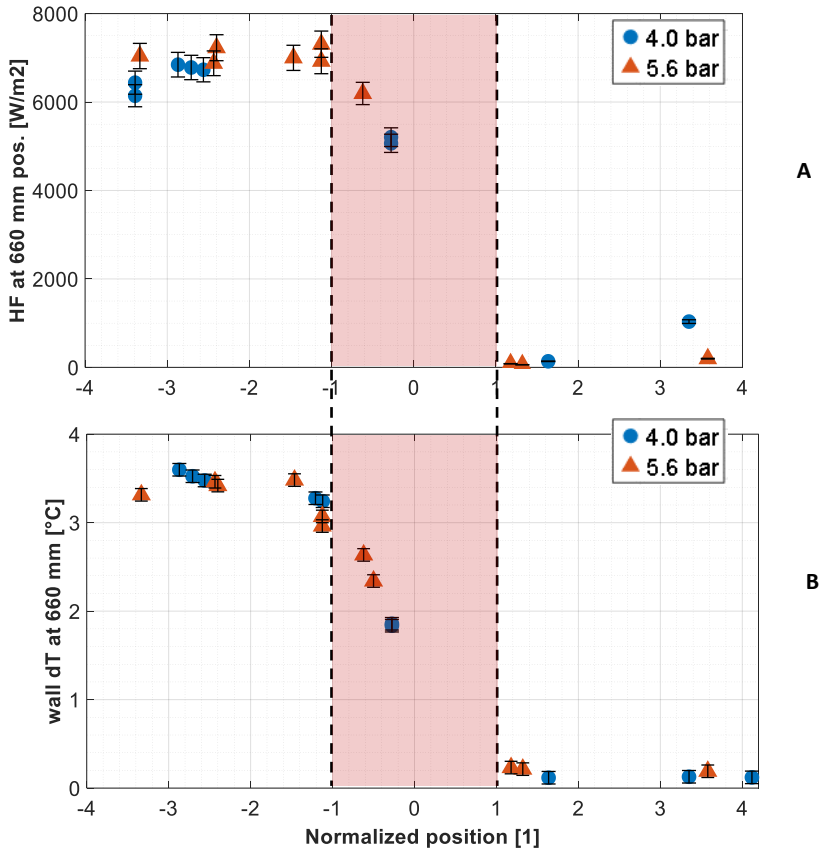

Figure 6-23 Heat flux (HF) (A) and wall temperature gradient (B) in normalized vertical coordinates. For data below -1, sensor is in condensation zone, -1 to 1 in the mixing zone and above in the NC gas plug

6.1.3.3 NC-MFR-PART-X

In this series of tests, the theoretical value of partial pressure of steam remains unchanged between the tests, with a constant amount of steam in the system. On the other hand, the absolute pressure changes but due to very efficient condensation retardation by non-condensables, only a narrow range of 2 to 2.5 bar could have been studied in these tests. As shown on Figure 6-24A, even though the overall pressure (marked in yellow) is lower than in the NC-MFR-ABS-X (marked in blue and red) tests, the condensation length follows the same basic relation to the N_2 content. Moreover, the overall pressure change within this test series is also small, having little impact on observed heat flux measured relative to the position of the mixing layer, Figure 6-24B.

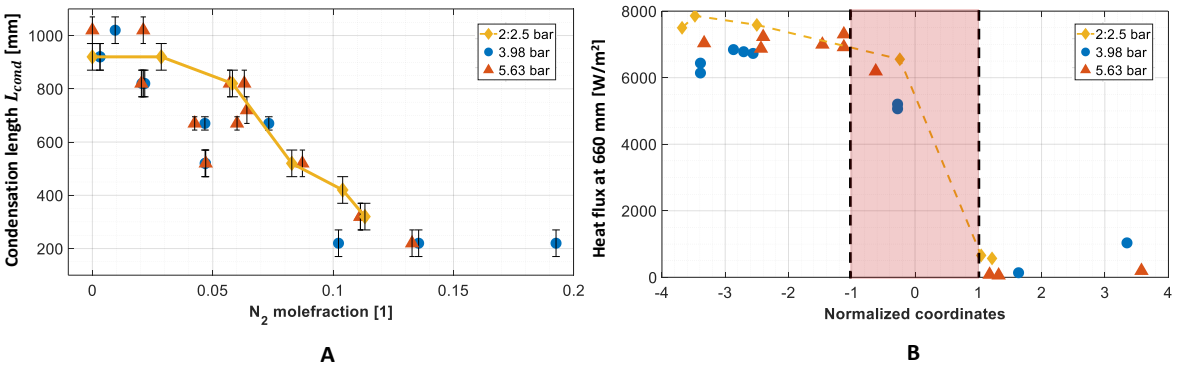

Figure 6-24 Condensation length at varying N2 mole fraction at different test runs (A) and heat flux recorded at 660 mm for the same test runs (B)

When temperature distributions at three different pressure levels and with nearly the same N_2 gas average molar fractions are compared. In Figure 6-25A, it is again visible that the absolute pressure has very little impact, if compared to mixture compositions. Figure 6-25B shows the temperature profiles normalized to range 0-1 with the maximum observed value for each profile.

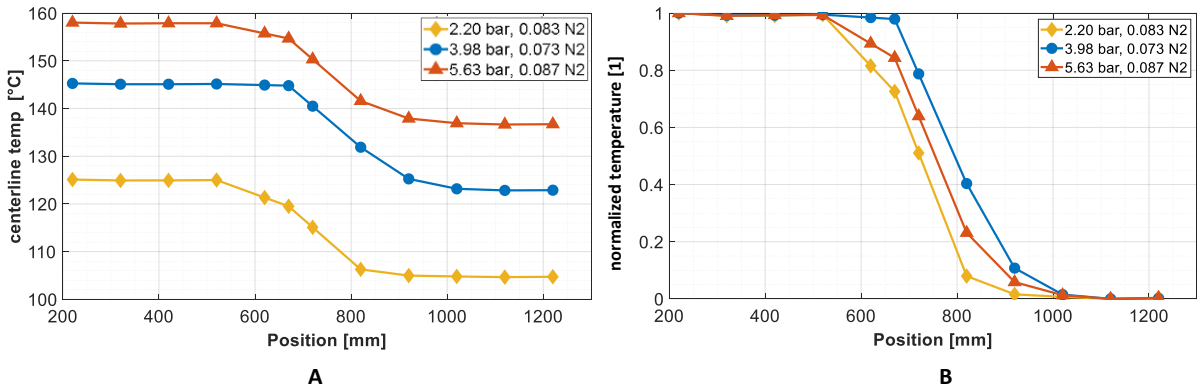

Figure 6-25 Measured (A) and normalized (B) vertical temperature distributions at various pressures

Overall, at all tested pressures, nitrogen behavior followed the same patterns, of forming a plug at the top of the tube, which size was dependent on the average mole fraction. The mixing zone between phases would change vertical localization in the tube, but the size was rather uniform and independent of the non-condensables amount or the test pressure. The decreasing steam content in the mixing zone was reflected in negligible heat flux and wall temperature difference, which can be interpreted as continuously decreasing condensation. This effect can be attributed to continuous steam depletion in the upward direction as well as condensation retardation effect of non-condensable gases. Major reduction was observed at even small NC mole fractions, however these series of tests provided only a few data points in the mixing region.

6.1.4 Impact of NC gases – helium

Up until this point all the experiments described used nitrogen as the investigated non-condensable gas. A series of tests with varying content of helium was setup. Helium and nitrogen have distinct properties, where the density in relation to steam is the most important one. While N_2 is heavier, He is lighter, and this difference can impact the observed gas stratification patterns in the tube.

6.1.4.1 Experiments summary

The same basic pattern was followed as with N_2 experiments, where the pressure was kept constant and average molar content of NC gas was varied between the tests. Coolant properties, i.e. mass flow and wall temperature gradient were also set to the same previously used values. Overview of the experiments is presented in the Table 6-4.

Table 6-4 Helium experiments summary

File name	NC gas mix mole fr.	N_2 fraction in NC gas mixture	Test press.	Test temp.	Coolant temp.	Coolant v. flow	Wall ΔT
Units	[1]	[1]	[bar]	[°C]	[°C]	[m³/h]	[°C]
NC-MFR-ABS-HE-1_5	0.000	0.00	4.00	143.6	123.6	2	20.0
NC-MFR-ABS-HE-2	0.050	0.00	4.00	141.8	121.8	2	20.0
NC-MFR-ABS-HE-2_5	0.100	0.00	4.00	139.9	119.9	2	20.0
NC-MFR-ABS-HE-3	0.150	0.00	4.00	137.9	117.9	2	20.0
NC-MFR-ABS-HE-4	0.200	0.00	4.00	135.7	115.7	2	20.0
NC-MFR-ABS-He-4_1	0.300	0.00	4.00	131.2	111.2	2	20.0
NC-MFR-ABS-He-4_1_5	0.050	0.00	4.00	141.8	121.8	2	20.0
NC-MFR-ABS-He-4_10	0.075	0.00	4.00	140.8	120.8	2	20.0
NC-MFR-ABS-He-4_2	0.500	0.00	4.00	120.2	100.2	2	20.0
NC-MFR-ABS-He-4_2_5	0.100	0.00	4.00	139.9	119.9	2	20.0
NC-MFR-ABS-He-4_3	0.125	0.00	4.00	138.9	118.9	2	20.0
NC-MFR-ABS-He-4_3_5	0.150	0.00	4.00	137.9	117.9	2	20.0
NC-MFR-ABS-He-4_4	0.175	0.00	4.00	136.8	116.8	2	20.0
NC-MFR-ABS-He-4_4_5	0.200	0.00	4.00	135.7	115.7	2	20.0
NC-MFR-ABS-He-4_5	0.225	0.00	4.00	134.7	114.7	2	20.0
NC-MFR-ABS-He-4_5_5	0.250	0.00	4.00	133.5	113.5	2	20.0
NC-MFR-ABS-He-4_6	0.275	0.00	4.00	132.4	112.4	2	20.0
NC-MFR-ABS-He-4_7	0.300	0.00	4.00	131.2	111.2	2	20.0
NC-MFR-ABS-He-4_8	0.350	0.00	4.00	128.7	108.7	2	20.0
NC-MFR-ABS-He-4_9	0.400	0.00	4.00	126.1	106.1	2	20.0

6.1.4.2 *Vertical and horizontal temperature fields*

Condensation rates with increasing average molar fraction of NC gases for nitrogen and helium experiments were compared, Figure 6-26. The clustering of the data points reveals a slight difference between the two, with helium being more efficient at decreasing condensation rates in the test tube. Since stratification of the gas was observed before, this effect can be probably ascribed to how the gases are distributed in the tube and the characteristics of the formed gas plug.

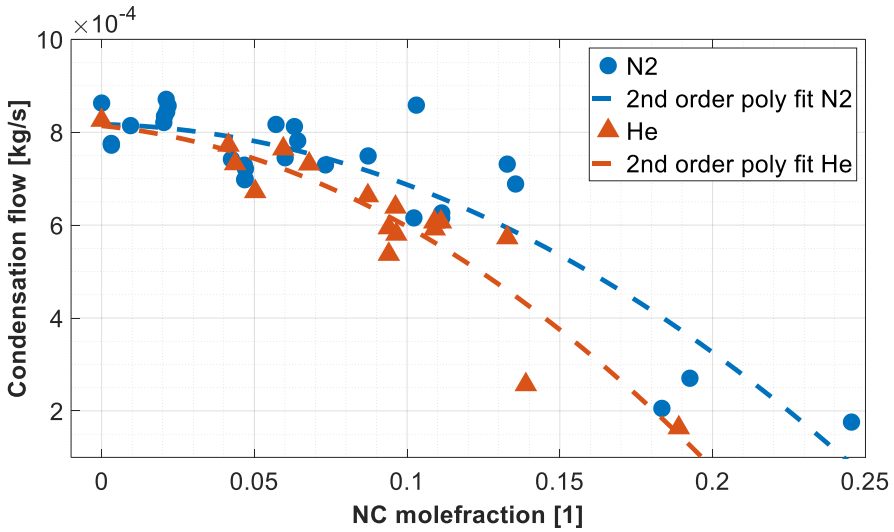

Figure 6-26 Condensation mass flow with increasing average NC mole fraction

This is indeed revealed when condensation and mixing region lengths are compared between pure He and N_2 experiments at 4 bar, Figure 6-27A & B. Evidently, for the comparable overall fractions of NC gas in the test tube, the more pronounced change is visible in Figure 6-27B. On average, the mixing zone was about 1.6 times longer for the heavy N_2 gas. The spread in the observed interface size values was also smaller when compared between experiments. On the other hand, the effect on the condensation length was not clearly discernible in the recorded data.

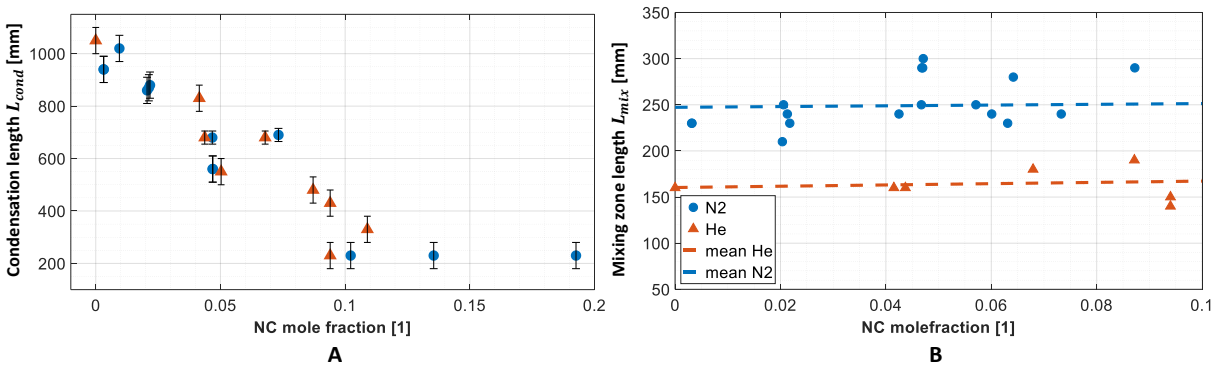

Figure 6-27 Condensation length (A) and mixing zone length (B) for different NC gases

When examining the temperature profiles for very similar mole fractions of N_2 and He in detail, one can observe the shape of the mixing layer changing between the two. For light He gas, the interface region is visibly narrower, Figure 6-28A. There is a slight variation in the average mole fraction between the compared cases. For the same two cases, the dynamics of the recorded data, expressed as a standard

deviation of temperature recorded by each thermocouple, are very different, depending on which NC gas is present, Figure 6-28B. The increase in the local temperature variation can be attributed to mixing between cold gas plug and hot fresh steam arriving from the tube's bottom. Therefore, the mixing region is not only wider for nitrogen cases, but also much more dynamic.

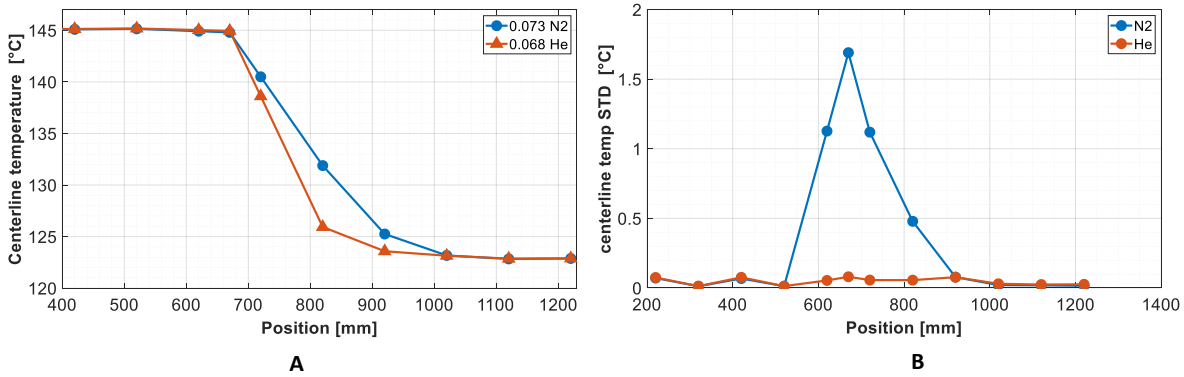

Figure 6-28 Temperature (A) and standard deviation (B) comparison between N2 and He tests at very close average mole fractions (0.068 for He and 0.073 for N_2) at 4 bar

When observed in normalized coordinates with data aggregated over many recordings but investigated at a singular location, the heat removal phenomena in the mixing regions seem to follow the same trends for He and N_2, Figure 6-29A & B. The decrease in the wall temperature gradient and recorded heat flux is roughly linear, when moving along the mixing layer. Again, limited data points within this region provide only an imperfect insight into the actual behavior within.

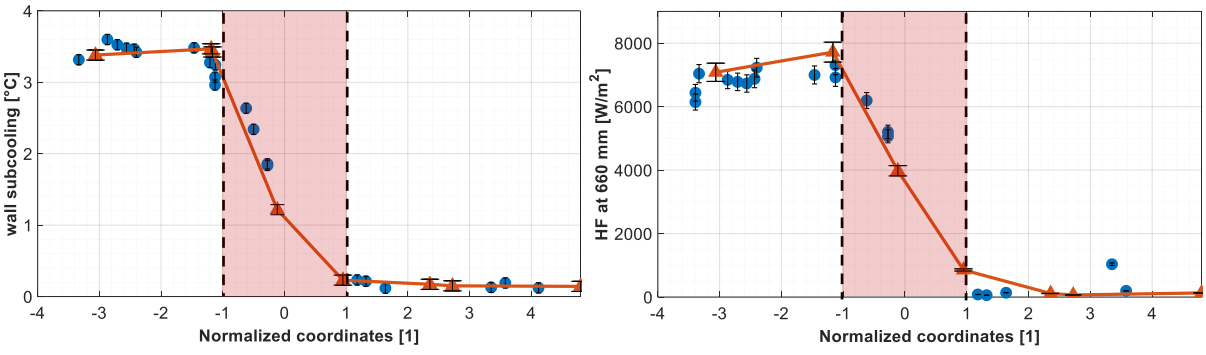

Figure 6-29 Wall temperature gradient (A) and heat flux (B) at the 660 mm elevation in normalized coordinates with N_2 and He

6.1.5 Impact of NC gases mixture composition

Steam interaction with NC gases, as observed in previous experiments, is highly affected by the type of the gas injected in the test tube. Although the pronounced vertical stratification occurs for both, the type of interface formed differs significantly. This series of experiments was designed to investigate the mixing behavior when a mixture of N_2 and He is used instead of a pure single gas. Composition of the mixture was varied between the experiments, to analyze the different contribution of each gas species based on its fractional content.

6.1.5.1 Experiments summary

To obtain a clear picture of the NC gases ratio impact on condensation and mixing process, all parameters but the ratio was kept constant throughout all the tests. The mixture composition was varied from pure helium to pure nitrogen with 0.25 fraction steps. Maintaining the average mole fraction proved to be the biggest challenge, as adjusting the proportions was a laborious manual process, contingent on numerous temperature and pressure readings. Thus, slight variation is present in the data, Figure 6-30.

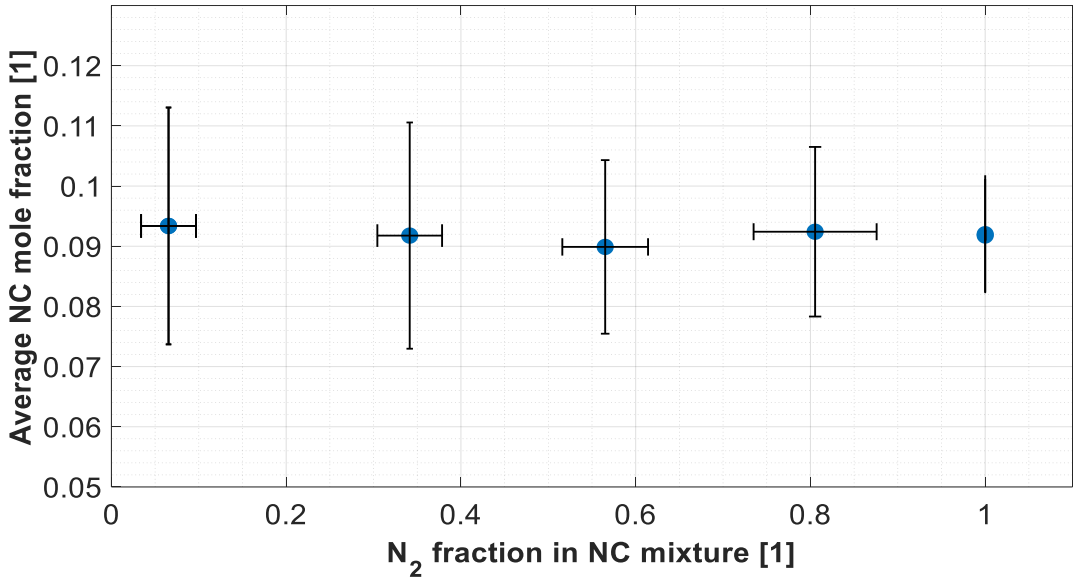

Figure 6-30 Average total mole fraction of non-condensables in the test tube at an increasing N_2 fraction in the N_2 / He mixture

All the data fall in the interval of 0.0899 to 0.1014 with an average 0.0931 and a standard deviation of 0.0029. The mole fraction estimation error is much more significant than this variation, due to the nature of the calculation, as explained in detail in the chapter 5.3, Table 6-5 shows the summary of conducted experiments.

Table 6-5 Varying NC mixture composition experiments summary

File name	NC gas mix mole fr.	N_2 fraction in NC gas mixture	Test press.	Test temp.	Coolant temp.	Coolant m. flow	Wall ΔT
Units	[1]	[1]	[bar]	[°C]	[°C]	[m³/h]	[°C]
NC-CMP-1	0.10/0.092	0.00/0.06	5.00	147.9	127.9	2	2
NC-CMP-2	0.10/0.092	0.25/0.34	5.00	147.9	127.9	2	2
NC-CMP-3	0.10/0.090	0.50/0.56	5.00	147.9	127.9	2	2
NC-CMP-4	0.10/0.092	0.75/0.81	5.00	147.9	127.9	2	2
NC-CMP-5	0.10/0.092	1.00/1.00	5.00	147.9	127.9	2	2

6.1.5.2 Condensation flow and temperature distribution

Even though the average mole fraction remained close to constant for all test runs, a variation in condensate flow was observed, Figure 6-31A. When pure helium case is compared with pure nitrogen, the condensate mass flow increased by a 27.4%. The trend seems to approach a plateau the more the mixture composition approaches pure N_2. Similarly, vertical temperature distribution in the tube was visibly affected, Figure 6-31B. For the heavy gas, observed decline in temperature is gradual and over considerable distance. However, when larger percentage of He is present, the decline in temperature is immediate and the profile is sharp, indicating even more heavily stratified gas distribution in the tube. The interface between pure steam condensation region and the NC gas plug also appears closer to the tube inlet.

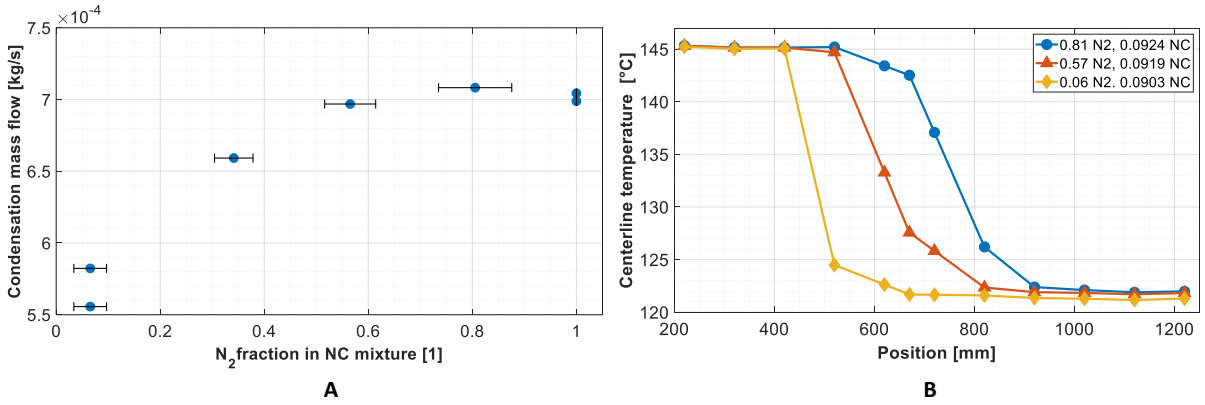

Figure 6-31 NC mixture composition impact on condensation mass flow (A) and temperature distribution in the tube (B)

Therefore, both, condensation and mixing zone lengths were affected, Figure 6-32. The gas mixing region length decreased threefold for He compared to N_2. At the same time condensation length also decreased by a but here the data spread is more pronounced and the effect less significant. This effect could be explained by varying density of the two gases and thus bouncy effects. For lighter gas, the tendency to interact with steam is greatly reduced. The intermediate cases fit roughly in between the extremes.

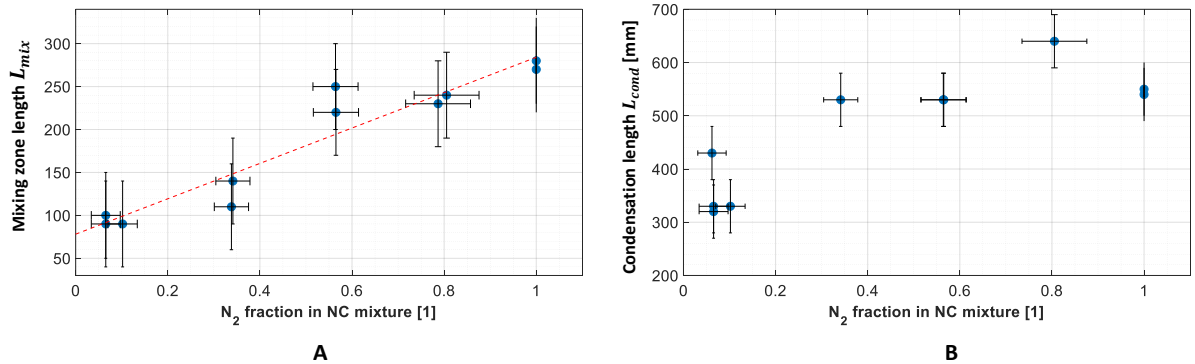

Figure 6-32 NC mixture composition impact on mixing zone length (A) and condensation length (B)

When the temperature profile in the mixing zone are overlaid, the difference becomes even more apparent, Figure 6-33A. The observations of time-averaged values can be further expanded by comparing the temperature variation during the steady-state. Figure 6-33B shows a contrast of recorded temperature profile variation for both gas species, expressed in terms of data standard deviation, as recorded by each thermocouple. The oscillations in the mixing zone are much more pronounced for N_2, which points to

more efficient penetration of steam in the upper parts of the tube. Again, when intermediate cases are investigated, there is a continuous and gradual change between the two extremes.

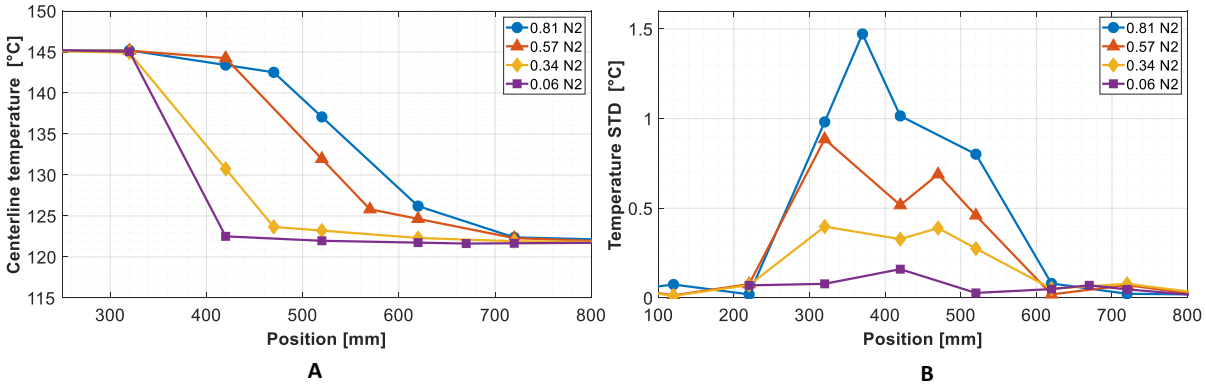

Figure 6-33 Temperature (A) and temperature standard deviation (B) distribution in the mixing zone at various gas fractions

As previously described, the temperature and heat flux behavior in the mixing region can be analyzed in normalized coordinates, with respect to the region center. Figure 6-34 presents data aggregate from various thermocouples and different tests performed with the scope of this experimental set. As one can see, even though the overall shape of the distribution is changing when the ratio of heavy to light gas is varied, but the relative temperature drop seems to follow the same pattern as observed in the previous experiments. For mixtures with higher He content, the gradient is just compressed in a smaller region.

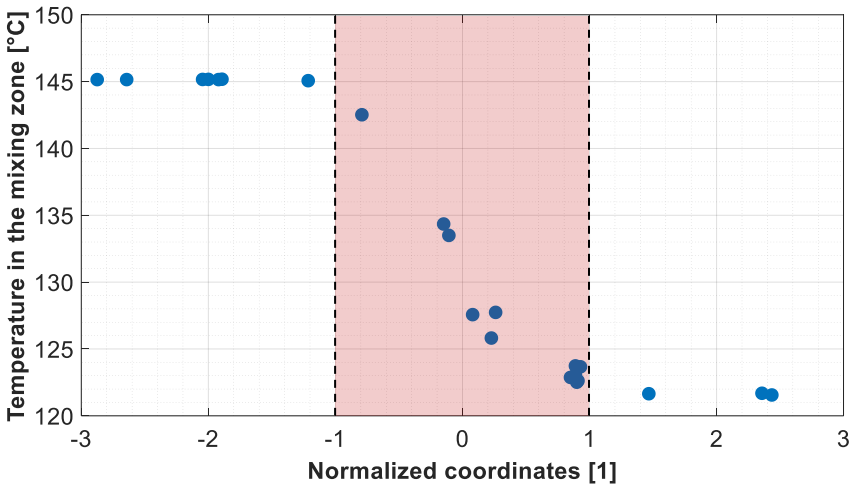

Figure 6-34 Temperature drop in the mixing zone in normalized coordinates

6.1.5.3 *Effects in the pure steam condensation region*

All the above-mentioned effects have little impact of the phase change process occurring in the pure steam zone. As one can see, the temperature values for this region remain virtually unchanged for all the experiments, and the values are very in terms of standard deviations. There is a difference between the range of non-condensable gases penetration into the upcoming steam flow, but below that no effects are discernible. Figure 6-35 shows horizontal temperature distributions across the test tube measured below the mixing region. Zero value indicates the tube's wall, and since the profiles were stable in the region close to the wall, the presented graph extends to only 3 mm.

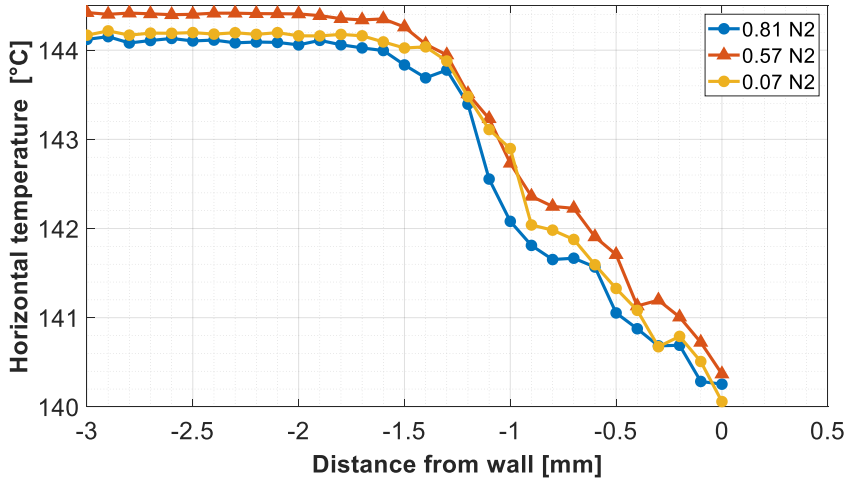

Figure 6-35 Horizontal temperature distribution in the test tube below the mixing region

With these experiments, it was very difficult to adjust the NC gas fraction so that the mixing region would end up at the elevation where the horizontal temperature measurement was taking place. Therefore, another set of experiments was designed and conducted, to address this issue, described in the section 6.2.

6.2 Continuous injection tests

As described previously, the three characteristic regions observed during every experimental run were difficult to capture and resolve spatially, due to the limits of instrumentation array. Therefore, a different set of tests was designed to address this issue. Here, due to continuous feeding of a gas into the test tube and a constant rate, NC gases are carried upwards with the continuous flow of steam and accumulate at the top of the tube. The plug of NC gas expands downwards in time and the passage of the mixing region can be observed in detail at multiple measurement points simultaneously. Therefore, the instrumentation spatial resolution was not limited by the physical arrangement of the sensor array.

6.2.1 Experiments summary

The test tube is first purged and almost all residual gases are removed – residual observed pressure after using the vacuum pump is below 0.01 bar, translating to less than 0.00375 average NC gas mole fraction at test conditions. Then, the primary loop is filled with water and the heating is started. After reaching test pressure of 4 bar and verifying steady state, the valve (VM9704, schematic in the appendix section 10.1) connecting the steam tank to the NC gas supply tank is opened. A steady flow of NC gas is facilitated by pressure difference, set to 0.2 or 0.5 bar, which resulted in an average mass flow rate of 0.000078 mol/s and 0.000227 respectively. To compensate for NC gas addition, the test pressure was monitored, and electrical power was adjusted accordingly. The tests were conducted with nitrogen, helium, and 1:1 molar mixture of both. The summary of the experiments is presented in the Table 6-6.

Table 6-6 Overview of continuous injection experiments

File name	NC tank pressure	Avg. gas injection rate	N_2 fraction in NC gas mixture	Test press.	Test temp.	Coolant temp.	Coolant v. flow	Wall ΔT
Units	[bar]	[mol/s]	[1]	[bar]	[°C]	[°C]	[m^3/h]	[°C]
CIN-He-4_2	4.2	0.000085	0.0	4.00	147.91	127.91	2	20
CIN-He-4_5	4.5	0.000226	0.0	4.00	147.91	127.91	2	20
CIN-N2-4_2	4.2	0.000070	1.0	4.00	147.91	127.91	2	20
CIN-N2-4_5	4.5	0.000236	1.0	4.00	147.91	127.91	2	20
CIN-MIX-4_5	4.5	0.000220	0.5	4.00	147.91	127.91	2	20

6.2.2 Mixing zone passage – calculations

To properly resolve the mixing zone, it's traversing velocity had to be estimated. It was calculated in two ways – by comparing the time at which temperature decrease and oscillations were observed by subsequent thermocouples and by measuring pressure drop in the NC gas supply tank.

The first method is straightforward and involves establishing a criterion to recognize that a mixing layer passage was detected by a given thermocouple. The devised algorithm is based on smoothing and normalizing the recorded temperature data to the range 0:1 and finding all sensors which belong within +/- 3% of the median value. Since the mixing zone passage is not only noticeable as a temperature drop, but as an increase in temperature oscillations, the estimated range was verified with these readings as well. Figure 6-36 shows an example of the algorithm performance. The first of the black dashed lines marks the arrival time of the mixing region t_{AR}, the solid green line indicates the highest temperature standard deviations (STD) and the second black dashed line specifies the departure time t_{DEP} of the region. The difference between t_{AR} and t_{DEP} is the residence time of the mixing front t_{RES}, observed at a given thermocouple.

The traversing velocity was then estimated based on the distance between subsequent thermocouples and the estimated mixing region arrival time:

$$v_{mix} = \frac{H_{TCn} - H_{TCn+1}}{t_{ARn+1} - t_{ARn}} \qquad (75)$$

where H_{TCn} and H_{TCn+1} describe vertical positions while t_{ARn}, t_{ARn+1} mixing zone arrival times for the subsequent thermocouples. This calculation was repeated for every thermocouple, thus for a given recording, any variation in the v_{mix} was also captured.

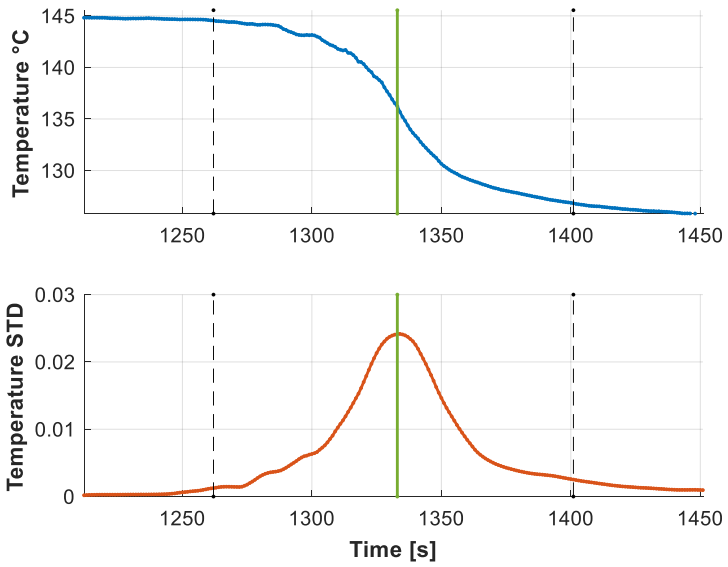

Figure 6-36 Mixing region as resolved by a single thermocouple

The second method, based on the measurement of pressure and temperature in the NC gas tank, relies on continuous estimation of the amount of NC gas moles amount in the tank. The difference at a given time t_1 and the moment the connecting valve is opened t_0 is the amount transferred to the test tube:

$$n_{NC}(t_1) = n_{NCTank}(t_0) - n_{NCTank}(t_1) \qquad (76)$$

The gas enters the primary circuit and accumulates at the top, thus using the ideal gas law and value of n_{NC}, the growing volume of the plug could be calculated. However, this step must include an estimate of the molar fraction of residual steam remaining in the top of the tube and mixed with the NC gas. Using the temperature of the gas plug, steam tables (IAPWS-IF97 implementation) and assuming thermodynamic equilibrium between the phases, partial pressure of steam can be obtained, (eq. (77)). Along with the measured total pressure P_{abs}, molar fractions can be estimated (eq. (78)) and the corresponding amount of steam present in the plug can be included in the calculation (eq. (79)).

$$P_{partH2O} = IAPWS\_IF97(T_{plug}) \quad (77)$$

$$X_{H2O} = \frac{P_{partH2O}}{P_{abs}} \quad (78)$$

$$n_{plug} = n_{NC}/(1 - X_{H2O}) \quad (79)$$

Finally, including information about the tube cross-section A_{cross}, the position of the mixing front H_{fr} can be precisely estimated as a function of time:

$$H_{fr}(t) = \left(\frac{n_{plug}(t)RT_{plug}(t)}{P_{abs}(t)}\right) / A_{cross} \quad (80)$$

The slope of the obtained function is the traversing velocity of the mixing front. A short time delay exists between the moment when NC gas feeding began, and the temperature drop is registered by the highest thermocouple, but the calculation accounts for that time and the corresponding injected NC gas mass is included in the total value. A more sophisticated approach using Redlich-Kwong equation of state instead of the ideal gas law was tested and the results where within 1% agreement. However, this method was much more computationally expensive to perform.

The mixing layer position obtained with both methods is in good agreement, Figure 6-37.

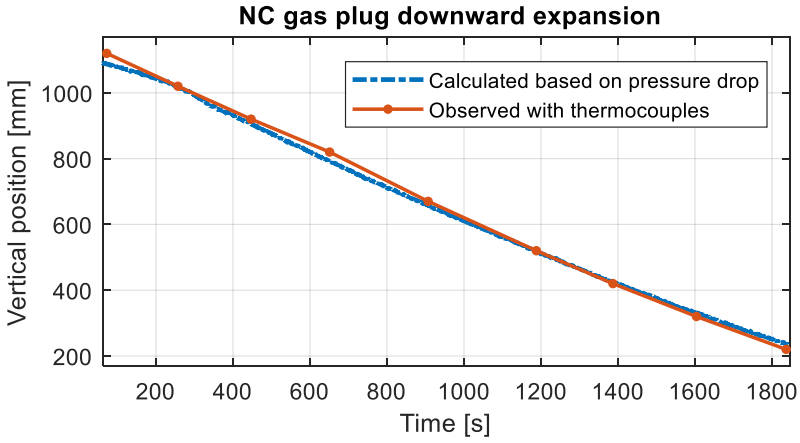

Figure 6-37 Mixing layer front vertical position in time (experiment CIN-He-4_2)

The estimate of the mixing layer velocity, along with the front residence time at every thermocouple allow to recalculate the length of the mixing layer:

$$L_{mix} = v_{mix} * t_{res} \quad (81)$$

This calculation was performed for every sensor of the thermocouple array, to observe potential change in the region size. Figure 6-38A shows the mixing zone shape in time coordinates (A) and recalculated length (B), as observed by a single thermocouple. Green dashed line is a moving average filter applied to the signal, to facilitate the viewing.

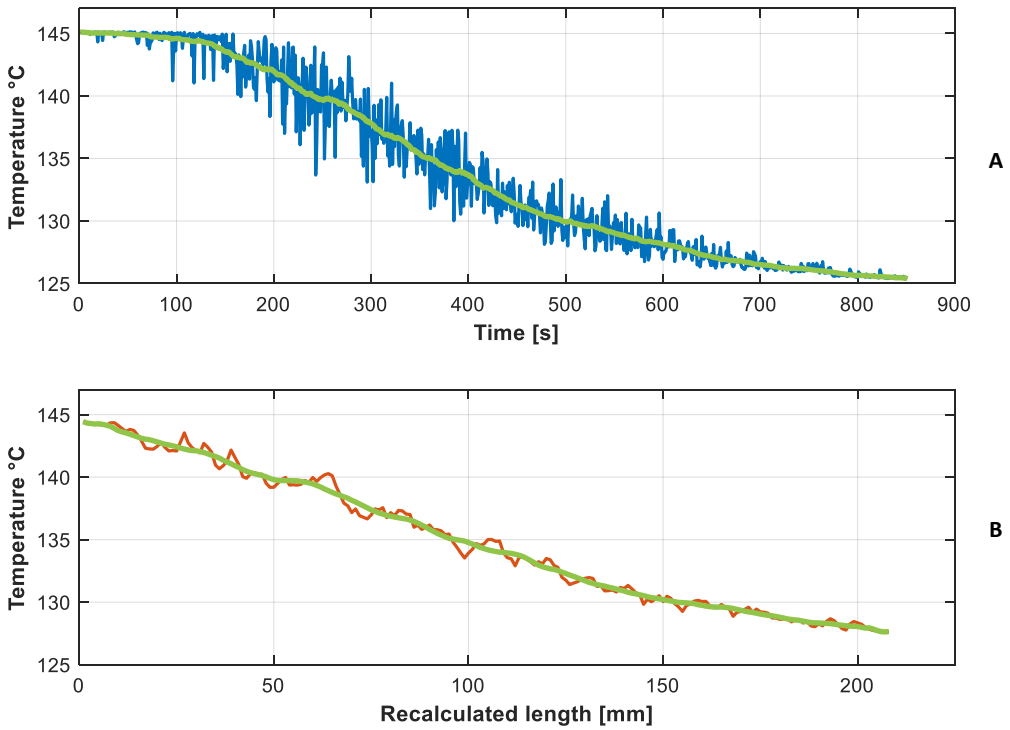

Figure 6-38 Mixing zone in time and recalculated length coordinates (experiment CIN-N2-4_2)

6.2.3 Mixing zone – He and N_2 effects

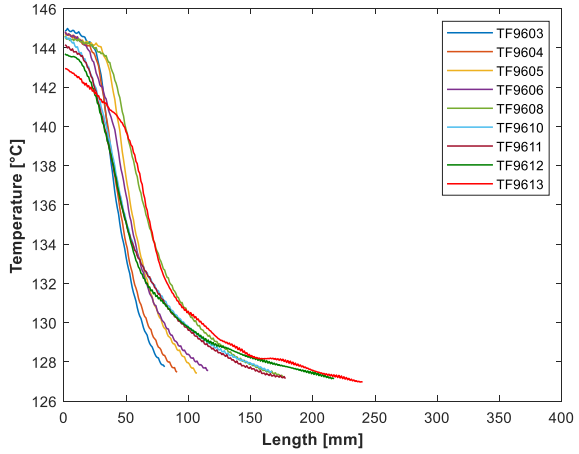

Figure 6-39 Mixing zone length for every thermocouple - CIN-HE-4_5

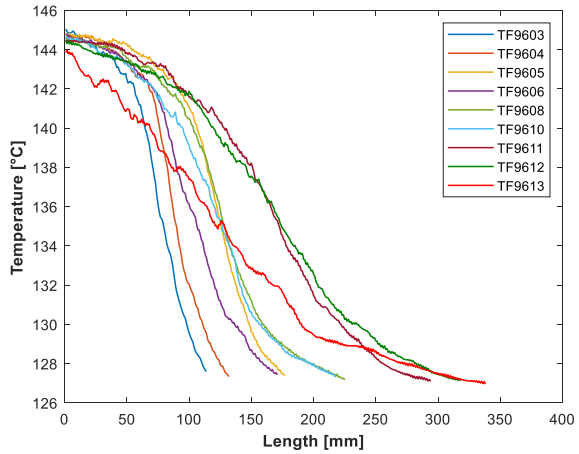

Figure 6-40 Mixing zone length for every thermocouple - CIN-MIX-4_5

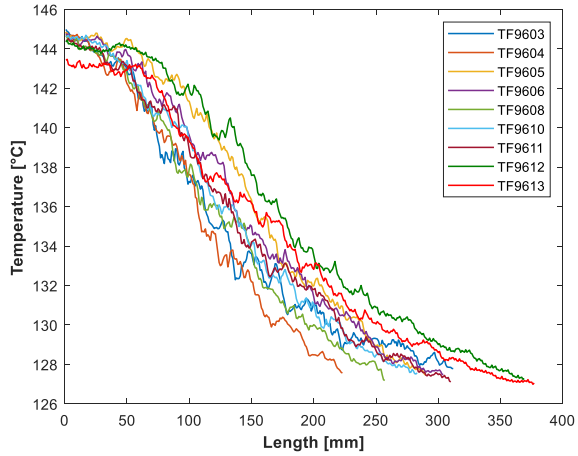

Figure 6-41 Mixing zone length for every thermocouple - CIN-N2-4_5

Figure 6-39, Figure 6-40 and Figure 6-41 present the recalculated mixing zone temperature profiles for injection tests with pure helium, 1:1 mole ratio mixture and pure nitrogen experiments respectively. Both the size and the dynamics of the mixing zone are captured and convoluted in these measurements, but the dissimilarities observed in steady-state experiments are confirmed.

Helium forms sharper and less dynamic mixing zones when compared to the heavier nitrogen. The behavior of the NC gas mixture possesses characteristics of both its constituent gases, in terms of mixing region size as well as dynamics.

Moreover, there is a slight variation of the length as registered by different sensors. The higher the sensor is located in the tube, the bigger the region's size. As shown in the, Figure 6-42A, this variation is also reflected in the residence time and the traversing velocity.

This inconsistency is largest for the mixture of gases. One of the reasons for the existence of such variation could be the changing NC gas injection rate, due to reduction in overpressure in the NC tank, which is the driving force of the process, Figure 6-42B. Another explanation could lie in the decreasing steam velocity – as a greater length of the tube becomes plugged, the heater must compensate by reducing the delivered power, resulting in less evaporative mass flux, and overall lower velocity of the steam/NC gas mixture entering the tube. This decreases the flow momentum and overall turbulence, negatively affecting mixing between gas phases and increasing stratification. Indeed, there seems to be positive correlation between flow velocity and mixing region, Figure 6-43A, observed for every injected composition. At the same time, there is not a

clear relation when comparing the temperature standard deviations, Figure 6-43B. It is important to mention that the standard deviation was calculated for the whole observed length of mixing zone passage for each thermocouple. To exclude the impact of gradual temperature decrease, high-pass filter with a cutoff frequency of 0.1 Hz was applied to the data.

Accounting for the observed differences, the observed mixing length varied between 80 to 240 mm for He, 110 to 340 mm for the mixture and 190 to 380 mm for pure N_2. Compared to steady state experiments, where average lengths were 250 mm and 160 mm for pure N_2 and He respectively, the results are in good agreement, when accounting for limited resolution of the thermocouple array.

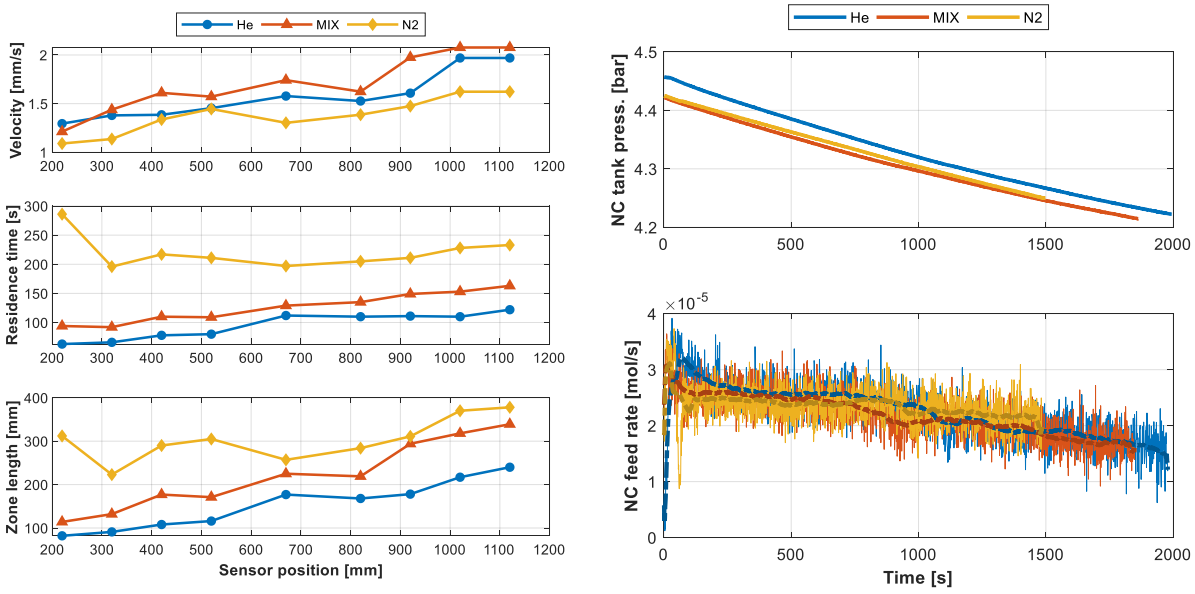

Figure 6-42 Mixing zone velocity, residence time and length for different NC gases (A); pressure drop in NC tank and recalculated NC gases feed rate (B). Experiments CINT-He-4_5, CINT-MIX-4_5, CINT-N2-4_5.

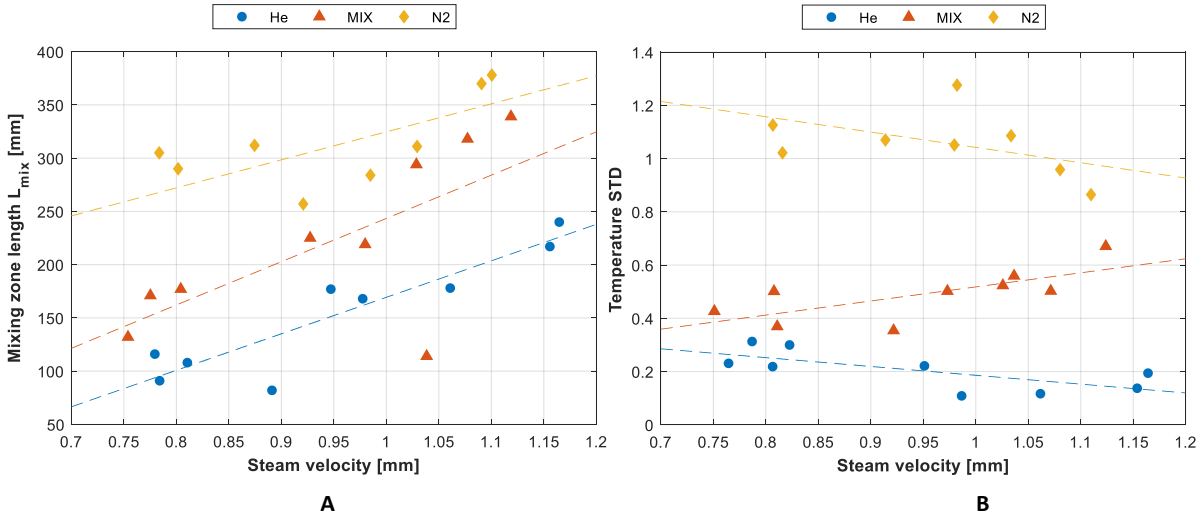

Figure 6-43 Mixing zone length (A) and temperature oscillations (B) with increasing steam velocity. Experiments CINT-He-4_5, CINT-MIX-4_5, CINT-N2-4_5. Linear trendlines added to support interpretation.

When comparing data observed with a single thermocouple, the differences between gas mixture behavior becomes even more apparent, Figure 6-44A. For observation clarity, Figure 6-44B shows temperature oscillations for every composition with applied high-pass filter with 0.1 Hz cutoff frequency.

Besides temperature measurement, local heat flux recordings also display significant difference. If nitrogen is present, the arrival of the region is accompanied by slight increase in the observed values.

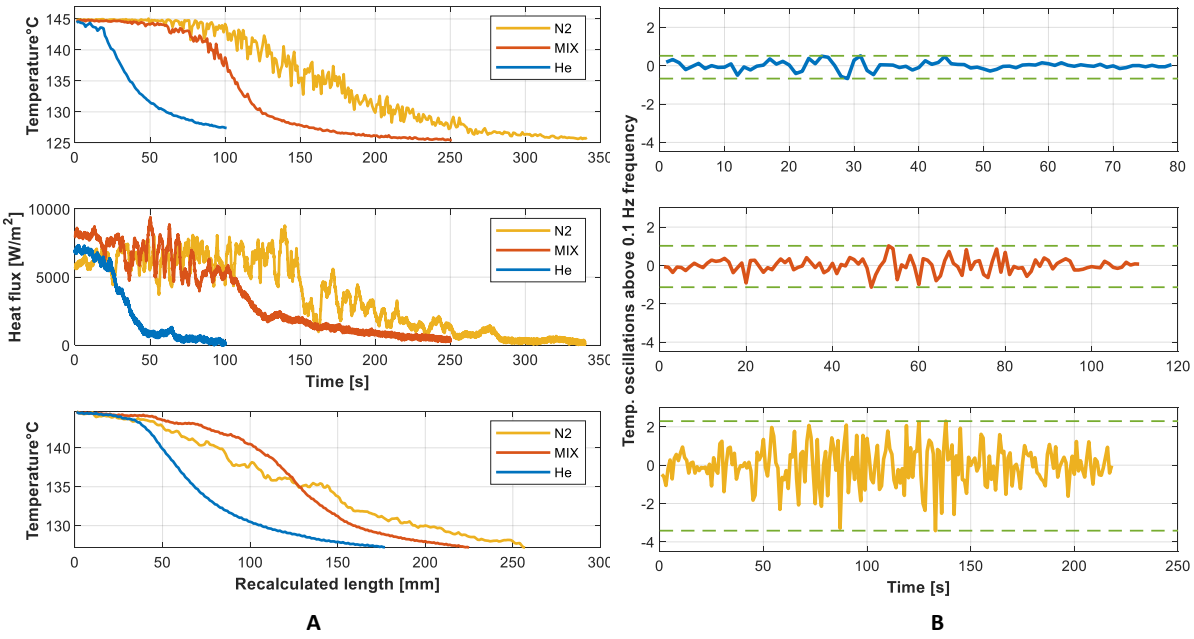

Figure 6-44 Mixing zone passage observed in temperature and heat flux signals and the recalculated length (A) and oscillations of temperature measurement over 0.1 Hz (B). Experiments CINT-He-4_5, CINT-MIX-4_5, CINT-N2-4_5.

One explanation could be attributed to increased turbulence in the region as well as decrease in the liquid film thickness covering the tube wall. Indeed, when observed with MCT probe, there are noticeable changes in the registered signal. Keeping in mind the extensive processing necessary to extract any useful signal front MCT probe data, the comments given here are done very tentatively – only qualitative observations are provided. First, considering signals amplitude, shortly after mixing region arrival, an occasional increase in signal is observed, Figure 6-45A. This goes against the intuition that with decreased film thickness signal should follow suit. However, this effect could potentially be explained by transition from film to dropwise condensation mode. During the probe development it was observed that if a film would breakup over the probe surface and drops started forming, an increase in the registered signal was observed. The identified cause of this phenomenon was interrupted electrical path to the conductive tube wall, surrounding the probe, which acted as a parasitic electrode, as explained in the chapter 3.4. Secondly, the signal dynamics undergo significant changes, Figure 6-45B. In the frequency domain no dominant frequencies of oscillations can be identified, but overall oscillations in the signal first significantly increase with the arrival of the mixing region, followed by a sharp decrease after it's departure. This further supports the explanation that the film-wise condensation is substituted with drop-wise regime, followed by dry out in the NC plug.

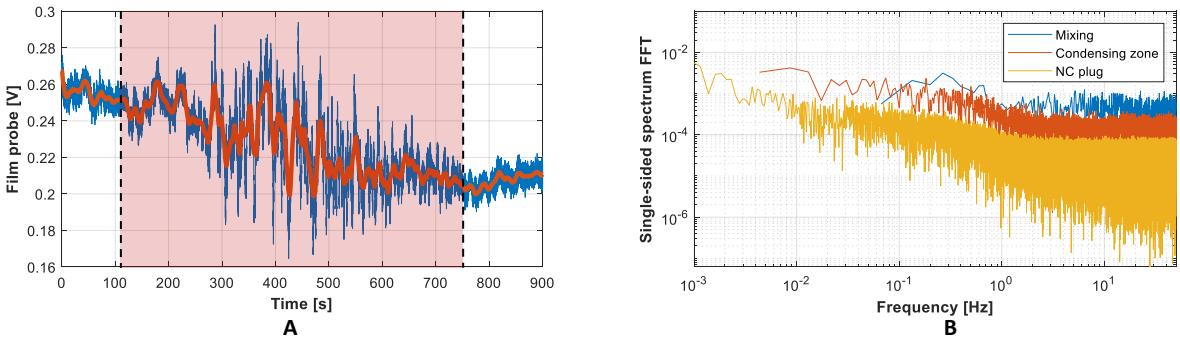

Figure 6-45 Mixing region arrival and departure observed with film probe in time domain (A) and frequency domain (B), experiment CINT-N2-4_2

The observed increase in the heat flux signal is temporary, accompanied with fervent oscillations. Signal decreases close to zero as the gas plug covers the sensor area. The difference between fluctuations when only helium is injected is rather striking (Figure 6-44B), and again confirms that the lighter gas forms much sharper and less volatile interface region. Heavier gas allows for continued steam condensation in the interface at a much higher rate.

6.3 Liquid film and thermal boundary layer

Due to hindering the condensation process, non-condensable gases have a direct impact on the behavior on the liquid film formed at the test tube wall. At the same time, variation in the film thickness in the steam-rich regions increases the overall thermal resistance to heat removal through condensation. In this chapter, the data gathered during previously discussed experiments is analyzed from the point of view of the behavior of the liquid layer. Additionally, temperature distributions across the test tube, measured with the MCT probe are examined, to establish the impact of non-condensable gases mole fraction and species on the steam condensation.

6.3.1 Traversing probe

Temperature profiles presented are time-averaged, as described in the chapter 3.4. To supplement the analysis, stability of the measured signal was assessed with standard deviation, calculated for each horizontal position point separately. Figure 6-46 shows the observed profiles for each of previously identified regions in the test tube. For the condensation zone measured temperatures were very stable. A significant drop was observed in a proximity to the wall. In this region, somewhat increased instabilities were also observed. This confirms the existence of well-developed thermal boundary layer. What remains unclear however, is what portion of this layer is actually comprised of liquid condensate film.

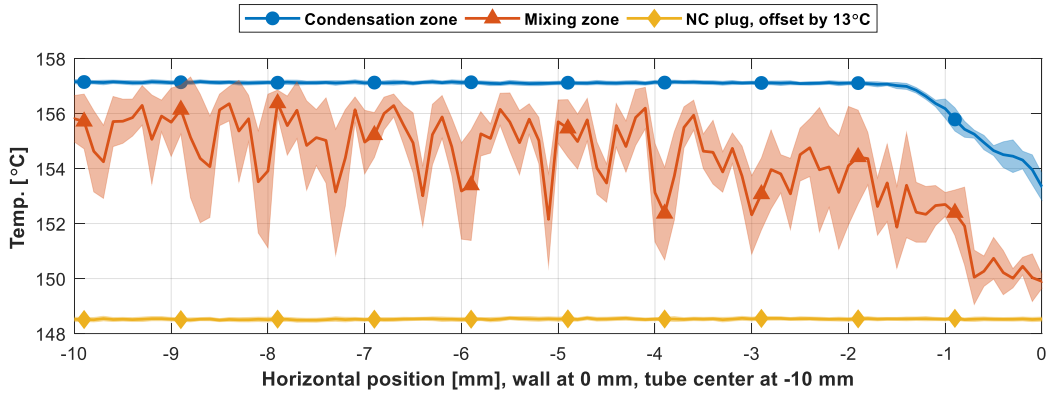

Figure 6-46 Horizontal temperature distributions at various NC gas concentrations. Filled regions represent standard deviation range of the signal. Temperature of the NC plug was offset with +13°C for readability. Experiments NC-MFR-ABS-N2-6-2, -2_5 and -4.

When the movable probe was located in the mixing region, measured profiles displayed high variations at every point throughout the tube cross-section. A temperature drop was still observed towards the tube's wall. Figure 6-46 presents data for experiments with pure N_2, and as was previously established, high degree of turbulence, and hence temperature oscillations is to be expected in the mixing region, as further supported by this observation. At the same time reconstructed profiles in the NC gas plug show uniform temperature values, with no discernible cooler region next to the wall. Thermal equilibrium exists in this region, as was previously observed, and no heat exchange takes place.

Figure 6-47 depicts temperature standard deviation calculated for each position across the tube. Clearly, the mixing region is the most dynamic of the three, but there is also some oscillation in the region close to the wall in the condensation zone. This might correspond to the liquid film waviness – as the temperature of the film is closer to the tube wall, and the surrounding gas layer slightly higher, the increase in variation suggests that in this region, the traversing thermocouple would periodically encounter cooler waves of the condensate.

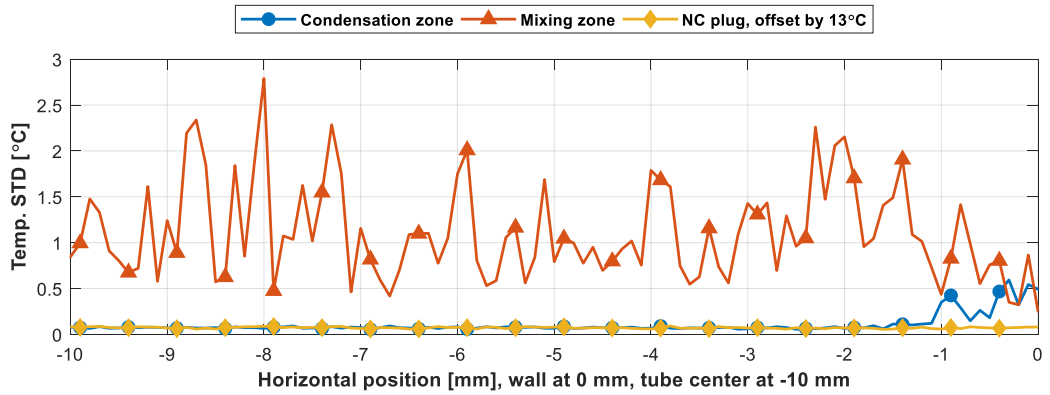

Figure 6-47 Local temperature oscillations expressed with standard deviation at various NC gas concentrations

To further investigate this effect, a comparison was made between the temperature signal and the simultaneously measured voltage on the traversing thermocouple shield. From this measurement, a horizontal "voltage" profile was reconstructed using the same approach as for the temperature. Figure 6-48

presents comparison between the two. Towards the wall, the time-averaged observed voltage values increase, starting at the same position as the observed temperature drop.

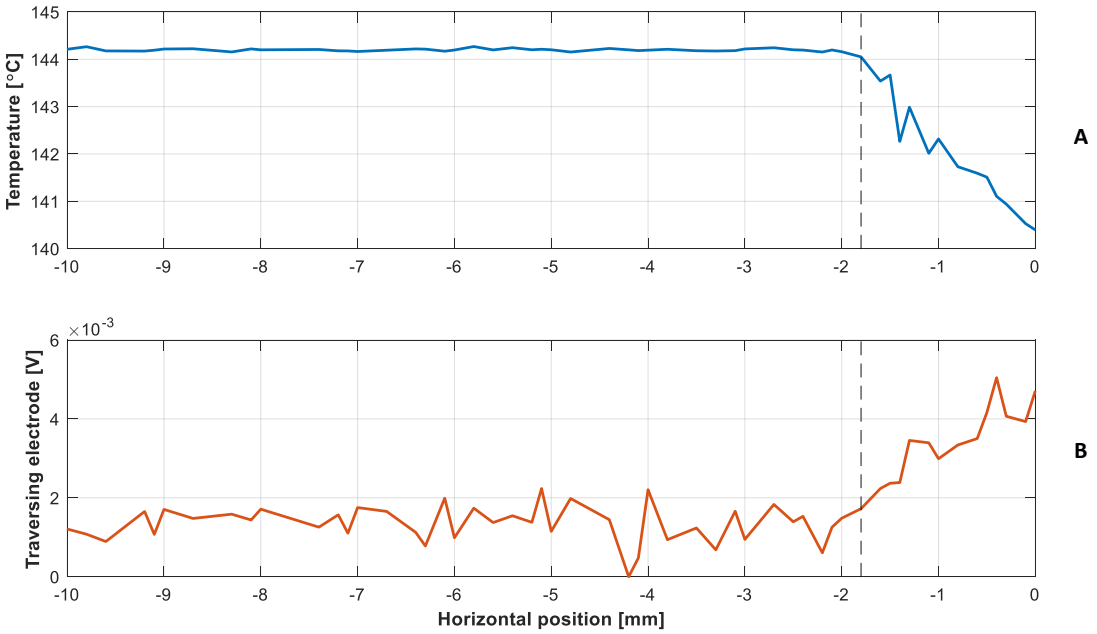

Figure 6-48 Thermal boundary layer observed with temperature (A) and voltage (B) measurements

Contrary to temperature measurements, no increase in signal standard deviation was observed in voltage measurement. This can be due to the low signal-to-noise ratio of this channel, which resulted in large signal oscillations at all horizontal positions. Furthermore, the change in observed voltage was very small (~0.003 V) compared to the voltage response of fixed electrode array, possibly due to much higher resistance of this particular one. Little information whether the electrode encountered liquid film can be extracted thus far.

6.3.2 Fixed array and electrical measurements

During initial testing of the fixed array moving traversing thermocouple it was observed that signal registered by the fixed part would decrease when the traversing thermocouple would encounter the liquid film. It was understood that underlaying mechanism lies in the parasitic current escaping to ground through the thermocouple shielding. When comparing time-resolved signals gathered with traversing and fixed electrodes, this phenomenon becomes evident, Figure 6-49. Due to significant noise in the data, extensive filtering was necessary to extract useful information from the recorded signal. Here, a median filter of order 10000 was applied – considering the data acquisition rate of 1 kHz, this means that for every point, the neighborhood of +/- 5 s was considered during filtering. This range was deemed reasonable, as the traversing velocity of the probe was low (>0.03 cm/s), and the average residence time of the probe in the thermal boundary layer was around 80 seconds.

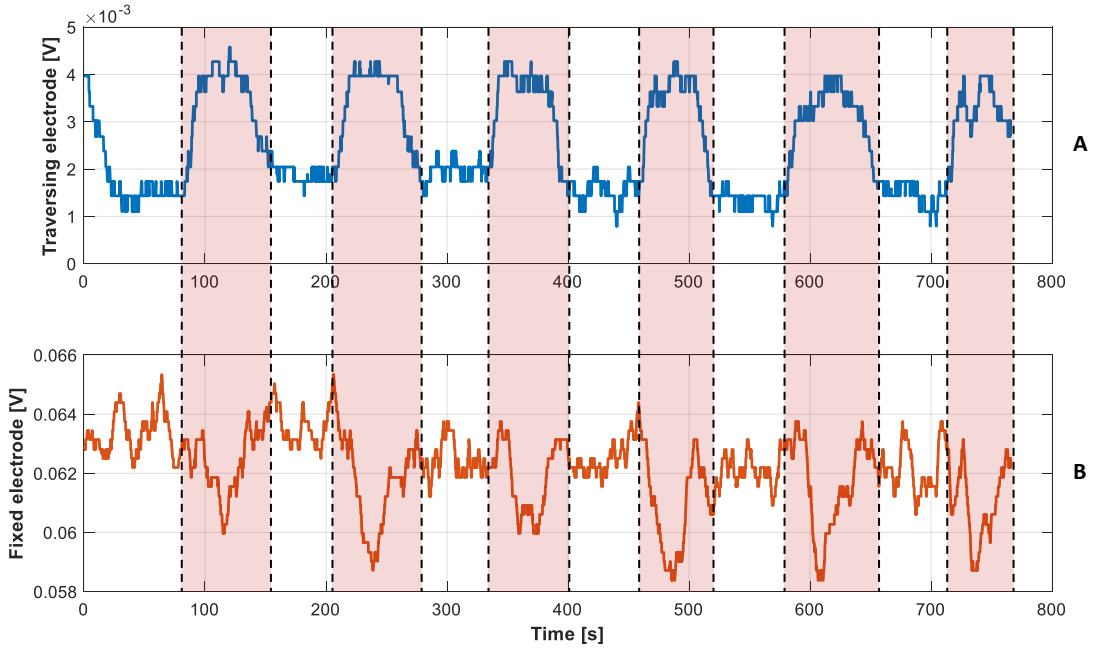

Figure 6-49 Voltage measured with traversing (A) and fixed (B) electrode. Median filter of the order 10000 was applied to both signals, which were recorded at 1kHz. Experiment NC-MFR-ABS-1_4_LF.

The time between registering subsequent peaks as observed on the graphs varied between 123.3 and 130.5 seconds, with an average of 126.2 s. When observed in the frequency domain, after applying a discrete Fourier transformation (DFT) algorithm to both the signals, the peak corresponding to the probe movement is visible in both spectra. It is also the most significant peak that can be identified, Figure 6-50.

The voltage observed with the traversing electrode increased slightly faster than the fixed electrode signal would show any change. At the same time, the fixed electrode would react faster during the traversing probe departure. This means that the voltage signal observed on the thermocouple shielding would react to the film presence prior to the actual contact and decrease only a short moment after the departure from the film.

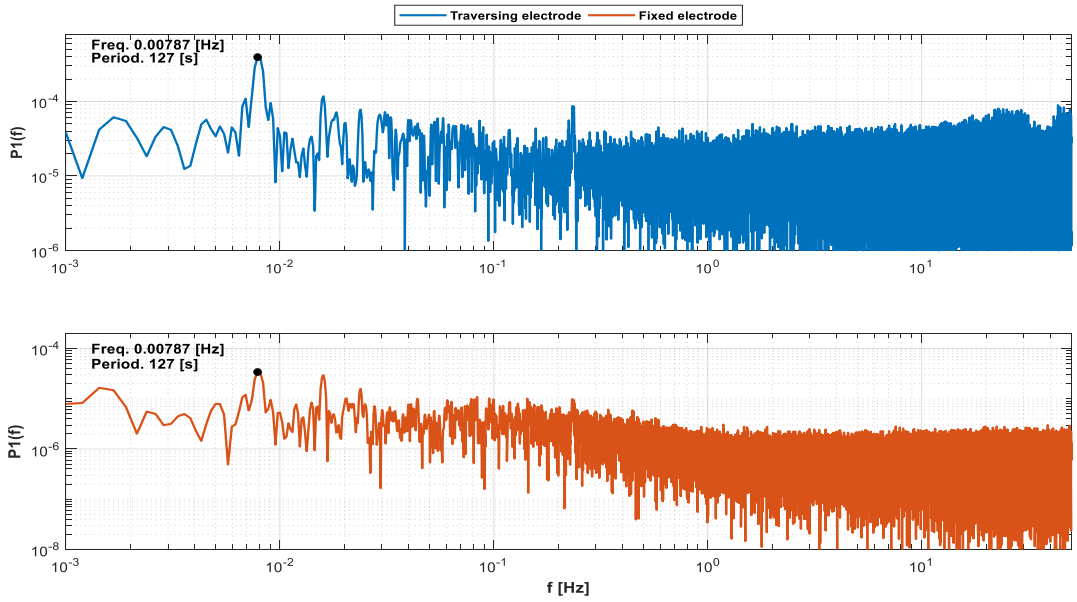

Figure 6-50 Discrete Fourier transform spectrum of voltage signal registered with traversing and fixed electrodes. The peak frequency corresponding to tube traversing period is clearly recognizable.

This observation seems to be confirmed by transforming the fixed array signal using previously established calibration functions to recalculate the film thickness in millimeters. Figure 6-51A presents the raw signal, while Figure 6-51B the calculated values. In both graphs, x-axis units are the normalized coordinates expressing relative position of the electrode array to the center of the mixing region. 0 value means that the center of the zone is at the probe position. Negative values mean that center of the region lies above the probe and positive, that it is below, in the test tube. Specifically, -1 and +1 signify the edges of the mixing zone being at the probe location.

The signal decreases continuously, the closer the mixing layer is to the probe, reaching lowest values when the array is located in the gas plug. When compared to the thermal boundary layer thickness, reconstructed from the traversing electrode temperature measurements, Figure 6-52, the difference becomes clear. On average, in the condensation zone, the thermal boundary layer possess thickness of close to 1.5 mm, while recalculated condensate film thickness varies between 0.8 and 1 mm. The thermal boundary layer observed with TC's should have been wider than the film itself, which seems to be confirmed by the data. However, the film thicknesses measured the fixed electrode array were obtained only after intensive signal processing, which might have affected the accuracy of the calculated values. Therefore, no confident quantitative assessment can be offered on this basis.

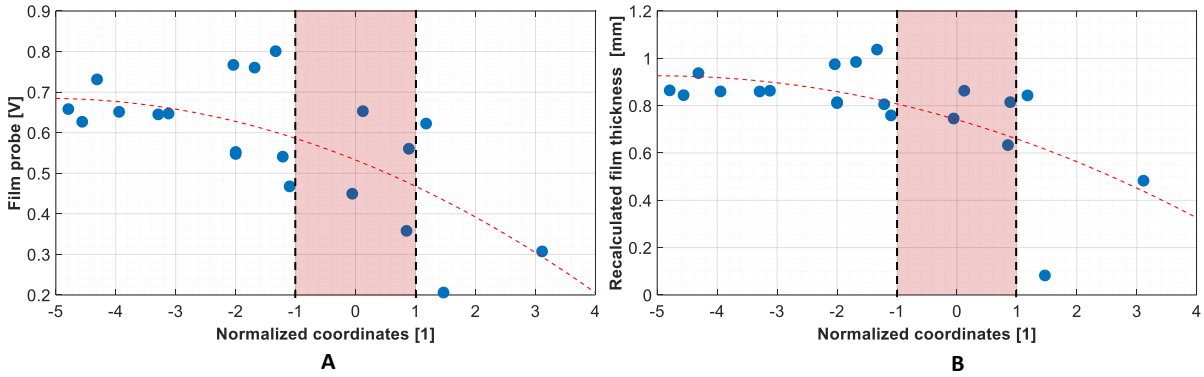

Figure 6-51 Film probe voltage (A) and recalculated film thickness (B), experiments NC-MFR-ABS-4-X and NC-MFR-HE-X

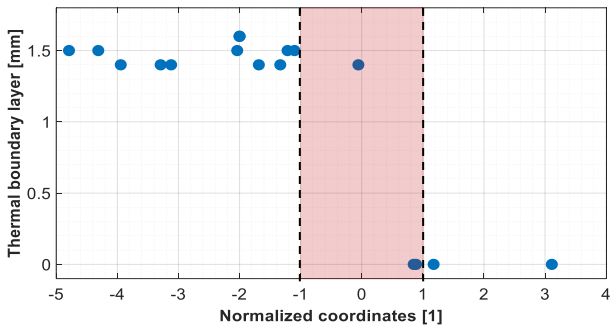

Figure 6-52 Thermal boundary layer identified with the traversing electrode, exp. NC-MFR-ABS-4-X and NC-MFR-HE-X

6.3.3 Thermal boundary layer and NC gas mixture composition

As observed in the previous chapters, the type of gas in the test tube has a significant impact on the vertical gas stratification as well as mixing between pure steam and NC plug above. It could potentially affect the thermal boundary layer as well as the condensate film thickness. As a first step, horizontal temperature distributions in the test tube were compared for varying gas mixtures, Figure 6-53. In the pure steam condensation region (Figure 6-53A) unsurprisingly there is no variation in the observed distributions. Here no NC gases are present thus no effect was expected. Similarly, since there is no temperature gradient in the NC gas plug region (Figure 6-53C), no oscillations and discernible difference can be identified. When the probe is located in the mixing zone (Figure 6-53B), the overall behavior also remains similar for all the compositions. This region is more turbulent, comparing to the other two, with small decrease of temperature towards the wall observed. Temperature deviations for experiments with He only are however somewhat smaller than those with N_2 present. The difference is less pronounced than in the observations conducted with vertical thermocouple array, as here the time oscillations are compounded with the traversing movement of the probe. Overall however, the NC gas mixture composition has no significant effect on the horizontal temperature profiles in any of the regions.

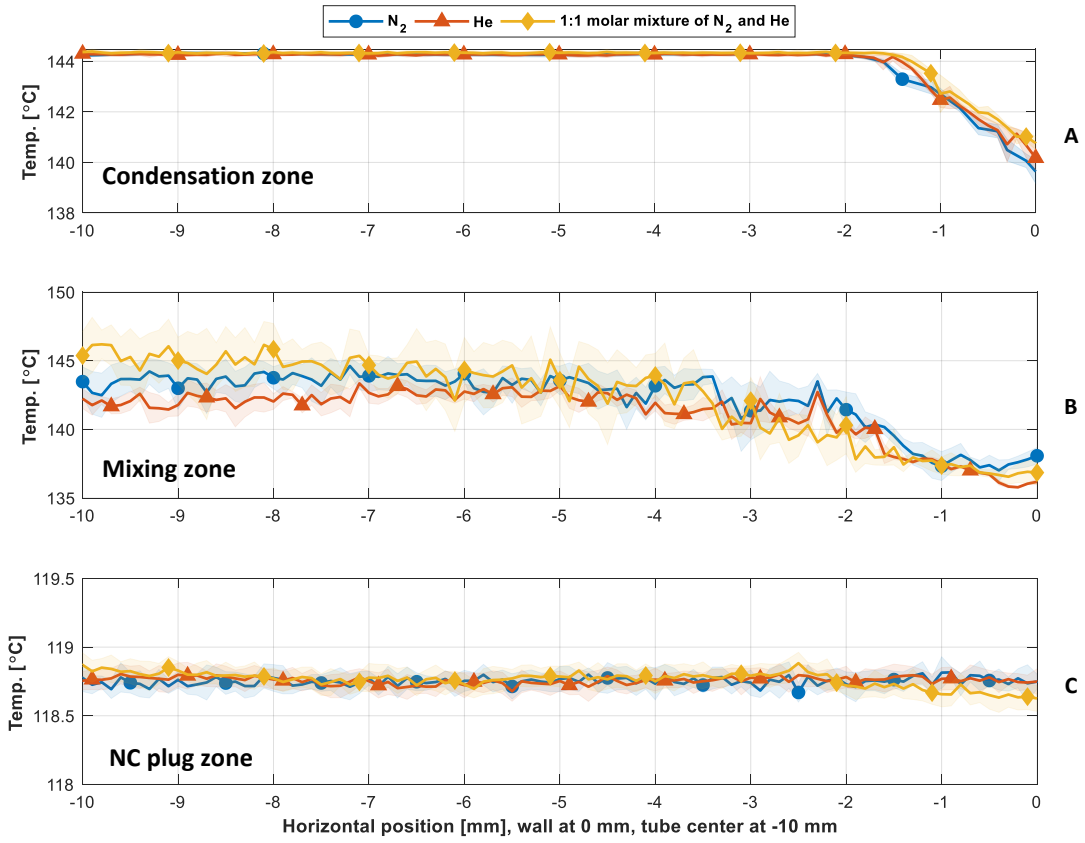

Figure 6-53 Horizontal temperature profiles with varying NC gas mixture compositions in (A) condensation zone, (B) mixing zone and (C) NC gas plug. Filled region represent temperature signal standard deviation calculated at each horizontal position.

6.4 Heat flux measurements

In this chapter, the overall analysis is expanded by discussion of measured heat flux values in the PRECISE facility. Effect of gas stratification, as well as steam/NC gas mixture composition is investigated. Moreover, the sensors installed in the PRECISE facility allowed for capturing the data at increased frequencies up to 100 kHz. Using this increased temporal resolution, the previously discussed experiments' results are analyzed to identify if and how non-condensable gases affect the dynamics of the condensation processes.

6.4.1 Gas stratification impact

Data gathered during steady-state experiments are analyzed. In these measurements, the vertical stratification of the gas mixtures was stable. The observed temporal variation in the recorded signal can be attributed purely to condensation processes in the steam-rich bottom region, or combined condensation and mixing in the mixing zone. Figure 6-54 presents calculated heat flux oscillations, obtained directly with the gradient heat flux sensors (GHFS, blue) and calculated from temperature difference measurements in the wall (red). From A to C, signal was recorded in the condensation zone, mixing zone and NC gas plug respectively. Note the scale change between (A, B) and (C).

A slight discrepancy exists between the two methods, both in amplitude (especially visible in measurement B) and in recorded oscillations (C). The first error could be accounted for by the measurement error, (about 8% for ΔT method and 4% for GHFS). The second inconsistency is mostly of much smaller amplitude and could exist due to different noise levels of each approach. Especially in Figure 6-54C, the unprocessed heat flux signal calculated from the ΔT measurement displays much greater peak-to-peak range, even though no condensation is occurring.

The mean signal amplitude is highest in the steam-rich region, followed closely by the mixing zone and approaches zero in the NC gas plug. It does not reach zero however, which can be attributed to the sensible heat still transported through the wall, or the conduction in vertical direction and corresponding slight heat-up of the wall itself.

As for the signal dynamics, in the condensation and, especially, in the mixing region slow oscillations, with periods ranging from 1 to 10 seconds, are recognizable. They are well reproduced by both measurement techniques. These heat flux oscillations can be attributed to dynamics of the condensation process, including the liquid film formation. However, in the mixing region, there is also the interaction between the NC gas and steam, which increases their magnitude. This behavior is consistent with the previously identified temperature oscillations phenomena. There seems however to be a small time-shift in heat flux as registered with the two techniques, most distinct in the mixing region, Figure 6-54B. To estimate its value a cross-correlation algorithm was applied to these two-time series. The obtained cross-correlation function did not produce a very prominent peak at any time-shift. Moreover, the peak and corresponding time-shift was very dependent on the data range supplied to the algorithm and if and how smoothing was applied. The obtained values varied between -2 and 4 seconds, giving no clear indication which of the two time-series was lagging and which was leading.

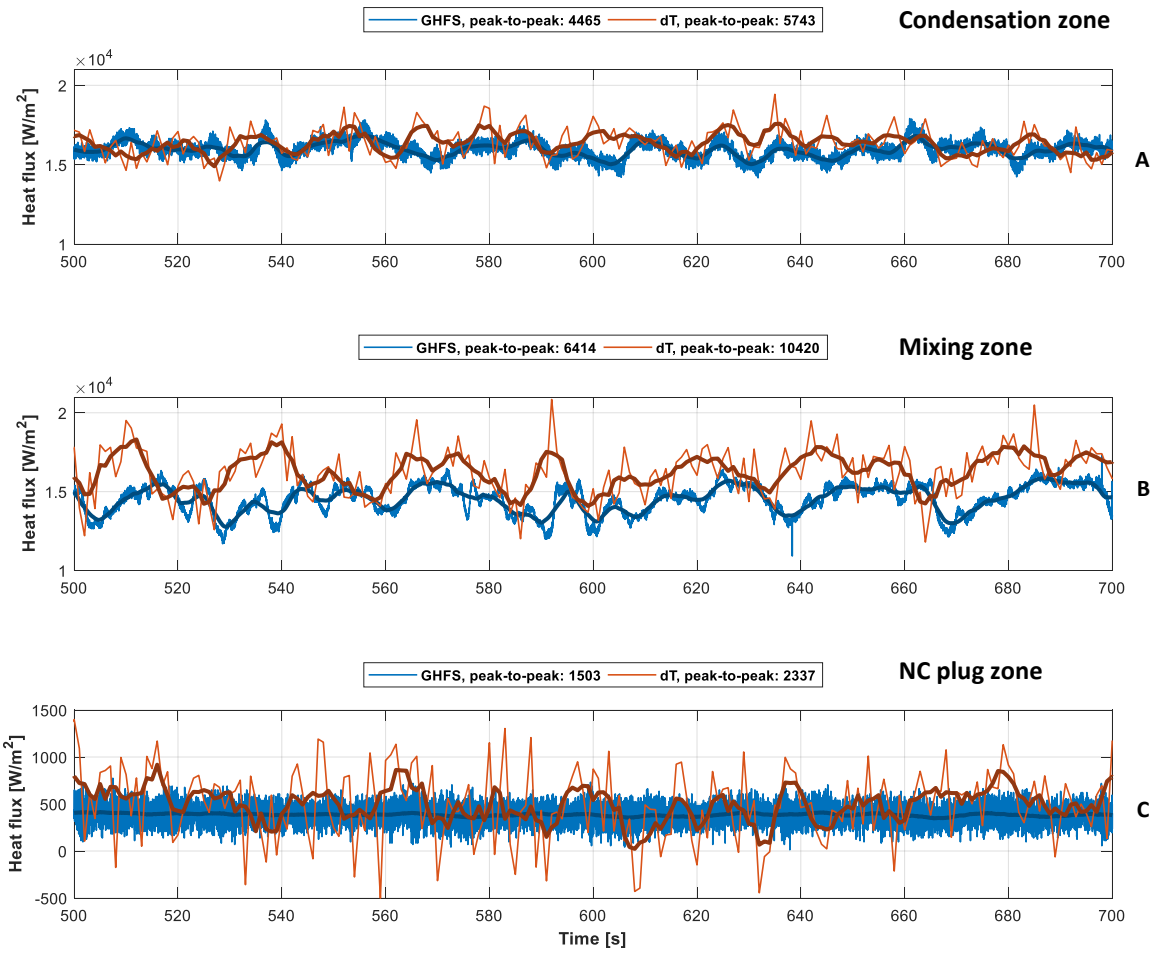

Figure 6-54 Heat flux signa measured in the condensation zone (A), mixing zone (B) and NC gas plug (C) with two measurement methods. Moving average filter with span of 100 was applied for clarity of viewing and plotted in bold. Experiments NC-CMP-5, NC-MFR-ABS-2_5_4 and NC-MFR-ABS-He-4_4.

After applying the Fast-Fourier transform algorithm, the signal dynamics differences are readily visible, and both methods display the same trends, Figure 6-55. The spectrum calculated form the ΔT measurement cuts off at 0.5Hz, as the acquisition frequency for thermocouples was fixed to 1Hz. Oscillations of similar power can be observed throughout the whole spectrum, while for direct heat flux measurement, they decrease with increasing amplitude. This suggests that most phenomena affecting the heat flux are of low-frequency nature. This claim is however investigated further, later in this chapter.

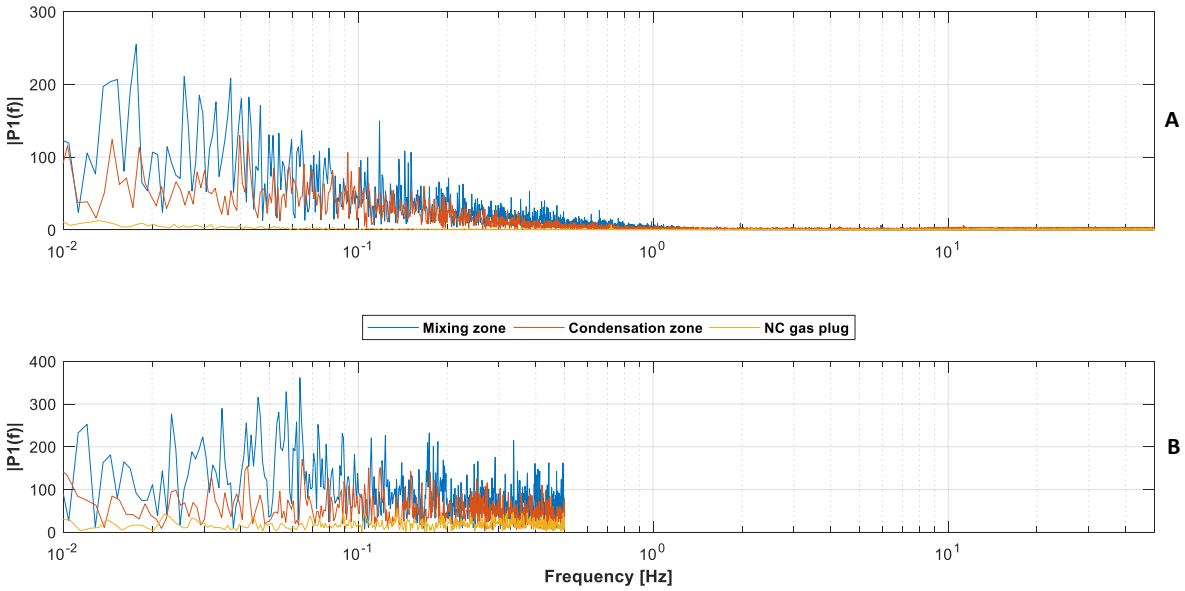

Figure 6-55 Heat flux signal recorded in each of three regions with heat flux sensors (A) and dual thermocouples (B) in frequency domain. Experiments NC-CMP-5, NC-MFR-ABS-2_5_4 and NC-MFR-ABS-He-4_4.

6.4.2 Gas mixture composition effect

As already shown by the temperature measurements, the type of the non-condensable gas injected in the test tube has an impact on observed heat flux. This effect varies however, depending on the stratification region, Figure 6-56. In the condensation zone (A) there is little distinction between recorded signals with He and N_2. Similarly, in the mixing region increased low-frequency oscillations can be observed in the signal. However, both in terms of the amplitude and data peak-to-peak values, experiments with the light gas show lower values. This can be the result of sharper stratification and decreased mixing, as observed with temperature measurements. At the same time, when comparing the normalized position of the measurement sensor with respect to the center of the mixing zone, Figure 6-57, it can be seen that in the helium experiment the GHFS was actually a bit deeper in the zone, with slightly lower fraction of steam present. The difference in recorded temperatures at the sensor level was 1 ±0.2 °C, or about 4% of the total decrease from pure steam to NC plug regions.

Finally, in the gas plug region, there is no difference between the two gases affecting the heat transfer. The same behavior is in agreement with previous findings from temperature measurements and traversing liquid film probe.

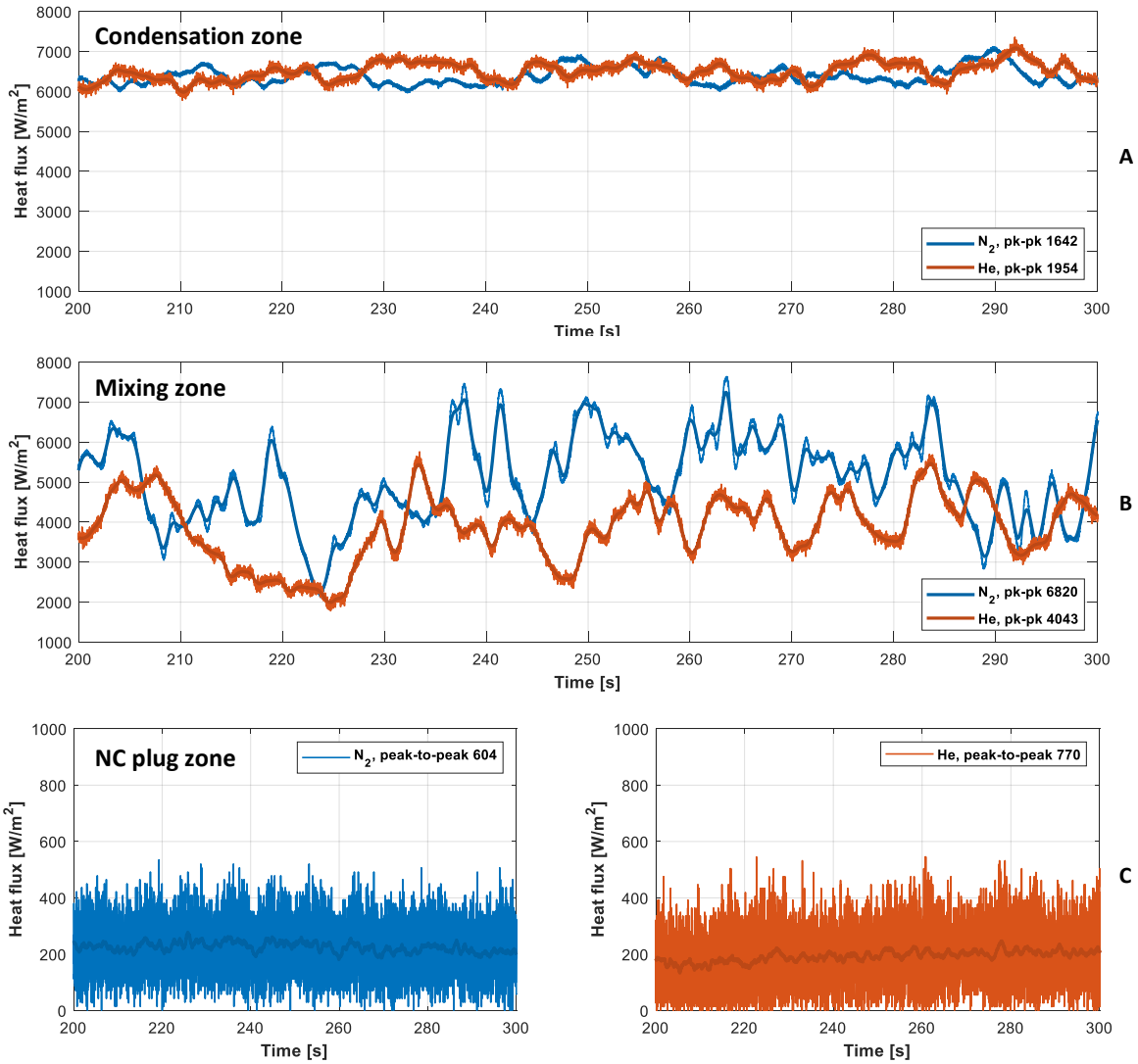

Figure 6-56 Heat flux signal measured in the condensation zone (A), mixing region (B) and gas plug (C) for experiments with N2 and He. Experiments NC-MFR-ABS-4_1 & NC-MFR-ABS-He-4_0, NC-MFR-ABS-4_2 & NC-MFR-ABS-He-4_1 and NC-MFR-ABS-4_6 & NC-MFR-ABS-He-4_5.

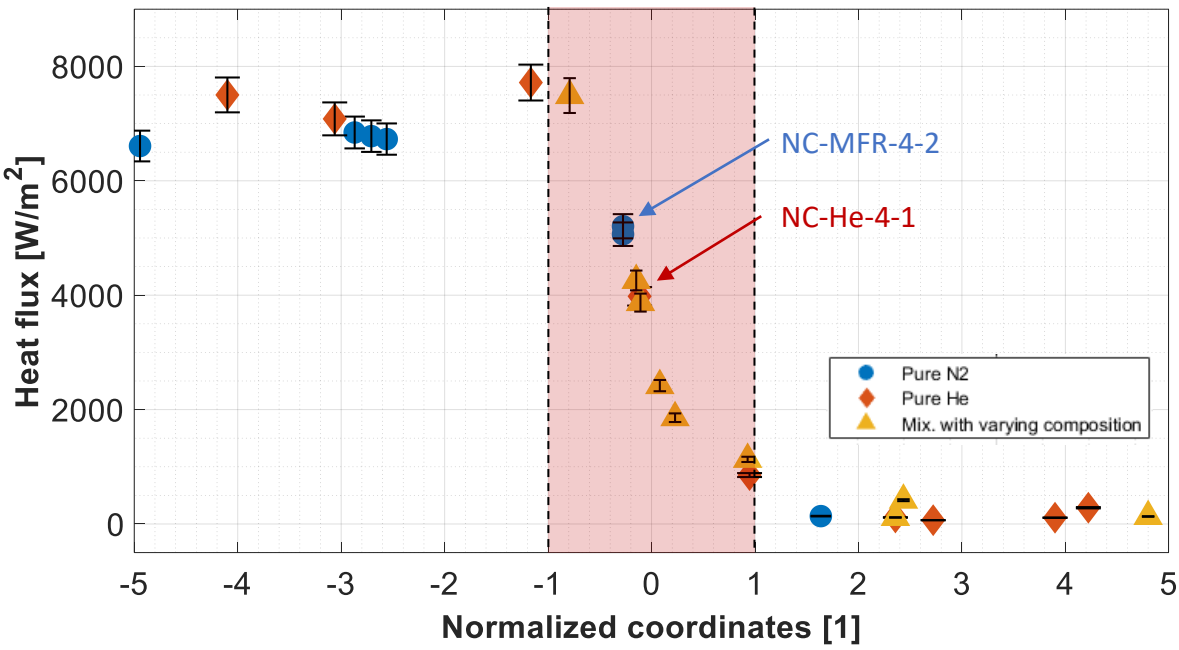

Figure 6-57 Heat flux observed in normalized coordinates, with respect to the position of the sensor (620 mm) and the mixing zone center. Experiments NC-MFR-ABS-4-X, NC-MFR-ABS-He-X and NC-CMP-X.

When plotted in the normalized coordinates, Figure 6-57, a heat flux decrease was observed with all variations of NC gas mixtures following the same pattern. As with the temperature measurements however, this calculated distribution has very low spatial distribution. To address that, data obtained with continuous injection of gases was also analyzed and discussed in the following sub-chapter.

6.4.3 Continuous injection tests

Heat flux profiles present in the mixing region behave correspondingly to the temperature profiles, as was briefly mentioned before in the section 6.2. Figure 6-58 depicts the passage of the mixing zone comprised of three different gas mixtures, recorded with a GHFS at 620 mm elevation in the tube. Supplementary, on the right y-axis, the temperature registered at the sensor elevation is also displayed. In each of the presented experiments, the gas feeding rate was the same, and thus the downwards velocity of the interface layer. As with temperature measurements, the differences in the size of the zone, as well as the dynamics are most significant when comparing pure He to N_2 or 1:1 mixture. The latter two vary mostly in the region length, with only a slight increase in the heat flux oscillations.

Calculating power spectrum with a DFT algorithm reveals that most of the signal oscillations are in frequencies below 5 Hz, Figure 6-59 (Kaiser window was used to carry out windowing). No consistent dominant frequencies can be identified. The difference in heat flux dynamics between He, N_2 and mixture of them is also indicated. This confirms previous observation made with steady-state experiments.

Mixing zone passage along the sensor can also be presented as a spectrogram, with the color scale indicating the relative level contained in certain frequencies at a given time, Figure 6-60. In every graph, the mixing zone arrival is set to roughly 2.5-minute mark. Clearly visible is the decrease in heat-flux oscillation amplitude in the mixing zone, and further in the plug, as well as the reduction of the dominant frequency range.

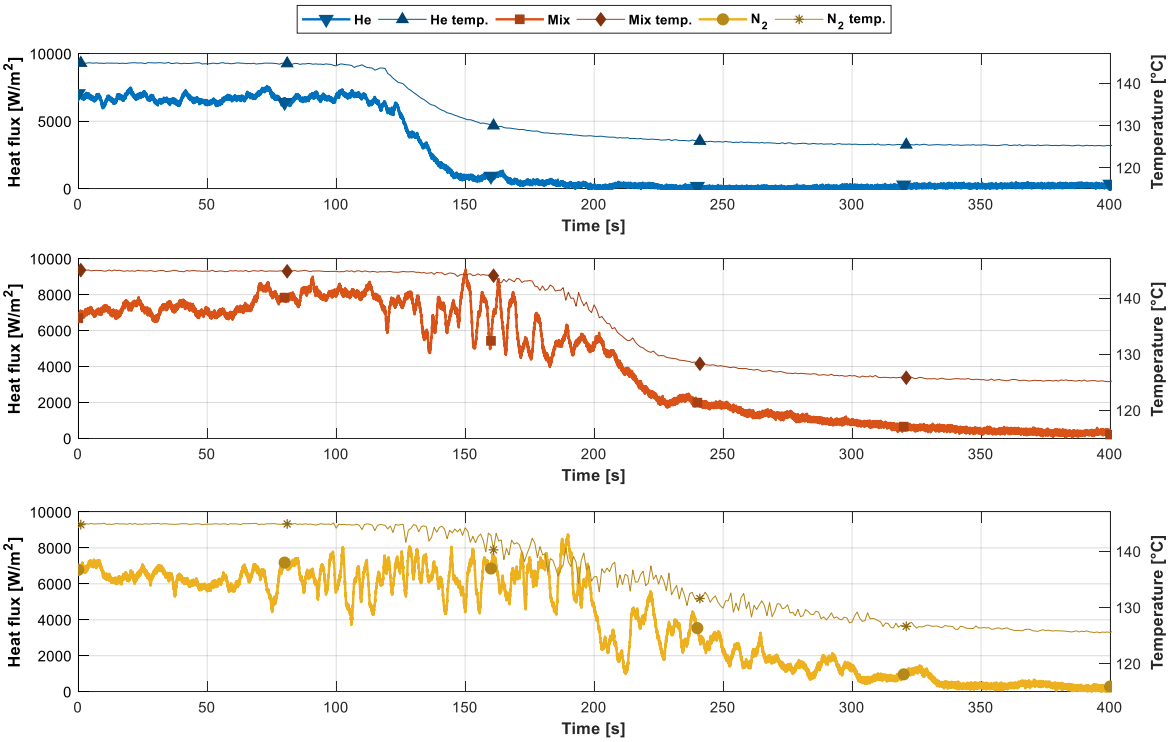

Figure 6-58 Mixing region passage observed with heat flux sensor and thermocouple located at 720 mm

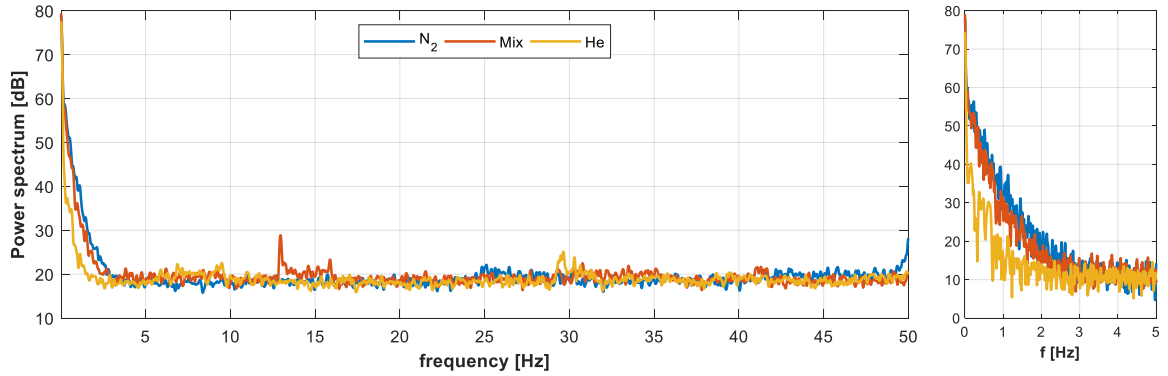

Figure 6-59 Power spectra of the heat flux signal acquired with various NC gases, computed with 0.1 Hz frequency resolution. Experiments CINT-He-4_5, CINT-MIX-4_5, CINT-N2-4_5.

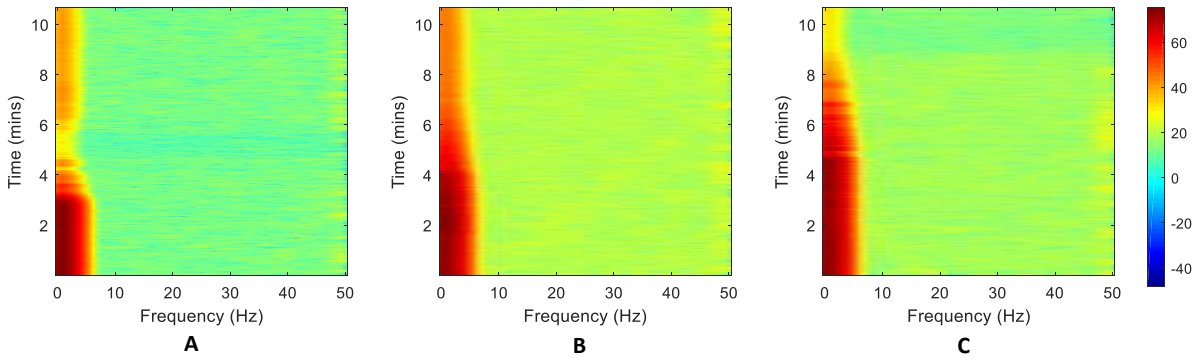

Figure 6-60 Spectrograms of mixing region for He (A), mixture (B) and N2 (C) gases injection. The arrival of the mixing zone is at 2.5 min.

6.4.4 Higher frequency phenomena

As discussed in the chapter 3.3.6, the heat flux sensors in most of the experiments were mounted inside the wall, 0.5 mm from the inner surface. This thin layer of steel acted as a physical low-pass filter, limiting the heat flux signal bandwidth visible by the sensors. However, some of the tests were conducted with the sensors mounted directly on the inner face of the test tube, completely exposed. In this section, these data are analyzed to investigate whether higher frequency phenomena are observable in the heat flux signal. All the presented power spectra were calculated in MATLAB, using *pspectrum* command, which applies Kaiser window to carry out windowing of the signal.

Figure 6-61 shows power spectra grouped by experiments. In these tests, the data acquisition rate was set to 10kHz and no filters were applied on the FPGA. Each graph depicts spectra of two sensors, located 200 mm apart vertically. Right side of the figure presents the lower end of the spectrum, 1-500 Hz. The experiments were chosen in such a fashion that during (A) both sensors are in the condensation zone, (B) has sensor one in the condensation zone while sensor two is in the mixing region, while in (C) both sensors are located in the gas plug.

Figure 6-61 Power spectra comparison of the measured heat flux signal recorded with two sensors and various experiments. Primary graphs on the left depict to whole available spectrum, computed with 10Hz frequency resolution. Secondary graphs on the right side depict lower end of the frequency spectrum, computed at 1Hz frequency resolution. Experiments, in order: NC-MFR-ABS-1 (A), NC-MFR-ABS-2 (B), NC-MFR-ABS-4 (C).

In the lower end of the spectrum, especially with GHFS1, the peaks corresponding to 50Hz noise and it's echoes at 100, 150, 250 and 350Hz clearly stand out. These also have the highest amplitude of all the observed peaks. When moving to higher frequencies, the power decreases significantly, roughly by 20dB, excluding other peaks. The spectra of the two sensors display high degree of similarity for each of the analyzed experiments, even for test (B), where they were located in different stratification regions. Only when comparing the very low frequencies, the difference becomes more visible, Figure 6-62. Just like in the experiments where GHFS's were embedded in the walls, most of the heat flux oscillations change occur in

the low frequencies. Starting with (A), the calculated Pearson correlation coefficient of the two sensors' spectra is 0. 9964, followed by 0.9983 for (B) and 0. 9930 for (C).

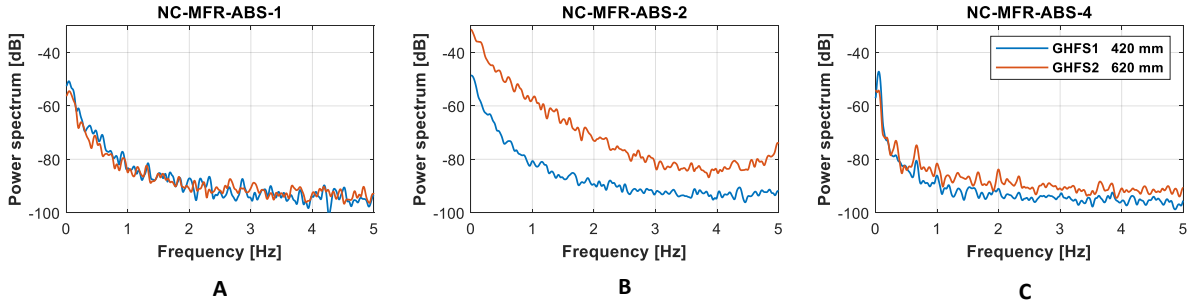

Figure 6-62 Power spectra comparison of the measured heat flux signal recorded with two sensors in various stratification regions, computed with 0.05 Hz frequency resolution. In order: (A) - both sensors in condensation zone, (B) – GHFS1 in condensation, GHFS2 in mixing region, (C) both in gas plug.

Figure 6-63 presents the same power spectra but grouped by sensor. For easy viewing, red and yellow graphs were offset by -15dB and -30dB respectively. Primary graphs on the left depict to whole available spectrum, computed with 10Hz frequency resolution. Secondary graphs on the right side depict lower end of the frequency spectrum, calculated with 1Hz frequency resolution. For the GHFS1 (A), recording 1 and 2 show spectra of the condensation process, while recording 4 shows response in the NC gas plug. For the GHFS2 (B) the topmost plot is the condensation region, followed by mixing zone and NC gas plug. The largest observed change occurs in the low end of the spectra, Figure 6-64, but there's a minor difference between the observed peaks at higher frequencies as well.

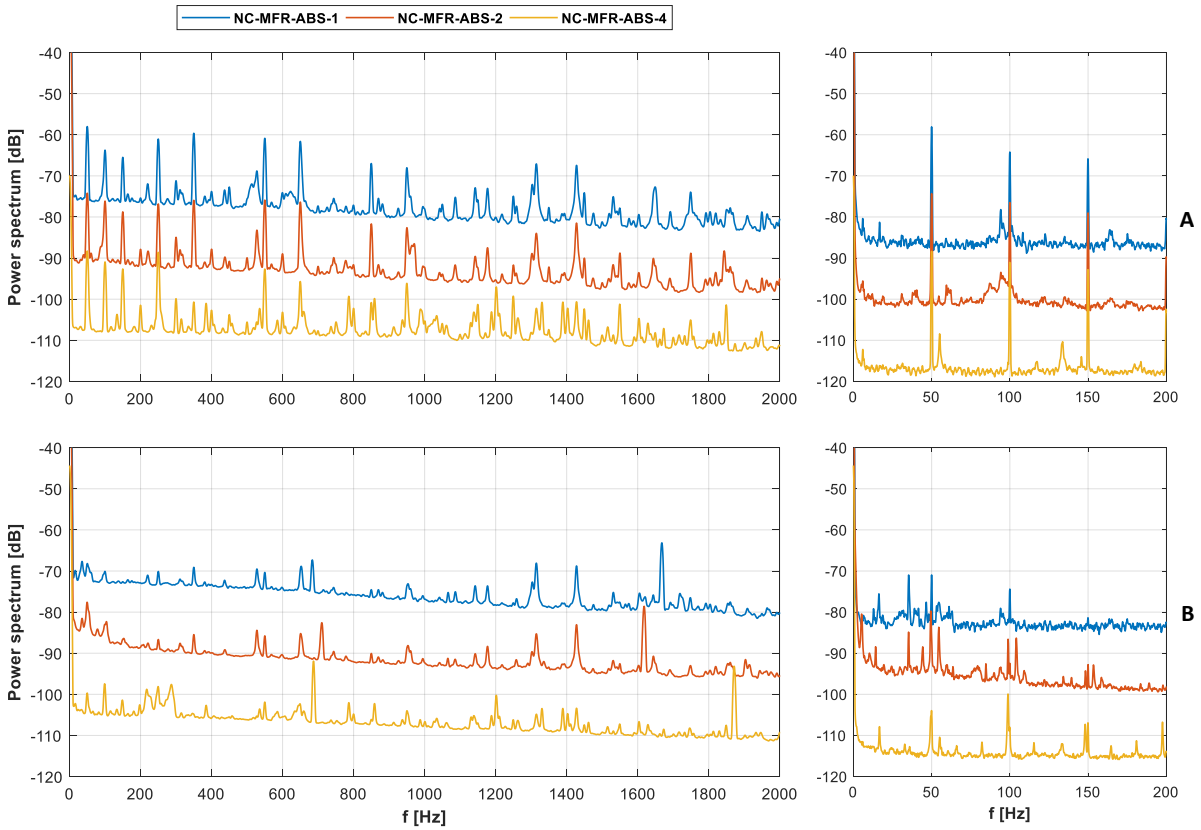

Figure 6-63 Power spectra comparison of the measured heat flux signal recorded with sensor 1 (A) and 2 (B), various experiments. For clarity of viewing, second and third spectrum offset by -15dB and -30dB. Experiments NC-MFR-ABS-1, NC-MFR-ABS-2, NC-MFR-ABS-4.

Overall, the greatest alteration of power spectra is between condensation/mixing region and NC gas plug. This reflects the observed high period (1-10s) oscillations, registered in this zone, by both heat flux and temperature measurement. To get a better measure of the high frequency part of the spectra, a cross power spectral density was calculated for each sensor, for each pair of experiments, Figure 6-65. For both sensors, the highest values of cross spectrum density values are calculated for condensation/condensation or condensation/mixing zone pairs.

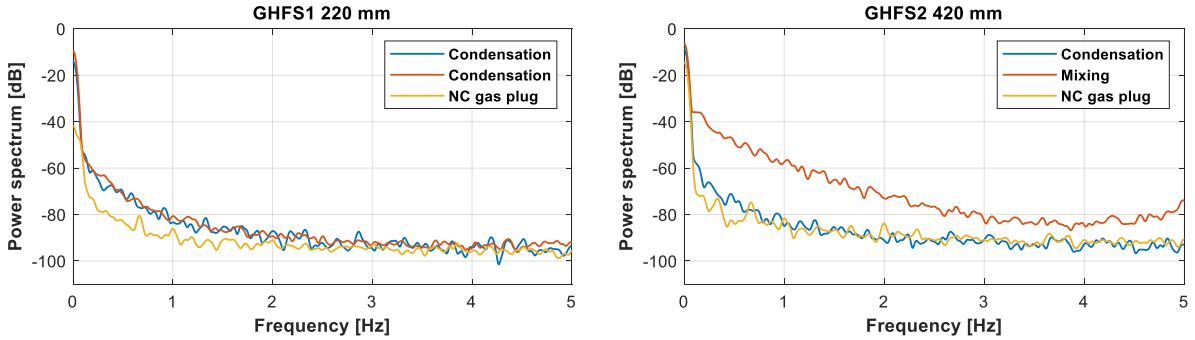

Figure 6-64 Low frequency end of power spectra registered with GHFS1 and GHFS2 at three experiments, NC-MFR-ABS-1, NC-MFR-ABS-2, NC-MFR-ABS-4, computed with 0.05 Hz frequency resolution

Condensation/plug and mixing zone/plug pairs achieve lower values, suggesting that the differences in calculated power spectra could be attributed to condensation processes. At the same time, for both sensors and all experiments, the peaks in the power spectra at higher frequencies are not very pronounced and the variation is very subtle. The degree of similarity observed for different stratification regions, particularly including the NC plug where no condensation occurs, suggests that the calculated peaks could represent the noise / frequency response of the GHFS/DAS system. In any case, the magnitude of power contained in the higher end of the frequency spectrum is much less significant, than the lower portion.

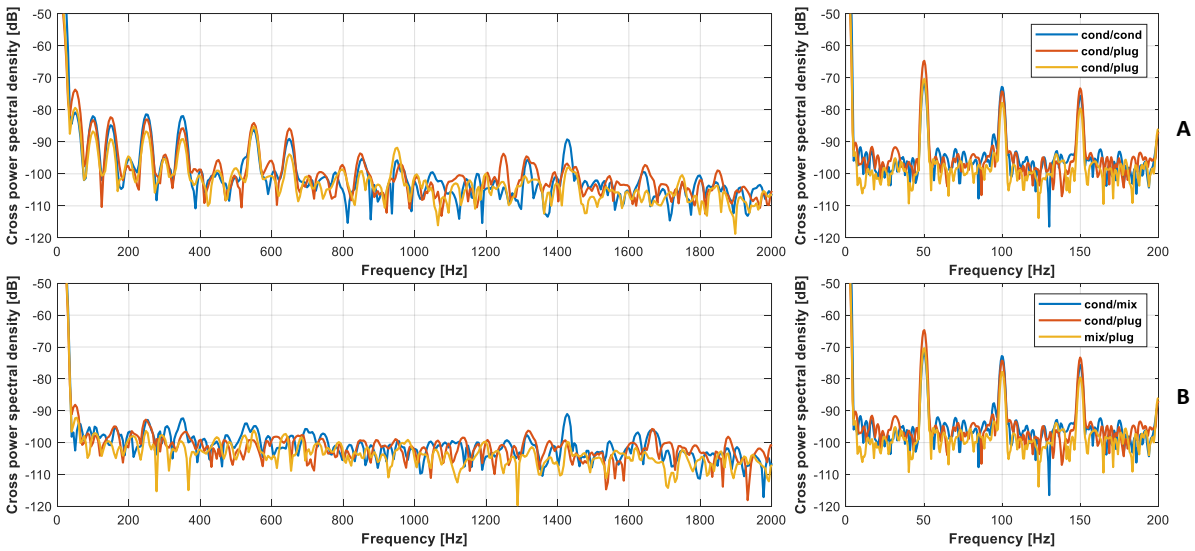

Figure 6-65 Cross power spectral density for GHFS1 (A) and GHFS2 (B), calculated for pair of experiments 1&2, 1&3 and 2&3, in order listed in Figure 6-64. Legend lists the zones in which the sensor was immersed during the test.

Overall, the spectral analysis of heat flux signal allows to distinguish mixing region from condensation zone and gas plug, when low frequency range 0-10 Hz is observed. Paired with examination of the signal

amplitude, each of the stratification zones can be easily identified. The condensations zone is characterized by high signal amplitude but does not show significant power contained in frequencies above 0.1 Hz. In the mixing zone, the observed heat flux signal can also be high and additionally, the spectra show elevated amount of power in carried in the frequencies up to 5 Hz. Last, in the NC plug, the there's minimum heat flux to be observed. Overall, no dominant frequencies, attributable to liquid film waves or droplets could be distinguished, suggesting that these phenomena are chaotic rather than periodic. Low amount of power carried in the higher frequency part of the signal also suggests lower significance to the overall heat transfer.

6.4.5 GHFS derived h_{tc} and theory

To provide a reference for the heat flux values measured with GHFS sensors the condensation heat transfer coefficient was calculated based on the observed heat flux $\dot{Q}$ and the wall temperature gradient ΔT in the following way:

$$h_{tc} = \frac{\dot{Q}}{\Delta T} \tag{82}$$

The obtained value was compared against three existing correlations proposed by Dehbi [231], Tagami [232] and Uchida [26]. The form of these correlations is, in order:

$$h_{tc-Dehbi} = \frac{L^{0.05}((3.7 + 28.7P) - (2438 + 458.3P) \times \log(X_{NC})}{(T_{sat} - T_{wall})} \tag{83}$$

$$h_{tc-Tagami} = 11.4 + 284\left(\frac{1 - X_{NC}}{X_{NC}}\right) \tag{84}$$

$$h_{tc-Uchida} = 380\left(\frac{X_{NC}}{1 - X_{NC}}\right)^{-0.707} \tag{85}$$

where P is pressure expressed in bar, X_{NC} is the non-condensable mole fraction, the logarithm is base 10 and L is the length of the condenser. Uchida and Tagami correlations are known to provide conservative values, while the Dehbi correlation, which also takes into account the pressure and wall subcooling provides more accurate values. It is important to mention, that data used to derive the Dehbi correlation were collected during experiments in which the condensation took place on the outside of the 0.038 m diameter, vertical tube. Uchida and Tagami correlations were derived based on data collected on a vertical condenser plates.

Figure 6-66 presents how the measured values of the heat flux and the wall temperature gradient were changing with the mixing zone passage and how this impacted the calculated parameters – steam mole fraction and h_{tc}. Clearly, the value of the heat transfer coefficient, as a ratio between heat flux and wall temperature difference was changing quite violently and was very sensitive to any oscillations in present in the data. Nevertheless, the calculated h_{tc} from experiments was plotted as a function of the non-condensables mole fraction along with the predicted values of the three correlations, Figure 6-67. The experimentally obtained h_{tc} follows the correct trend of decreasing with an increase of NC gases content, and its value is in the correct ballpark. The full trend is not completely reproduced; however, this can be attributed to the dynamic nature of continuous injection tests, where the descending NC gas plug affected GHFS and wall ΔT resulting in value oscillations.

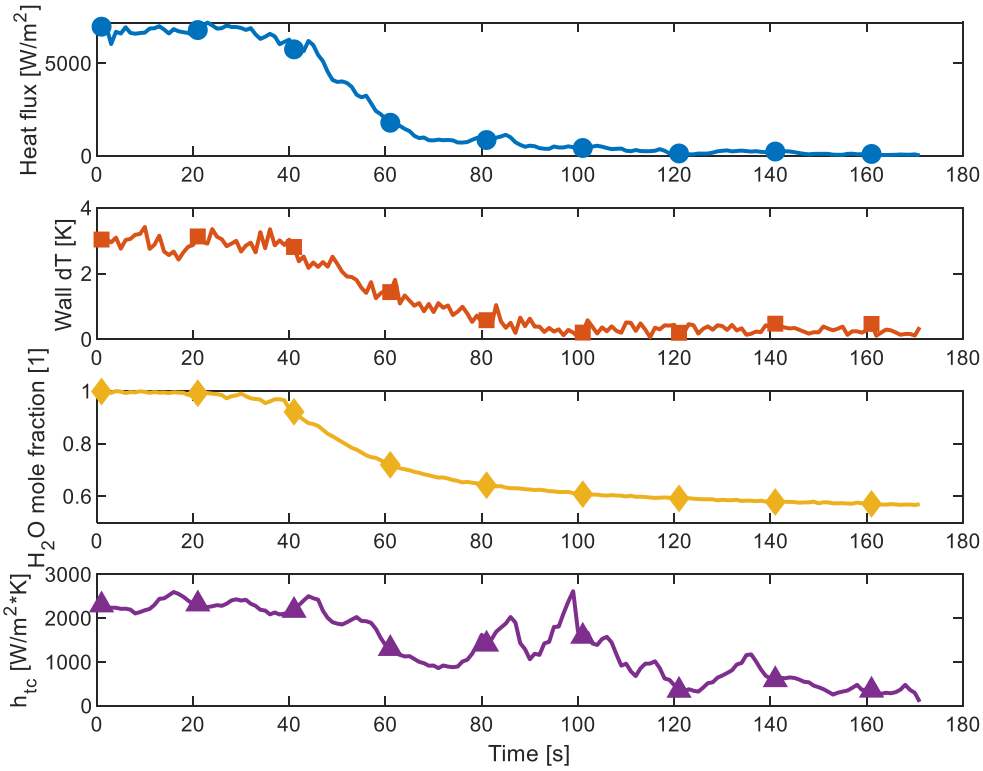

Figure 6-66 Mixing zone passage impact on various local parameters at 660 mm elevation, experiment CIN-He-4_2

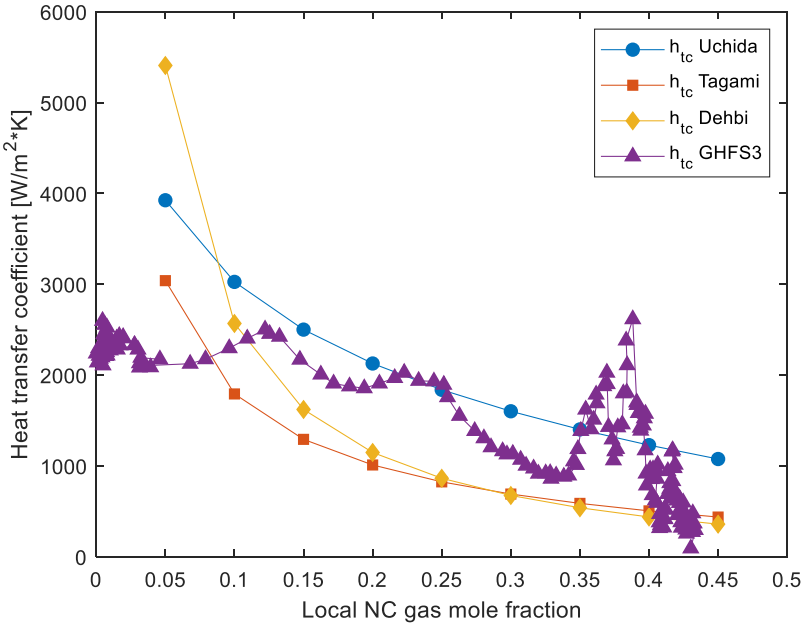

Figure 6-67 Calculated heat transfer coefficients using three empirical correlations and GHFS data, experiment CIN-He-4_2

Chapter 7 RELAP5 calculations

7.1 Overview

Due to the highly complex nature of nuclear power plant installations a need for specialized calculation tools arisen to model various operation condition transients as well as address postulated accidents. In recent years, events such as accident at Fukushima Daiichi Nuclear Power plan were also extensively modelled by the scientific community in order to better understand the progression of the incident ([233]–[236]). System codes were developed to address Design Basis Accidents (e.g. TRACE, RELAP5) and Beyond Design Basis Accidents (e.g. MELCOR) and has been continually advanced for more than two decades.

While providing accurate results where possible and conservative values where uncertainty in implemented models exists, system codes provide a valuable tool which can model the entirety of nuclear installations. On the contrary other tools such as computational fluid dynamic codes, while theoretically providing greater accuracy and resolution of results, are not suitable for the task due to limitations of current hardware. Therefore, system codes remain the main interest of researchers and plant operators working on the topic of nuclear safety.

7.2 RELAP5 reflux condensation modelling

Reactor Excursion and Leak Analysis Program RELAP5 was previously used by researchers to study condensation in the presence of NC gases. Lee [189] use RELAP5/MOD3 release to model inverted U-tube and analyze transient conditions. The code was able to predict major thermal-hydraulic phenomena, observed in the accompanying experiment, including three observed flow mode: reflux condensation, oscillatory flow and natural circulation. However, the calculated pressure and length of a formed liquid column in the rising part of the U-tube were both overpredicted.

Similarly, Susyadi and Yonomoto [237] used the same code version to investigated natural circulation cooling in SG tubes. The simulation was modelled on previously executed ROSA/LSTF tests [238] and focused on non-uniform flow between SG U-tubes (the model included 9). Calculations reproduced various observed flow phenomena, but difficulties to reach steady-state were met during low pressure calculations.

Park and No [120], used the updated version MOD3.2 developed a model of condensation in a passive containment cooling system tubes of a proposed CP-1300 reactor. They compared the calculation results against data obtained during the accompanying condensation experiments. In this case the steam is flowing downwards through the inner tube, while cooling water is flowing around, upwards, in the cooling jacket. Default condensation model of the code underpredicted the heat transfer coefficients. Suggestion was made that this underestimation maybe the result of the Colburn-Hougen's diffusion calculation, used to quantify the effects of non-condensable gases, while interfacial shear effects are completely ignored.

Moon et al. [164] using the same release of RELAP5 code, modelled an upward half of the steam generator U-tube surrounded by a cooling channel. In the experiment used for assessing RELAP5 performance, a mixture of steam/air was continuously fed to the tube and then removed at the top of the tube. They concluded that the then standard condensation model under predicted the heat transfer coefficients with underprediction increasing proportionately to air mass fraction in the mixture.

In 2007 Nagae et al. [175] developed a modified correlation for reflux condensation for MOD3.2 version as well and benchmarked it's performance against Moon et al. [164] data. It achieved good agreement with the experimental data, while the default model resulted in overestimated mixture temperatures. They concluded that one possible reason is due to the vapor-diffusion model underestimating heat transfer coefficients at higher pressures. In the same year, Nagae et al. [239] used RELAP5/MOD3.2 to investigate different flow patterns observed in SG U-tubes in test 7.2c in Bethsy facility [240]. The calculated nitrogen recirculation, pressure drop and temperature distribution in the tubes were very sensitive to the used heat transfer coefficient correlation.

Zhou et al. [241] modelled the passive containment condenser system using RELAP5/MOD3.3 beta version and compared the calculation results against single- and tube-bundle experiments conducted at Purdue University. The wall condensation model in the code produced results which agreed with the experimental results for complete condensation mode. However, for the flow-through mode, the default model has shown some discrepancy.

In this work, modelling of reflux condensation is enhanced by using the latest available stable release at the time - RELAP5/MOD3.4. Moreover, the used geometry is modelled after PRECISE facility, where no complete flow-through the condensation tube is possible. Therefore, the investigated case best reflects a plugged single, vertical SG tube at conditions reflecting those of the mid-loop operation in PWR.

7.3 RELAP5 Variable glossary

RELAP5 uses specific variable names in code. The list below provides a shorthand summary for terms used in the results discussion section.

7-1 RELAP5 variable names summary

Abbreviation	Unit	Description
htrnr	[W/m2]	heat flux
htvat	[K]	heat structure temperature
p	[1]	pressure normalized against pressure at inlet
quals	[1]	volume static quality
quala	[1]	volume noncondensable mass fraction
sattemp	[K]	saturation temperature [K]
tempf	[1]	temperature of fluid normalized against temperature at inlet
tempg	[1]	temperature of has normalized against temperature at inlet
vapgen	[kg/(m3*s)]	vapor generation rate
velf	[m/s]	average velocity of liquid volume
velg	[m/s]	average velocity of vapor volume
Pps	[bar]	primary side steam partial pressure
Tps	[K]	primary side superheat
Helium	[1]	mass fraction of He in NC gas mixture
NCmassfr	[1]	mass fraction of NC gases in the mixture with steam
Tss	[K]	secondary (coolant) side temperature
Mflowss	[kg/h]	secondary (coolant) side mass flow rate

7.4 PRECISE nodalization

7.4.1 Nodalization scheme 1

Since the PRECISE facility is a small installation, a model with large amount of subdivision of condensation volumes could be prepared without negatively affecting the computational performance. Previously conducted work ([167], [242], [243]) revealed that portions of the system experience steep large gradients in temperature. Those regions could benefit from such modelling approach, as greater spatial resolution is provided.

Overall, the calculation domain is divided into two volume sets – first corresponding to the primary condensation tube with steam generator tank and the second to coolant water jacket with inlet and outlet plenums. Mass exchange is permitted only within each set while the heat exchange is permitted between them. The overview of the nodalization is shown in Figure 7-1.

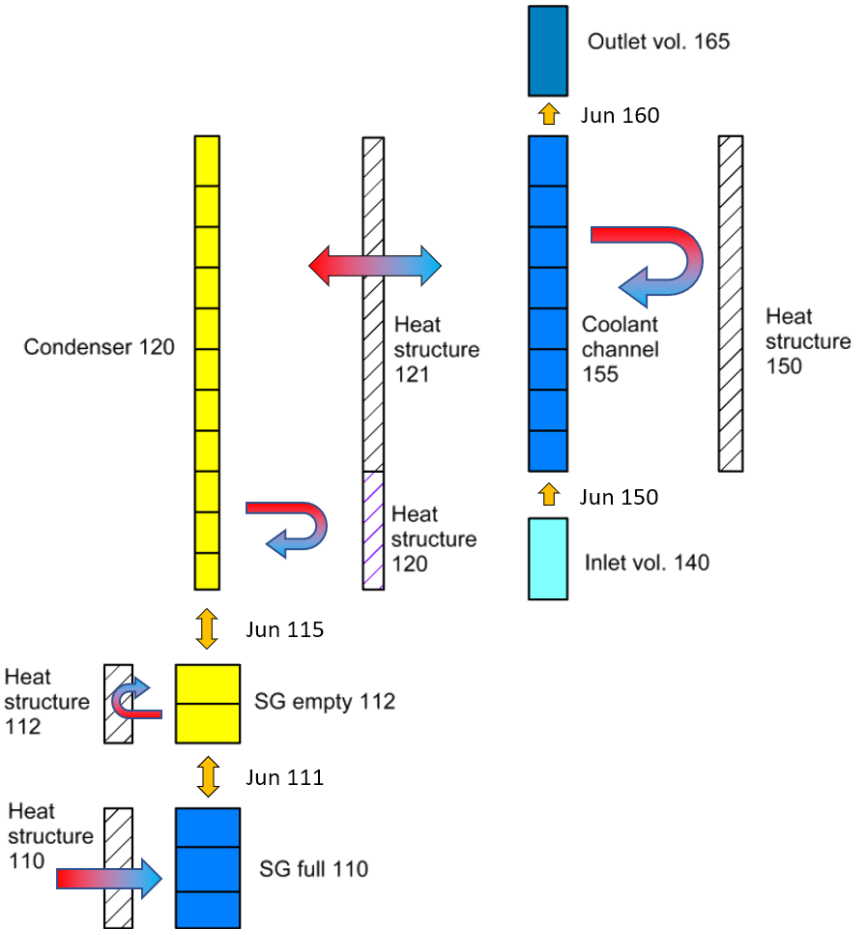

Figure 7-1 PRECISE facility nodalization type 1. Mass exchange marked with yellow arrows; heat exchange marked with red / blue arrows.

Volumes 110 and 112 represent the steam generator – the part filled with water and the empty space over the water surface respectively. They are modelled as pipe elements with adjustable amount of sub-volumes. Directly above volume 120, modelling the condensation tube, is connected via junction to the volume 112, allowing for mass exchange. For each volume momentum equations for liquid and gaseous phase are solved separately, allowed for counter-current flow of condensate and steam/NC mixture.

In the secondary side, volume 140 acts as an inlet plenum and a constant mass flow is imposed using time-dependent junction 150 into the coolant jacket volume 155. Upwards, a single junction connects to the outlet plenum.

To allow for heat exchange in the computational domain, heat structures are included. Starting with the primary side, structure 110 is connected to the volume 110 and models the electrical heater from the PRECISE facility. A constant heat-flux boundary conditions is applied to its outside. Upwards, heat structure 112 ensures adiabatic boundary condition in the gaseous zone of the steam generator. Next, heat structure 120 is included to model the insulated part of the condensation tube and the Teflon cone insert in the facility. Finally, structure 121 models the condenser tube's wall and is connected to the upper portion of volume 120 and coolant volume 155. The exact height at which the heat structure is attached to condenser tube is defined as the top of the Teflon cone in the actual facility, leaving the same size of heat exchange area available.

In the secondary side, there also heat structure 150 included, modelling the outer wall of the facility. For simplicity, an adiabatic boundary condition is applied there.

All the components, including volumes, heat structures and junctions are summarized in Table 7-2 to Table 7-4.

Table 7-2 Summary of volumes for nodalization scheme 1

Physical component	Group	No.	Type	Sections	Cross-section [m²]	Height [m]	Junctions	Heat structures
SG / heated	Primary	110	Pipe	4	0.005502	0.32	111	110
SG / adiabatic	Primary	112	Pipe	4	0.005502	0.32	111, 115	112
Tube / condenser	Primary	120	Pipe	15	0.000314	1.2	115	120,121
Inlet plenum	Secondary	140	Time-dep. vol.	1	0.008642	1	150	none
Coolant jacket	Secondary	155	Pipe-annulus	10	0.008642	0.8	150, 160	121,150
Outlet plenum	Secondary	165	Time-dep. vol.	1	0.008642	1	160	none

Table 7-3 Summary of heat structure for nodalization scheme 1

Physical component	No.	Ø inner [m]	Ø outer [m]	Mesh points	Type	Volumes
SG - Heater	110	0.0837	0.0889	4	Heat flux	110
SG - Insulation	112	0.0837	0.0889	4	Adiabatic	112
Condenser - insulated	120	0.02	0.03	4	Adiabatic	120
Condenser - heat exchanger	121	0.02	0.03	4	Convective	120, 155
Outer wall	150	0.1091	0.1143	4	Adiabatic	150

Table 7-4 Summary of junction for nodalization scheme 1

Connection	No.	Type	Volumes	Control
Water surface in SG	111	Single	110 & 112	-
SG and condenser tube	115	Single	112 & 120	-
Inlet to coolant jacket	150	Time-dependent	140 & 155	Mass flow
Outlet of coolant jacket	160	Single	155 & 165	-

7.4.2 Nodalization scheme 2

The shortcoming of the nodalization scheme 1 presented above is that RELAP5 does not solve separate momentum equations for each present gas species, just for the gaseous phase together. In other words, all the gas species included in the mixture must move in the same direction. This prevents any possibility of NC gases recirculation. To address this issue, a modified nodalization scheme was proposed, Figure 7-2.

Compared to the first nodalization scheme a couple components are added. The most important change is the split of condensation tube into two elements – the inner column 120 and the condenser annulus 121. The cold area near the tube's wall where the condensation occurs was separated from the central bulk, where higher temperatures and velocities are expected. This allows for recirculation of gas species to develop. Both volumes were modelled as pipe elements, with the outer region being set to annulus. They share the exact same number of vertical sub-volumes and the sum of volume in both is exactly the volume of the physical condensation tube. To allow for mass exchange, they are connected by a multiple-junction, which defines a single junction for each pair of inner column and annulus elements. Moreover, junction 115 was split into 115 and 116, but the sum of cross-sectional area remains the same. In terms of heat exchange to the coolant ring, in this configuration heat structures 120 and 121 are connected only to the condenser annulus. The summary of all the components in the nodalization scheme 2 are presented in Table 7-5 to Table 7-7.

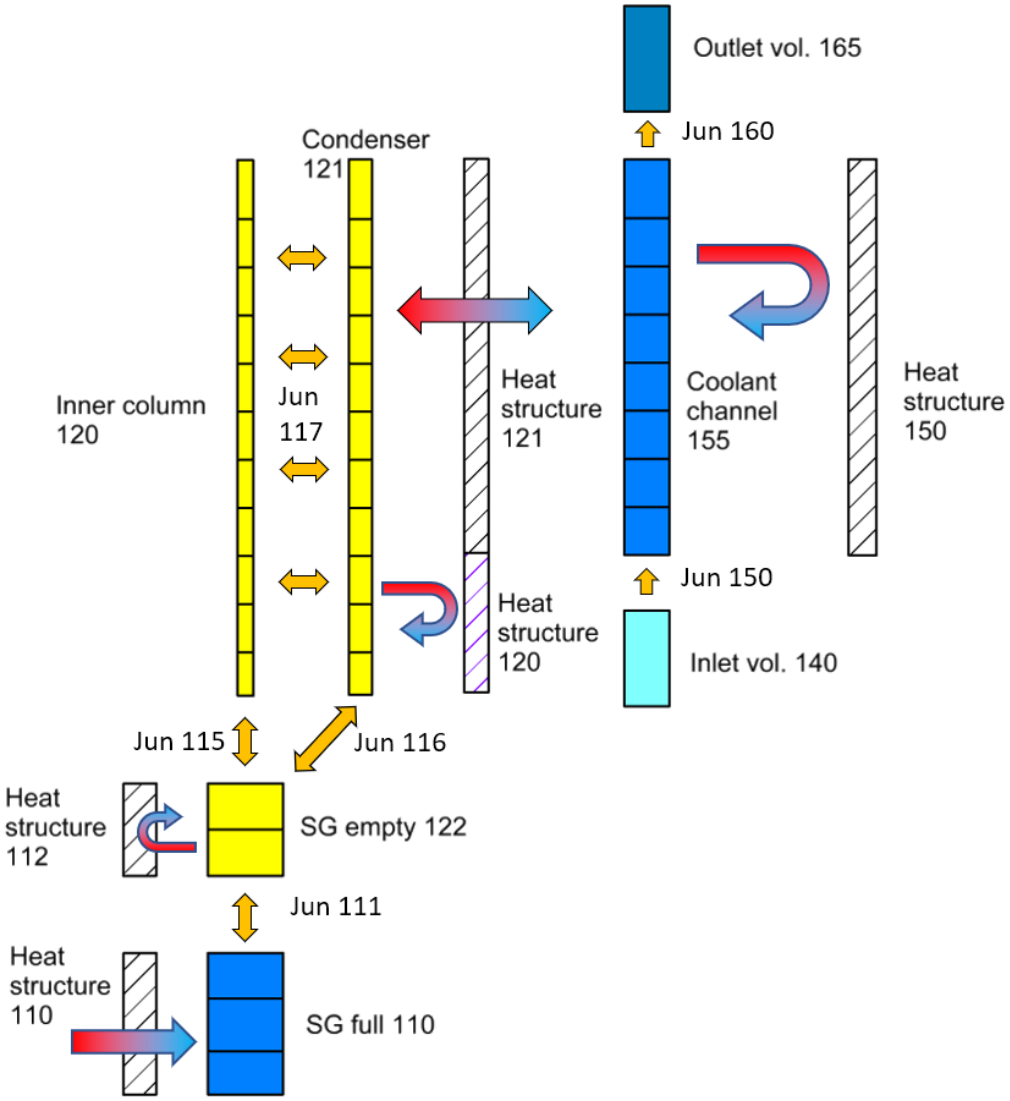

Figure 7-2 PRECISE facility nodalization type 2. Mass exchange marked with yellow arrows; heat exchange marked with red / blue arrows.

Table 7-5 Summary of volumes for nodalization scheme 2

Physical component	Group	No.	Type	Sections	Cross-section [m²]	Height [m]	Junctions	Heat structures
SG / heated	Primary	110	Pipe	4	0.005502	0.32	111	110
SG / adiabatic	Primary	112	Pipe	4	0.005502	0.32	111, 115,116	112
Tube / inner column	Primary	120	Pipe	15	0.000201	1.2	115,117	none
Tube / condenser annulus	Primary	121	Pipe - annulus	15	0.000113		116,117	120,121
Inlet plenum	Secondary	140	Time-dependent vol.	1	0.008642	1	150	none
Coolant jacket	Secondary	155	Pipe - annulus	10	0.008642	0.8	150,160	121,150
Outlet plenum	Secondary	165	Time-dependent vol.	1	0.008642	1	160	none

Table 7-6 Summary of heat structures for nodalization scheme 2

Physical component	No.	Ø inner [m]	Ø outer [m]	Mesh points	Type	Volumes
SG - Heater	110	0.0837	0.0889	4	Heat flux	110
SG - Insulation	112	0.0837	0.0889	4	Adiabatic	112
Condenser - insulated	120	0.02	0.03	4	Adiabatic	121
Condenser - heat exchanger	121	0.02	0.03	4	Convective	121, 155
Outer wall	150	0.1091	0.1143	4	Adiabatic	150

Table 7-7 Summary of junctions for nodalization scheme 2

Connection	No.	Type	Volumes	Control
Water surface in SG	111	Single	110 & 112	-
SG and tube inner column	115	Single	112 & 120	-
SG and condenser annulus	116	Single	112 & 121	-
Inner column and annulus	117	Multiple	120 & 121	-
Inlet to coolant jacket	150	Time-dependent	140 & 155	Mass flow
Outlet of coolant jacket	160	Single	155 & 165	-

7.4.3 Nodalization and calculation results

Two nodalization schemes presented above were tested to check how the obtained calculation results compare with obtained experimental values. Moreover, for each nodalization scheme the height of sub-volumes for each pipe vas varied to see the results independence of the picked size. Smaller elements allowed for greater vertical resolution in the calculation results, but at the same time increased the computation time necessary.

For consistency, each sub-volume in the calculation domain was assigned the same height. Three values were tested – 0.02, 0.04 and 0.08 meters. The test results revealed very weak relation, Figure 7-3.

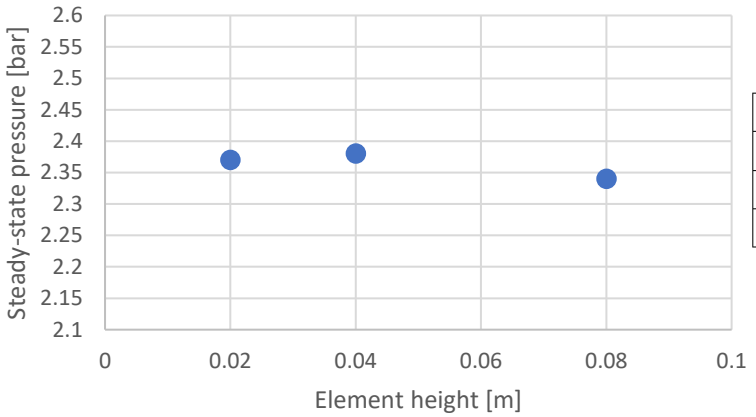

Element height	Cell number
0.02	92
0.04	46
0.08	23

Figure 7-3 Element height impact on steady state pressure

Moreover, for bigger elements, the calculated estimate of mass error (EMASS) in all volumes was smallest, Figure 7-4. Therefore, since the size of 0.08 m provided satisfactory vertical resolution for comparison with experiments and did not decrease the accuracy of the results, while at the same time reducing the computation time, it was chosen as the default value for all the following calculations.

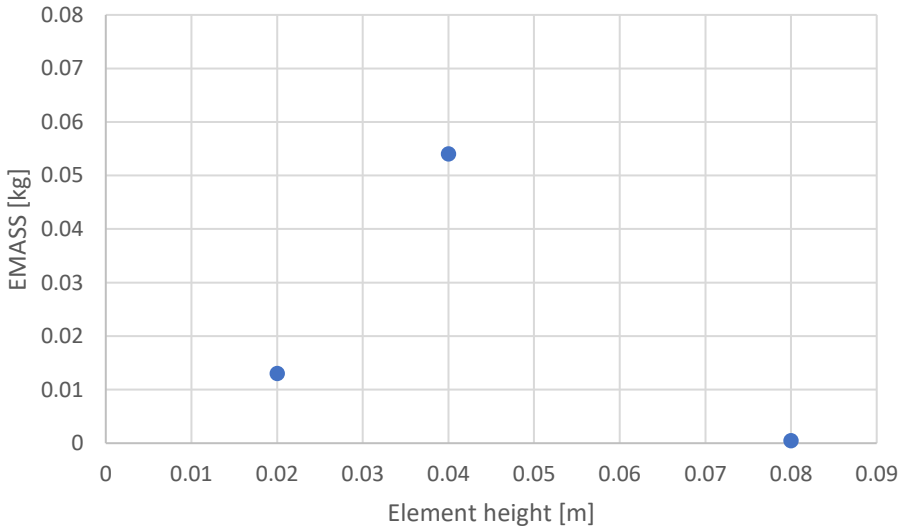

Figure 7-4 Dependence of RELAP5 estimate of mass error in all volumes on element height

In the next step, performance of nodalization scheme 1 and 2 were compared. Additionally, for nodalization scheme 2, the thickness of the introduced condensing annulus was varied from 0.5 to 5 mm to check impact of this parameter on the calculation results, Figure 7-5. As a reference, case without the condensing annulus, or thickness 0 mm, is also included in both plots. Each calculation was done with the same set of initial / boundary conditions. Both, pure steam cases and with NC gases were tested.

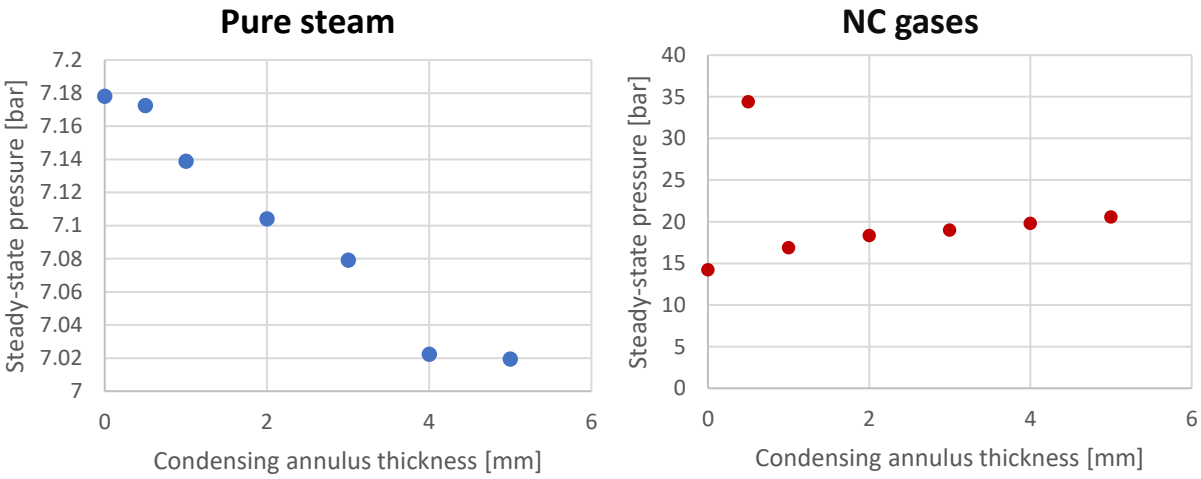

Figure 7-5 Steady state pressure calculated with different condensing annulus thicknesses for pure steam and NC gases cases

The increase of the annulus cross-section resulted in a minor decrease of calculated pressure for pure steam cases. On the contrary, when NC gases were included, the overall calculated pressure was not only much larger, but the annulus cross-section resulted in significant increase in the steady-state value. Since the annulus was introduced to address the issue with NC gases recirculation the latter finding seemed to undermine validity of this approach. For further tests thickness of 2 mm was chosen.

To get the better understanding of the issue, the results of calculations based on pure steam experiments P-ABS-PURE 1 to 5 with nodalization scheme 1 and 2 were compared against the actual experimental data, Figure 7-6. The lack of any sort of NC gases in the calculation domain resulted in almost identical results for both schemes. Moreover, the results were in pretty good agreement with experimental values. Neither of nodalization schemes proved consistently more accurate with pure steam cases, hence the simpler scheme was chosen for the following calculations without NC gases.

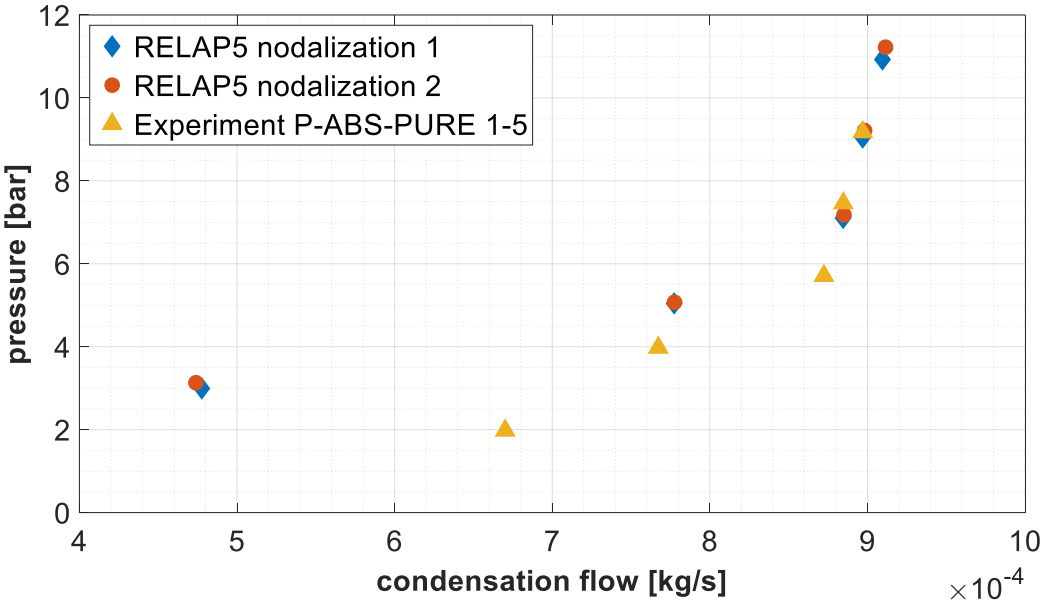

Figure 7-6 Steady-state pressure calculated with RELAP5 with various nodalization schemes and experimental boundary condition values, pure steam

However, in more complex cases with NC gases present, the type of nodalization has shown a significant impact on the calculated steady-state pressures, Figure 7-7 Values calculated with RELAP5 using more complex nodalization schemes are around 30% higher when compared to simple nodalization. However calculated values with both schemes are significantly greater than recorded during the experiment. This inconsistency pointed to possible issues with the way non-condensable gases are modelled in RELAP5.

Simpler nodalization approach produced results closer to reality, yet the overestimation of pressure was quite significant. Therefore, calculations were continued with both nodalization schemes and in the following chapters the possible cause for the observed behavior is investigated.

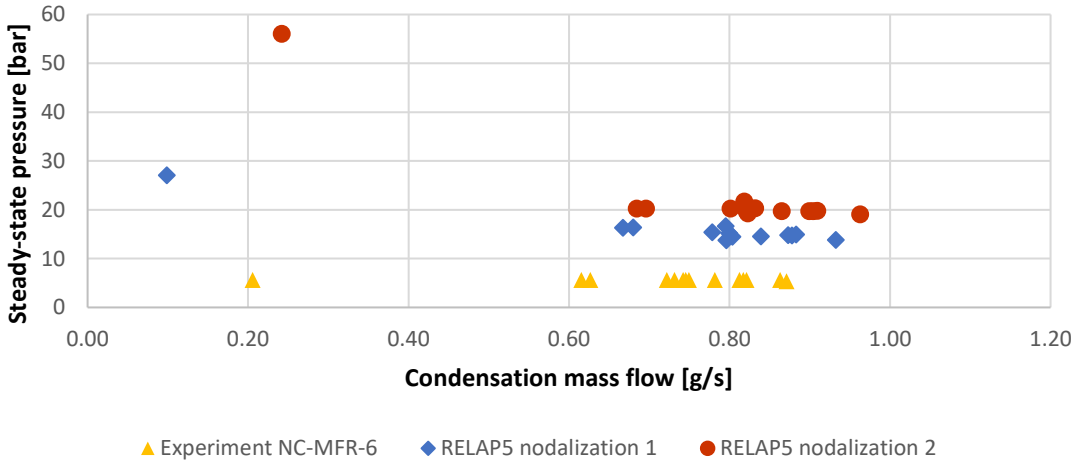

Figure 7-7 RELAP5 steady-state pressure and experimental values – NC-MFR-ABS-6

7.5 Boundary and initial conditions

During the experiments in PRECISE facility the dependent variables were the condensation flux and temperature / gas distribution in the tube as recorded at different NC gas mixture mole fractions and compositions, wall ΔT's, coolant velocities and pressures. As explained in previous sections, the controller logic adjusted the delivered electrical power to maintain the setpoint pressure, defined for each test. In RELAP5 calculations this was somewhat modified, and the pressure was a free parameter instead. The condensation flux, expressed in terms of heat, was applied as a boundary condition to heat structure 111. Therefore, for the same content of NC gases and coolant water parameters, the comparison could be made between the pairs of pressures/condensation fluxes observed during experiments and calculated with RELAP5 model.

Overall a set of parameters in the RELAP5 model were used as boundary and initial conditions. Values for these were derived from the data recorded during experiments and preparation steps. Table 7-8 presents an overview.

Table 7-8 Boundary and initial conditions used in RELAP5 modelling

Parameter	Defines	Applies to	Type
Pps	Pressure in primary side	Volumes 110, 112, 120, 121	Initial condition
Tps	Temperature in primary side	Volumes 110, 112, 120, 121, heat str. 110, 112, 120, 121	Initial condition
N2	Mole fraction of nitrogen	Volumes 110, 112, 120, 121	Initial condition
Helium	Mole fraction of helium	Volumes 110, 112, 120, 121	Initial condition
Power	Heat flux	Heat structure 111	Boundary condition
Pss	Pressure in coolant channel	Volumes 155	Initial condition
		Volume 140, 165	Boundary condition
Tss	Coolant temperature	Volumes 155	Initial condition
		Volume 140, 165, heat str. 150	Boundary condition
Mflowss	Coolant mass flow	Junction 150	Boundary condition
		Junction 160	Initial condition

7.6 Calculation results – reaching steady state

As described in the previous section, the calculations were setup in such a way to mimic the experiments conducted in the PRECISE facility most closely. Therefore, starting with the initial state of the facility and reaching the final steady state as time progressed. Obtained data was processed in such a way to show the flow development in the tube by means of different variables. Some of the graphs presented in this and following sections are a bit unusual and merit short explanation. The main body of the figures is colored matrix in which horizontal direction is time and vertical direction is the tube's geometry. Color is used to display the value of the plotted variable. In this way it is possible to observe variables' value change for each RELAP5 volume forming the primary side of the calculation domain. Horizontal time axis is discretized in time increments of 10 seconds, corresponding to major updates stored by RELAP5 in result files. Vertical axis discretization corresponds primary side division in vertical volumes, as shown in Figure 7-1 and Figure 7-2. Example of such graph is shown in Figure 7-8.

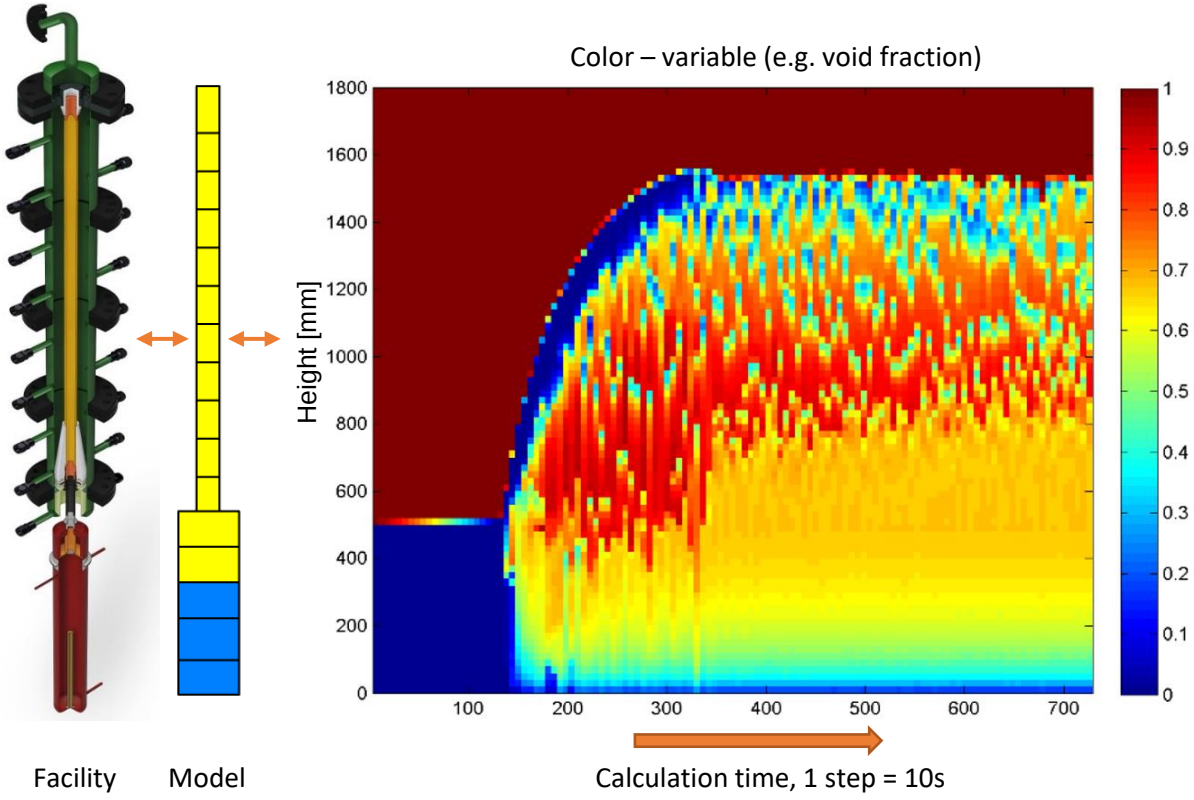

Figure 7-8 Void fraction in the test tube during calculation

Additionally, to assess the performance of the simulation, comparison of mass flows is used to verify that non-desirable mass imbalance occurs. Ultimately, evaporation should only occur in the SG full volume 110 and condensation should occur only in the modelled test tube. In the beginning however, some condensation also occurs in the volume SG empty 122, due to its low initial temperature, which effect diminishes over time, Figure 7-9.

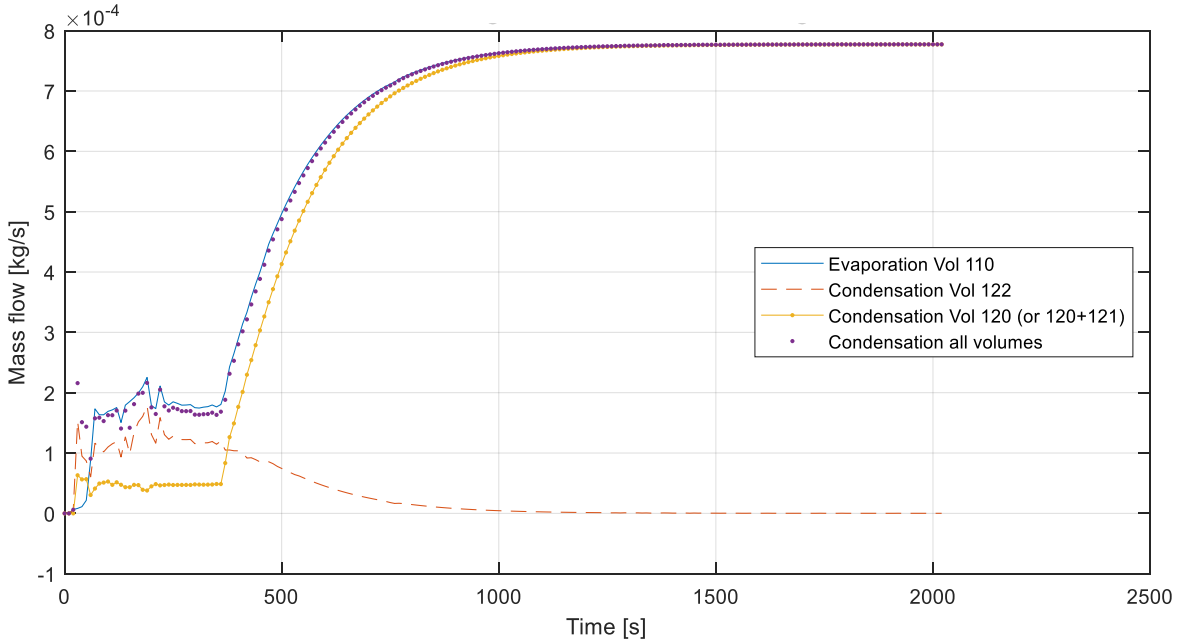

Figure 7-9 Change of evaporation / condensation mass flows in various volumes. Experiment P-ABS-PURE-1, nodalization scheme 2.

For the case presented in Figure 7-9 above, the flows stabilized at the following values:

- Evaporation flow 0.7773 g/s
- Condensation flow volume 122 0.0001407 g/s
- Condensation flow volume 120+121 0.77716 g/s

Overall mass imbalance remained and 0.0000028522 g/s, or 0.00037% of the total evaporation flow, which indicated that steady-state was reached. The equalization of condensation and evaporation flows is also very well visible in the pressure development, which stabilizes as the steam mass balance is reached, Figure 7-10.

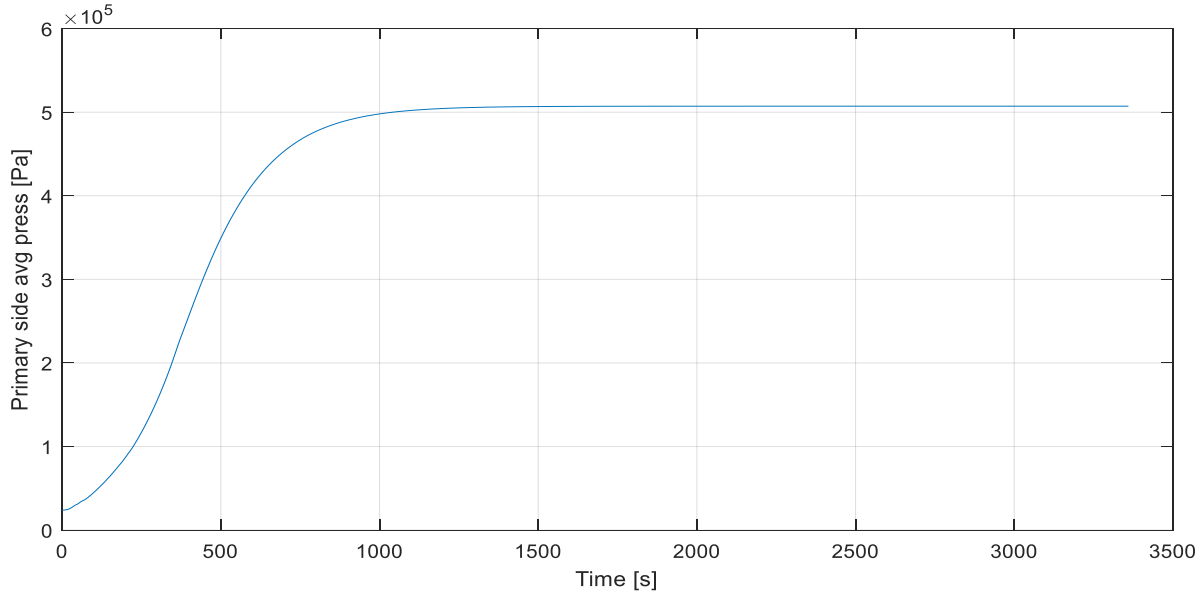

Figure 7-10 Average pressure in the primary side of the simulation over time

As a final confirmation, an integral heat balance, including primary side and the coolant side is calculated, Figure 7-11. The overall achieved agreement between delivered and removed heat from the calculation domain was very good.

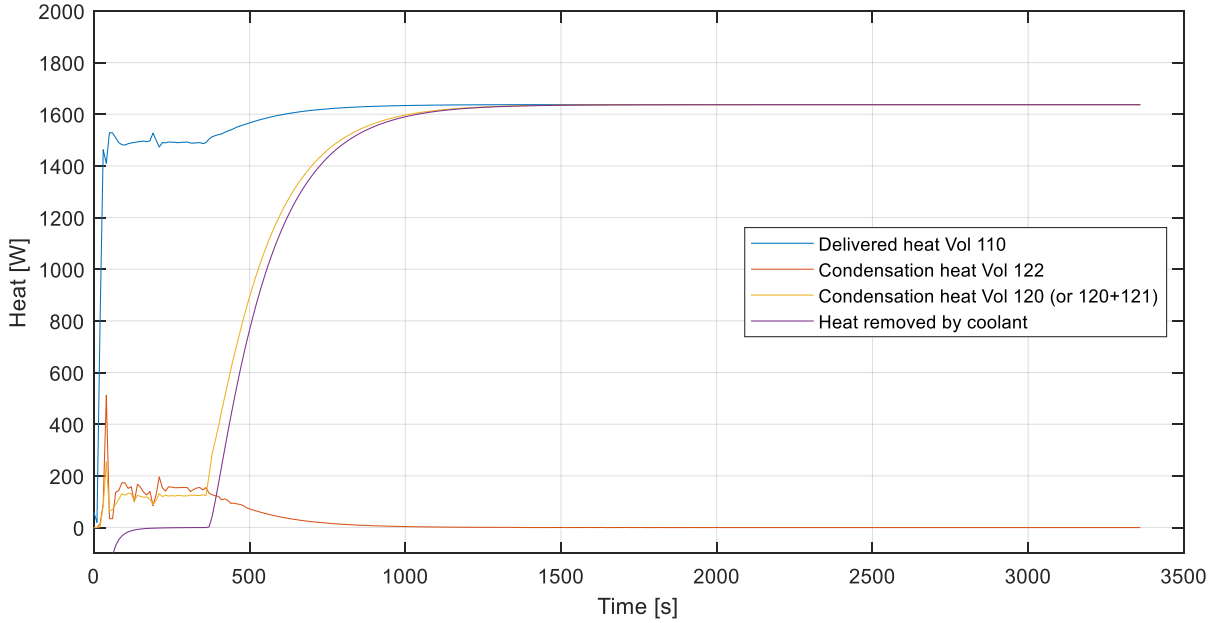

Figure 7-11 Heat balance of RELAP5 simulation. Initial negative value of removed heat is due to warmer coolant water entering the domain that the initial condition temperature.

7.7 Calculation results – pure steam

7.7.1 Residual NC gases modelling

In this section, RELAP5 calculations based on pure steam experiments series VEL-CLNT-PURE-X, VEL-DT-PURE-X and Pabs-PURE-X are discussed. Two approaches were used to address the simulations' setup. In the first one, the NC model in RELAP5 was completely disabled, by setting the inventory to pure steam only. This however was not fully corresponding to the conducted experiments. Some small but measurable quantity of residual NC gas was usually present, due to imperfections in volume evacuation and water degassing processes. Therefore, calculations were repeated with NC model turned on in RELAP5 and the residual non-condensables accounted for in initial conditions definition.

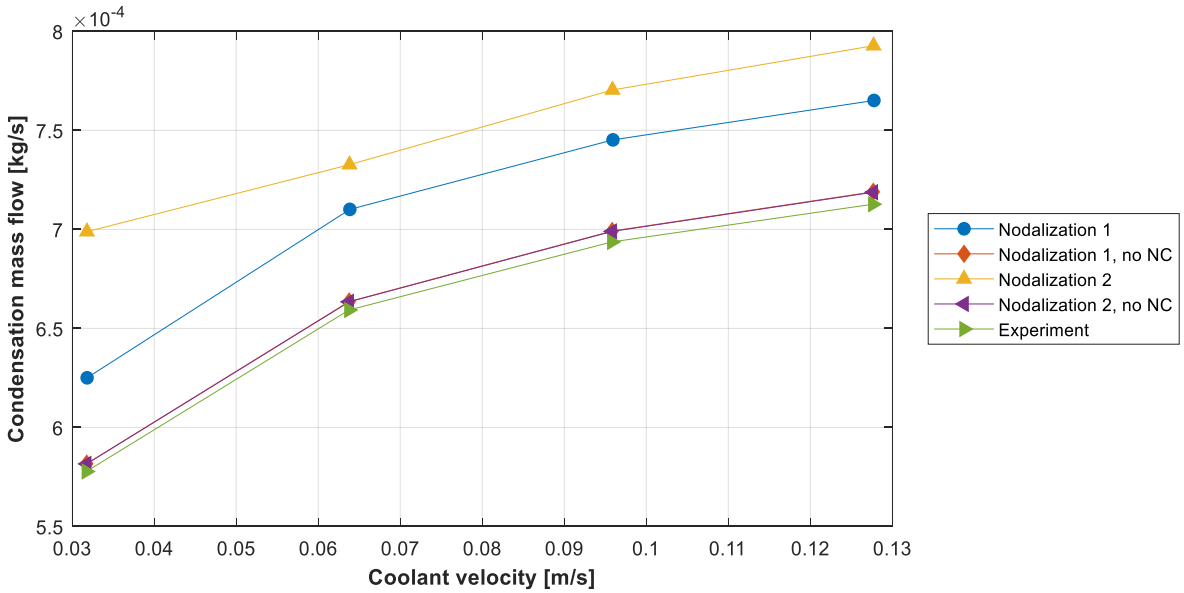

Figure 7-12 Comparison of two nodalization types and performance of RELAP5 NC modelling, experiments VEL-CLNT-PURE

Figure 7-12 shows the calculated condensation mass flow as a function of coolant velocity. Both nodalization schemes with NC gases completely excluded from the calculation domain performed most accurately against the experimental data. Correspondingly, for experiment series CLNT-DT-PURE, where the coolant temperature was continuously lowered, agreement with experimental is quite good as long as the NC modelling is turned off, and better for nodalization scheme 1, Figure 7-13. As a remark, on this graph the condensation flow does not continue to increase with ever lower coolant temperature, due to limitation of the heater used.

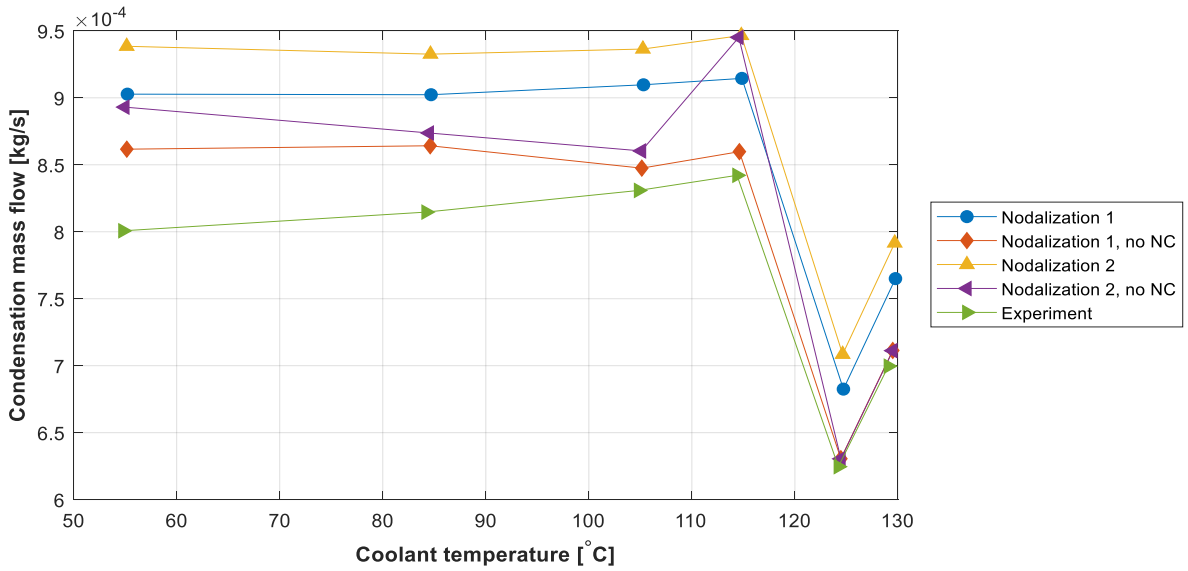

Figure 7-13 Condensation mass flow with varying coolant temperature

The most striking difference between different approaches performance can be however observed when the calculated steady-state pressure is plotted against the experimental values. On the Figure 7-14 calculations based on P-ABS-PURE experiment series are shown. Clearly, the pressures calculated with NC modelling enabled are an order of magnitude higher than the observed values.

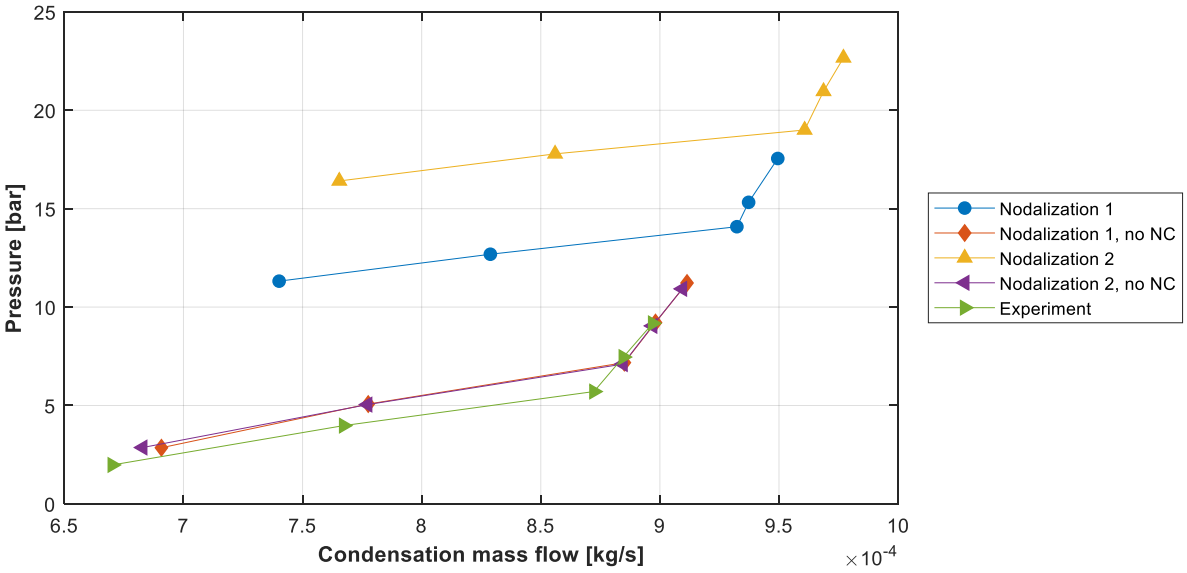

Figure 7-14 Reached steady-state pressure with increasing condensation flow

It is important to remark that such high pressures were reached even though the actual amount of NC gases that used for initial conditions definitions was minimal and had little to no impact during the experiments. To investigate this issue further, in post-processing, the evolution of inventory mass in the condensation tube / tube-annulus locations as well as the integral value were tracked. Masses of NC gas species, complete gas phase and overall mass (in condensation tube 120/121 and steam generator volumes 110 & 122) of both phases were investigated. Figure 7-15 presents development of each listed mass type for various calculation settings. For cases Figure 7-15 A & C, since no NC's are introduced, their mass is predictable a constant zero throughout the whole calculation. The mass of steam in the condensation

volume increases for some time to stabilize afterwards, matching the calculation time at which steady pressure was achieved. The overall mass remains constant, as no mass is produced or lost in these volumes taken together.

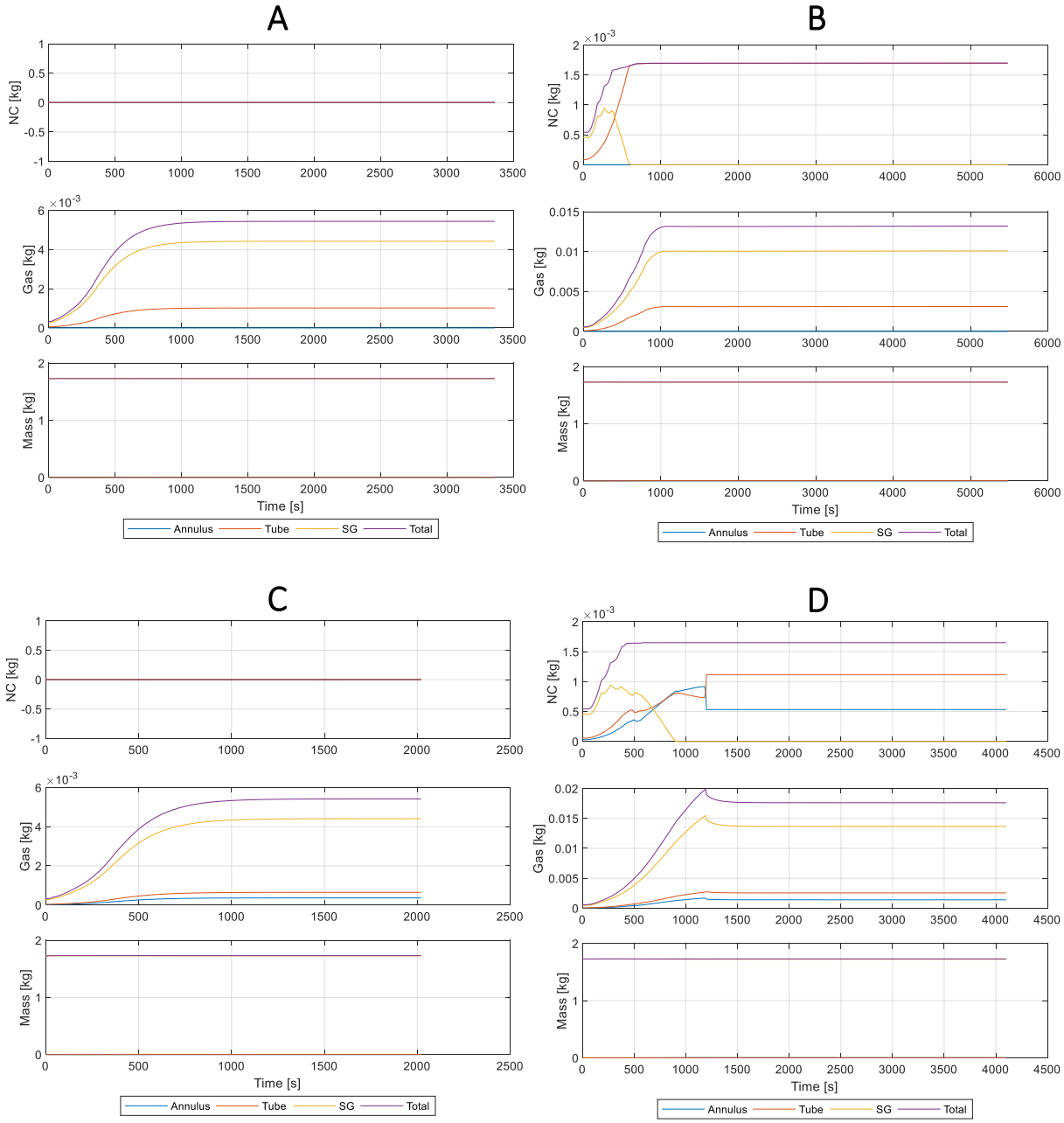

Figure 7-15 Inventory evolution during calculation for nodalization 1 (A, B) and 2 (C, D) with NC model disabled (A, C) and enabled (B, D)

However, for both nodalization schemes (Figure 7-15 B&D) the situation is quite different. In the simulation, neither source nor sink for NC gases are included in the setup, thus the overall mass of these species should remain constant. Unfortunately, this is not the case. As the computation time progresses, gradual removal of the NC gases from SG tank is observed towards the condensation tube. In effect, all non-condensables are in the latter after some time – phenomenon which was also observed during the experiments, Figure 7-16.

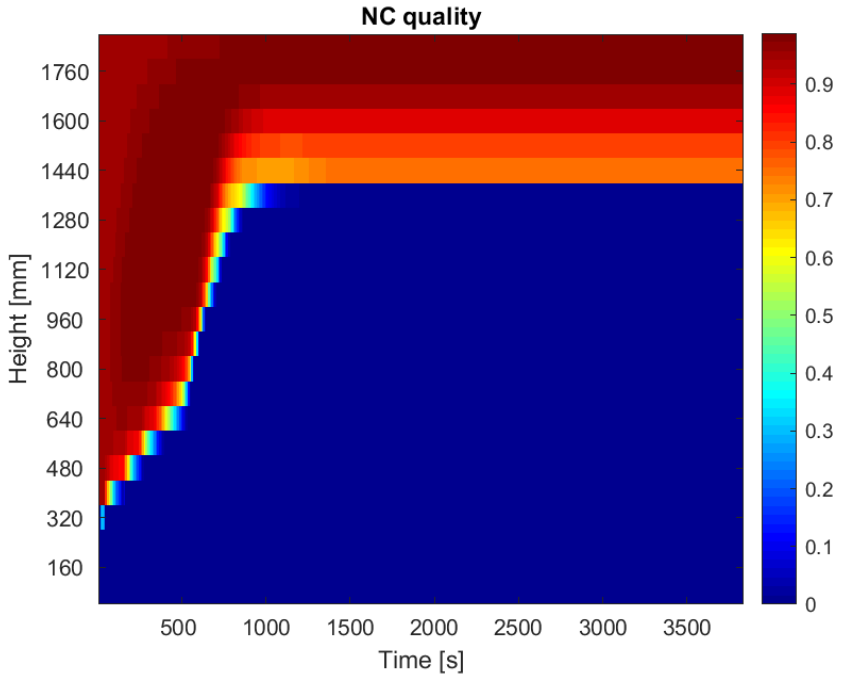

Figure 7-16 Distribution of NC gases in the tube over time - calculation based on PABS-PURE-4 experiment

However, the total sum of NC species mass is also increasing, which phenomenon should not take place. This behavior was observed for a wide range of time step values (0.0001s to 0.1 s). The mass balance for NC gases is not achieved, and it can be verified by analyzing the behavior of the variable EMASS, which is the mass error in kg, stored independently of the above calculation, directly by RELAP5. With NC modelling disabled, the error initially increases quite fast to stabilize and remain at a relative value below 0.2% overall. In the other case, the mass error stabilizes later and reaches slightly higher values, below 0.4%, Figure 7-17.

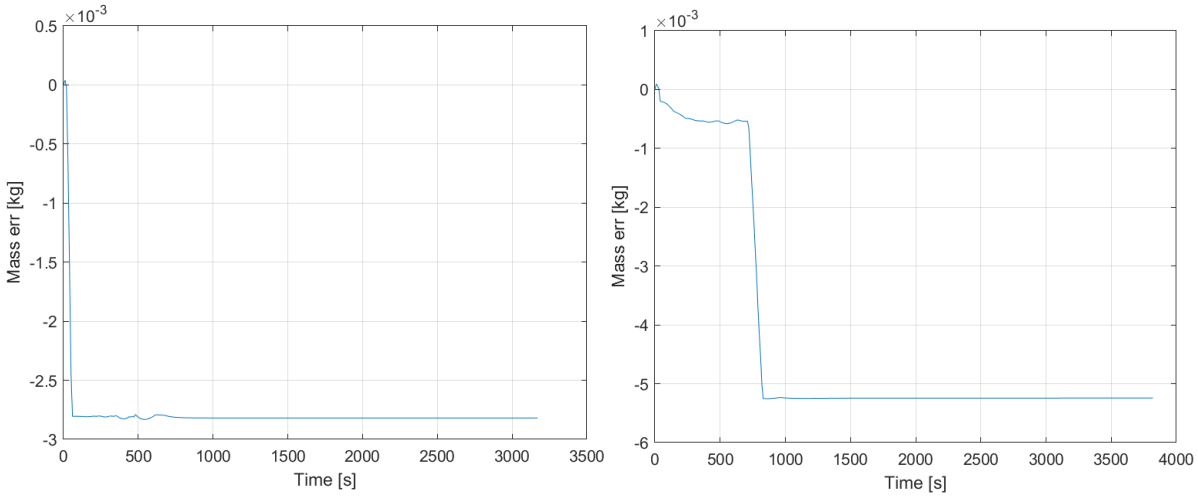

Figure 7-17 Mass error with NC modelling disabled (left) and enabled (right)

Even though the overall increase in the total mass in the primary side of the simulations is low, it affects the species ratios in the gaseous mixtures to significant degree. From previously discussed literature, it was concluded that default RELAP5 correlations in previous code releases were overestimating the impact

of NC gases. Thus, such change in the gas mixture composition would strongly affect the overall calculated results. This pattern of code behavior seems to be repeated in the MOD3.4 version as well.

The slow increase in the mass of NC gases was not report previously, as most of the time the, other researchers' models were not closed volumes without inlets and / or outlets as the case is in this work. The slow accumulation would not be visible if the mixtures would be continuously replenished at the bottom of the test tube and removed at the top.

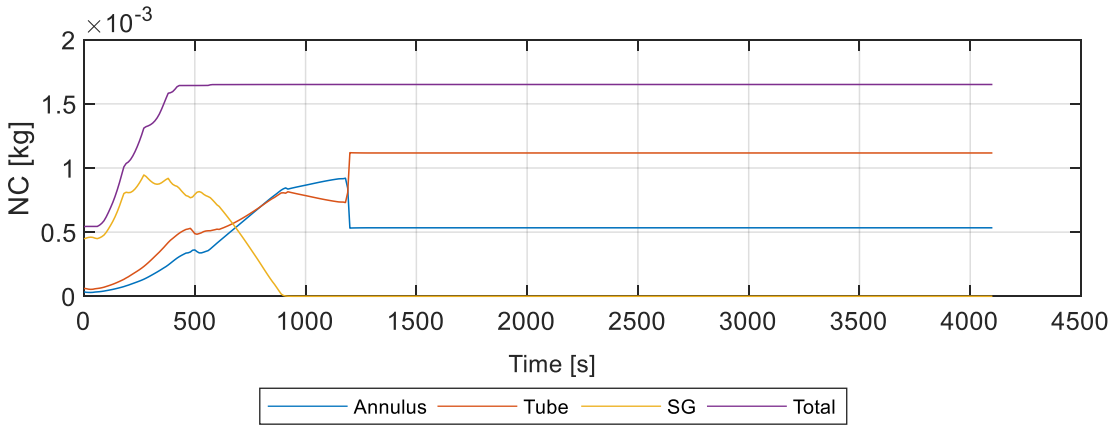

Figure 7-18 NC mass distribution reversal between inner the column and the condensation annulus around t=1000 s

Another interesting pattern observed for all calculation using nodalization scheme 2 and with NC modelling enabled, was the step-wise change in the distribution of non-condensables between inner column and surrounding annulus in the condensation tube, Figure 7-15 D, Figure 7-18. After the reversal is complete, the new distribution remains stable over time, and at this moment the pressure reaches steady-state. Since in case of nodalization 2, all the condensation takes place in the annulus part of the condenser, significant reduction of the NC gas content in this area helps to stabilize condensation flux that equalizes the evaporation in the SG tank below. Before and after reversal, the flow regime calculated by RELAP5 does not change and is marked as annular-mist. The exact cause of this behavior was not identified.

7.7.2 Gas and temperature distributions

Besides integral values of various parameters, RELAP5 simulations were assessed considering their calculated spatial distributions in the model. Figure 7-19 shows an example where temperature in the condensation tube's center is considered. All executed calculations overestimate it – with NC modelling disabled, the overestimation in this case remains below 4% for the most of the tube's height, just to diverge at the top. This inconsistency can be attributed to the residual NC gases present in the experiment. However, in the calculation approach that attempts to account for this residual quantity, the divergence is even greater. This mismatch can also be observed in the volume-averaged non-condensables mass fraction, Figure 7-20. The increase in this value corresponds to the decrease in centerline temperature. The limitation of both approaches to simulation is clear in the obtained results.

On the other hand, the temperature increase in the coolant water is well modelled by all considered techniques, Figure 7-21. Low spatial resolution of the experimental data limits the accuracy of the comparison, but overall temperature change between inlet and outlet is accurate to +/- 0.1°C. This agrees well with the previously considered integral values, Figure 7-11. Even though RELAP5 does not accurately

predict pressures or temperature spatial distributions in the single condensation tube, the integral heat balance is accurately simulated.

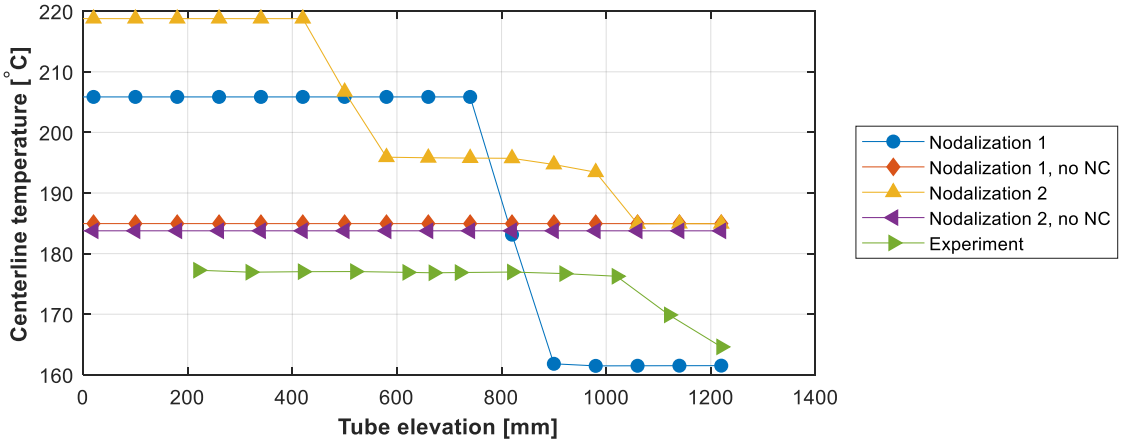

Figure 7-19 Temperature in the condensation tube center (exp. PABS-PURE-5)

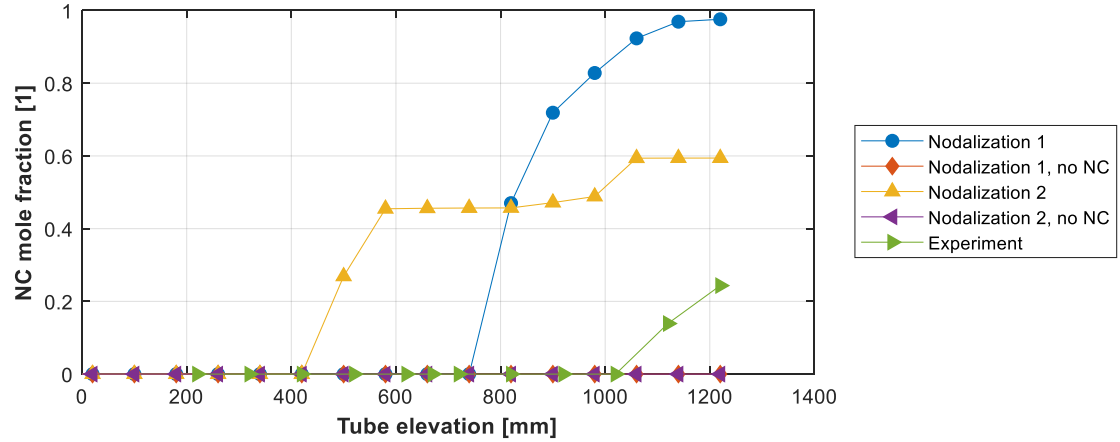

Figure 7-20 NC gas fraction along the condensation tube (exp. PABS-PURE-5)

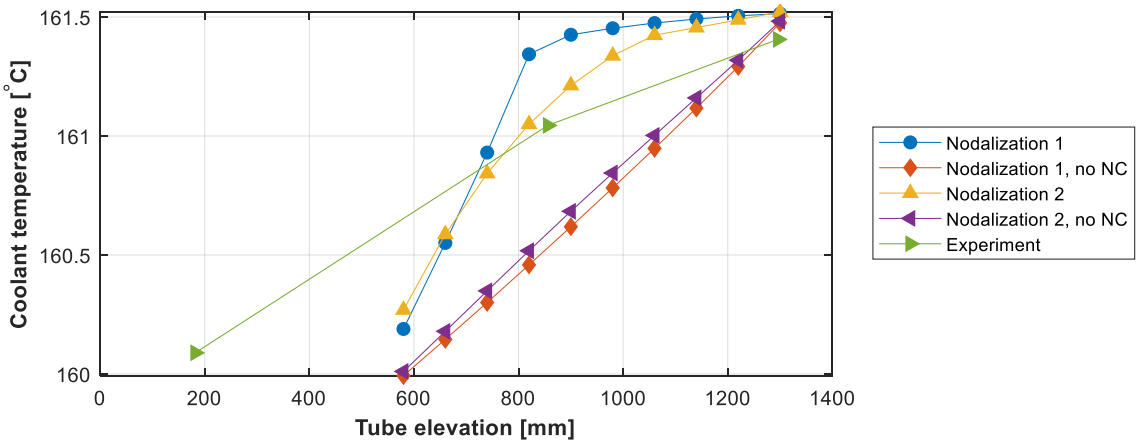

Figure 7-21 Change in the coolant water temperature along the coolant channel (exp. PABS-PURE-5)

7.8 Calculation results – NC gases

In this section, results of RELAP5 calculations with NC gases are presented. The discussion is divided in three subsections, depending on the composition of the modelled gas mixture. The experiments that formed the basis for initial/boundary conditions and later comparison are listed in each relevant section.

7.8.1 Nitrogen

Calculations with N_2 were based on experiments NC-MFR-ABS-4-X, NC-MFR-ABS-6-X and Pabs-MFR-X. As it was observed in the section above, NC gases modelling in RELAP5 highly overestimated the steady-state pressures at which the calculation stabilized, when compared to the measured data. This behavior was observed due to imbalance in noncondensable gases mass, which would increase as soon as they were included in the simulation. To investigate this behavior further by conducting simulations with varying fractions of added non-condensables. Figure 7-22 shows the calculated and measured pairs of pressure and condensation flow values. The former overestimation very pronounced for each simulated test.

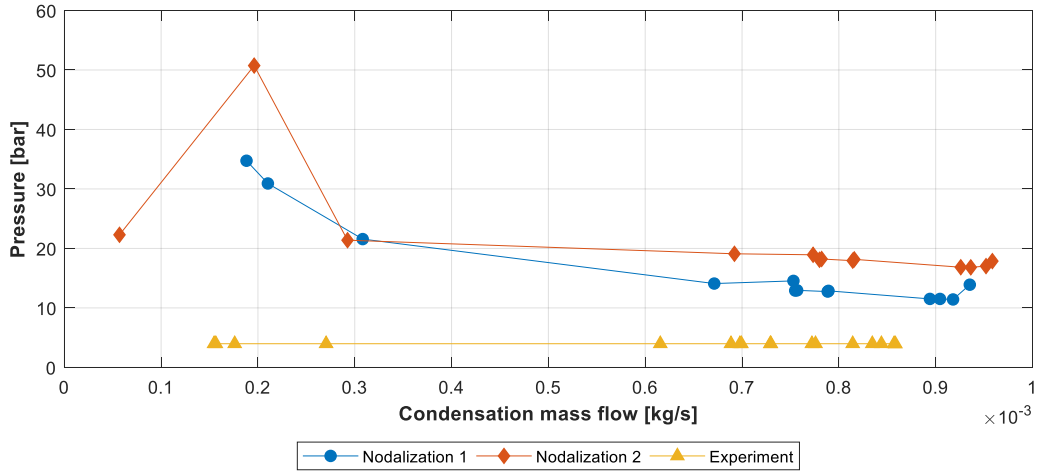

Figure 7-22 RELAP5 steady-state pressure and experimental values – NC-MFR-ABS-4

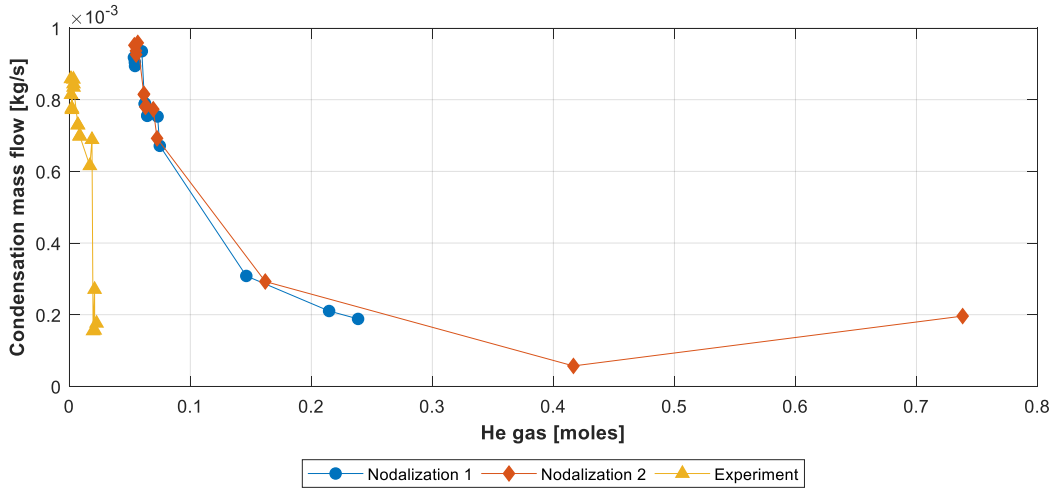

Figure 7-23 Increasing mass of added N_2 gas impact on condensation flow – NC-MFR-ABS-4

This result is well corroborated by the molar content of nitrogen that the calculations arrive to at the steady state, Figure 7-23. Both nodalization schemes exhibit overestimation ranging from factor of 5 at

lower non-condensable fraction to over 70 for higher ones. At the same time, the integral heat balance in each calculation is maintained, Figure 7-24 and steady-state can be reached with both nodalization schemes. When nodalization scheme 2 is used, the mass reversal can be observed, as with the calculations based on pure steam experiments, Figure 7-25.

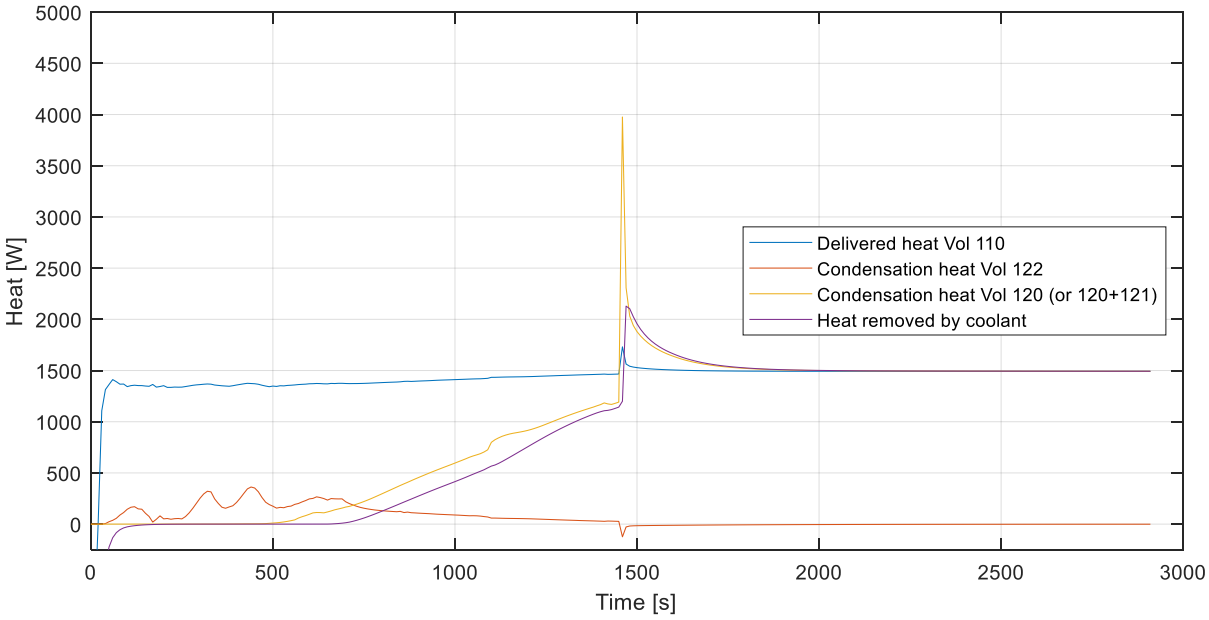

Figure 7-24 Heat balance for simulation of experiment NC-ABS-4_2, nodalization 2

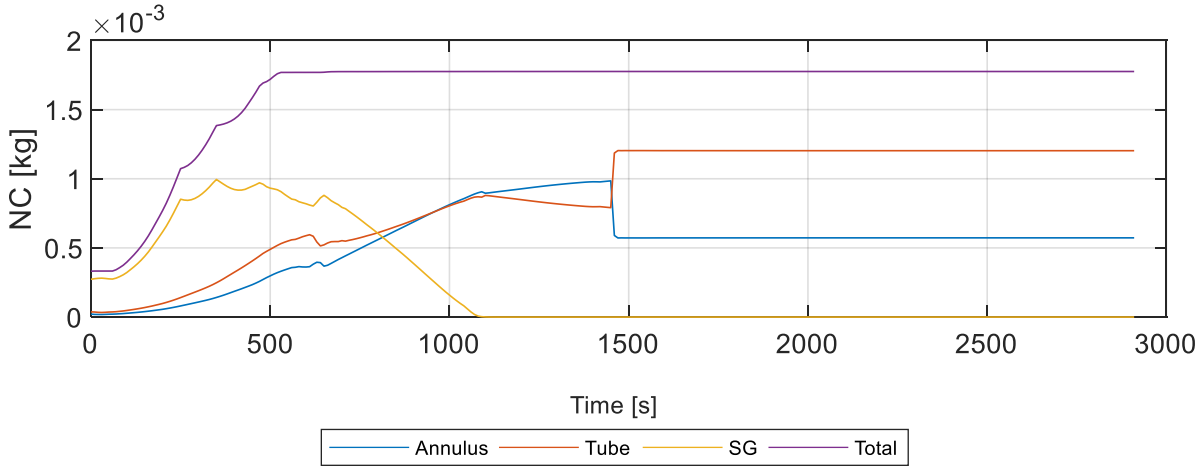

Figure 7-25 NC mass distribution reversal between inner the column and the condensation annulus, exp. NC-ABS-4_2, nodalization 2

To investigate the behavior of non-condensables further, volume-averaged velocities of liquid and gas phase, for both nodalization schemes were analyzed, Figure 7-26, for nodalization scheme 2. On this graph, each pair of columns represent velocities in tube center (left) and annulus (right). Last 5 times steps of each calculation are presented, spanning 60 seconds of flow time, to verify the stability of the plotted values.

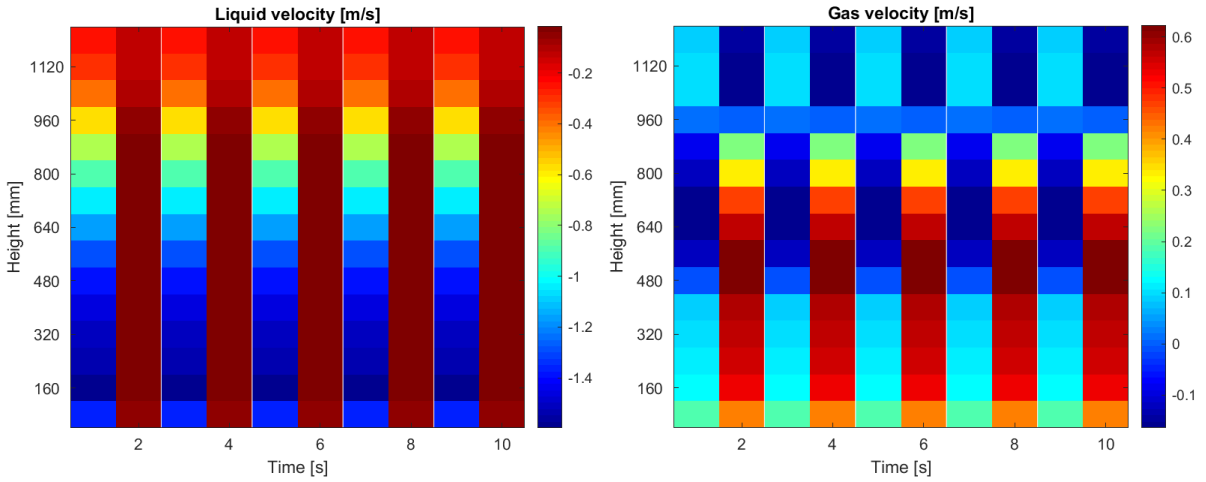

Figure 7-26 Gas and liquid velocities distribution in the tube center and annulus, based on exp. NC-ABS-4_2

Velocity of the liquid phase is both volumes is negative, indicating flow back towards the steam generator. With the gaseous phase, the velocity vector changes direction between the two – recirculation is established, with steam entering the condensation tube via annulus (positive velocity) and then recirculating back in the tube center (negative velocity). This describes the post-mass-reversal regime, where most of the non-condensables gases mass is located in the tube's center. Steam-rich flow enters the annulus, and the NC gas fraction gradually increases as the steam is depleted through condensation process, Figure 7-27.

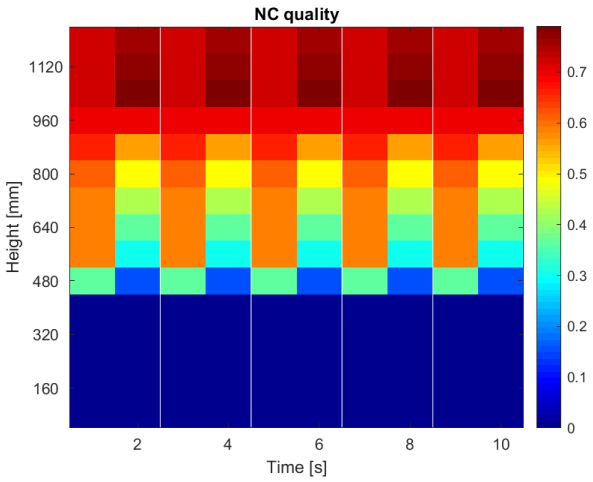

Figure 7-27 NC gas quality (mass fraction) in the tube center an annulus, based on exp. NC-ABS-4_2

This calculation result is contrary to what should normally occur in such situation, since the velocity across the tube diminishes in the direction of the wall, due to interphase or gas/wall friction. However, this artefact was is introduced due to explicit separation of volume near the wall and the "bulk" of the flow in the tube center. Ultimately, this approach to modelling the condensation tube did not accurately reproduced the experimental data. The achieved recirculation, even though expected due to higher density of the nitrogen gas when compared to steam, was not correctly simulated.

On the other hand, in the nodalization scheme 1, no recirculation was possible to calculate at all, due to a single transport equation solved for the gaseous phase by RELAP5, without differentiating between

species present in the mixture. In these cases, liquid velocity was always in the negative, while the gas phase velocity remained always positive, Figure 7-28.

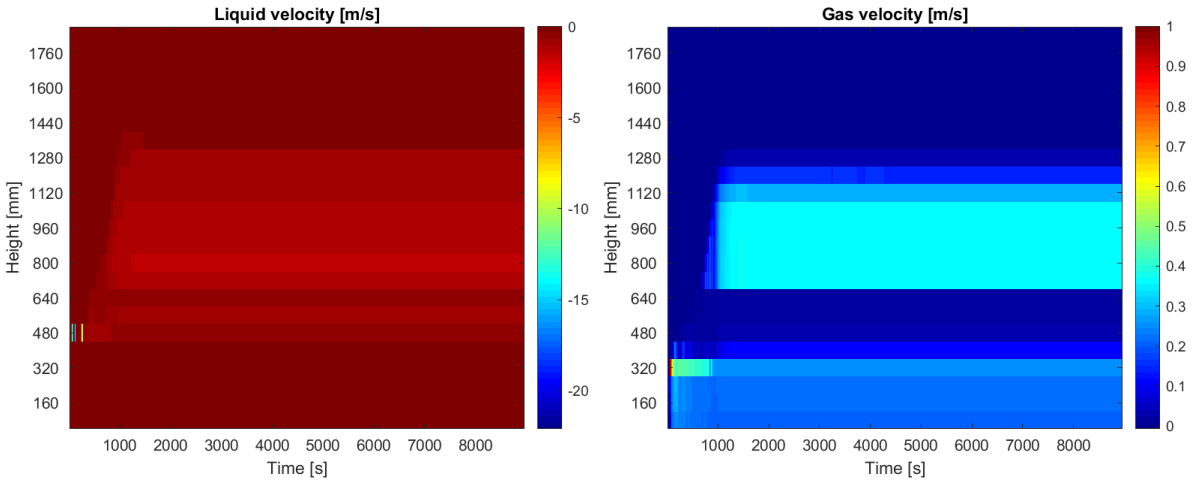

Figure 7-28 Liquid phase (left) and gaseous phase (right) velocities, nodalization 1, based on exp. NC-ABS-4_2

7.8.2 Helium

Calculations with helium presented in this chapter are based on experiment series NC-MFR-ABS-He-4. The issues with the NC gas recirculation were not expected to be the case in these simulations, due to the lower density of helium compared to steam, which removed the possible driving force of such a phenomenon.

As with previous calculations, the overall heat balance for each calculation was achieved and steady-state pressures could have been reached, Figure 7-29 (left). Issues with NC gas mass imbalance persisted for this gas species as well, Figure 7-29 (right).

The condensation/evaporation during the simulations is eventually reached, Figure 7-30, but at much elevated pressures, as was the case with N_2. Ultimately, a meaningful comparison of RELAP5 condensation flux estimation at a given molar content of non-condensables was thus prevented.

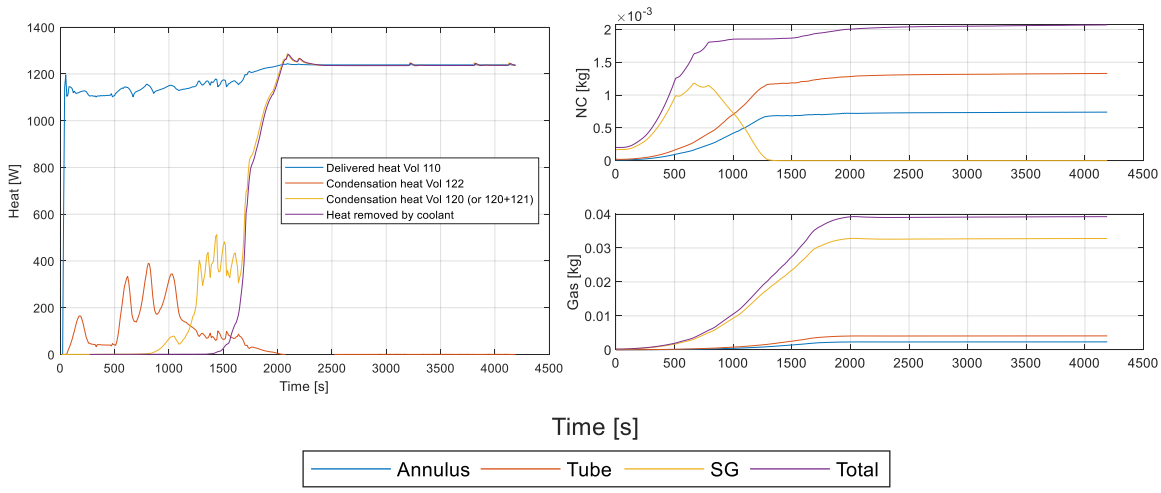

Figure 7-29 Integral heat balance (left) and mass accumulation (right) for calculations with helium, based on exp. HE-ABS-2_2

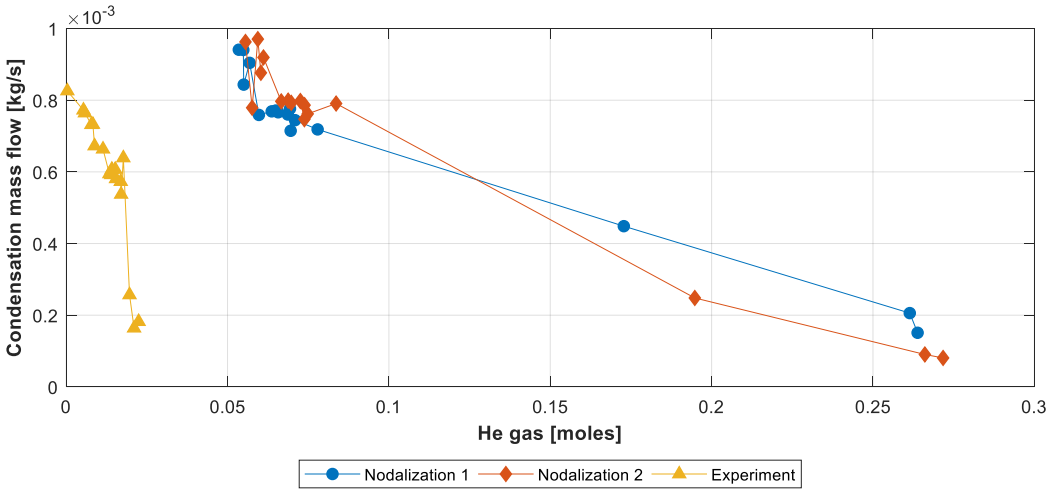

Figure 7-30 Relationship between condensation mass flow and helium gas molar content, based on exp. HE-ABS-2_2

7.9 RELAP5 calculations - summary

Conducted calculations with RELAP5/MOD3.4 encompassed a range of approaches to physical domain nodalization and treatment of non-condensables. Obtained results make it clear that if NC models are disabled in RELAP5, accurate temperature distributions and steady-state pressures can be successfully reproduced. By enabling NC gas models, the present work encountered a previously not reported issue of non-condensables mass imbalance. As stated, previous work usually modelled flow-through facilities, where small increase of NC gases mases would be masked by continuously replenished new gas mixture entering the calculation domain. This precluded meaningful assessment of the performance of the default condensation models.

Nevertheless, even with the encountered problems, RELAP5 was always able to reproduce the integral heat flow balance – from the heater, through steam evaporation, condensation, conduction to coolant water and ultimately removal through coolant water outlet. With the increase mass of non-condensables, the calculations could have only stabilized and much higher pressures than observed in the experiments.

Further investigation and possible amendment to the implemented condensation models in RELAP5 is recommended, to address the detected malfunctions.

Chapter 8 Summary and outlook

In this chapter the overview of the outcomes of the performed experiments and accompanying calculations is presented. The summary is organized by topic, addressing each of the three main areas of this work: novel measurement techniques, reflux condensation experiments utilizing it and the accompanying numerical work. Finally, the possible further work is discussed, based on the gained experience, observed shortcomings and identified development paths.

8.1 Measurement technique

In the PRECISE facility two novel measurement sensors were implemented and used for the first time in the context of reflux condensation experiments. Both required the development of methods of installation and data acquisition / calibration techniques. Besides providing added insight into the reflux condensation phenomenon, the implementations itself present an addition to the measurement technique field.

8.1.1 Movable conductivity and temperature probe

Two parts of this probe should be analyzed separately – the traversing temperature / voltage and the voltage measurement with a fixed electrode array. Considering the former, it should be noted that measuring transverse profiles of temperature across the condensation tube was achieved successfully. The observed profiles were reliably and consistently reproduced at different operating conditions. The temperature data however did not provide a clear way of differentiating at which point the gradual value decrease towards the tube's wall was due to the developed thermal boundary layer and at which to the liquid film itself. By analyzing the dynamics of the reconstructed profiles, it was however possible to differentiate the pure steam zones and areas with NC gas – steam mixing, with the latter being much more dynamic.

At the same time, the liquid film detection through measurement of the voltage signal on the traversing thermocouple shield proved unreliable. To extract the signal from the measured data, a high degree of signal processing was required due to poor signal-to-noise ratio. Rather than the expected step-like voltage-increase at the point of contact, a diffuse, gradual rise was observed instead, possibly due to extensive signal processing. Even though the voltage signal mimicked the temperature response well, the clear conclusion about the gas-liquid interface was impossible to be made.

The position tracking with the open-loop stepper motor pulse counting and added error correction by two end switches proved sufficient to achieve accurate location information. Inclusion of the position encoder could further increase the precision in the further iterations of the probe. Since the probe poses a physical obstacle to the flow of gas / condensate, future iterations should make an attempt at further reducing the size of the traversing part, without compromising its mechanical integrity.

Despite best effort, the second part of the probe - the electrode array - did not provide sufficient resolution to satisfactorily measure the liquid film thickness in the experimental conditions. While the distinction between dry/wet condition was very clear, the low signal-to-noise ratio prevented calculating confident values on the actual flowing layer depth. On the other hand, the temporal analysis of the measured signal has shown a clear distinction between pure-steam zones, with stable signal values and non-condensables – steam mixing region, where high oscillations were observed.

During the development of the calibration procedure, it was also observed, and later confirmed numerically, that the presence of the grounded tube at the array perimeter affected the signal correlation to the liquid layer thickness. Instead of the predicted signal saturation for sufficiently thick films, after reaching a maximum value, a gradual signal decrease was observed, which made distinguishing very thick and thin films difficult. Further iterations of the electrode array should consider an addition of a shielding electrode or expanded non-conductive surrounding area, to minimize the impact of the grounded test tube.

8.1.2 Heat flux sensor

For measurements in the PRECISE facility with the new type of heat flux sensors (GHFS [202]) two methods of instrument embedding in the test tube were designed, realized and tested. The main goal of these techniques was to minimize any possible interference in the heat transfer path through the wall, which was aided by the steel-nickel composition of the used sensors and their low thickness. The challenge of the task was the possible high operational temperature in the facility, which limited the range of available materials. An appropriate, electrically insulating epoxy with high thermal conductivity and working temperature was identified and used for successful sensor embedding. The best possible temporal resolution of the measured signal was observed with sensors' surface exposed to the condensation flux directly. However, due to problems with durability of the used epoxy in contact with superheated steam, the second -best method was utilized, where the HFS resided behind a thin layer of protective steel. This allowed to eliminate the observed shortcomings of the first method and resulted in a reliable way of HFS embedding with minimal interference in the heat transfer through the condensation tube's wall. This method was further successfully utilized during an Innosuise (Schweizer Agentur für Innovationsförderung, former KTI) funded industry collaboration project[37] including GHFS.

The main limitation of the used sensors was their low Voltage/Watt sensitivity, which resulted in the observed signals in the range of μV. The developed two-stage amplifier chain paired with a high-frequency DAS allowed to overcome these limitations and achieve satisfactory signal-to-noise ratios.

The interpretation of the measured signals was only possible in conjunction with the developed calibration technique. The well-defined thermal-radiation-driven environment of the calibration setup allowed to create reliable correlations between observed voltages and heat-flux values. The sensor's sensitivity variation with temperature was included in the calibration method.

Measured signal was in good agreement with the more typical technique of using differential temperature measurement together with information about the tube's wall geometrical / thermal properties to recalculate the heat flux. Large temporal resolution of the direct heat flux measurement allowed to investigate the dynamics of the condensation process well into higher-frequency phenomena. This proved useful in allowing differentiation of zones with diverse gaseous composition in the test tube. The observed higher frequency phenomena, up to 10 Hz, in the heat flux signal were uniquely characteristic of the mixing zone between steam and NC gases. The amplitude of these oscillations was also indicative of the type of non-condensable present during the experiment.

Overall, insights gained from analyzing both – the time averaged values and the dynamic properties of the recorded heat flux signal provided useful characterization of the non-condensables mixing behavior and the condensation distribution in the tube. The future usage of this type of HFS should consider using

[37] KTI project Nr. 25435.1 PFIW-IW, "Optimierung der vereinfachten Kalorimetrie mit dem Automatischen Laborreaktor der Systag AG"

sensors with higher Voltage/Watt sensitivity, produced of alternative material pairs. Devices made of Al-Si should be investigated, as the possible replacement, due to their exceptional electrical performance [203].

8.2 Condensation experiments

The main topic of interest for the presented work was the behavior of non-condensable gases in the steam generator tube and their effect on the condensation process. Additionally, the performed experiment investigated impact of other thermodynamic properties including pressure, wall temperature gradient and coolant water velocity. Overall, data was acquired in the pressure range of 1-10 bars, corresponding to the temperature range of 100 to 180°C. Two non-condensable species He and N_2 as well as mixture of the two were used in average molar fraction ranging from 0 up to 0.9. The test conditions are relevant to a nuclear power plant mid-loop operation. In total, data from over 110 individual experimental runs were reported. The main findings from the performed tests are summarized in the following sections.

8.2.1 Effect of test pressure, temperature and coolant water properties

The results obtained by varying the operational conditions were in good agreement with the previous body of research in the field. Pure steam condensation, extremely effective at heat removal, is further enhanced with increasing pressure, coolant water heat transfer coefficient and test tube's wall temperature gradient. The last of the three had the most significant impact on the observed condensation rates – large enough to overcome the capabilities of the installed electrical heater. As was the case with non-condensables gases present, decreasing the coolant water temperature was also the most effective method to promote condensation.

The distribution of gases in the test tube is also strongly affected by the pressure. By enhancing the condensation rates, the gas mixture became depleted of steam at lower elevations, resulting in shorter effective condensation lengths.

8.2.2 Non-condensable gas plug formation

For both, heavy N_2 and light He gases a strong stratification was observed in the test tube. In every experiment three distinct areas in the condensation volume have been observed – the pure-steam zone at the tube's bottom, followed by an intermediate mixing zone and finally a NC plug on top. Each zone exhibited significant variation in the observed temperature, heat flux and film thickness. The steam rich zone was characterized by high temperature, equivalent to that of the water boiling point at a given pressure throughout its whole length, accompanied by large condensation rates observed as high heat flux values. Horizontal temperature profiles exhibited a strong tendency to decrease towards the wall. The usual drop-off distance began between 1.5 to 2 mm from the wall and the typical decrease was in the range of 4°C. The temperature away from the wall remained stable, with oscillations increasing towards the tube's wall. Overall, in the steam-rich condensation zone, the recorded signals exhibited low variation and remained stable. Similar to the topmost zone, NC plug did not present significant variation in recorded values. However, the temperature in this volume was almost equal to that of the cooling water stream and practically no heat transfer through the wall took place. Horizontal temperature profiles across the test tube were flat and stable in this region.

The most interesting region for analysis was the transitional mixing zone. Its shape and behavior were most strongly affected by the type of the non-condensable gas present. Light gas formed thin and stable interface, while heavy gas a diffuse and very dynamic one. In case of a mixture of non-condensable gas species, the properties of the mixing zone were strongly correlated to the composition, smoothly transitioning from pure light gas to pure heavy gas characteristic behavior.

At the same time, when observed in normalized spatial coordinates, for both gas species and their blends the mixing zone was similarly characterized by a gradual decrease in temperature, condensation heat flux and liquid film thickness. The drop-off slope was similar for each of these mixtures, in normalized coordinates.

The horizontal temperature profiles in the mixing zone have shown the tendency to decrease towards the wall, similar to the ones in the steam condensation zone. The change in values was larger, reaching up to 9-10°C. The drop-off would start at around 3-4 mm distance. However, the significantly increased temperature oscillations prevented its accurate localization. Surprisingly, these temperature profiles were not significantly affected by the composition of the used non-condensables mixture. This was true for each of the distinguished zones.

The analysis of the dynamics of the recorded temperature / heat flux / film thickness signals in the transition area allowed for an easy identification of the type of the NC gas. Large amplitude oscillations interpreted as a high degree of steam-NC gas mixing were characteristic for the nitrogen. This turbulent behavior was caused by the higher molecular weight of nitrogen compared to water and the thus unstable density stratification. It resulted in an increased condensation rates when compared against the same average molar fraction of helium.

Experiments with continuous injection of non-condensables allowed for an accurate spatial resolution measurement of the mixing zone properties. Greatest oscillations of acquired signals were confidently observed in the center of the mixing zone, as it was passing along each sensor. The distinction of the zone width was also observed, bolstering the finding of steady state tests.

For both types of tests, the increased amount of non-condensables resulted in greater part of the test tube volume being plugged. This shifted the location of the mixing zone but did not affect its width or dynamism. The non-condensables plug, formed above the mixing zone, did not exhibit temperature / heat flux signal variations and remained essentially a dead-zone.

8.2.3 Higher frequency phenomena

While the dynamics of the mixing layer was indicative of the type of NC gas present, the analysis of heat flux and liquid film signals above frequencies of 10 Hz did not reveal any consistent patterns. Liquid film behavior, such as waviness, or drops of condensate passing over sensors' area could not have been confidently distinguished. No dominant frequencies in condensation process could have been detected and can be concluded that these phenomena behavior is chaotic rather than periodic.

8.3 RELAP5 simulations

The calculations executed with the Reactor Excursion and Leak Analysis Program RELAP5/MOD3.4 revealed significant shortcomings of the default condensation model with NC gases, when applied to the closed volumes. The effect of mass imbalance in the species equation, leading to continuous build-up of non-condensables in the computational domain, was emphasized due to lack of inlets/outlets in the domain. The analyzed problem might thus lie outside of the range for which the models were properly validated, and more work is needed to address this deficiency. Moreover, the models used in RELAP5 are conservative by design, and as noted in the previous analysis, tend to overestimate the effect of NC gases on condensation. These two effects together led to the inability to properly reproduce the experiments from the PRECISE facility. Future work should focus on modifying the existing models, to at least minimize the numerical error of non-condensable mass imbalance.

8.4 Outlook and recommendations

Findings presented in this work provide a good basis for further investigation of reflux condensation in the presence of varied non-condensable gas species. The experience gained with the PRECISE facility revealed several areas in which the experimental technique could be expanded and few others that merit further development of the existing methods. The abovementioned modifications to the two novel sensor types would increase the measurement resolution and accuracy. Especially, the performance of electrode array should be addressed, in order to provide reliable data on the film thickness. Increased number of electrodes could allow to detect not only localized film thickness, but to recognize film waviness and even distinguish condensation modes between film-wise and droplet-wise [225]. Implementation of such a sensor is however a significant technical challenge, especially due to elevated temperatures present even at the limited operating pressure range of the PRECISE facility.

Moreover, the maximum operating pressure of the facility should be increased. This move would improve the relevance of the data collected to match the conditions characteristic for the predicted severe accident scenarios in PWRs. The recognized challenge of this development is further narrowing of the materials and sensors capable of withstanding the harsher conditions. While in principle both, GHFS and movable temperature/conductivity probe should be able to survive the increased temperature, their mounting / implementation would need to be modified, to eliminate reliance on currently used epoxy.

Furthermore, the investigation of interaction of steam and NC gases plug should be further supplemented by performing experiments in the full U-tube geometry, including the downward part and allowing for plug recirculation through the system. While the gathered data provided valuable insights in the interface zone properties, allowing the plug to react to the incoming steam flow momentum would clarify how these interfaces behave in the typical PWR steam generator.

On a technical note, one of the shortcomings of the presented work was the imperfect evacuation of air from the test tube during the experiment setup, resulting in small but nevertheless present amount of residual NC gases. This reduced the precision of the inventory control and required extensive data processing treatment to accurately estimate the actual gas mixture composition. The control of the intentionally added amount of He or N_2 for was also challenging. The presented method should be further developed to address both of those issues.

Lastly, in the course of this work besides 1D code calculations with RELAP5, an attempt was made at utilizing computational fluid dynamics (CFD) code (ANSYS Fluent, versions up to 19.1) to predict NC gas behavior in the PRECISE facility. A custom user defined function (UDF) function [244] was utilized to predict condensation rates. Unfortunately, it's performance in the closed volume was unsatisfactory, due to mass imbalance of the NC gas species. The description of the calculations was therefore omitted from the thesis body but, nevertheless, appropriate development of the UDF condensation function could address the observed issues. CFD calculations are an increasingly more relevant tool in the field of nuclear safety and improving the accuracy of the available tools should remain a high priority for the future work.

Chapter 9 Bibliography

[1] International Atomic Energy Agency (IAEA), "Operational & Long-Term Shutdown Reactors," 2016. [Online]. Available: https://www.iaea.org/PRIS/WorldStatistics/OperationalReactorsByCountry.aspx. [Accessed: 01-Apr-2019].

[2] A. Markandya and P. Wilkinson, "Electricity generation and health," *Lancet*, vol. 370, no. 9591, pp. 979–990, Sep. 2007.

[3] P. Burgherr and S. Hirschberg, "Comparative assessment of natural gas accident risks," Villigen, 2005.

[4] F. D'Auria and M. Frogheri, "Use of a natural circulation map for assessing PWR performance," *Nucl. Eng. Des.*, vol. 215, no. 1–2, pp. 111–126, 2002.

[5] H. Yong Jeong, B. Nyun Kim, and K. Lee, "Thermal-hydraulic phenomena during reflux condensation cooling in steam generator tubes," *Ann. Nucl. Energy*, vol. 25, no. 17, pp. 1419–1428, Nov. 1998.

[6] K. Kawanishi, A. Tsuge, M. Fujiwara, T. Kohriyama, and H. Nagumo, "Experimental study on heat removal during cold leg small break LOCAs in PWRs," *J. Nucl. Sci. Technol.*, vol. 28, no. 6, pp. 555–569, 1991.

[7] S. Al Issa and R. Macian, "A review of CCFL phenomenon," *Ann. Nucl. Energy*, vol. 38, no. 9, pp. 1795–1819, Sep. 2011.

[8] B. Chatterjee *et al.*, "Analyses for VVER-1000 / 320 reactor for spectrum of break sizes along with SBO," *Ann. Nucl. Energy*, vol. 37, no. 3, pp. 359–370, 2010.

[9] O. Kauppinen, V. Kouhia, V. Riikonen, J. Hyvärinen, and H. Sjövall, "Computer analyses on loop seal clearing experiment at PWR PACTEL," *Ann. Nucl. Energy*, vol. 85, pp. 47–57, 2015.

[10] W. W. Wang, G. H. Su, S. Z. Qiu, and W. X. Tian, "Thermal hydraulic phenomena related to small break LOCAs in AP1000," *Prog. Nucl. Energy*, vol. 53, pp. 407–419, 2011.

[11] Y. Kim and K. Kang, "Overview of an investigation into SBLOCA tests of ATLAS facility," *Ann. Nucl. Energy*, vol. 102, pp. 386–401, 2017.

[12] J. Freixa, F. Reventós, C. Pretel, L. Batet, and I. Sol, "SBLOCA with boron dilution in pressurized water reactors . Impact on operation and safety," *Nucl. Eng. Des.*, vol. 239, pp. 749–760, 2009.

[13] J. Birchley, T. J. Haste, and M. Richner, "Accident management following loss of residual heat removal during mid-loop operation in a Westinghouse two-loop PWR," *Nucl. Eng. Des.*, vol. 238, pp. 2173–2181, 2008.

[14] D. Dumont, G. Lavialle, B. Noel, and R. Deruaz, "Loss of residual heat removal during mid-loop operatio : BETHSY experiments," *Nucl. Eng. Des.*, vol. 149, pp. 365–374, 1994.

[15] C. Fletcher, P. McHugh, S. Naff, and G. Johnsen, "Thermal-hydraulic processes involved in loss of residual heat removal during reduced inventory operation. Revision 1," 1991.

[16] P. Kral and U. J. V Rez, "Sources and Effect of Non - Condensable Gases in Reactor Coolant System of Lwr," *Nureth-16*, no. September, pp. 5194–5208, 2015.

[17] Y. Liao, S. Guentay, D. Suckow, and a. Dehbi, "Reflux condensation of flowing vapor and non-condensable gases counter-current to laminar liquid film in a vertical tube," *Nucl. Eng. Des.*, vol. 239, no. 11, pp. 2409–2416, Nov. 2009.

[18] W. Minkowycz and E. Sparrow, "Condensation heat transfer in the presence of noncondensables, interfacial resistance, superheating, variable properties, and diffusion," … *J. Heat Mass Transf.*, 1966.

[19] V. E. Denny, V. J. Jusionis, and L. Angeles, "Effects of noncondensable gas and forced flow on laminar film condensation," *Int. J. Heat Mass Transf.*, vol. 15, pp. 315–326, 1972.

[20] H. T. Chen, S. M. Chang, and Z. Lan, "Effect on noncondensable gas on laminar film condensation along a vertical plate fin," *Int. J. Heat Fluid Flow*, vol. 19, no. 4, pp. 374–381, Aug. 1998.

[21] C. J. Tu and C. Y. Wang, "Noncondensable gas effect on condensation in a separate type two-phase

closed thermosyphon," *Warme- und Stoffubertragung*, vol. 23, no. 3, pp. 153–158, 1988.

[22] L. Yuquan, H. Botao, Z. Jia, and W. Nan, "Comparative Experiments to Assess the Effects of Accumulator Nitrogen Injection on Passive Core Cooling During Small Break LOCA," *Nucl. Eng. Technol.*, vol. 49, no. 1, pp. 54–70, 2017.

[23] B. Schoen and P. Weber, "Nitrogen in a steam generator of a PWR under SBLOCA conditions: Experimental investigations in the PKL test facility and comparison with analytical studies," *Exp. Therm. Fluid Sci.*, vol. 15, no. 3, pp. 238–252, Oct. 1997.

[24] D. F. Othmer, "The Condensation of Steam," *Ind. Eng. Chem.*, vol. 21, no. 6, pp. 576–583, 1929.

[25] S. J. Meisenburg, *The influence of small concentrations of air in steam on the steam-film coefficient of heat transfer.* [Philadelphia, 1935.

[26] H. Uchida, A. Oyama, and Y. Toga, "Evaluation of post-incident cooling systems of light-water power reactors," in *Third International Conference on the Peaceful Uses of Atomic Energy*, 1964.

[27] H. Al-Diwany and J. Rose, "Free convection film condensation of steam in the presence of non-condensing gases," *Int. J. Heat Mass Transf.*, vol. 16, pp. 1359–1369, 1973.

[28] C. L. Henderson and J. M. Marchello, "Film Condensation in the Presence of a Noncondensable Gas," *J. Heat Transfer*, vol. 91, no. 3, p. 447, Aug. 1969.

[29] D. G. Kroger and W. M. Rohsenow, "Condensation heat transfer in the presence of a non-condensable gas," *Int. J. Heat Mass Transf.*, vol. 11, no. 1, pp. 15–26, Jan. 1968.

[30] M. K. Bologa, I. K. Savin, and A. B. Didkovsky, "Electric-field-induced enhancement of vapour condensation heat transfer in the presence of a non-condensable gas," *Int. J. Heat Mass Transf.*, vol. 30, no. 8, pp. 1577–1585, Aug. 1987.

[31] M. Yasuo and H. Kunio, "Free convective condensation heat transfer with noncondensable gas on a vertical surface," *Int. J. Heat Mass Transf.*, vol. 16, no. 12, pp. 2229–2240, Dec. 1973.

[32] T. D. Karapantsios and A. J. Karabelas, "Direct-contact condensation in the presence of noncondensables over free-falling films with intermittent liquid feed," *Int. J. Heat Mass Transf.*, vol. 38, no. 5, pp. 795–805, Mar. 1995.

[33] H. C. Kang and M. H. Kim, "Effect of non-condensable gas and wavy interface on the condensation heat transfer in a nearly horizontal plate," *Nucl. Eng. Des.*, vol. 149, no. 1–3, pp. 313–321, Sep. 1994.

[34] S. K. Park, M. H. Kim, and K. J. Yoo, "Condensation of pure steam and steam-air mixture with surface waves of condensate film on a vertical wall," *Int. J. Multiph. Flow*, vol. 22, no. 5, pp. 893–908, Sep. 1996.

[35] S. K. Park, M. H. Kim, and K. J. Yoo, "Effects of a wavy interface on steam-air condensation on a vertical surface," *Int. J. Multiph. Flow*, vol. 23, no. 6, pp. 1031–1042, Nov. 1997.

[36] H. M. Sabir, I. W. Eames, and K. O. Suen, "The effect of non-condensable gases on the performance of film absorbers in vapour absorption systems," *Appl. Therm. Eng.*, vol. 19, no. 5, pp. 531–541, May 1999.

[37] J. W. Rose, "Surface Tension Effects and Enhancement of Condensation Heat Transfer," *Chem. Eng. Res. Des.*, vol. 82, no. 4, pp. 419–429, Apr. 2004.

[38] E. Schmidt, W. Schurig, and W. Sellschopp, "Versuche über die Kondensation von Wasserdampf in Film- und Tropfenform," *Tech. Mech. und Thermodyn.*, vol. 1, no. 2, pp. 53–63, Feb. 1930.

[39] J. W. Rose, "Dropwise condensation theory and experiment: A review," *Proc. Inst. Mech. Eng. Part A J. Power Energy*, vol. 216, no. 2, pp. 115–128, Jan. 2002.

[40] R. D. Mathurkar, "Review on Steam Condensation Heat Transfer Coefficient in Vertical Mini Diameter Tube," *Int. Res. J. Eng. Technol.*, vol. 4, no. 5, pp. 705–710, 2017.

[41] J. Huang, J. Zhang, and L. Wang, "Review of vapor condensation heat and mass transfer in the presence of non-condensable gas," *Applied Thermal Engineering*, vol. 89. Pergamon, pp. 469–484, 05-Oct-2015.

[42] M. Jakob, "Heat Transfer in Evaporation and Condensation," *Mech. Eng.*, vol. 58, pp. 729–739, 1936.

[43] E. Baer and J. M. Mckelevy, "Heat transfer in dropwise condensation," in *ACS Delaware Science Symposium*, 1958.

[44] J. F. Welch and J. W. Westwater, "Microscopic Study of Dropwise Condensation," *Int. Dev. Heat Transf.*, vol. 2, pp. 302–309, 1961.

[45] S. Sugawara and K. Katsuta, "Fundamental study on dropwise condensation," in *Proceedings of the Third International Heat Transfer Conference, Chicago*, 1966, p. 354.

[46] A. Majumdar and I. Mezic, "Instability of Ultra-Thin Water Films and the Mechanism of Droplet Formation on Hydrophilic Surfaces," *J. Heat Transfer*, vol. 121, no. 4, p. 964, Nov. 1999.

[47] J. L. McCormick and J. W. Westwater, "Nucleation sites for dropwise condensation," *Chem. Eng. Sci.*, vol. 20, no. 12, pp. 1021–1036, Dec. 1965.

[48] A. C. Peterson and J. W. Westwater, "Dropwise Condensation of Ethylene Glycol," in *Chemical Engineering Progress Symposium Series*, 1966, vol. 62, no. 64, pp. 135–142.

[49] A. Umur and P. Griffith, "Mechanism of Dropwise Condensation," *J. Heat Transfer*, vol. 87, no. 2, p. 275, May 1965.

[50] L. Tianqing, M. Chunfeng, S. Xiangyu, and X. Songbai, "Mechanism study on formation of initial condensate droplets," *AIChE J.*, vol. 53, no. 4, pp. 1050–1055, Apr. 2007.

[51] C. Mu, J. Pang, Q. Lu, and T. Liu, "Effects of surface topography of material on nucleation site density of dropwise condensation," *Chem. Eng. Sci.*, vol. 63, no. 4, pp. 874–880, Feb. 2008.

[52] N. Miljkovic and E. N. Wang, "Condensation heat transfer on superhydrophobic surfaces," *MRS Bull.*, vol. 38, no. 05, pp. 397–406, May 2013.

[53] A. Bani Kananeh, M. H. Rausch, A. P. Fröba, and A. Leipertz, "Experimental study of dropwise condensation on plasma-ion implanted stainless steel tubes," *Int. J. Heat Mass Transf.*, vol. 49, no. 25–26, pp. 5018–5026, Dec. 2006.

[54] M. H. Rausch, A. P. Fröba, and A. Leipertz, "Dropwise condensation heat transfer on ion implanted aluminum surfaces," *Int. J. Heat Mass Transf.*, vol. 51, no. 5–6, pp. 1061–1070, Mar. 2008.

[55] R. Wilmshurst and J. W. Rose, "Dropwise and filmwise condensation of aniline, ethanediol and nitrobenzene," in *Proceedings of 5th International Heat Transfer Conference*, 1974, pp. 269–273.

[56] N. Miljkovic *et al.*, "Jumping-Droplet-Enhanced Condensation on Scalable Superhydrophobic Nanostructured Surfaces," *Nano Lett.*, vol. 13, no. 1, pp. 179–187, Jan. 2013.

[57] T. Takeyama and S. Shimuzu, "On the transition of drop-film condensation," in *Proceedings of 5th International Heat Transfer Conference*, 1974, pp. 274–279.

[58] U. Yoshio, S. Akio, and Y. Hiroyuki, "On the mechanism determining the transition mode from dropwise to film condensation," *Int. J. Heat Mass Transf.*, vol. 31, no. 5, pp. 1113–1120, May 1988.

[59] S. A. Stylianou and J. W. Rose, "Drop-to-filmwise condensation transition: Heat transfer measurements for ethanediol," *Int. J. Heat Mass Transf.*, vol. 26, no. 5, pp. 747–760, May 1983.

[60] Y. Utaka, A. Saito, and H. Yanagida, "An experimental investigation of the reversibility and hysteresis of the condensation curves," *Int. J. Heat Mass Transf.*, vol. 33, no. 4, pp. 649–659, Apr. 1990.

[61] I. Tanasawa and Y. Utaka, "Measurement of Condensation Curves for Dropwise Condensation of Steam at Atmospheric Pressure," *J. Heat Transfer*, vol. 105, no. 3, p. 633, Aug. 1983.

[62] X. Li and P. Cheng, "Lattice Boltzmann simulations for transition from dropwise to filmwise condensation on hydrophobic surfaces with hydrophilic spots," *Int. J. Heat Mass Transf.*, vol. 110, pp. 710–722, Jul. 2017.

[63] Q. Sheng, J. Sun, Q. Wang, W. Wang, and H. S. Wang, "On the onset of surface condensation: formation and transition mechanisms of condensation mode.," *Sci. Rep.*, vol. 6, p. 30764, 2016.

[64] S. Toxvaerd, "Molecular dynamics simulation of heterogeneous nucleation at a structureless solid surface," *J. Chem. Phys.*, vol. 117, no. 22, pp. 10303–10310, Dec. 2002.

[65] D. Niu and G. H. Tang, "The effect of surface wettability on water vapor condensation in nanoscale.," *Sci. Rep.*, vol. 6, p. 19192, Jan. 2016.

[66] K. Rykaczewski *et al.*, "Dropwise condensation of low surface tension fluids on omniphobic surfaces.," *Sci. Rep.*, vol. 4, p. 4158, Mar. 2014.

[67] Y. Wu and C. Zhang, "Analysis of anti-condensation mechanism on superhydrophobic anodic aluminum oxide surface," *Appl. Therm. Eng.*, vol. 58, no. 1–2, pp. 664–669, Sep. 2013.

[68] D. W. Tanner, D. Pope, C. J. Potter, and D. West, "Heat transfer in dropwise condensation at low steam pressures in the absence and presence of non-condensable gas," *Int. J. Heat Mass Transf.*, vol. 11, no. 2, pp. 181–190, Feb. 1968.

[69] D. W. Tanner, C. J. Potter, D. Pope, and D. West, "Heat transfer in dropwise condensation—Part I

The effects of heat flux, steam velocity and non-condensable gas concentration," *Int. J. Heat Mass Transf.*, vol. 8, no. 3, pp. 419–426, Mar. 1965.

[70] C.-J. Chang, C.-H. Lee, W.-T. Hong, and L. L. C. Wang, "IIST small break LOCA experiments with passive core cooling injection," *Nucl. Eng. Des.*, vol. 236, no. 1, pp. 19–34, Jan. 2006.

[71] X. H. Ma, X. D. Zhou, Z. Lan, Y. M. LI, and Y. Zhang, "Condensation heat transfer enhancement in the presence of non-condensable gas using the interfacial effect of dropwise condensation," *Int. J. Heat Mass Transf.*, vol. 51, no. 7–8, pp. 1728–1737, Apr. 2008.

[72] C. Bum-Jin, K. Sin, K. Min Chan, and M. Ahmadinejad, "Experimental comparison of film-wise and drop-wise condensations of steam on vertical flat plates with the presence of air," *Int. Commun. Heat Mass Transf.*, vol. 31, no. 8, pp. 1067–1074, Nov. 2004.

[73] J. Niknejad and J. W. Rose, "Interphase matter transfer: an experimental study of condensation of mercury," *Proc. R. Soc. London A Math. Phys. Eng. Sci.*, vol. 378, no. 1774, pp. 305–327, Oct. 1981.

[74] C. A. Miller and P. (Partho) Neogi, "INTERFACIAL PHENOMENA (Equilibrium and Dynamic Effects)," *J. Dispers. Sci. Technol.*, vol. 7, no. 1, pp. 127–128, 1986.

[75] W. Nusselt, "Die Oberflächenkondensation des Wasserdampfes," *Zeitschrift des Vereins Dtsch. Ingenieure*, vol. 60, no. 27, pp. 541–546, 1916.

[76] W. M. Rosenhow, "Heat transfer and temperature distribution in laminar film condensation," *Trans. Am. Soc. Mech. Eng.*, vol. 78, pp. 1645–1648, 1956.

[77] L. A. Bromley, "Effect of Heat Capacity of Condensate," *Ind. Eng. Chem.*, vol. 44, no. 12, pp. 2966–2969, 1952.

[78] P. L. Kapitsa, "Wave flow of thin layers of viscous liquid. Part I. Free flow," *Zh. Eksperim Teor. Fiz.*, vol. 18, p. 3, 1948.

[79] W. H. McAdams, *Heat Transmission, McGraw-Hill*, 3rd ed. New York: McGraw-Hill, 1954.

[80] A. Gollan and S. Sideman, "On the wave characteristics of falling films," *AIChE J.*, vol. 15, no. 2, pp. 301–303, Mar. 1969.

[81] A. Miyara, "Flow Dynamics and Heat Transfer of Wavy Condensate Film," *J. Heat Transfer*, vol. 123, no. 3, p. 492, Jun. 2001.

[82] S. Thumm, C. Philipp, and U. Gross, "Film condensation of water in a vertical tube with countercurrent vapour flow," *Int. J. heat mass …*, vol. 44, no. 22, pp. 4245–4256, Nov. 2001.

[83] U. Gross, T. Storch, C. Philipp, and A. Doeg, "Wave frequency of falling liquid films and the effect on reflux condensation in vertical tubes," *Int. J. Multiph. Flow*, vol. 35, no. 4, pp. 398–409, Apr. 2009.

[84] S. S. Kutateladze, *Fundamentals of Heat Transfer*. New York: Academic Press, 1963.

[85] E. M. Sparrow and E. Marschall, "Binary, gravity-flow film condensation," *J. Heat Transfer*, vol. 91C, no. 2, pp. 205–211, May 1969.

[86] J. W. Cipolla, H. Lang, and S. K. Loyalka, "Kinetic theory of condensation and evaporation. II," *J. Chem. Phys.*, vol. 61, no. 1, pp. 69–77, Jul. 1974.

[87] M. Bond and H. Struchtrup, "Mean evaporation and condensation coefficients based on energy dependent condensation probability," *Phys. Rev. E - Stat. Nonlinear, Soft Matter Phys.*, vol. 70, no. 6 1, pp. 1–21, 2004.

[88] J. P. Caputa and H. Struchtrup, "Interface model for non-equilibrium evaporation," *Phys. A Stat. Mech. its Appl.*, vol. 390, no. 1, pp. 31–42, 2011.

[89] L. D. Koffman, M. S. Plesset, and L. Lees, "Theory of evaporation and condensation," *Phys. Fluids*, vol. 27, no. 4, pp. 876–880, Jun. 1984.

[90] I. N. Knacke, O. & Stranski, "The mechanism of evaporation," *Prog. Met. Phys.*, vol. 6, pp. 181–235, Jan. 1956.

[91] H. Cammenga, "Evaporation mechanisms of liquids," in *Current Topics in Materials Science*, E. Kaldis, Ed. North-Holland, 1980, pp. 335–446.

[92] A. H. Persad and C. A. Ward, "Expressions for the Evaporation and Condensation Coefficients in the Hertz-Knudsen Relation," *Chemical Reviews*, vol. 116, no. 14. American Chemical Society, pp. 7727–7767, 27-Jul-2016.

[93] K. Nabavian and L. A. Bromley, "Condensation coefficient of water," *Chem. Eng. Sci.*, vol. 18, no. 10, pp. 651–660, Oct. 1963.

[94] J. Barrett and C. Clement, "Kinetic evaporation and condensation rates and their coefficients," *J. Colloid Interface Sci.*, vol. 150, no. 2, pp. 352–364, May 1992.

[95] T. Ytrehus and S. Østmo, "Kinetic theory approach to interphase processes," *Int. J. Multiph. Flow*, vol. 22, no. 1, pp. 133–155, Feb. 1996.

[96] R. S. Silver and H. C. Simposion, "The condensation of superheated steam," in *Proceedings of a Converence Held at the National Engineering Laboratory, Glasgow, Scotland*, 1961.

[97] M. Knudsen, *Kinetic Theory of Gases*, 3rd ed. London: Methuene, 1950.

[98] P. Davidovits *et al.*, "Mass accommodation coefficient of water vapor on liquid water," *Geophys. Res. Lett.*, vol. 31, no. 22, pp. 1–4, Nov. 2004.

[99] M. Kulmala and P. E. Wagner, "Mass accommodation and uptake coefficients - A quantitative comparison," *J. Aerosol Sci.*, vol. 32, no. 7, pp. 833–841, Jul. 2001.

[100] J. Julin, M. Shiraiwa, R. E. H. Miles, J. P. Reid, U. Pöschl, and I. Riipinen, "Mass accommodation of water: Bridging the gap between molecular dynamics simulations and kinetic condensation models," *J. Phys. Chem. A*, vol. 117, no. 2, pp. 410–420, 2013.

[101] R. Hołyst *et al.*, "Evaporation of freely suspended single droplets: Experimental, theoretical and computational simulations," *Reports Prog. Phys.*, vol. 76, no. 3, p. 034601, Mar. 2013.

[102] R. Marek and J. Straub, "Analysis of the evaporation coefficient and the condensation coefficient of water," *Int. J. Heat Mass Transf.*, vol. 44, no. 1, pp. 39–53, Jan. 2001.

[103] M. Mozurkewich, "Aerosol growth and the condensation coefficient for water: A review," *Aerosol Sci. Technol.*, vol. 5, no. 2, pp. 223–236, 1986.

[104] G. T. Barnes, "The effects of monolayers on the evaporation of liquids," *Advances in Colloid and Interface Science*, vol. 25, no. C. Elsevier, pp. 89–200, 01-Jan-1986.

[105] E. J. Davis, "A history and state-of-the-art of accommodation coefficients," *Atmos. Res.*, vol. 82, no. 3–4, pp. 561–578, Dec. 2006.

[106] W. R. Schrage, *A theoretical study of interphase mass transfer*. New York: Columbia University Press, 1953.

[107] T. Tsuruta and G. Nagayama, "A microscopic formulation of condensation coefficient and interface transport phenomena," *Energy*, vol. 30, no. 6, pp. 795–805, May 2005.

[108] C. A. Ward and G. Fang, "Expression for predicting liquid evaporation flux: Statistical rate theory approach," *Phys. Rev. E - Stat. Physics, Plasmas, Fluids, Relat. Interdiscip. Top.*, vol. 59, no. 1, pp. 429–440, Jan. 1999.

[109] G. Fang and C. A. Ward, "Temperature measured close to the interface of an evaporating liquid," *Phys. Rev. E - Stat. Physics, Plasmas, Fluids, Relat. Interdiscip. Top.*, vol. 59, no. 1, pp. 417–428, 1999.

[110] F. Duan, I. Thompson, and C. A. Ward, "Statistical rate theory determination of water properties below the triple point," *J. Phys. Chem. B*, vol. 112, no. 29, pp. 8605–8613, 2008.

[111] F. Duan and C. A. Ward, "Surface excess properties from energy transport measurements during water evaporation," *Phys. Rev. E - Stat. Nonlinear, Soft Matter Phys.*, vol. 72, no. 5, p. 056302, Nov. 2005.

[112] E. M. Sparrow, W. J. Minkowycz, and M. Saddy, "Forced convection condensation in the presence of noncondensables and interfacial resistance," *Int. J. Heat Mass Transf.*, vol. 10, no. 12, pp. 1829–1845, 1967.

[113] A. Ganguli, a. G. Patel, N. K. Maheshwari, and a. B. Pandit, "Theoretical modeling of condensation of steam outside different vertical geometries (tube, flat plates) in the presence of noncondensable gases like air and helium," *Nucl. Eng. Des.*, vol. 238, no. 9, pp. 2328–2340, Sep. 2008.

[114] Y. Liao and K. Vierow, "A Generalized Diffusion Layer Model for Condensation of Vapor With Noncondensable Gases," *J. Heat Transfer*, vol. 129, no. 8, p. 988, Aug. 2007.

[115] A. P. Colburn and O. A. Hougen, "Design of Cooler Condensers for Mixtures of Vapors with Noncondensing Gases," *Ind. Eng. Chem.*, vol. 26, no. 11, pp. 1178–1182, Nov. 1934.

[116] P. F. Peterson, V. E. Schrock, and T. Kageyama, "Diffusion Layer Theory for Turbulent Vapor Condensation With Noncondensable Gases," *J. Heat Transfer*, vol. 115, no. 4, p. 998, Nov. 1993.

[117] T. Kageyama, P. F. Peterson, and V. E. Schrock, "Diffusion layer modeling for condensation in vertical tubes with noncondensable gases," *Nucl. Eng. Des.*, vol. 141, pp. 289–302, 1993.

[118] H. Araki, Y. Kataoka, and M. Murase, "Measurement of Condensation Heat Transfer Coefficient Inside a Vertical Tube in the Presence of Noncondensable Gas," *J. Nucl. Sci. Technol.*, vol. 32, no. 6, pp. 517–526, Jun. 1995.

[119] G. Caruso, D. Vitale Di Maio, and A. Naviglio, "Film condensation in inclined tubes with noncondensable gases: An experimental study on the local heat transfer coefficient," *Int. Commun. Heat Mass Transf.*, vol. 45, pp. 1–10, Jul. 2013.

[120] H. S. Park and H. C. No, "A Condensation Experiment in the Presence of Noncondensables in a Vertical Tube of a Passive Containment Cooling System and Its Assessment with RELAP5/MOD3.2," *Nucl. Technol.*, vol. 127, no. 2, pp. 160–169, Aug. 1999.

[121] H. Xu, H. Gu, and Z. Sun, "Forced convection condensation of steam in the presence of multicomponent noncondensable gases inside a horizontal tube," *Int. J. Heat Mass Transf.*, vol. 104, pp. 1110–1119, Jan. 2017.

[122] T. Chataing, P. Clement, and J. Excoffon, "'A general correlation for steam condensation in case of wavy laminar flow along vertical tubes," *Proc. 9th Int. Top. Meet. Nucl. …*, 1999.

[123] I. K. Huhtiniemi and M. L. Corradini, "Condensation in the presence of noncondensable gases," *Nucl. Eng. Des.*, vol. 141, no. 3, pp. 429–446, Jul. 1993.

[124] S. Z. Z. Kuhn, V. E. E. Schrock, and P. F. F. Peterson, "An investigation of condensation from steam-gas mixtures flowing downward inside a vertical tube," *Nucl. Eng. Des.*, vol. 177, no. 1–3, pp. 53–69, Dec. 1997.

[125] A. Dehbi, "A generalized correlation for steam condensation rates in the presence of air under turbulent free convection," *Int. J. Heat Mass Transf.*, vol. 86, pp. 1–15, Jul. 2015.

[126] H. A. Hasanein, M. S. Kazimi, and M. W. Golay, "Forced convection in-tube steam condensation in the presence of noncondensable gases," *Int. J. Heat Mass Transf.*, vol. 39, no. 13, pp. 2625–2639, Sep. 1996.

[127] W. C. Lee and J. W. Rose, "Forced convection film condensation on a horizontal tube with and without non-condensing gases," *Int. J. Heat Mass Transf.*, vol. 27, no. 4, pp. 519–528, Apr. 1984.

[128] H. Xu, Z. Sun, H. Gu, and H. Li, "Forced convection condensation in the presence of noncondensable gas in a horizontal tube; Experimental and theoretical study," *Prog. Nucl. Energy*, vol. 88, pp. 340–351, Apr. 2016.

[129] V. M. Borishanskiy *et al.*, "Effect of uncondensable gas content on heat transfer in steam condensation in a vertical tube," *Heat Transf. - Sovier Res.*, vol. 9, pp. 35–42, 1987.

[130] V. M. Borishanskiy *et al.*, "Heat transfer from steam condensing inside vertical pipes and coils," *Heat Transf. - Sovier Res.*, vol. 10, pp. 44–58, 1987.

[131] V. M. Borishanskiy, D. I. Volkov, N. I. Ivaschenko, O. P. Krektunov, N. M. Fishman, and I. N. Chirkov, "Shell-side coefficient of heat transfer from steam contaminated with noncondensbile gases," *Heat Transf. - Sov. Res.*, vol. 14, pp. 1–5, 1982.

[132] A. Dehbi, "The effects of Noncondensable gases on steam condensation under turbulent Natural Convection Conditions," 1991.

[133] K. Vierow, "Behavior of steam-air systems condensing in cocurrent vertical downlflow," University of California, Berkley, 1990.

[134] D. G. Ogg, "Vertical downflow condensation heat transfer in gas-steam mixtures," University of California, 1991.

[135] K.-W. W. Lee, H. C. No, I.-C. C. Chu, Y. M. Moon, and M.-H. H. Chun, "Local heat transfer during reflux condensation mode in a U-tube with and without noncondensible gases," *Int. J. Heat Mass Transf.*, vol. 49, no. 11–12, pp. 1813–1819, Jun. 2006.

[136] T. H. Chilton and A. P. Colburn, "Mass transfer (absorption) coefficients," *Ind. Eng. Chem.*, vol. 26, pp. 1183–1187, 1934.

[137] W. W. Akers, S. H. Davis Jr., and J. E. Crawford, "Condensation of a vapor in the presence of a noncondensing gas," in *Engineering Progress Symposium Series No. 30*, 1960, pp. 139–144.

[138] F. Votta and C. A. Walker, "Condensation of vapor in the presence of noncondensing gas," *AIChE J.*, vol. 4, no. 4, pp. 413–417, 1958.

[139] M. L. Corradini, "Turbulent condensation on a cold wall in the presence of a noncondensable gas," *Nucl. Technol.*, vol. 64, no. May, pp. 186–195, 1984.

[140] M. . Kim and M. . Corradini, "Modeling of condensation heat transfer in a reactor containment," *Nucl. Eng. Des.*, vol. 118, no. 2, pp. 193–212, Mar. 1990.

[141] H. C. No and H. S. Park, "Non-iterative condensation modeling for steam condensation with non-condensable gas in a vertical tube," *Int. J. Heat Mass Transf.*, vol. 45, no. 4, pp. 845–854, Feb. 2002.

[142] N. . Maheshwari, D. Saha, R. . Sinha, and M. Aritomi, "Investigation on condensation in presence of a noncondensable gas for a wide range of Reynolds number," *Nucl. Eng. Des.*, vol. 227, no. 2, pp. 219–238, Jan. 2004.

[143] S. Oh and S. T. Revankar, "Experimental and theoretical investigation of film condensation with noncondensable gas," *Int. J. Heat Mass Transf.*, vol. 49, no. 15–16, pp. 2523–2534, Jul. 2006.

[144] C. Chantana and S. Kumar, "Experimental and theoretical investigation of air-steam condensation in a vertical tube at low inlet steam fractions," *Appl. Therm. Eng.*, vol. 54, no. 2, pp. 399–412, May 2013.

[145] L. Slegers and R. . Seban, "Laminar film condensation of steam containing small concentrations of air," *Int. J. Heat Mass Transf.*, vol. 13, no. 12, pp. 1941–1947, Dec. 1970.

[146] F. Legay-Desesquelles and B. Prunet-Foch, "Dynamic behaviour of a boundary layer with condensation along a flat plate: comparison with suction," *Int. J. Heat Mass Transf.*, vol. 28, no. 12, pp. 2363–2370, Dec. 1985.

[147] D. Galamba, V. K. Dhir, and K. Taghavi, "Analytical and experimental investigation of simultaneous melting-condensation on a vertical wall in the presence of a noncondensable gas," *Int. J. Heat Mass Transf.*, vol. 29, no. 12, pp. 1869–1880, Dec. 1986.

[148] J. J. Barry, "Effects of Interfacial structure on film condensation," University of Wisconsin, 1987.

[149] H. Kutsuna, K. Inour, and S. Nakanisji, "Filmwise condensation of vapor containing non-condensable gas in a horizontal duct," in *International Symposium on Heat Transfer*, 1987.

[150] R. P. Stein, D. H. Cho, and G. A. Lambert, "Condensation of steam on the underside of a horizontal surface in the presence of air and helium." Argonne, IL, p. Medium: ED; Size: Pages: 8, 01-Jan-1987.

[151] A. J. Robinson and S. R. Windebank, "Measurement of condensation heat transfer coefficients in a steam chamber using a variable conductance heat pipe," in *2nd UK National Conference on Heat Transfer*, 1988.

[152] A. C. Bannwart and A. Bontemps, "Condensation of a vapour with incondensables: An improved gas phase film model accounting for the effect of mass transfer on film thickness," *Int. J. Heat Mass Transf.*, vol. 33, no. 7, pp. 1465–1474, Jul. 1990.

[153] K. M. Vierow and V. E. Schrock, "Condensation in a natural circulation loop with noncondensable gases , 1," in *Proceedings of the international conference on multiphase flows '91-Tsukuba*, 1991, vol. 24, pp. 183–186.

[154] M. Murase, Y. Kataoka, and T. Fujii, "Evaporation and condensation heat transfer with a noncondensable gas present," *Nucl. Eng. Des.*, vol. 141, no. 1–2, pp. 135–143, Jun. 1993.

[155] M. Siddique, M. W. Golay, and M. S. Kazimi, "Local Heat Transfer Coefficients for Forced-Convection Condensation of Steam in a Vertical Tube in the Presence of a Noncondensable Gas," *Nucl. Technol.*, vol. 102, no. 3, pp. 386–402, Jun. 1993.

[156] S. Z. Kuhn, "Investigation of Heat Transfer from Condensing Steam-Gas Mixtures and Turbulent Films Flowing Downward Inside a Vertical Tube," University of California, Berkley, 1995.

[157] H. K. Oh, J. I. Yoon, O. B. Kwon, S. L. Chen, and C. L. Tien, "Low Quality Flow Condensation inside a Vertical Tube in the Presence of a Noncondensable Gas," *Multiph. Flow 1995*, pp. 473–481, Jan. 1995.

[158] C. Lee, T. Liu, Y. Way, and D. Hsia, "Investigation of mid-loop operation with loss of RHR at INER integral system test (IIST) facility," *Nucl. Eng. Des.*, vol. 163, pp. 349–358, 1996.

[159] B. Noel and D. Dumont, "Effect of non-condensible gas on steam generator condensation heat transfer: Bethsy Test 10.2," in *Proceedings of ICONE 5 5th International Conference on Nuclear Engineering*, 1997, pp. 1–10.

[160] M. H. Anderson, L. E. Herranz, and M. L. Corradini, "Experimental analysis of heat transfer within the AP600 containment under postulated accident conditions," *Nucl. Eng. Des.*, vol. 185, no.

2–3, pp. 153–172, Oct. 1998.

[161] Y. Moon, H. No, and Y. Bang, "Local Heat Transfer Coefficients for Reflux Condensation Experiment in a Vertical Tube in the Presence of Noncondensible Gas," *Journa Korean Nucl. Soc.*, vol. 31, no. 5, pp. 486–497, 1999.

[162] S. J. Kim and H. C. No, "Turbulent film condensation of high pressure steam in a vertical tube," *Int. J. Heat Mass Transf.*, vol. 43, no. 21, pp. 4031–4042, Nov. 2000.

[163] H. Liu, N. E. Todreas, and M. J. Driscoll, "Experimental investigation of a passive cooling unit for nuclear plant containment," *Nucl. Eng. Des.*, vol. 199, no. 3, pp. 243–255, Jul. 2000.

[164] Y. M. Moon, H. S. Park, and Y. S. Bang, "Assessment of RELAP5/MOD3.2 for reflux condensation experiment (NUREG/IA-0181)," 2000.

[165] T.-J. T. Liu, "Reflux condensation behavior in a U-tube steam generator with or without noncondensables," *Nucl. Eng. Des.*, vol. 204, no. 1–3, pp. 221–232, Feb. 2001.

[166] C. Sarrette, "Effect of Noncondensable Gases on Circulation of Primary Coolant in Nuclear Power Plants in Abnormal Situations," *Acta Univ. Lappeenrantaensis*, no. February, 2003.

[167] K. Vierow, T. Nagae, and T. Wu, "Experimental investigation of reflux condensation heat transfer in PWR steam generator tubes in the presence of non-condensable gases," in *The 10th International Topical Meeting on Nuclear Reactor Thermal Hydraulics (NURETH-10)*, 2003, p. 17 pp.

[168] S. B. Al-Shammari, D. R. Webb, and P. Heggs, "Condensation of steam with and without the presence of non-condensable gases in a vertical tube," *Desalination*, vol. 169, no. 2, pp. 151–160, Oct. 2004.

[169] M. Murase, T. Nagae, and N. Minami, "Evaluation of Non-condensable Gas Recirculation Flow in Steam Generator U-tubes during Reflux Condensation," *intechopen.com*, 2005.

[170] S. Oh and S. T. Revankar, "Effect of noncondensable gas in a vertical tube condenser," *Nucl. Eng. Des.*, vol. 235, no. 16, pp. 1699–1712, Jul. 2005.

[171] T. Wu and K. Vierow, "Horizontal in-tube condensation in the presence of a noncondensable gas," in *The 11th International Topical Meeting on Nuclear Reactor Thermal-Hydraulics (NURETH-11)*, pp. 1–14.

[172] T. Wu and K. Vierow, "Local heat transfer measurements of steam/air mixtures in horizontal condenser tubes," *Int. J. Heat Mass Transf.*, vol. 49, no. 15–16, pp. 2491–2501, Jul. 2006.

[173] H.-S. Park, D.-J. Euh, K.-Y. Choi, T.-S. Kwon, and W.-P. Baek, "An assessment of a LBLOCA similarity for a reduced-height integral effect test loop design for PWRs," *Ann. Nucl. Energy*, vol. 34, no. 11, pp. 931–937, Nov. 2007.

[174] A. M. Zhu, S. C. Wang, J. X. Sun, L. X. Xie, and Z. Wang, "Effects of high fractional noncondensable gas on condensation in the dewvaporation desalination process," *Desalination*, vol. 214, no. 1–3, pp. 128–137, Aug. 2007.

[175] T. Nagae, M. Murase, T. Chikusa, K. Vierow, and T. Wu, "Reflux Condensation Heat Transfer of Steam-Air Mixtures under Turbulent Flow Conditions in a Vertical Tube," *J. Nucl. Sci. Technol.*, vol. 44, no. 2, pp. 171–182, Feb. 2007.

[176] K. Y. Lee and M. H. Kim, "Experimental and empirical study of steam condensation heat transfer with a noncondensable gas in a small-diameter vertical tube," *Nucl. Eng. Des.*, vol. 238, no. 1, pp. 207–216, Jan. 2008.

[177] H. Li, L. Wang, and D. Yu, "Flow and condensation of vapor with high partial pressure non-condensable gas in a separate heat pipe," *Beijing Keji Daxue Xuebao/Journal Univ. Sci. Technol. Beijing*, vol. 30, no. 3, 2008.

[178] J. W. Kim, Y. G. Lee, H. K. Ahn, and G. C. Park, "Condensation heat transfer characteristic in the presence of noncondensable gas on natural convection at high pressure," *Nucl. Eng. Des.*, vol. 239, no. 4, pp. 688–698, Apr. 2009.

[179] K. Umminger, L. Dennhardt, S. Schollenberger, and B. Schoen, "Integral Test Facility PKL : Experimental PWR Accident Investigation," *Sci. Technol. Nucl. Install.*, vol. 2012, 2011.

[180] F. F. Czubinski, M. B. H. Mantelli, and J. C. Passos, "Condensation on downward-facing surfaces subjected to upstream flow of air-vapor mixture," *Exp. Therm. Fluid Sci.*, vol. 47, pp. 90–97, May 2013.

[181] J. Su, Z. Sun, M. Ding, and G. Fan, "Analysis of experiments for the effect of noncondensable

gases on steam condensation over a vertical tube external surface under low wall subcooling," *Nucl. Eng. Des.*, vol. 278, pp. 644–650, Oct. 2014.

[182] G. Caruso and D. Vitale Di Maio, "Heat and mass transfer analogy applied to condensation in the presence of noncondensable gases inside inclined tubes," *Int. J. Heat Mass Transf.*, vol. 68, pp. 401–414, Jan. 2014.

[183] B. Ren, L. Zhang, J. Cao, H. Xu, and Z. Tao, "Experimental and theoretical investigation on condensation inside a horizontal tube with noncondensable gas," *Int. J. Heat Mass Transf.*, vol. 82, pp. 588–603, Mar. 2015.

[184] Y. Jang, D. Choi, Y. Lee, K. Sin, and D. Jerng, "Experimental Study of Condensation Heat Transfer in the Presence of Noncondensable Gas on the Vertical Tube," pp. 6096–6109, 2015.

[185] H. W. Hu, G. H. Tang, and D. Niu, "Experimental investigation of convective condensation heat transfer on tube bundles with different surface wettability at large amount of noncondensable gas," *Appl. Therm. Eng.*, vol. 100, pp. 699–707, May 2016.

[186] Q. Yi, M. Tian, W. Yan, X. Qu, and X. Chen, "Visualization study of the influence of non-condensable gas on steam condensation heat transfer," *Appl. Therm. Eng.*, vol. 106, pp. 13–21, Aug. 2016.

[187] J. J. Wen, Z. Yin, F. N. Cheng, M. Zeng, and Q. W. Wang, "Experimental investigation on steam flow condensation in the presence of noncondensable gas inside horizontal multi-head spiral channels," *Exp. Therm. Fluid Sci.*, vol. 70, pp. 155–165, Jan. 2016.

[188] G. Fan, P. Tong, Z. Sun, and Y. Chen, "Experimental study of pure steam and steam–air condensation over a vertical corrugated tube," *Prog. Nucl. Energy*, vol. 109, pp. 239–249, Nov. 2018.

[189] S. Y. Lee, "Transient analysis of a condensation experiment in the noncondensable gas-filled closed loop using an inverted U-tube," *Ann. Nucl. Energy*, vol. 23, no. 14, pp. 1179–1188, Sep. 1996.

[190] N. Minami, T. Chikusa, and M. Murase, "RELAP5 Analyses of Thermal-Hydraulic Behavior in Steam Generator U-tubes during Reflux Condensation," *Nucl. Technol.*, pp. 265–277, 2008.

[191] R. Girard and J. S. S. Chang, "Reflux condensation phenomena in single vertical tubes," *Int. J. Heat Mass Transf.*, vol. 35, no. 9, pp. 2203–2218, 1992.

[192] H. Purhonen, M. Puustinen, V. Riikonen, R. Kyrki-Rajamäki, and J. Vihavainen, "PACTEL integral test facility – Description of versatile applications," *Ann. Nucl. Energy*, vol. 33, no. 11–12, pp. 994–1009, Aug. 2006.

[193] A. Jasiulevicius, "TRACE assessment : integral tests PKL and ROSA," 2007.

[194] W. Wagner *et al.*, "The IAPWS Industrial Formulation 1997 for the Thermodynamic Properties of Water and Steam," *J. Eng. Gas Turbines Power*, vol. 122, no. 1, p. 150, 2000.

[195] H. Y. Jeong, "Prediction of counter-current flow limitation at hot leg pipe during a small-break LOCA," *Ann. Nucl. Energy*, vol. 29, no. 5, pp. 571–583, Mar. 2002.

[196] G. B. Wallis, "Flooding Velocities for air and Water in Vertical Tubes," *UKAEA Report*, vol. AAEW-R 123. 1961.

[197] S. S. Kutateladze, "Elements of the hydrodynamics of gas-liquid systems," *J. Fluid Mech. -Soviet Res.*, vol. 1, no. 4, pp. 62–74, 1972.

[198] K. D. Kok, *Nuclear engineering handbook*. CRC Press, 2009.

[199] N. Wynne, M. Garza, K. Vierow, and D. L. Aumiller, "Air-Water and Steam-Water Onset of Flooding Data at Variable Pressure in a Large Diameter Tube," in *Proc. of Advanced Thermal Hydraulics '16, embedded topical in the 2016 ANS Summer Meeting.*

[200] S. Jayanti, A. Tokarz, and G. F. Hewitt, "Theoretical investigation of the diameter effect on flooding in countercurrent flow," *Int. J. Multiph. Flow*, vol. 22, no. 2, pp. 307–324, Apr. 1996.

[201] S. Z. Sapozhnikov, V. Y. Mityakov, and a. V. Mityakov, "Gradient heat-flux sensors: Possibilities and prospects of use," *Therm. Eng.*, vol. 53, no. 4, pp. 270–278, Apr. 2006.

[202] A. V. Mityakov, S. Z. Sapozhnikov, V. Y. Mityakov, A. a. Snarskii, M. I. Zhenirovsky, and J. J. Pyrhönen, "Gradient heat flux sensors for high temperature environments," *Sensors Actuators A Phys.*, vol. 176, pp. 1–9, Apr. 2012.

[203] A. Kyarad and H. Lengfellner, "Al-Si multilayers: A synthetic material with large thermoelectric anisotropy," *Appl. Phys. Lett.*, vol. 85, no. 23, pp. 5613–5615, 2004.

[204] M. Lindorf, H. Rohrmann, G. Span, S. Raoux, J. Jordan-Sweet, and M. Albrecht, "Structural and thermoelectric properties of SiGe/Al multilayer systems during metal induced crystallization," *J. Appl. Phys.*, vol. 120, no. 20, 2016.

[205] D. K. C. McDonald, *Thermoelectricity: An Introduction to the Principles*. Wiley, 1962.

[206] K. Fischer, C. Stoiber, A. Kyarad, and H. Lengfellner, "Anisotropic thermopower in tilted metallic multilayer structures," *Appl. Phys. A Mater. Sci. Process.*, vol. 78, no. 3, pp. 323–326, 2004.

[207] T. Zahner, R. Förg, and H. Lengfellner, "Transverse thermoelectric response of a tilted metallic multilayer structure," *Appl. Phys. Lett.*, vol. 73, no. 10, pp. 1364–1366, 1998.

[208] F. Cardarelli, *Material Handbook - A Concise Desktop Reference*. Springer Handbook, 2008.

[209] S. Raphael-Mabel, "Design and Calibration of a Novel High Temperature Heat Flux Sensor," 2005.

[210] E. Piccini, S. M. Guo, and T. V. Jones, "The development of a new direct-heat-flux gauge for heat-transfer facilities," *Meas. Sci. Technol.*, vol. 11, no. 4, pp. 342–349, 2000.

[211] B. S. Mann and B. S. Mann, "Transverse Thermoelectric Effects for Cooling and Heat Flux Sensing By Transverse Thermoelectric Effects for Cooling and Heat Flux Sensing," 2006.

[212] P. R. Bandaru, K. P. Vemuri, F. M. Canbazoglu, and R. S. Kapadia, "Layered thermal metamaterials for the directing and harvesting of conductive heat," *AIP Adv.*, vol. 5, no. 5, 2015.

[213] T. Meier, P. Stathopoulos, and P. R. Von Rohr, "Design and convective calibration of a transverse heat flux sensor," *Exp. Heat Transf.*, vol. 29, no. 2, pp. 139–150, 2016.

[214] C. W. Kovach, "High-Performance Stainless Steels." Nickel Development Institute, p. 94, 2016.

[215] H.-M. Prasser, A. Böttger, J. Zschau, and T. Gocht, "Needle shaped conductivity probes with integrated micro-thermocouple and their application in rapid condensation experiments with non-condensable gases," *Kerntechnik*, vol. 68, no. 3, pp. 114–120, 2003.

[216] T. H. Lyu and I. Mudawar, "Simultaneous measurements of thickness and temperature profile in a wavy liquid film falling freely on a heating wall," *Experimental Heat Transfer*, vol. 4, no. 3. pp. 217–233, 1991.

[217] T. Fukano and A. Ousaka, "Prediction of the circumferential distribution of film thickness in horizontal and near-horizontal gas-liquid annular flows," *Int. J. Multiph. Flow*, vol. 15, no. 3, pp. 403–419, 1989.

[218] H. Takahama and S. Kato, "Longitudinal flow characteristics of vertically falling liquid films without concurrent gas flow," *Int. J. Multiph. Flow*, vol. 6, no. 3, pp. 203–215, 1980.

[219] M. Damsohn and H.-M. Prasser, "High-speed liquid film sensor for two-phase flows with high spatial resolution based on electrical conductance," *Flow Meas. Instrum.*, vol. 20, no. 1, pp. 1–14, Mar. 2009.

[220] D. R. Webb and G. F. Hewitt, "Downwards co-current annular flow," *Int. J. Multiph. Flow*, vol. 2, no. 1, pp. 35–49, 1975.

[221] J. Cho, M. Perlin, and S. L. Ceccio, "Measurement of near-wall stratified bubbly flows using electrical impedance," *Meas. Sci. Technol.*, vol. 16, no. 4, pp. 1021–1029, Apr. 2005.

[222] T. N. Wong, K. T. Ooi, and S. P. Zhu, "A calibration technique for a parallel-wire depth probe with conductivity compensation," *Exp. Fluids*, vol. 20, no. 6, pp. 429–432, 1996.

[223] H. C. Kang and M. H. Kim, "The development of a flus-wire probe and calibration method for measuring liquid film thickness," *Int. J. multi*, vol. 18, no. 3, pp. 423–437, 1992.

[224] J. E. E. Koskie, I. Mudawar, and W. G. G. Tiederman, "Parallel-wire probes for measurement of thick liquid films," *Int. J. Multiph. Flow*, vol. 15, no. 4, pp. 521–530, Jul. 1989.

[225] F. P. D'Aleo, P. Papadopoulos, and H.-M. Prasser, "Miniaturized liquid film sensor (MLFS) for two phase flow measurements in square microchannels with high spatial resolution," *Flow Meas. Instrum.*, vol. 30, pp. 10–17, Apr. 2013.

[226] G. Chou and J. Chen, "A general modeling for heat transfer during reflux condensation inside vertical tubes surrounded by isothermal fluid," *Int. J. Heat Mass Transf.*, 1999.

[227] G. Chou and J. Chen, "Heat transfer characteristics of reflux condensation phenomena in a single vertical tube," *Nucl. Sci. Eng.*, pp. 220–229, 1997.

[228] G. Soave, "20 years of Redlich-Kwong equation of state," *Fluid Phase Equilib.*, vol. 82, no. C, pp.

333–344, 1993.

[229] F. P. Incropera, D. P. Dewitt, T. L. Bergmann, and A. S.- Lavine, *Fundamentals of Heat and Mass Transfer*, 6th ed. Wiley, 2007.

[230] W. M. Rohsenow, J. P. Hartnett, and Y. I. Cho, *Handbook of heat transfer media*, 3rd ed. McGraw-Hill, 1998.

[231] A. Dehbi, M. W. Golay, and M. S. Kazimi, "Condensation experiments in steam-air and steam-air-helium mixtures under turbulent natural convection," in *AIChE Symp. Ser.AIChE (American Institute of Chemical Engineers) Symposium Series*, 1991, pp. 19–28.

[232] T. Tagami, "Interim report on safety assessments and facilities establishment project for June 1965. No. 1," 1965.

[233] K. R. Robb, M. T. Farmer, and M. W. Francis, "Fukushima Daiichi Unit 1 Ex-Vessel Prediction: Core-Concrete Interaction," *Nucl. Technol.*, vol. 196, no. 3, pp. 475–488, Dec. 2016.

[234] H. Bonneville, L. Carenini, and M. Barrachin, "Core Melt Composition at Fukushima Daiichi: Results of Transient Simulations with ASTEC," *Nucl. Technol.*, vol. 196, no. 3, pp. 489–498, Dec. 2016.

[235] M. Pellegrini *et al.*, "Benchmark Study of the Accident at the Fukushima Daiichi NPS: Best-Estimate Case Comparison," *Nucl. Technol.*, vol. 196, no. 2, pp. 198–210, Nov. 2016.

[236] H. Lopez, N. Erkan, and K. Okamoto, "Reactor core isolation cooling system analysis of the Fukushima Daiichi Unit 2 accident with RELAP/ScdapSIM," *J. Nucl. Sci. Technol.*, vol. 53, no. 11, pp. 1899–1905, Nov. 2016.

[237] S. Susyadi and T. Yonomoto, "ANALYSIS ON NON-UNIFORM FLOW IN STEAM GENERATOR DURING STEADY STATE NATURAL CIRCULATION COOLING," pp. 103–116, 2012.

[238] T. Yonomoto, I. Ohtsu, and Y. Anoda, "Thermal–hydraulic characteristics of a next-generation reactor relying on steam generator secondary side cooling for primary depressurization and long-term passive core cooling," *Nucl. Eng. Des.*, vol. 185, no. 1, pp. 83–96, Sep. 1998.

[239] T. Nagae, T. Chikusa, M. Murase, and N. Minami, "Analysis of noncondensable gas recirculation flow in steam generator U-tubes during reflux condensation using RELAP5," *J. Nucl. …*, vol. 44, no. 11, pp. 1395–1406, 2007.

[240] B. Noel and R. Deruaz, "Reflux condenser mode with non-condensible gas: assessment of Cathare against Bethsy test 7.2C," *Nucl. Eng. Des. ng Des.*, vol. 149, pp. 291–298, 1994.

[241] W. Zhou, B. Wolf, and S. Revankar, "Assessment of RELAP5/MOD3.3 condensation models for the tube bundle condensation in the PCCS of ESBWR," *Nucl. Eng. Des.*, vol. 264, pp. 111–118, Nov. 2013.

[242] T. Nagae, M. Murase, T. Wu, and K. Vierow, "Modeling of reflux condensation heat transfer in the presence of a noncondensable gas," no. 2003, pp. 1–9, 2005.

[243] L. Pilon, G. Geffraye, and T. Chataing, "Validation of the CATHARE film condensation model on COTURNE experiment," *6th Int. Conf. Nucl. Eng.*, pp. 1–14, 1998.

[244] A. Dehbi, F. Janasz, and B. Bell, "Prediction of steam condensation in the presence of noncondensable gases using a CFD-based approach," *Nucl. Eng. Des.*, vol. 258, pp. 199–210, May 2013.

Chapter 10 Appendix

10.1 PRECISE facility primary loop schematic

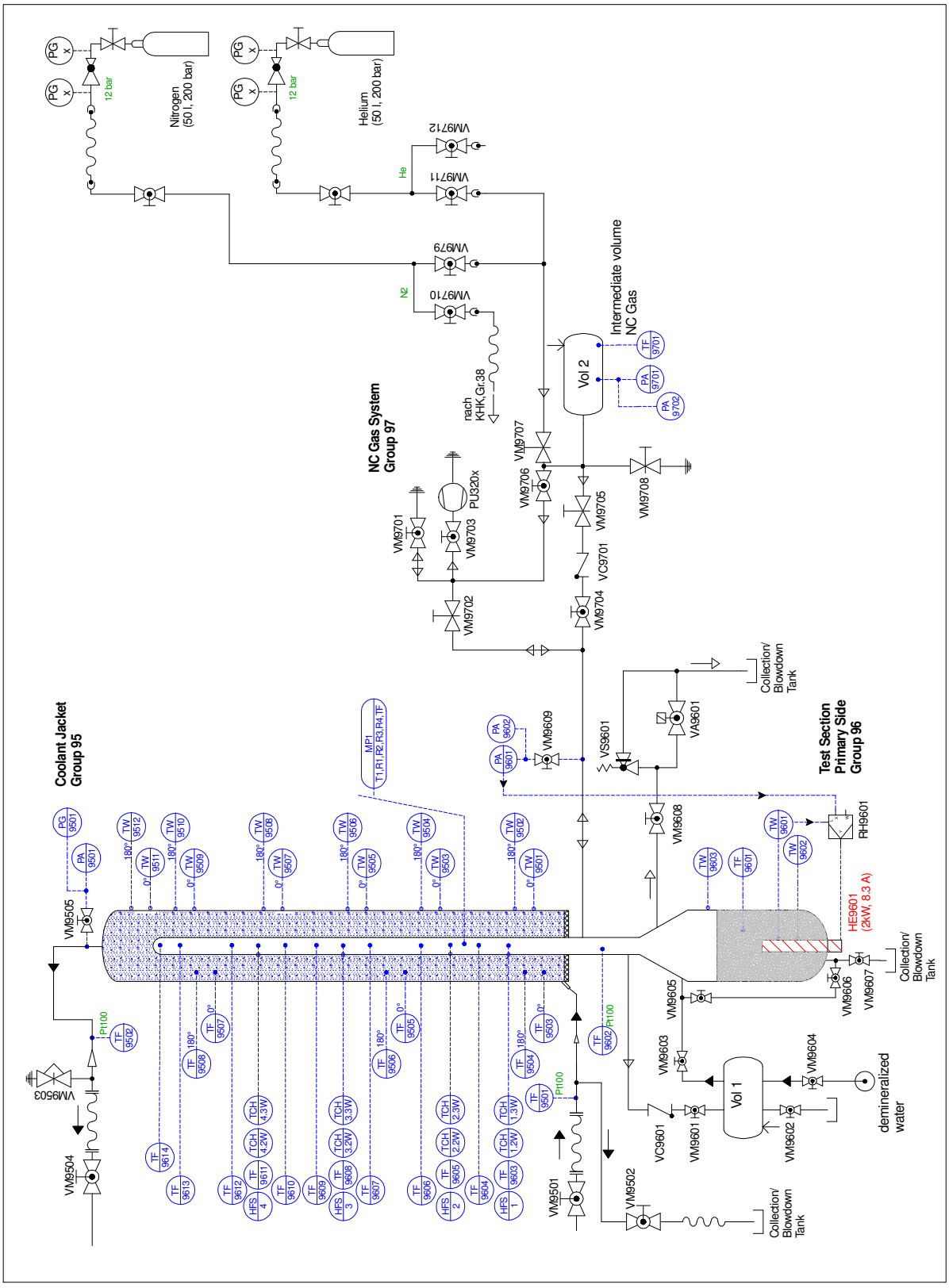

10.2 PRECISE facility secondary loop schematic

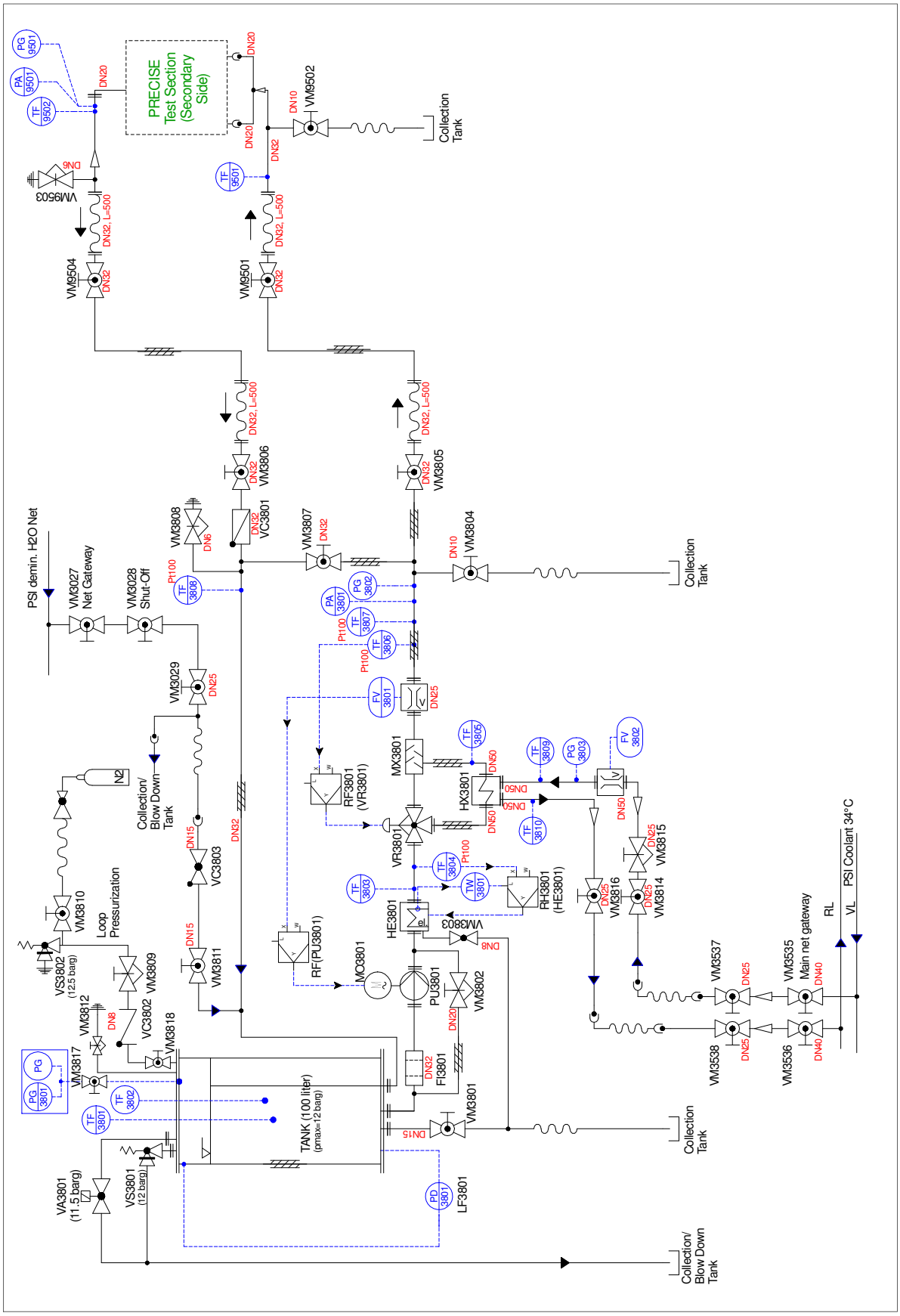

10.3 PRECISE facility and cooling-heating loop instrumentation

DAS Tag	*Sub. name*	*Signal output*	*Description*	*Type*	*Range*
Heating / cooling loop, group 38					
PA3801		24 VDC, 4-20 mA	Absolut pressure	Transmitter	0-15 bar
PG3801		24 VDC, 4-20 mA, display	Gauge pressure water storage tank	Transmitter/manometer	0-16 bar
PD3801		24 VDC, 4-20 mA	Differential pressure	Transmitter	0-150 mbar
LF3801		-	Water level	Digital display	0-1999
VR3801		-	Diverter valve to HX3801/Bypass	Three-way valve control valve	Kvs=16m3/h
	.Y	24 VDC, 4-20 mA	Valve opening signal 0-100%	Power controller	
VA3801		24 VDC, 9 W	Safety pressure release valve	Spring-loaded valve	DN15
PU3801		-	Circulation pump coolant	Rotary pump	0-6 m3/h
	.SW	24 VDC	Start / Stop Pump		
FV3801		2-Leiter, 24 VDC	Coolant flow	Vortex flow meter	0.6-18m3/h (5m3/h)
	.X2	24 VDC, 4-20 mA	Coolant flow, actual value to PU3801 controller		
	.X3	4-20 mA	Coolant flow, actual value to cRIO-DAS		
	.W		Coolant flow, setpoint to PU3801 controller		
HE3801	.SW	-	Relay, release HE3801 (inhibit)	Heater	9 kW, 3x400V
HE3801	.P		Power HE3801	Power controller	
TF3801		mV	Temperature in water storage	Thermocouple	0-200 °C
TF3803		mV	Temperature after HE3801	Thermocouple	0-200 °C
TF3804	.X	mV	Temperature after HE3801, actual value of HE3801	Pt-100, Class 1/3B	0-200 °C
	.W	-	Temperature after HE3801, setpoint to HE3801		0-200 °C
TF3805		mV	Temperature after HX3801, VL mixer	Thermocouple	0-200 °C
TF3806	.X	mV	Temperature after mixer, actual value of RF3801	Pt-100, Class 1/3B	0-200 °C
	.W	-	Temperature after mixer, setpoint of RF3801		0-200 °C
TF3807		mV	Temperature after mixer	Pt-100, Class 1/3B	0-200 °C
TF3808		mV	Temperature - test section RL	Pt-100, Class 1/3B	0-200 °C
TF3809		mV	Heat exchanger HX3801, sec. side VL	Thermocouple	0-200°C
TF3810		mV	Heat exchanger HX3801, sec. side RL	Thermocouple	0-200°C
TW3801		mV	Temperature limit to heater HE3801	Thermocouple	0-500°C

RF3801			Controller 3-way-valve	Elect. controller	
RH3801			Controller water heater	Elect. controller	
GW3801	.AL		Limit, alarm from HE3801		
LS3801					
SW3801			Push button, emergency stop (SW5)		
Blow Down Tank, group 39					
LS 3901		0/24 VDC	Level switch min. level		Switch 0/1
LS 3902			Level switch setpoint level		Switch 0/1
LS 3903			Level switch max. level		Switch 0/1
PU 3901			Pump ON/OFF signal		Switch 0/1
Cooling Jacket, group 95					
TF 9501		100-175 Ω	Coolant jacket inlet temperature	Pt-100	10-200°C
TF 9502		100-175 Ω	Coolant jacket outlet temperature	Pt-100	10-200°C
TF 9503		0.397-8.138 mV	Coolant temp. Pos. 1-0°	Thermocouple, type K	10-200°C
TF 9504		0.397-8.138 mV	Coolant temp. Pos. 1-180°	Thermocouple, type K	10-200°C
TF 9505		0.397-8.138 mV	Coolant temp. Pos. 2-0°	Thermocouple, type K	10-200°C
TF 9506		0.397-8.138 mV	Coolant temp. Pos. 2-180°	Thermocouple, type K	10-200°C
TF 9507		0.397-8.138 mV	Coolant temp. Pos. 3-0°	Thermocouple, type K	10-200°C
TF 9508		0.397-8.138 mV	Coolant temp. Pos. 3-180°	Thermocouple, type K	10-200°C
TW 9501		0.397-8.138 mV	Wall temp. cooling jacket, Pos. 1-0°	Thermocouple, type K	10-200°C
TW 9502		0.397-8.138 mV	Wall temp. cooling jacket, Pos. 1-180°	Thermocouple, type K	10-200°C
TW 9503		0.397-8.138 mV	Wall temp. cooling jacket, Pos. 2-0°	Thermocouple, type K	10-200°C
TW 9504		0.397-8.138 mV	Wall temp. cooling jacket, Pos. 2-180°	Thermocouple, type K	10-200°C
TW 9505		0.397-8.138 mV	Wall temp. cooling jacket, Pos. 3-0°	Thermocouple, type K	10-200°C
TW 9506		0.397-8.138 mV	Wall temp. cooling jacket, Pos. 3-180°	Thermocouple, type K	10-200°C
TW 9507		0.397-8.138 mV	Wall temp. cooling jacket, Pos. 4-0°	Thermocouple, type K	10-200°C
TW 9508		0.397-8.138 mV	Wall temp. cooling jacket, Pos. 4-180°	Thermocouple, type K	10-200°C
TW 9509		0.397-8.138 mV	Wall temp. cooling jacket, Pos. 5-0°	Thermocouple, type K	10-200°C
TW 9510		0.397-8.138 mV	Wall temp. cooling jacket, Pos. 5-180°	Thermocouple, type K	10-200°C
TW 9511		0.397-8.138 mV	Wall temp. cooling jacket, Pos. 6-180°	Thermocouple, type K	10-200°C
TW 9512		0.397-8.138 mV	Wall temp. cooling jacket, Pos. 6-180°	Thermocouple, type K	10-200°C

PA 9501		4-20 mA	Pressure at the top	Transmitter	0-15 bar
Test Tube, group 96					
TF 9601		0.397-8.138 mV	Water temperature	Thermocouple, type K	10-200°C
TF 9602		100-175 Ω	Steam temperature - tube inlet	Pt-100	10-200°C
TW 9602		0.397-8.138 mV	Heating rod temperature - DAS control	Thermocouple, type K	10-200°C
TW 9603		0.397-8.138 mV	Steam generator wall temperature	Thermocouple, type K	10-200°C
TF 9603	I-20	0.397-8.138 mV	Test tube centerline temperature 220 mm (from condensation tube inlet)	Thermocouple, type K	10-200°C
TF 9604	G29	0.397-8.138 mV	Test tube centerline temperature 320	Thermocouple, type K	10-200°C
TF 9605	G30	0.397-8.138 mV	Test tube centerline temperature 420	Thermocouple, type K	10-200°C
TF 9606	O-20	0.397-8.138 mV	Test tube centerline temperature 520	Thermocouple, type K	10-200°C
TF 9607	I-18	0.397-8.138 mV	Test tube centerline temperature 620	Thermocouple, type K	10-200°C
TF 9608	I-19	0.397-8.138 mV	Test tube centerline temperature 670	Thermocouple, type K	10-200°C
TF 9609	I-17	0.397-8.138 mV	Test tube centerline temperature 720	Thermocouple, type K	10-200°C
TF 9610	O-19	0.397-8.138 mV	Test tube centerline temperature 820	Thermocouple, type K	10-200°C
TF 9611	G21	0.397-8.138 mV	Test tube centerline temperature 920	Thermocouple, type K	10-200°C
TF 9612	G22	0.397-8.138 mV	Test tube centerline temperature 1020	Thermocouple, type K	10-200°C
TF 9613	A9	0.397-8.138 mV	Test tube centerline temperature 1120	Thermocouple, type K	10-200°C
TF 9614	J9	0.397-8.138 mV	Test tube centerline temperature 1220	Thermocouple, type K	10-200°C
TW 9601		0.397-8.138 mV	Wall-temp. heater tank, limiter value to GW9601	Thermocouple, type K	10-200°C
PA 9601		4-20 mA	Absolute pressure	Transmitter	0-15 bar
	.W		Absolute pressure, setpoint to RH9601		0-15 bar
	.X2		Absolute pressure, actual value to RH9601		0-15 bar
RH 9601			Steam generator - controller	Regulator	
VA 9601		0/24VDC	Safety pressure release valve	Automatic valve	Open/Close
HE 9601	.P	0-20 mA	Electrical heating rod - steam generating		0-2 kW, 8.9 A
	.SW	0/24 VDC	Control heater HE9601		Switch 0/1
SW9601			Emergency stop button		
SW9602			Emergency signal light		

Test Tube TC Heat Flux, TCHx					
TCH1	.1F	0.397-8.138 mV	Test tube centerline temperature 320	Thermocouple, type K	10-200°C
	.2W	0.397-8.138 mV	TW Temp. wall, condensation side	Thermocouple, type K	10-200°C
	.3W	0.397-8.138 mV	TW Temp. wall, coolant side	Thermocouple, type K	10-200°C
TCH2	.1F	0.397-8.138 mV	Test tube centerline temperature 520	Thermocouple, type K	10-200°C
	.2W	0.397-8.138 mV	TW Temp. wall, condensation side	Thermocouple, type K	10-200°C
	.3W	0.397-8.138 mV	TW Temp. wall, coolant side	Thermocouple, type K	10-200°C
TCH3	.1F	0.397-8.138 mV	Test tube centerline temperature 670	Thermocouple, type K	10-200°C
	.2W	0.397-8.138 mV	TW Temp. wall, condensation side	Thermocouple, type K	10-200°C
	.3W	0.397-8.138 mV	TW Temp. wall, coolant side	Thermocouple, type K	10-200°C
TCH4	.1F	0.397-8.138 mV	Test tube centerline temperature 920	Thermocouple, type K	10-200°C
	.2W	0.397-8.138 mV	TW Temp. wall, condensation side	Thermocouple, type K	10-200°C
	.3W	0.397-8.138 mV	TW Temp. wall, coolant side	Thermocouple, type K	10-200°C
Test Tube Gradient Heat Flux					
HFS1		+/- 10 V	Heat flux through the tube wall	GHFS	0-200 kW/m2
HFS2		+/- 10 V	Heat flux through the tube wall	GHFS	0-200 kW/m2
HFS3		+/- 10 V	Heat flux through the tube wall	GHFS	0-200 kW/m2
HFS4		+/- 10 V	Heat flux through the tube wall	GHFS	0-200 kW/m2
Moveable Probe 1, MP1					
MP1	.R1	0 - 10 V	Film thickness, electrode 1, center	St. steel wire	0-2 mm
	.R2	0 - 10 V	Film thickness, electrode 2, side	St. steel wire	0-2 mm
	.R3	0 - 10 V	Film thickness, electrode 3, top	St. steel wire	0-2 mm
	.R4	0 - 10 V	Film thickness, traversing electrode	St. steel wire	0-10 mm
	.TF	0.397-8.138 mV	Horizontal temperature profile	Thermocouple, type K	10-200°C
	.MST	N/A	Stepper motor, position feedback	Encoder	0- 400 Hz
	.MS1	0/5V	Stepper motor, end switch 1	End switch	Switch 0/1
	.MS2	0/5V	Stepper motor, end switch 2	End switch	Switch 0/1
Vacuum/NC Gas, Gr. 97					
PA 9701		4-20 mA	Absolute pressure	Transmitter	0-15 bar
TF 9701		100-175 Ω	Gas temperature	Pt-100	10-200°C

10.4 Non-condensables estimation MATLAB function

This function was singled out for inclusion in the presented work due to its significance to estimating the actual non-condensables inventory in the test tube. The complete data processing program developed for the PRECISE facility can be downloaded from the web repository under the following link:

https://github.com/FilipJanasz/Data_analysis

Furthermore, the scripts developed to interface MATLAB and RELAP5/MOD3.4 and used to conduct the calculations described in this thesis are available under:

https://github.com/FilipJanasz/2017ClosedTubeSimulator

It is recommended to use MATLAB R2018a or newer, as this was the latest release used for the code development. The repository includes code not written by the author of the thesis – in such cases, these parts of code were distributed as free to use by their authors and the appropriate licensing text files are included.

```
function [h2o_mole_frac, N2_mole_frac,
He_mole_frac,moles_h2o_test,moles_N2_htank,moles_He_htank,N2_mole_frac_init,He_mole_frac_init]
=NCfilling_evaluation_fun(arg,disp_flag,eos)

    %% PURPOSE OF THIS CODE
    % Enter measured values for pressure and temperature at following stages of
    % facility filling:
    % 1. vacuum in heater tank and in NC tank
    % 2. water filling in heater tank
    % 3. 1st NC component filling to NC tank
    % 4. 2nd NC component filling to NC tank
    % 5. Filling NC mixture to heater tank
    % From this, estimate the exact mass / molar fractions of H2O, N2 and He for a given test

    %% GAS PROPERTIES
        %molar mass
%         mol_m_air=28.966;
%         mol_m_N2=28.0134;
%         mol_m_He=4;
%         mol_m_h2o=18.02;
%
%         mol_m(1)=mol_m_N2;
%         mol_m(2)=mol_m_He;  %put molar masses into one var for Equation Of State
%         mol_m(3)=mol_m_h2o;

        %critical pressure in Bar
http://en.wikipedia.org/wiki/Critical_point_%28thermodynamics%29
        pc_N2=33.9;
        pc_He=2.27;
        pc_h2o=220.58;

        pc(1)=pc_N2;
        pc(2)=pc_He;    %put pc's into one var for Equation Of State
        pc(3)=pc_h2o;

        %critical temperature in K
http://en.wikipedia.org/wiki/Critical_point_%28thermodynamics%29
        Tc_N2=126.2;
        Tc_He=5.19;
        Tc_h2o=647.096;

        Tc(1)=Tc_N2;
        Tc(2)=Tc_He;    %put Tc's into one var for Equation Of State
        Tc(3)=Tc_h2o;

        %gas constant
        R=8.3144621;

    %% GEOMTERY
        vol.heaterTank=0.00419;
        vol.NCtank=0.005;
```

```
        vol.waterTank=0.003;

    %% EOS choice
        % eos=1 - ideal gas
        % eos=2 - Redlich Kwong

    %% GET CONDITIONS
        %remove erronerous negative pressures of some recordings
        for arg_ctr=1:numel(arg)
            if arg(arg_ctr)<0
                arg(arg_ctr)=0.00001;
            end
        end

        %test conditions
        P_Htank_test=arg(1);
        T_Htank_test=arg(2)+273.15;

        % 1. Vacuum in heater tank
        P_Htank_vac=arg(3);
        T_Htank_vac=arg(4)+273.15;

        % 2. Vacuum in NC tank
        P_NCtank_vac=arg(5);
        T_NCtank_vac=arg(6)+273.15;

        % 3. Water filled to heater tank
        P_Htank_h2o=arg(7);
        T_Htank_h2o=arg(8)+273.15;

        % 4. First NC component (He) filled in NC tank
        P_NCtank_He=arg(9);
        T_NCtank_He=arg(10)+273.15;

        % 5. Second NC component (N2) filled in NC tank
        P_NCtank_full=arg(11);
        T_NCtank_full=arg(12)+273.15;

        % 6. Heater tank filled with NC
        P_htank_full=arg(13);
        T_htank_full=arg(14)+273.15;


    %% Calculaion 1 - Vacuum in heater tank
    % assume there's only nitrogen in air mixture
    % define equation of state for pure nitrogen
        if eos==1
            %in case of ideal gas equation, equation of state always looks the
            %same
            Vm_fun_N2=@(P,T) R*T/P;  %simplify maths
        elseif eos==2
            reset(symengine) %clears symbolic variables
            [~,Vm_fun_N2,~]=Redlich_Kwong(R,Tc_N2,pc_N2,1);
        end

        molar_vol_Htank_vac=Vm_fun_N2(P_Htank_vac*10^5,T_Htank_vac);   % times 10^5 to convert
bar to Pa
        moles_N2_Htank_vac=vol.heaterTank/real(molar_vol_Htank_vac(1));

    %% Calculation 2 Vacuum in NC tank
    % assume there's only nitrogen in the remaining air mixture, reuse function from step 1
    % (same composition)
    if ~P_NCtank_full==0
        molar_vol_NCtank_N2=Vm_fun_N2(P_NCtank_vac*100000,T_NCtank_vac);
        moles_N2_NCtank_vac=vol.NCtank/real(molar_vol_NCtank_N2(1));
    end

    %% Calculation 3 Water filled to heater tank
    % make an initial guess about mole fraction of steam in gas mixture
        moles_h2o_Htank_filling=P_Htank_h2o*100000*vol.heaterTank/R/T_Htank_h2o-
moles_N2_Htank_vac;
mole_fr_h2o_Htank=moles_h2o_Htank_filling/(moles_h2o_Htank_filling+moles_N2_Htank_vac);
```

```
     % check what equation of state was chosen and act accordingly
        if eos==1
            %initial guess is final guess in this case

        elseif eos==2
            flag=0;
            % this checks if first guess of mole fraction was good and if does
            % not meet "condition" (currently set to 0.0001, repeat estimation
            % of Redlich Kwong parameters with updated mole fraction, compare
            % again and so on

            while flag==0
                mole_fr_array=[1-mole_fr_h2o_Htank,mole_fr_h2o_Htank];  % first term is NC
mole fraction
                [~,Vm_fun,~]=Redlich_Kwong(R,Tc([1,3]),pc([1,3]),mole_fr_array);
                molar_vol_Htank_filling=Vm_fun(P_Htank_h2o*100000,T_Htank_h2o);
                moles_h2o_Htank_filling_temp=vol.heaterTank/real(molar_vol_Htank_filling(1))-
moles_N2_Htank_vac;

mole_fr_h2o_Htank=moles_h2o_Htank_filling_temp/(moles_h2o_Htank_filling_temp+moles_N2_Htank_va
c);
                condition=abs(moles_h2o_Htank_filling_temp-
moles_h2o_Htank_filling)/moles_h2o_Htank_filling_temp;
                moles_h2o_Htank_filling=moles_h2o_Htank_filling_temp;
                if condition<0.0001
                    flag=1;
                end
            end
        end

        %CHECK measured and calculated temp values
        T_Htank_h2o_IAPWS_sat=IAPWS_IF97('Tsat_p',P_Htank_h2o*mole_fr_h2o_Htank/10);  %divide
by 10 to convert bar to MPa
        if abs(T_Htank_h2o-T_Htank_h2o_IAPWS_sat)>0.1
            if disp_flag==1
                disp('Step 3 error - measured T larger than T sat from tables. Adjusting T')
                disp('No calculations involved - just steam tables, so check initial
conditions file but leave code alone')
                disp('calculated Tsat:')
                disp(T_Htank_h2o_IAPWS_sat)
                disp('Measured T: ')
                disp(T_Htank_h2o)
            end
            T_Htank_h2o=T_Htank_h2o_IAPWS_sat;
            moles_h2o_Htank_filling=P_Htank_h2o*100000*vol.heaterTank/R/T_Htank_h2o-
moles_N2_Htank_vac;
mole_fr_h2o_Htank=moles_h2o_Htank_filling/(moles_h2o_Htank_filling+moles_N2_Htank_vac);
        end
        %after the heater tank is separated from water tank, parts of the
        %moles of water and gas are left in the latter, thus while fraction
        %remains the same, absolute amount changes
        %  (vol.heaterTank-vol.waterTank)/vol.heaterTank - water from vol.waterTank is
stransferred to vol.heaterTank
        volume_ratio=(vol.heaterTank-vol.waterTank)/vol.heaterTank;
        moles_h2o_Htank_filling=moles_h2o_Htank_filling*volume_ratio;
        moles_N2_Htank_filling=moles_N2_Htank_vac*volume_ratio;

    %do steps 4 and 5 only if it is not a pure steam test
    if ~P_NCtank_full==0
    %% Calculation 4 First NC component (He) filled in NC tank
        molar_vol_NCtank_step_4=Vm_fun_N2(P_NCtank_He*100000,T_NCtank_He);
        moles_He_NCtank=vol.NCtank/real(molar_vol_NCtank_step_4(1))-moles_N2_NCtank_vac;

    % Caculation 5 Second NC component (N2) filled in NC tank
    % make an initial guess about mole fraction of N2 in NC gas mixture
        molar_vol_NCtank_step_5=Vm_fun_N2(P_NCtank_full*100000,T_NCtank_full);
        moles_N2_NCtank=vol.NCtank/real(molar_vol_NCtank_step_5(1))-moles_He_NCtank;

    % get the gas ratio
        mole_fr_He_NCtank=moles_He_NCtank/(moles_He_NCtank+moles_N2_NCtank);

        % check what equation of state was chosen and act accordingly
        if eos==1
            %initial guess is final guess in this case
```

```
        elseif eos==2
            flag=0;
            % this checks if first guess of mole fraction was good and if does
            % not meet "condition" (currently set to 0.0001, repeat estimation
            % of Redlich Kwong parameters with updated mole fraction, compare
            % again and so on

            while flag==0
                mole_fr_array=[1-mole_fr_He_NCtank,mole_fr_He_NCtank];
                [~,Vm_fun,~]=Redlich_Kwong(R,Tc([1,2]),pc([1,2]),mole_fr_array);
                molar_vol_NC_tank=Vm_fun(P_NCtank_full*100000,T_NCtank_full);
                moles_He_NCtank_temp=vol.NCtank/real(molar_vol_NC_tank(1))-moles_N2_NCtank;
                %make sure there actually is any He filled into the tank
                if moles_He_NCtank ~= 0

mole_fr_He_NCtank=moles_He_NCtank_temp/(moles_He_NCtank_temp+moles_N2_NCtank);
                    condition=abs(moles_He_NCtank_temp-moles_He_NCtank)/moles_He_NCtank_temp;
                    moles_He_NCtank=moles_He_NCtank_temp;
                else %and if not, break the loop - otherwise it goes on forever
                    mole_fr_He_NCtank=0;
                    condition=0;
                end
                if condition<0.0001
                    flag=1;
                end
            end
        end

            %At this point, composition of NC gas mixture is set finally
    end
    %% Calculation 6 Heater tank filled with NC
    % At this point we know total amount of moles of each species in the system.
    % After the valve between NC tank and heater tank is opened, pressure will
    % equalize (rise in htank and fall in NC tank), thus some of steam will
    % condense back - that's the only unknown at this point

    %initial guess (ideal gas eq)
    %if we have 0 NC filled from NC tank, skip this step

        moles_h2o_htank=moles_h2o_Htank_filling;
        moles_total=P_htank_full*100000*(vol.heaterTank-vol.waterTank)/R/T_htank_full;

    %perform NC filling calculation only if this is not a PURE STEAM test
    %that's what the below if clause does
    if P_NCtank_full==0
        moles_N2_htank=moles_N2_Htank_filling;
        moles_He_htank=0;
        % those two below are to pass values outside back to main program
        N2_mole_frac_init=0;
        He_mole_frac_init=0;
    else
        flag=0;

        while flag==0
%
            moles_NC=moles_total-moles_h2o_htank-moles_N2_Htank_filling;   %these are moles
that entered heater tank from NC tank, hence substract the original leftovers
            moles_N2_htank=moles_N2_Htank_filling+moles_NC*(1-mole_fr_He_NCtank);
            moles_He_htank=moles_NC*mole_fr_He_NCtank;
            mole_fr_h2o_htank_full=moles_h2o_htank/moles_total;
            part_press_h2o=P_htank_full*mole_fr_h2o_htank_full;
            Tsat_h2o=IAPWS_IF97('Tsat_p',part_press_h2o/10);

            %check if initial guess is OK - if the while loop below would
            %start with Tsat_h2o smaller than T_htank_full, it breaks
            if Tsat_h2o<T_htank_full
                if disp_flag==1
             disp('Step 6 error - measured T larger than T sat. Adjusting T')
                    disp('calculated Tsat_full:')
                    disp(Tsat_h2o)
                    disp('Measured T_full: ')
                    disp(T_htank_full)
                end
                T_htank_full=Tsat_h2o;
            end
```

```
 %define fraction by which steam is condensing at each iteration (start with 0.5)
            cond_frac=0.1;
            %the while loop condenses surplus of steam to reach
            %thermodynamic balance
            while abs(Tsat_h2o-T_htank_full)>0.1
                moles_total_temp=moles_total-moles_h2o_htank*cond_frac;
                moles_h2o_htank_temp=moles_h2o_htank*(1-cond_frac);

       mole_fr_h2o_htank_full_temp=moles_h2o_htank_temp/moles_total_temp;
                part_press_h2o_temp=P_htank_full*mole_fr_h2o_htank_full_temp;
                Tsat_h2o_temp=IAPWS_IF97('Tsat_p',part_press_h2o_temp/10);

                if Tsat_h2o_temp>=T_htank_full
                    moles_total=moles_total_temp;
                    moles_h2o_htank=moles_h2o_htank_temp;
                    mole_fr_h2o_htank_full=mole_fr_h2o_htank_full_temp;
                    Tsat_h2o=Tsat_h2o_temp;
   %in case our temperature fallen too low, go a step back - reduce cond_frac
   %by half and recalculate T_sat_temp with values from previous step,
   %thus the loop will repeat current iteration with lower cond_frac
                elseif Tsat_h2o_temp<T_htank_full
                    cond_frac=0.5*cond_frac;
                end
            end

            if eos==1
                flag=1;
            elseif eos==2
                %with a good estimate of h2o molar fraction we can now check
                %total mole estimation with Redlich Kwong equation
                mole_fr_N2_htank_full=moles_N2_htank/moles_total;
                mole_fr_He_htank_full=moles_He_htank/moles_total;
                %redlich kwong needs to be redefined each time to account
                %for appropriate mixture of gases

mole_fr_array=[mole_fr_N2_htank_full,mole_fr_He_htank_full,mole_fr_h2o_htank_full];
                [~,Vm_fun,~]=Redlich_Kwong(R,Tc,pc,mole_fr_array);
                molar_vol_htank=Vm_fun(P_htank_full*100000,T_htank_full);
             %here, we check if Redlich Kwong and inital guess give the same
              %result, if not, we go back to the beginning of the while loop
                %with updated molar values
                moles_total_temp=(vol.heaterTank-vol.waterTank)/real(molar_vol_htank(1));
                condition=abs(moles_total_temp-moles_total)/moles_total_temp;
                if condition>0.001
                    moles_total=moles_total_temp;
                else
                    flag=1;
                end
            end
        end

        % those two below are to pass values outside back to main program
        mole_fr_N2_htank_full=moles_N2_htank/moles_total;
        mole_fr_He_htank_full=moles_He_htank/moles_total;

        N2_mole_frac_init=mole_fr_N2_htank_full;
        He_mole_frac_init=mole_fr_He_htank_full;
    end
    %% Calculation 7 Test conditions
    %initial guess with ideal gas
    moles_evaporated=P_Htank_test*100000*(vol.heaterTank-vol.waterTank)/R/T_Htank_test-
moles_total;
    moles_h2o_test=moles_evaporated+moles_h2o_htank;
    h2o_mole_frac=moles_h2o_test/(moles_h2o_test+moles_total);
    N2_mole_frac=moles_N2_htank/(moles_h2o_test+moles_total);
    He_mole_frac=moles_He_htank/(moles_h2o_test+moles_total);
end
```

10.5 PRECISE facility and instrumentation - technical drawings

In this part of the appendix a few drawings of the facility assembly, the test tube, movable conductivity and temperature probe as well as GHFS mounting in the tube are provided.

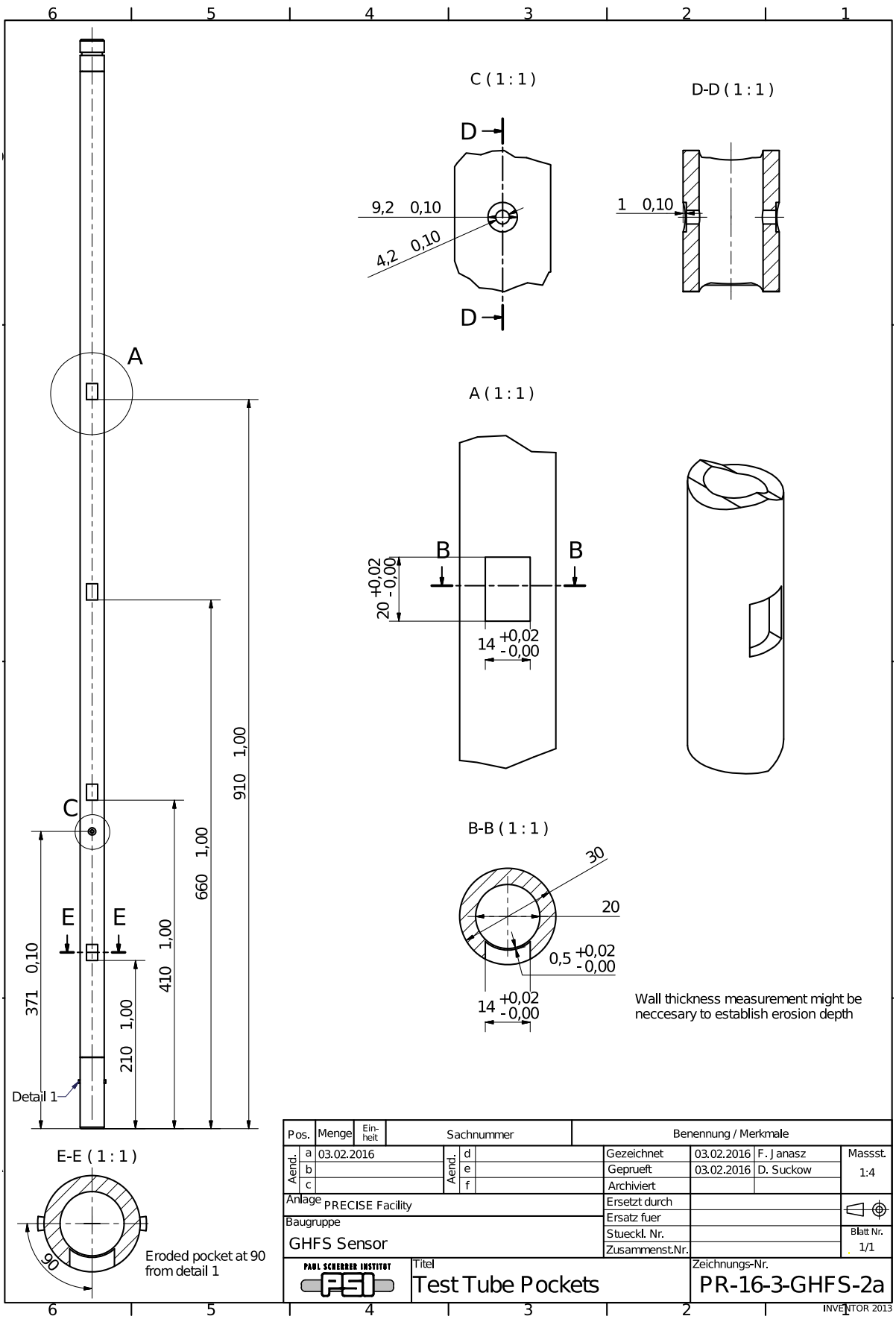

Pos.	Menge	Einheit	Sachnummer	Benennung / Merkmale

Aend.			Aend.						
	a	03.02.2016		d		Gezeichnet	03.02.2016	F. J anasz	Massst. 1:4
	b			e		Geprueft	03.02.2016	D. Suckow	
	c			f		Archiviert			

Anlage	PRECISE Facility	Ersetzt durch
		Ersatz fuer
Baugruppe	GHFS Sensor	Stueckl. Nr.
		Zusammenst.Nr.

Blatt Nr. 1/1

PAUL SCHERRER INSTITUT PSI

Titel: Test Tube Pockets

Zeichnungs-Nr.: PR-16-3-GHFS-2a

INVENTOR 2013

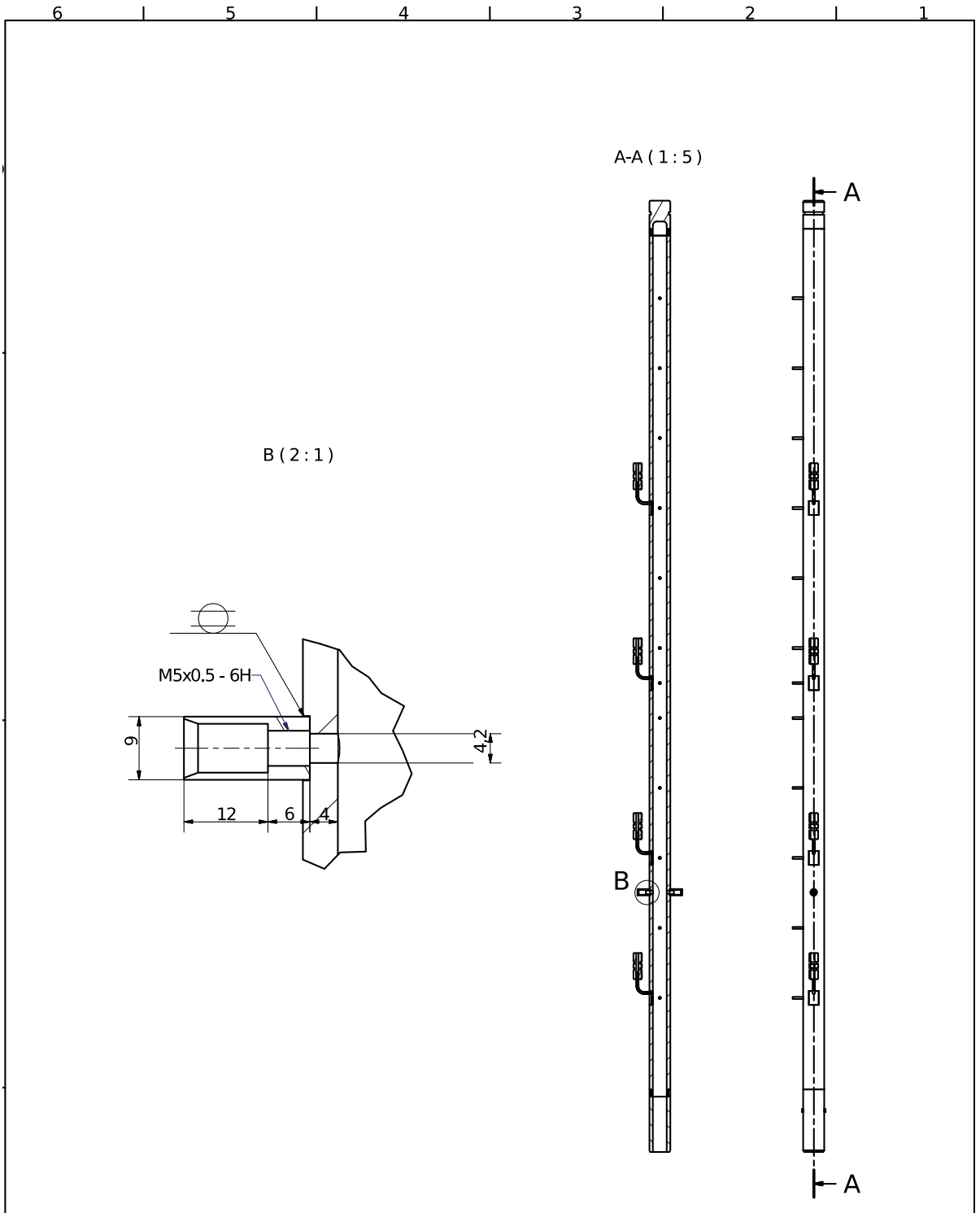

Pos.	Menge	Einheit	Sachnummer	Benennung / Merkmale

Aend.			Aend.					
	a	17.03.2016		d		Gezeichnet	17.03.2016 F. Janasz	Massst. 1:5
	b	31.03.2016		e		Geprueft		
	c			f		Archiviert		

Anlage	PRECISE Facility
Baugruppe	Test Tube Assembly
Ersetzt durch	
Ersatz fuer	
Stueckl. Nr.	
Zusammenst.Nr.	
Blatt Nr.	1/1

PAUL SCHERRER INSTITUT PSI

Titel: TC Positioning

Zeichnungs-Nr.: PR-16-3-TT-1b

INVENTOR 2013

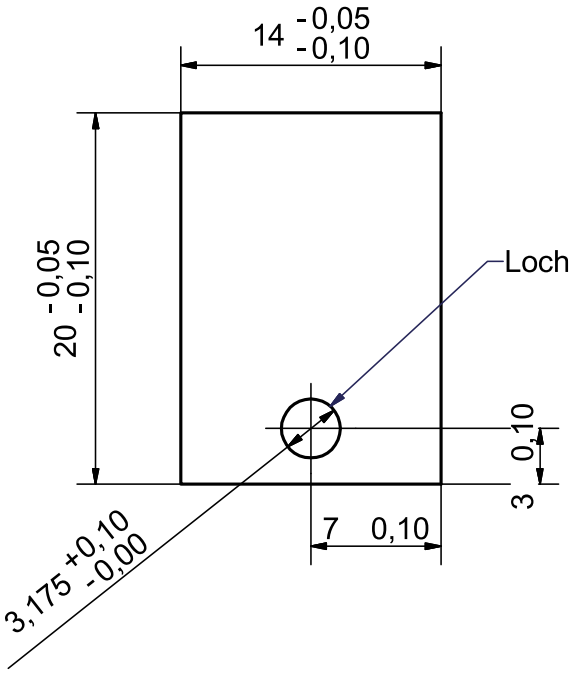

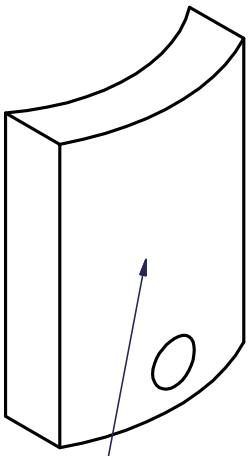

Auf dieser Fl che,
lassen Kanten scharf

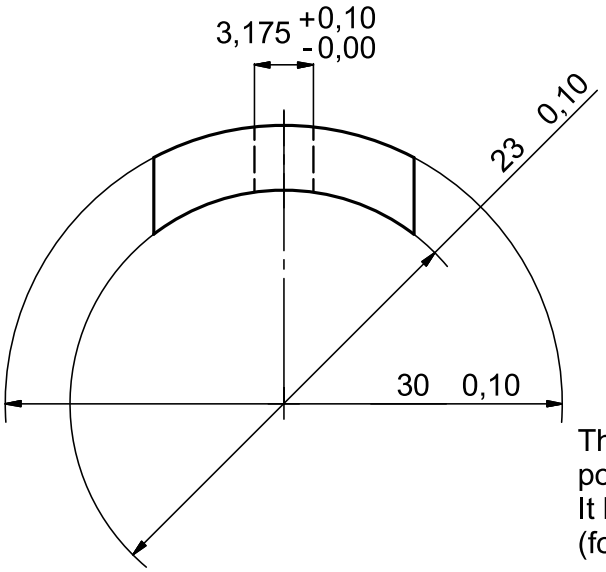

This plug is a corresponding part to pockets shown in PR-16-4-GHFS-2a
It has to fit the pocket with tight fit (for laser welding later on)

Pos.	Menge	Einheit	Sachnummer	Benennung / Merkmale

Aend.			Aend.					
a	30.02.2016		d		Gezeichnet	03.02.2016	F. Janasz	Massst. 3:1
b			e		Geprueft	03.02.2016	D. Suckow	
c			f		Archiviert			

Anlage PRECISE Facility	Ersetzt durch	
	Ersatz fuer	
Baugruppe GHFS Sensor	Stueckl. Nr.	Blatt Nr. 1/1
	Zusammenst.Nr.	

PAUL SCHERRER INSTITUT PSI	Titel GHFS Plug	Zeichnungs-Nr. PR-16-4-GHFS-1a

INVENTOR 2013

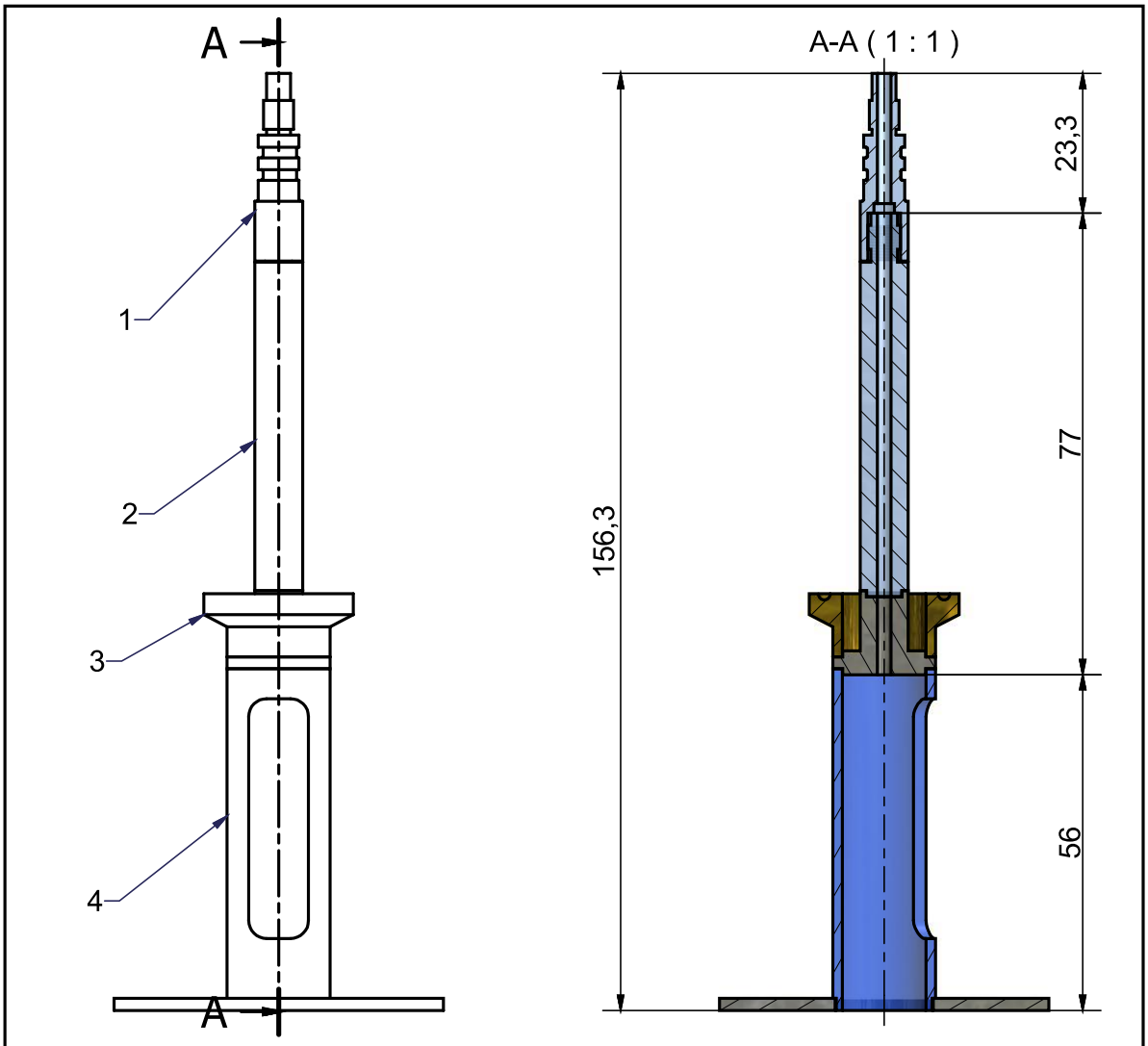

Pos.	Menge	Einheit	Sachnummer	Benennung / Merkmale
4	1	Stk.	PR-3-2014-MP5-c	Probe Engine Mount
3	1	Stk.	PR-4-2014-MP8-a	Probe Guide Ferrule DN10A
2	1	Stk.	PR-4-2014-MP5-b	Probe Guide Back
1	1	Stk.	PR-4-2014-MP5-a	Probe Guide Front

Aend.			Aend.					
	a	20.03.2014		d		Gezeichnet	20.03.2014	20.03.2014
	b			e		Geprueft		
	c			f		Archiviert		

Massst. 1:1

Anlage PRECISE Facility

Baugruppe

Movable Probe

Ersetzt durch	
Ersatz fuer	
Stueckl. Nr.	
Zusammenst.Nr.	

Blatt Nr. 1/1

PAUL SCHERRER INSTITUT PSI

Titel

Movable Probe Guide

Zeichnungs-Nr.

PR-4-2014-MP6-a

INVENTOR 2013

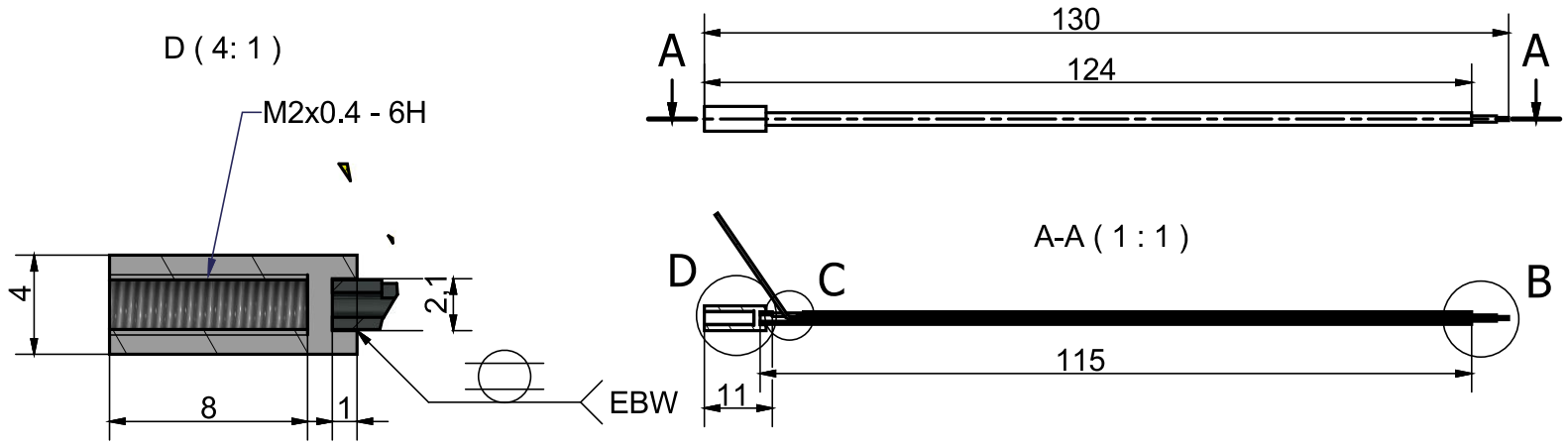

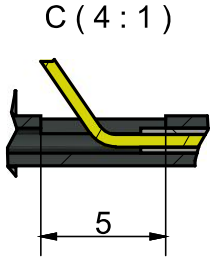

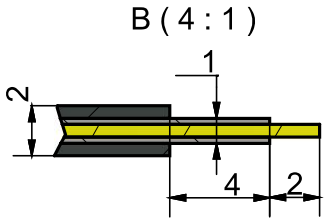

Pos.	Menge	Einheit	Sachnummer	Benennung / Merkmale
4	1			
3	1			
2	10	mm	1.4404, PSI 02.025.1004	Rundstahl, rostfrei, 4 mm
1	107	mm	1.4301, PSI 02.043.0020	Kapillarrohr rostfrei, 2.0 x 1.0 mm

Aend.			Aend.					
a	19.03.2014		d			Gezeichnet	19.03.2014	Filip Janasz
b			e			Geprueft		
c			f			Archiviert		

Massst. 1:1

Anlage PRECISE Facility

Baugruppe Movable Probe

Ersetzt durch

Ersatz fuer

Stueckl. Nr.

Zusammenst.Nr.

Blatt Nr. 1/1

PAUL SCHERRER INSTITUT PSI

Titel: Movable Electrode/TC

Zeichnungs-Nr.: PR-4-2014-MP4-b

INVENTOR 2013

All O-ring groove radii 0.25
and tolerances 0.07
O-ring ID 5 x 1 mm

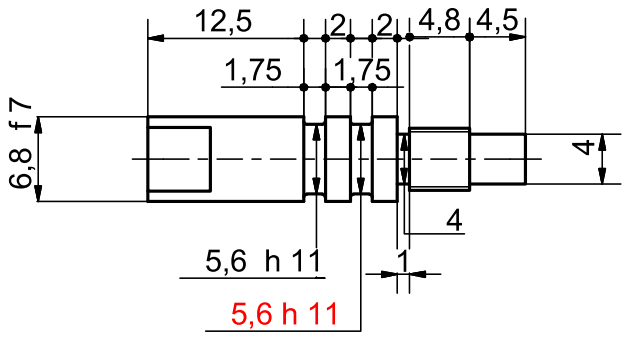

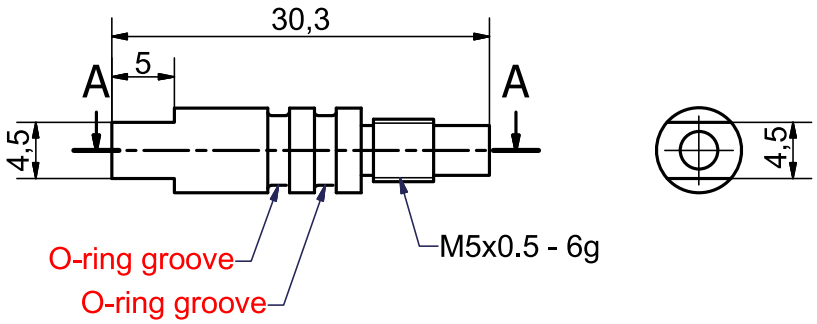

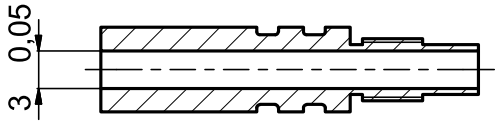

A-A (2 : 1)

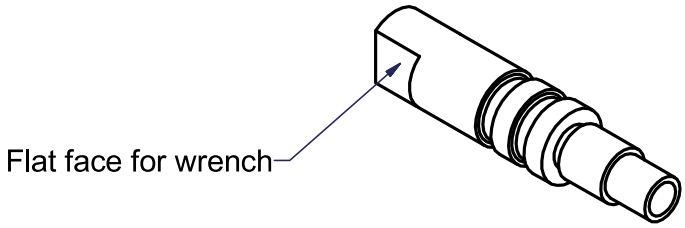

1	30	mm	1.4404, PSI 02.025.1008	Rundstahl, rostfrei, 8 mm
Pos.	Menge	Ein-heit	Sachnummer	Benennung / Merkmale

Aend.			Aend.					
a	19.03.2014		d		Gezeichnet	19.03.2014	Filip Janasz	Massst.
b	09.04.2014		e		Geprueft			2:1
c	15.09.2014		f		Archiviert			

Anlage PRECISE Facility		Ersetzt durch	
		Ersatz fuer	
Baugruppe		Stueckl. Nr.	Blatt Nr.
Movable Probe		Zusammenst.Nr.	1/1

PAUL SCHERRER INSTITUT PSI	Titel Fixed Probe Shielding	Zeichnungs-Nr. PR-4-2014-MP1-a

INVENTOR 2013

a